

UCSF

UC San Francisco Electronic Theses and Dissertations

Title

Understanding ECM Remodeling and Signaling in Breast Tumor Progression and Therapy Response

Permalink

<https://escholarship.org/uc/item/29f2w2d6>

Author

Drain, Allison Paige

Publication Date

2020

Peer reviewed|Thesis/dissertation

Understanding ECM Remodeling and Signaling in Breast Tumor Progression and Therapy Response

by
Allison Drain

DISSERTATION
Submitted in partial satisfaction of the requirements for degree of
DOCTOR OF PHILOSOPHY

in
Bioengineering

in the
GRADUATE DIVISION

of the
UNIVERSITY OF CALIFORNIA, SAN FRANCISCO
AND
UNIVERSITY OF CALIFORNIA, BERKELEY

Approved:

DocuSigned by:
Valerie Weaver Valerie Weaver
48C0A2F0F26A4A7... Chair

DocuSigned by:
Zena Werb Zena Werb

DocuSigned by:
Daniel Fletcher Daniel Fletcher
DD28103531044C7...

Committee Members

Copyright 2020
by
Allison P. Drain

Acknowledgements

First, thank you to my mentor and advisor, Dr. Valerie Weaver. I have learned so much from you, and I am truly grateful to have had the opportunity to work in your laboratory. You provided every opportunity to learn, network, and explore my interests. Furthermore, your frank assessments of the state of the field and academic life were invaluable insights that together with exceptional scientific training, have thoroughly prepared me for the next stage of my career and beyond.

I'd like to thank my committee: Dr. Zena Werb, Dr. Daniel Fletcher, and Dr. Matthew Spitzer for their guidance and advice both regarding the contents of this dissertation and regarding my future pursuits.

Thank you to my family for their unwavering support and encouragement. Thank you especially to my mother who has always backed me 100% no matter where my interests and ambitions carried me. All of my successes are your successes.

I am also enormously grateful for the extraordinary colleagues I've had the pleasure of working with throughout my time in the Weaver lab. First and foremost, thank you to Dr. Ori Maller for his mentorship, his patience and generosity to teach me, and his friendship. I feel incredibly fortunate to have learned so much from such a thoughtful, intelligent, and savvy scientist. Thank you, Janna and Mike, for fielding and endless barrage of questions and not completely losing patience with me. Thank you, FuiBoon for all the jokes, conversations, and advice that brightened many days, nights, and weekends.

Graduate school has not been without its difficult times, and I am immeasurably thankful for many wonderful friends without whom the last six years would have likely proven unbearable. My friends inspire me in many ways to be the very best version of myself. They have challenged

me to be kinder and more confident, to think deeply about ethics and pressing philosophical questions, and to be more self-aware. Thank you, Bridgette for your listening ear, for being the most dependable friend, and most importantly, for the drinks. Thank you, Rami, Karen, Jon, Courtney, Dave, and Roberto for all the fun times, all the serious times, and excellent debates. I cannot imagine a better group of friends to go through graduate school with.

Contributions

1. Leight, J. L., Drain, A. P. and Weaver, V. M. Extracellular Matrix Remodeling and Stiffening Modulate Tumor Phenotype and Treatment Response. *Annu. Rev. Cancer Biol.* **1**, 313–334 (2017).
2. Drain, A.P. and Weaver, V.M. Matrix Molecules and Their Ligands. Chapter 8 *Principles of Tissue Engineering 5th Edition*. (2020).
3. Takai, K., Drain, A.P., Lawson, D.A., Littlepage, L.E., Karpuj, M., Kessenbrock, K., Le, A., Inoue, K., Weaver, V.M., and Werb, Z. Discoidin domain receptor 1 (DDR1) ablation promotes tissue fibrosis and hypoxia to induce aggressive basal-like breast cancers. *Genes Dev.* **32**, 244–257 (2018).
4. Maller, O., Drain, A.P., Barrett, A.S., *et al.* Inflammation promotes tumor aggression by stimulating stromal cell-dependent collagen crosslinking and stromal stiffening. *bioRxiv* 2020.02.13.948141 (2020). doi:10.1101/2020.02.13.948141

Understanding ECM Remodeling and Signaling in Breast Tumor Progression and Therapy Response

Allison P. Drain

Abstract

Breast cancer is the second leading cause of cancer-related death among women in the United States. While the five-year survival rate of premetastatic tumors is high, nearly 90%, this plummets to 27% once metastasis is detected within a distant organ, underscoring a pressing unmet clinical need to prevent and treat metastatic breast cancer. Excessive extracellular matrix (ECM) deposition and remodeling occurs alongside breast tumor progression and has been directly implicated in facilitating breast tumor metastasis. However, many of the mechanisms by which tumor-associated ECM remodeling promotes metastasis are unclear. This thesis addresses this knowledge gap from multiple angles, clarifying prometastatic mechanisms of biochemical and biomechanical ECM signaling as well as in-depth characterization of the causes and nature of pathological ECM remodeling in breast cancer. This research utilizes techniques across a spectrum of length scales including *in vitro* cell culture manipulations, orthotopic and genetically engineered mouse models, and human patient samples to establish robust, clinically relevant findings. First, this thesis examines the role of collagen-discoidin domain receptor 1 (DDR1) signaling and shows that DDR1 expression may play an important role dictating mammary epithelial differentiation and loss of DDR1 signaling may in part explain how highly aggressive, basal-like tumors form. The next chapter characterizes collagen remodeling in human breast tumors and shows triple negative tumors are particularly enriched for collagen crosslinks. Manipulations in mice suggest stromal cells primarily drive collagen crosslinking, and infiltrating macrophages activate stromal cells in the early stages of tumor development. Moreover, we identify stromal lysyl hydroxylase 2, the enzyme responsible for the formation of high valency collagen crosslinks found in rigid and fibrotic tissues, as a predictor of poor survival and a potentially useful biomarker to stratify patients for therapy. The following chapter examines how

ECM stiffness in triple negative breast cancer influences therapy response. We demonstrate that treatment resistant residual disease occupies a soft ECM niche and that a compliant matrix tunes the NF- κ B – JNK signaling axis to promote cell survival upon administration of apoptosis-inducing therapeutics such as chemotherapy and radiation. Finally, we explore the relationship between ECM stiffness and prometastatic tumor immunity. Collectively, these findings advance our understanding of mechanisms that promote breast tumor metastasis and provide considerable insights to inform the development of effective therapeutic strategies to prevent and treat metastatic disease.

Table of Contents

Chapter 1: Introduction.....	1
Chapter 2: Discoidin domain receptor 1 (DDR1) ablation promotes an aggressive, basal-like breast tumor phenotype	10
Chapter 3: Collagen crosslinking and stiffening in breast tumors is primarily regulated by macrophage-stimulated fibroblasts and promotes tumor aggression.....	38
Chapter 4: Extracellular matrix compliance drives treatment resistance in triple negative breast cancer through elevated NF- κ B signaling	81
Chapter 5: LOX-mediated ECM stiffening reshapes immune cell populations and regulates tumor metastasis.....	115
Chapter 6: Conclusions and Future Directions	139
References	152

List of Figures

Figure 2.1: DDR1 is expressed in luminal epithelial cells and regulates basal/myoepithelial cells.	15
Figure 2.2: DDR1 ^{-/-} mammary tumors grow faster and are more basal and necrotic.	17
Figure 2.3: PyMT/DDR1 ^{-/-} tumors have increased fibrosis and exhibit increased mechanochemical tension.....	22
Figure 2.4: Loss of DDR1 results in increased lung metastases.....	23
Figure 2.5: CD90 ⁺ CD24 ⁺ cells from PyMT/DDR1 ^{-/-} tumors transplanted into wild-type mice yield high-grade tumors resembling the PyMT/DDR1 ^{-/-} primary tumors.....	25
Figure 2.6: DDR1 expression predicts prognosis in breast cancer..	27
Figure 3.1: Hydroxylysine collagen crosslink abundance correlates with human breast cancer aggression..	44
Figure 3.2: LOX and PLOD2 are enriched in TNBC and predominantly expressed by stromal cells..	47
Figure 3.3: Epithelial-derived collagen crosslinking enzymes fail to induce collagen crosslinking.	50
Figure 3.4: Stromal-derived LOX regulates collagen crosslinking and stiffening.....	52
Figure 3.5: Tumor infiltrating macrophages secrete TGF β to activate stromal-mediated collagen crosslinking.....	56
Figure 3.6: Stromal LH2 predicts poor patient outcomes.....	61
Figure 4.1: Treatment resistant residual disease localizes within a soft ECM niche..	85
Figure 4.2: Stiff ECM enhances chemotherapeutic efficacy.....	88
Figure 4.3: ECM stiffness sensitizes tumors to chemotherapy in mice.	89
Figure 4.4: Stiff ECM enhances efficacy of radiation therapy.	91

Figure 4.5: Proliferation cannot explain ECM stiffness-mediated sensitivity to apoptosis-inducing therapies.....	92
Figure 4.6: ECM stiffness broadly sensitizes cells to apoptosis through proliferation-independent pathways.	94
Figure 4.7: Enhanced JNK activity in cells on stiff ECM sensitizes cells to chemotherapy.....	96
Figure 4.8: A soft ECM increases NF-κB signaling to regulate JNK activity and apoptosis.....	97
Figure 4.9: NF-κB activity antagonizes tumor therapy..	99
Figure 5.1: Stromal LOX overexpression causes neutrophil accumulation in tumors.....	121
Figure 5.2: Stromal LOX overexpression modulates some cytokines related to neutrophil production and chemotaxis.	123
Figure 5.3: Neutrophils in LOX overexpressing tumors are older but do not alter metastasis. .	126
Figure 5.4: Stromal LOX overexpression using the Pdgfrb promoter increases lung neutrophil abundance and modulates metastasis.....	128
Figure 5.5: PDXs with soft ECM have more lung neutrophils and increased proinflammatory signaling.....	129

Chapter 1: Introduction

Breast cancer is the most commonly diagnosed malignancy in women in the US, with 268,600 new cases and 41,760 deaths reported annually¹. The primary cause of breast cancer-related mortality is metastasis, the colonization of distant organs such as bone, liver, lung, and brain by disseminated breast tumor cells. Indeed, after a tumor has metastasized the five year survival rate plummets from 90% to 27%¹. This suggests that while clinicians achieve moderate success in treating localized tumors, there is a pressing unmet clinical need to treat metastatic disease and if possible, prevent it altogether. Metastasis proceeds through a well-defined series of steps beginning with tumor cell invasion into the parenchyma and intravasation into lymphatic or hematologic vasculature. While the vast majority of intravasated cells will die prior to extravasation, a small subset will successfully exit circulation and enter a potential site of distant metastasis. Yet only a subset of these cells will persist in the secondary site, and these disseminated cells may remain dormant for many years before growing into an established metastatic tumor. Insights into both the biological factors that support progression through the metastatic cascade and impede therapeutic efficacy will be critical in reducing breast cancer specific mortality.

Alongside breast tumor growth and progression of the metastatic cascade is a progressive accumulation and remodeling of extracellular matrix (ECM). Importantly, the ECM has been directly implicated in promoting tumor metastasis and impairing therapeutic efficacy. The ECM is a complex, polymeric extracellular network of glycoproteins and proteoglycans that acts as a scaffold to support tissue structure, supports tissue organization, and provides signaling cues to orchestrate cell- and tissue-level behaviors. The broad spectrum of ECM functions within tissue can be ascribed to the extensive diversity and organizational complexity of constituent ECM molecules. Moreover, most ECM proteins contain multiple domains that incorporate various biological activities within a single protein. Many domains serve as binding sites for other common

ECM domains and thus facilitates the polymeric assembly of an extensively interconnected insoluble protein matrix.

Cells receive both biochemical and mechanical signals from ECM. Biochemical signals can be direct through cell ligation of different ECM proteins or indirect through ECM binding and sequestration of growth factors like TGF β , FGF, and many others, thus regulating their availability for cell signaling. Glycosaminoglycan content also regulates tissue osmolarity that can affect cell behavior²⁻⁴. Cells sense and respond to a variety of physical and mechanical properties. ECM viscoelasticity plays a significant role regulating cellular activities. Viscoelasticity is a property of materials that display both elastic and viscous characteristics upon deformation. While it is known that most native ECMs are viscoelastic, due to technical limitations, only the elastic component has been well characterized in most tissues. Only recently has attention been devoted to understanding the biological implications of viscous effects upon ECM deformations^{5,6}. Consequently, the terms ECM “stiffness” or “rigidity” in the literature often refer exclusively to ECM elasticity, and will be used as such hereafter. In addition to stiffness, matrix topology, that is the shape of assembled ECM network, can regulate cell motility and polarity⁷⁻¹⁰. Porosity, the size and quantity of pores within a 3D matrix also influences motility, and cell confinement can elicit unique cell behaviors as well¹⁰⁻¹². Both ECM composition and organization significantly influence physical and mechanical ECM properties.

Cells use a variety of cell surface receptors to bind and interact with ECM proteins. The most prominent and well-characterized class of ECM receptors are the integrins^{13,14}. Integrins are obligate heterodimers consisting of one α subunit and one β subunit. In human cells there are 18 known α subunits and 8 β subunits that combine to form 24 unique integrin pairs. Integrins vary in specificity, with some binding only one ligand and others capable of binding multiple. The cytoplasmic tail of integrins binds cytoskeletal elements thus connecting the ECM to intracellular activities. Tension generated by actomyosin contractility through integrin-mediated adhesions is

a dominant mechanism by which cells sense ECM stiffness^{14–18}. Cells also bind ECM proteins and proteoglycans through several other receptors including discoidin domain receptors (DDR), some transmembrane heparan sulfate proteoglycans like syndecans and agrin, laminin receptor, various hyaluronan receptors, lipoprotein receptors, immunoglobulin-like collagen receptors, collagen-binding mannose receptors, and others.

ECM is highly tissue specific, and in the human breast consists of two distinct ECM structures: a basement membrane surrounding milk ducts and an outlying interstitial matrix between ducts. The basement membrane organizes into a mesh-like architecture composed largely of laminin and collagen IV. Cell adhesion to the basement membrane is necessary for ductal epithelial cell survival and polarization¹⁹. Once neoplastic cells breach the basement membrane and invade into the interstitial space, they are defined as malignant tumor cells. At this stage, the tumor cells interact directly with the collagen I rich interstitial matrix. Collagen I forms a fibrillar matrix that can drastically vary in its mechanical properties depending on its architecture and abundance^{20–22}.

Extensive ECM deposition and remodeling coincide with breast tumorigenesis. Breast tumor ECM is largely comprised of collagen I, which is progressively reorganized and stiffens as tumors evolve. This fibrotic tumor-associated ECM both compromises therapeutic efficacy and promotes metastatic dissemination^{23–25}. The characteristically more aggressive breast tumor subtypes, basal-like and HER2 positive, have thicker collagen fibers and overall stiffer collagen ECM compared to luminal breast tumors²⁶. A stiff ECM promotes cell invasion through enhanced integrin clustering and Rho GTPase that mediates the assembly of filopodia and invadosomes^{27–29}. Thick, linearized bundles of collagen fibers also facilitate the migration of tumor cells out of the tumor core toward sites of intravasation^{30,31}. Moreover, a stiff ECM can promote cell survival and proliferation via multiple molecular mechanisms including elevated focal adhesion kinase (FAK) activity and enhanced sensitivity to growth factor signaling^{27,32–34}. A major factor increasing

collagen stiffness is enhanced intramolecular crosslinking catalyzed by the lysyl oxidase (LOX) family of enzymes. My lab has previously shown that orthotopically injected tumors grow substantially larger after LOX conditioning of the mammary fat pad and that attenuating collagen crosslinking using the pharmacological inhibitor β -aminopropionitrile (BAPN) reduces the number of circulating tumor cells and inhibits the formation of distant metastases³⁵ (unpublished data). These findings stress the clinical relevance of ECM stiffness to malignancy and metastasis and underscore the need to clarify the molecular pathways by which the ECM promotes metastasis and identify therapeutically actionable targets to antagonize them.

Despite an abundance of evidence establishing a link between ECM mechanics and breast tumor metastasis, our understanding is far from complete. Several crucial outstanding questions remain:

1. How does signaling with the collagen matrix alter tumor progression and metastasis?
2. What triggers the development of a fibrotic tumor-associated ECM and how does the ECM evolve with tumor progression?
3. How can ECM signaling pathways be targeted to enhance therapeutic efficacy and reduce metastasis?
4. How do stromal cells respond to tumor-associated ECM and how might this contribute to metastatic progression?

The principal motif of my thesis centers around expanding our understanding of precise mechanisms by which the ECM is modified throughout tumor progression and the molecular mediators of prometastatic cell-ECM signaling. I took a highly quantitative approach utilizing both *in vitro* and *in vivo* models as well as human patient data to gain insight into these phenomena. Specifically, this motif is born out in four sections:

1. Investigating the role of DDR1 signaling in breast homeostasis and tumor phenotype

2. Understanding the origin and nature of collagen crosslinks in breast tumors and their contribution to poor patient outcome
3. ECM regulation of therapy response in triple negative breast cancer
4. Examining cooperation of collagen crosslinking and ECM stiffening with prometastatic immune cell phenotypes in the primary tumor and premetastatic niche

Investigating the role of DDR1 signaling in breast homeostasis and tumor phenotype

The discoidin domain receptor 1 is over-expressed in breast carcinoma cells. Low DDR1 expression is associated with worse relapse-free survival reflecting its controversial role in cancer progression. We detected DDR1 on luminal cells, but not on myoepithelial cells of DDR1^{+/+} mice. We found DDR1 loss compromises cell adhesion, consistent with data that older DDR1^{-/-} mammary glands had more basal/myoepithelial cells. Basal cells isolated from older mice exerted higher traction forces than the luminal cells, in agreement with increased mammary branches observed in older DDR1^{-/-} mice and higher branching by their isolated organoids. When we crossed DDR1^{-/-} mice with MMTV-PyMT mice, the PyMT/DDR1^{-/-} mammary tumors grew faster, had increased epithelial tension and matricellular fibrosis, with a more basal phenotype and increased lung metastases. DDR1 deletion induced basal differentiation of CD90⁺CD24⁺ tumor initiating cells, and the increase correlated with tumor cell mitoses. K14⁺ basal cells including K8⁺K14⁺ cells were increased adjacent to necrotic fields. These data suggest that the absence of DDR1 provides a growth and adhesion advantage that favors the expansion of basal cells, potentiates fibrosis and enhances necrosis/hypoxia and basal differentiation of transformed cells to increase their aggression and metastatic potential.

Understanding the origin and nature of collagen crosslinks in breast tumors and their contribution to poor patient outcome

Collagen deposition and stromal stiffening accompany malignancy, compromise treatment, and promote tumor aggression. Clarifying the molecular nature of and the factors that

regulate extracellular matrix stiffening in tumors should identify biomarkers to stratify patients for therapy and therapeutic interventions to improve outcome. We profiled lysyl hydroxylase- and lysyl oxidase-mediated collagen crosslinks and quantified the greatest abundance of total and complex collagen crosslinks in more aggressive human breast cancer subtypes with the stiffest stroma. These tissues also harbored the highest number of tumor-associated macrophages (TAM), whose therapeutic ablation not only reduced metastasis, but also concomitantly decreased accumulation of collagen crosslinks and stromal stiffening. Epithelial-targeted expression of the crosslinking enzyme lysyl oxidase had no impact on collagen crosslinking in PyMT mammary tumors, whereas stromal cell targeting did. Consistently, stromal cells in microdissected human tumors expressed the highest level of collagen crosslinking enzymes. Immunohistochemical analysis of a cohort of breast cancer patient biopsies revealed that stromal expression of lysyl hydroxylase two, an enzyme that induces hydroxylysine aldehyde-derived collagen crosslinks and stromal stiffening correlated significantly disease specific mortality. The findings link tissue inflammation, stromal cell-mediated collagen crosslinking and stiffening to tumor aggression and identify lysyl hydroxylase two as a novel stromal biomarker.

ECM regulation of therapy response in triple negative breast cancer

Triple negative breast cancers (TNBCs) are associated with poor survival, which can be predicted in part by lack of response to neoadjuvant chemotherapy. TNBCs are highly fibrotic, yet little is known regarding how the extracellular matrix (ECM) evolves following therapy and whether it may impact treatment response. Analysis revealed that while primary untreated TNBCs are surrounded by a highly rigid microenvironment, treatment resistant residual tumors following neoadjuvant chemotherapy inhabit a softer niche. This suggests that the biophysical properties of the tumor microenvironment regulate treatment resistance. Consistently, 3D organoid cultures and xenograft studies of premalignant and malignant TNBC showed organoids interacting with a soft ECM exhibited a striking resistance to chemotherapy, ionizing radiation and death receptor

ligand TRAIL. A stiff ECM enhanced pro-apoptotic JNK activity to sensitize cells to treatment, whereas a soft ECM promoted treatment resistance by elevating NF- κ B activity and compromising JNK activity. Critically, treatment resistant residual human TNBCs residing within soft stroma had elevated NF- κ B levels, and disengaging NF- κ B activity sensitized tumors in a soft matrix to therapy. Accordingly, the biophysical properties of the ECM modify treatment response, and ancillary agents that modulate stiffness-dependent NF- κ B or JNK activity could enhance chemotherapeutic efficacy in patients with TNBC.

Examining cooperation of collagen crosslinking and ECM stiffening with prometastatic immune cell phenotypes in the primary tumor and premetastatic niche

ECM remodeling modulates many facets of the tumor microenvironment and potentiates metastatic progression. Immune cells comprise a prominent portion of the tumor microenvironment and exert potent effects at multiple levels of the metastatic cascade. Reshaping immune cell phenotypes to antagonize tumor growth and metastasis also holds immense promise as a therapeutic strategy. Thus, understanding factors that influence immune phenotypes and function is critically important. Here, we examined how ECM stiffness may alter immune cell populations and phenotypes in the primary tumor and the premetastatic niche. We characterized immune cell infiltrate into the primary tumors and lungs of LOX overexpressing mice and found an increased accumulation of neutrophils, which we attribute primarily to prolonged survival and in part to increased bone marrow production and chemotaxis. Neutrophils may adopt either anti- or pro-tumorigenic phenotypes, and while our analysis of phenotype is not conclusive, the overall cytokine milieu of LOX overexpressing tumors supports conjecture of an anti-tumor neutrophil phenotype. In contrast, mice bearing PDX tumors injected in softer collagen matrix show higher levels of inflammatory signaling and have more neutrophils in the premetastatic lung. Moreover, LOX overexpression shows a strain-specific metastasis phenotype in which stromal overexpression promotes metastasis on the FVB background and restrains metastasis on the

C57BL6. These data point to a complex interplay of ECM stiffness, LOX, and neutrophil regulation that should be explored further.

Chapter 2: Discoidin domain receptor 1 (DDR1) ablation promotes an aggressive, basal-like breast tumor phenotype

In collaboration with: Ken Takai^{1,2}, Devon A. Lawson^{1,a}, Laurie E. Littlepage^{1,b}, Marcela Karpuj^{1,c}, Kai Kessenbrock^{1,d}, Annie Le¹, Kenichi Inoue², Valerie M. Weaver^{3,4,5} and Zena Werb^{1,6}

¹Department of Anatomy, University of California, San Francisco, San Francisco, California 94143;

²Division of Breast Oncology, Saitama Cancer Center, Saitama 362-0806, Japan;

³Department of Surgery and Center for Bioengineering and Tissue Regeneration, University of California, San Francisco, San Francisco, California 94143;

⁴Department of Bioengineering and Therapeutic Sciences, University of California, San Francisco, San Francisco, California 94143;

⁵Department of Radiation Oncology, University of California, San Francisco, San Francisco, California 94143.

Contributions from previously published work: Takai et al. *Genes and Development* **2018**³⁶

Introduction

The discoidin domain receptors (DDRs) are a unique subfamily of receptor tyrosine kinases (RTKs) that bind various types of collagen. DDR1 is widely expressed in human and mouse epithelial cells including mammary epithelium, while DDR2 is prominent in mesenchymal cells and connective tissue³⁷. Both fibrillar and nonfibrillar collagens serve as ligands for DDR1, but fibrillar collagen binding has been more well characterized and is much better understood³⁸⁻⁴⁰. In contrast to most RTKs, DDRs do not dimerize upon ligand binding but rather exist as stable dimers on the cell surface, even in the absence of ligand⁴¹⁻⁴³. Instead, collagen binding induces DDR1 clustering on the cell surface, and DDR1 dimers phosphorylate neighboring dimers in trans leading to receptor activation⁴⁴. This likely explains in part why DDR1 exhibits much slower phosphorylation kinetics relative to other RTKs. DDRs are known to play a key role in embryonic development and have been linked to many pathologies including fibrosis, inflammation, atherosclerosis, and cancer⁴⁵. DDR activation is known to regulate ECM remodeling and MMPs expression, but many of the specific tyrosine phosphorylations that occur within the DDR1 cytoplasmic domain have not been mapped to phenotypes⁴⁵.

DDR1 is critical for mammary gland development⁴⁶. In mice, DDR1 knockout results in delayed pubertal mammary ductal outgrowth. However, by 3 months of age, the mammary glands of DDR1^{-/-} mice show increased mammary branching along with a high rate of mammary epithelial proliferation and increased levels of stromal collagen. In part, these divergent roles of DDR1 in mammary development may be explained by the previous reports showing that *in vitro*, DDR1 promotes cell proliferation, differentiation and migration by degrading collagen⁴⁷⁻⁵¹. However, the possible mechanism of mammary hyperproliferation and hyperbranching by DDR1 ablation at later stages remains obscure.

Because tumor progression often mirrors developmental events, understanding of the role of DDR1 in development may yield insights into the role of DDR1 in cancer. Nevertheless,

the results of mammary development in *DDR1*^{-/-} mice make it difficult to hypothesize whether DDR1 will promote or suppress cancer. Indeed, conflicting evidence exists suggesting both a pro- and anti-tumor role for DDR1. DDR1 is overexpressed in breast, ovarian, and lung carcinoma cell lines^{37,52-57}, and high expression of DDR1 correlates with poor prognosis of serous ovarian cancer, lung cancer and pancreatic ductal adenocarcinoma⁵⁸⁻⁶⁰. Activation of DDR1 by collagen promotes pro-tumorigenic phenotypes, including upregulation of the expression of MMP-1, 2 and 9, increased degradation of collagen, upregulation of expression of SOX2 and NANOG, promotion of cell invasion, metastasis and regulation of cancer stem cell traits^{47,48,60,61}. DDR1 stabilizes E-cadherin and mediates suppression of actomyosin at cell-cell contacts to promote collective cell migration^{51,62,63}. Interference with DDR1 signaling in metastatic breast cancer cell lines decreases their ability to colonize lung tissue^{60,63}. Moreover, knockdown of DDR1 decreases viability of breast, pancreatic, and ovarian cancer cell lines⁶⁴. These studies indicate that DDR1 might function as an oncogene.

In contrast, a moderate reduction in DDR1 mRNA levels was shown in the majority of middle to high-grade human breast carcinomas compared to normal mammary tissues⁴⁹. Another clinical study of lung cancer showed that low expression of DDR1 is associated with a worse prognosis than its high expression⁵⁷. Also, a clinical study of breast cancer patients showed that DDR1 expression was not predictive for survival⁶⁵. Furthermore, induction of DDR1 may inhibit migration of a DDR1-deficient breast cancer cell line⁶⁶. Disruption of DDR1 in cell-cell contacts in cancer may favor metastasis by invading blood vessels⁶³. These data indicate that deletion of DDR1 might promote aggressive cancer. As a result, the role of DDR1 in cancers is controversial.

To understand the role of DDR1 in breast tumorigenesis, we established an animal model using DDR1-knockout mice crossed into the MMTV-PyMT mouse and tested the hypothesis that

DDR1 ablation leads to an aggressive form of breast cancer. We then analyzed breast cancer databases to establish how DDR1 levels are related to prognosis.

Results

DDR1 is expressed in luminal epithelial cells and regulates basal/myoepithelial cells

Since effects of genes in development may give insights into their roles in cancer, we first verified the role of DDR1 in normal mammary gland development using the DDR1^{-/-} mouse model. When we analyzed the mammary gland tissues from DDR1^{+/+} mice by immunostaining with anti-DDR1 antibody and anti- α -smooth muscle actin (α -SMA) antibody, which is a marker of myoepithelial cells, we detected DDR1 in the luminal cell compartment, but not on myoepithelial cells (Fig. 2.1A), as was found in the kidney, where DDR1 expression also does not co-localize with staining for α -SMA following kidney injury⁶⁷.

In whole-mount carmine red-stained mammary gland tissues in DDR1^{+/+} and DDR1^{-/-} mice, we observed two distinct phenotypes, one during active pubertal growth and another in adult mammary gland. Mammary development, as assayed by primary duct lengths and frequency of mammary duct branches, was delayed in 5-week-old DDR1^{-/-} mice but was accelerated in 8-week-old DDR1^{-/-} mice (Fig. 2.1B and 2.1C). Our results showing distinct stage-specific effects of DDR1 are consistent with a previous analysis showing that development of mammary glands was delayed in 3-week-old DDR1^{-/-} mice, but that the number of mammary ducts was increased in 12-week-old DDR1^{-/-} mice due to hyper-proliferation of the epithelium⁴⁶.

To determine the mechanisms that might be involved in the altered branching phenotype, we generated a cell line with a DDR1 knockdown. Consistent with the literature, the DDR1 knockdown mammary epithelial cells were slower in attaching to collagen than the wild type control^{68,69} (Fig. A1.1A). In keeping with this phenotype, the DDR1 knockdown cells were less contractile when seeded within collagen gels (Fig. A1.1B). These data along with the known role

of DDR1 in supporting collective cell migration, suggest that DDR1 knockout directly impairs the ability of the luminal population to properly organize and execute branching morphogenesis⁶³. Indeed, by flow cytometry analysis, we observed that the basal/myoepithelial CD24^{low}CD49^{high} cell population was similar in DDR1^{-/-} and DDR1^{+/+} mice in puberty at 5 weeks of age, but was significantly increased in adult 8-week-old DDR1^{-/-} mouse mammary glands compared to DDR1^{+/+} mice (**Fig. 2.1D** and **2.1E**).

Collagen contraction assays and traction force microscopic analysis of the basal versus the luminal isolated populations revealed that the basal cells are significantly more contractile (**Fig. 2.1F**). The relevance of the altered ratio of highly contractile basal cells to luminal cells was explored by co-culturing aggregates of luminal and basal cells and assaying for branching morphogenesis. First, we crossed K14-GFP mice with the DDR1 knockout mouse line. We then isolated K14⁻ luminal cells and K14⁺ basal/myoepithelial cells from K14⁺/DDR1^{+/+} mouse mammary glands by flow cytometry (**Fig. A1.1C**), aggregated the K14⁻ luminal cells with and without K14⁺ highly contractile basal cells overnight, collected the cell aggregates, and cultured them in Matrigel for 3D organoid branching assays. Aggregating K14⁻ luminal cells with K14⁺ contractile basal/myoepithelial cells promoted mammary branching (Supplemental Fig. S1D). We then isolated K14⁻ luminal cells and K14⁺ basal/myoepithelial cells from K14/DDR1^{+/+} mice and K14/DDR1^{-/-} mice by flow cytometry and aggregated K14⁻/DDR1^{+/+} and K14⁻/DDR1^{-/-} luminal cells with K14⁺/DDR1^{+/+} and K14⁺/DDR1^{-/-} basal cells (**Fig. 2.1G**). K14⁺/DDR1^{-/-} contractile basal/myoepithelial cells promoted mammary branching (**Fig. 2.1H**). Since DDR1 is not expressed on myoepithelial cells and incubation of K14⁻/DDR1^{-/-} luminal cells with K14⁺/DDR1^{+/+} basal/myoepithelial cells did not promote mammary branching (**Fig. 2.1H**), this result indicates that DDR1 on luminal cells and interaction with K14⁺ contractile basal/myoepithelial cells is required

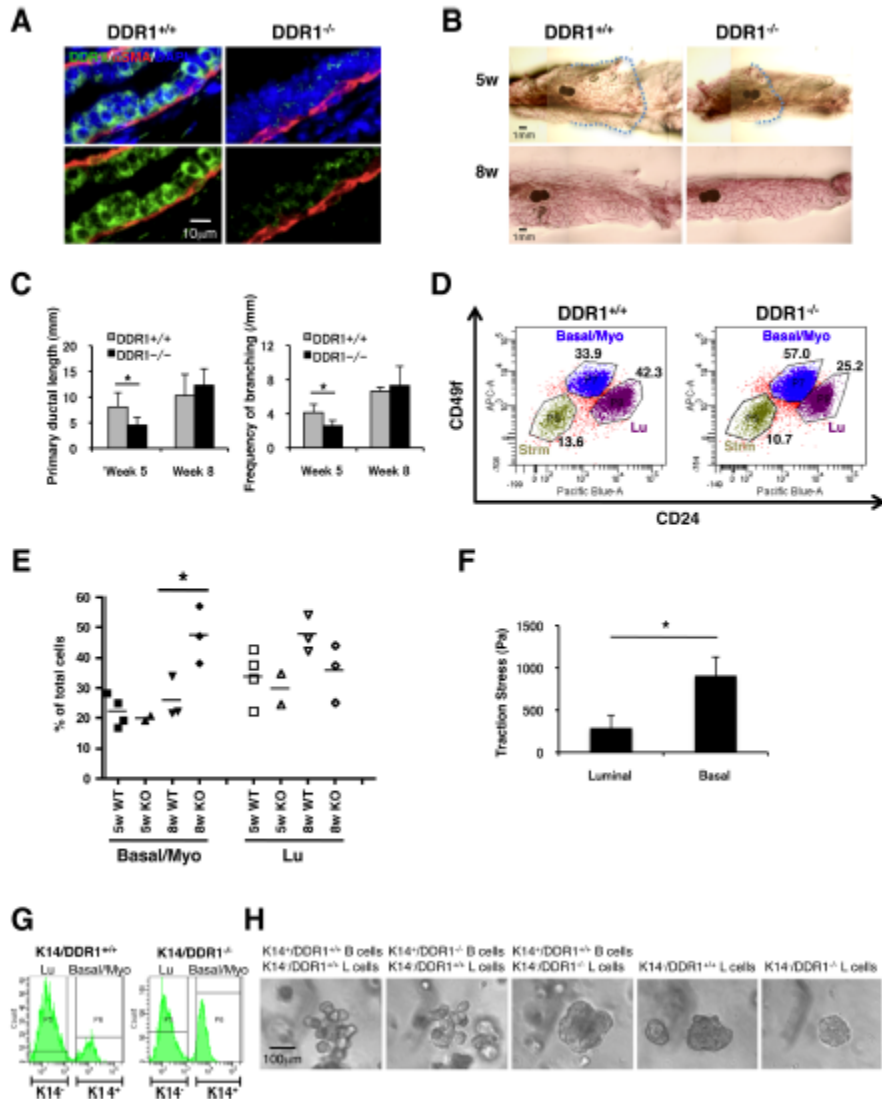


Figure 2: DDR1 is expressed in luminal epithelial cells and regulates basal/myoepithelial cells. (A) Immunofluorescence of DDR1 (green) and α-SMA (red) in mammary glands from wildtype and DDR1^{-/-} mice. (B) Representative images of carmine red wholemount staining from wildtype and DDR1^{-/-} mice. Dashed line indicates extent of ductal outgrowth at 5 weeks of age. (C) Quantification of primary ductal length and frequency of mammary branching from carmine red wholemounts. Data are shown as mean ± SD. n = 3-4 mice per group. Statistical analysis was performed using unpaired Student's t test, *p < 0.05. (D) Representative flow cytometry analysis of mammary epithelial and developmental cell populations: basal/myoepithelial cells (Basal/Myo), luminal cells (Lu), and stromal cells (Strm). (E) Quantification of cell population abundance from flow cytometry. Statistical analysis was performed using one-way ANOVA and unpaired Student's t test, *p < 0.05. (F) Quantification of maximum traction stresses generated by individual sorted luminal and basal/myoepithelial cells isolated from wildtype murine mammary glands. Statistical analysis was performed using unpaired Student's t test, **p < 0.01. (G) Populations of K14⁺ (basal/myoepithelial) and K14⁻ (luminal) cells in the mammary glands of wildtype and DDR1^{-/-} mice. (H) Phase contrast images of a three-dimensional branching assay from mixed luminal and basal/myoepithelial cells from wildtype and DDR1^{-/-} mice.

for mammary branching, likely mediated through a combination of tension-mediated interactions and paracrine signaling.

These data suggest stage-specific roles for DDR1 during mammary development. Thus, reduction of mammary branching at 5 weeks of age in DDR1^{-/-} mice may owe to the loss of DDR1 functions as a collagen receptor and collective cell migration in luminal cells, whereas the accelerated branching in DDR1^{-/-} mice at 8 weeks of age may be the result of the expansion of the basal/myoepithelial compartment.

DDR1^{-/-} mammary tumors grow faster and are more basal and necrotic

To determine how DDR1 alters in breast tumor prognosis we determined whether deletion of DDR1 leads to more aggressive breast tumors. We crossed DDR1^{-/-} mice with MMTV-PyMT mice, a transgenic luminal B breast cancer model⁷⁰ (**Fig. A1.2A**). We validated DDR1 expression levels in primary tumors of PyMT/DDR1^{+/+}, PyMT/DDR1^{+/-} and PyMT/DDR1^{-/-} mice by qPCR. As expected, PyMT/DDR1^{-/-} mice did not express DDR1, whereas DDR1 expression in PyMT/DDR1^{+/-} was intermediate as compared to PyMT/DDR1^{+/+} (**Fig. A1.2B**). In support of this model, we found that DDR1 expression was higher in luminal-type than basal-type human cancer cells⁷¹ (**Fig. A1.2C**).

Tumors from both PyMT/DDR1^{+/-} and PyMT/DDR1^{+/+} mice had similar growth rates (**Fig. 2.2A**). In contrast, primary tumors of PyMT/DDR1^{-/-} mice grew faster although there were no differences in the tumor onset (**Fig. 2.2A** and **Fig. A1.3A**), and they often showed necrotic areas with hemorrhage (**Fig. A1.3B**). In H&E stained tissue sections, the tumor tissues had large necrotic regions with more differentiated epithelial clusters surrounding the necrotic regions. The DDR1^{+/+} and DDR1^{+/-} mammary tumors were largely made up of large epithelial glandular clusters, while the DDR1^{-/-} mammary tumors had small areas of differentiated

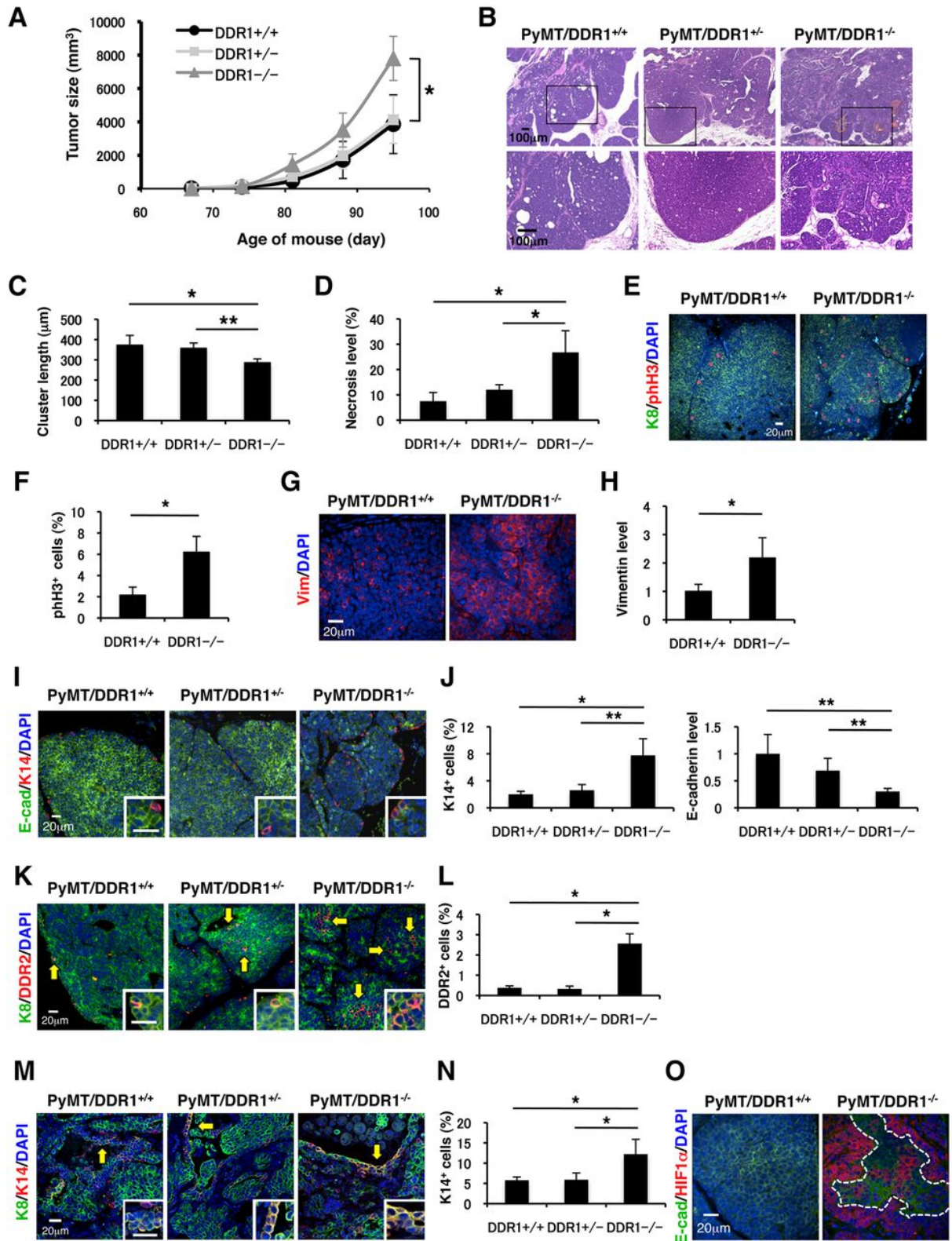


Figure 2.2: DDR1^{-/-} mammary tumors grow faster and are more basal and necrotic. (A) Primary tumor burden of PyMT/DDR1^{-/-} mice compared to PyMT/DDR1^{+/+} and PyMT/DDR1^{+/-} mice. PyMT/DDR1^{-/-} mammary tumors grow faster than control tumors. Data are shown as mean

± SD, n=4-7, * p < 0.02 (one-way ANOVA and unpaired Student's t test). **(B)** DDR1^{+/+} and DDR1^{-/-} mammary tumors showed large epithelial clusters and DDR1^{-/-} tumor showed multiple small clusters and central necrosis (orange dots) by H&E staining. Representative photographs are shown (13 weeks). n=3. **(C)** Length of epithelial tumor clusters was measured. DDR1^{-/-} primary tumors show small size clusters by H&E staining. Data are shown as mean ± SD, n=3, * p < 0.05, ** p < 0.02 (one-way ANOVA and unpaired Student's t test). **(D)** Percent of necrotic clusters out of small clusters (200-300 μm length) was measured. Necrotic small clusters increased in DDR1^{-/-} tumors. Data are shown as mean ± SD, n=3, * p < 0.01, ** p < 0.02 (one-way ANOVA and unpaired Student's t test). **(E,F)** Immunofluorescence of DDR1^{+/+} and DDR1^{-/-} mammary tumor tissues used anti-keratin 8 (green) and anti-phospho-histone H3 (phH3) (red) antibodies. DAPI (blue) stained nuclei. Representative photographs are shown **(E)**. PhH3⁺ cells were present mainly at the edge of the epithelial clusters. The percent of phH3⁺ cells per epithelial cell (keratin 8⁺ and phospho-histone H3⁺) show that DDR1^{-/-} mammary tumor cells are more proliferative (Data are shown as mean ± SD, n=3, * p < 0.02, unpaired Student's t test) **(F)**. **(G)** Immunofluorescence of DDR1^{+/+} and DDR1^{-/-} mammary tumor tissues using anti-vimentin (red) antibody and DAPI (blue) stained nuclei. Representative photographs are shown. **(H)** Expression levels of vimentin were quantified by using ImageJ software. Vimentin levels increased in DDR1^{-/-} epithelial clusters. Data are shown as mean ± SD, n=4, * p < 0.05 (unpaired Student's t test). **(I,J)** Immunofluorescence of DDR1^{+/+}, DDR1^{+/-} and DDR1^{-/-} mammary tumor tissues using anti-E-cadherin (green), anti-keratin 14 (red) antibodies, and DAPI (blue) stained nuclei. K14⁺ basal cells were mainly at the edge of the epithelial clusters. Representative photographs are shown **(I)**. The ratio of K14⁺ basal cells per epithelial (E-cadherin⁺ and K14⁺) cell increased (* p < 0.02, ** p < 0.05, one-way ANOVA and unpaired Student's t test) **(J, left panel)** and expression of E-cadherin decreased in DDR1^{-/-} epithelial clusters (** p < 0.05, one-way ANOVA and unpaired Student's t test) **(J, right panel)**. Data are shown as mean ± SD, n=3. **(K,L)** Immunofluorescence of the primary tumors was performed by using anti-keratin 8 (green) and anti-DDR2 (red) antibodies. DAPI (blue) stained nuclei. Representative photos of tumor epithelial clusters are shown **(K)**. The ratio of DDR2⁺ cells per epithelial cell increased significantly in DDR1^{-/-} epithelial clusters **(L)**. Data are shown as mean ± SD, n=3, * p < 0.01 (one-way ANOVA and unpaired Student's t test). **(M,N)** Immunofluorescence of DDR1^{+/+}, DDR1^{+/-} and DDR1^{-/-} mammary tumor tissues was conducted by using anti-keratin 8 (green) and anti-keratin 14 (red) antibodies. DAPI (blue) stained nuclei. Representative photos of tumor necrotic areas are shown **(M)**. K14⁺ basal cells including K8⁺K14⁺ basal-like cells (yellow) significantly increased near necrotic fields of DDR1^{-/-} mammary tumor tissues **(N)**. Data are shown as mean ± SD, n=3, * p < 0.05 (one-way ANOVA and unpaired Student's t test). **(O)** Immunofluorescence of DDR1^{-/-} mammary tumor tissues using anti-E-cadherin (green) and anti-HIF1α (red) antibodies and DAPI (blue) stained nuclei. The white dots represent a border between an epithelial and necrotic field (right panel). HIF1α is expressed and localized near necrosis.

epithelial clusters with increased areas of necrosis (**Fig. 2.2B-D**). Even small clusters had necrotic areas in the DDR1^{-/-} mammary tumors (**Fig. A1.3C**).

We next determined if the proliferative status of these tumors was related to their growth rates by staining tissues for phospho-histone H3 (pH3). PhH3⁺ cells were localized in the tumors mainly around the edge of the epithelial clusters. PyMT/DDR1^{-/-} mammary tumors had significantly more pH3⁺ cells than control tumors that expressed DDR1 (**Fig. 2.2E** and **2.2F**). This suggests that DDR1^{-/-} mammary tumors are more proliferative than DDR1^{+/+}.

We also examined expression of luminal markers (E-cadherin and keratin 8) and basal markers (keratin 14, vimentin and DDR2) in primary tumors by immunofluorescence. Vimentin expression levels increased in DDR1^{-/-} epithelial clusters (**Fig. 2.2G** and **2.2H**). K14⁺ basal cells mainly encircled the edge of the epithelial clusters in all three genotypes (**Fig. 2.2I**). However, K14⁺ basal cells in DDR1^{-/-} tumor epithelial clusters increased in numbers, while the expression levels of E-cadherin in DDR1^{-/-} epithelial clusters decreased (**Fig. 2.2I** and **2.2J**).

Since DDR2 also affects tumor progression, we asked if its expression was changed in the absence of DDR1^{72,73}. We observed that the number of DDR2⁺ cells increased in DDR1^{-/-} epithelial clusters and near necrotic areas (**Fig. 2.2K** and **2.2L**; **Fig. A1.3D** and **A1.3E**).

We also observed a trend towards increased K8⁺K14⁺ basal-like cells in DDR1^{-/-} epithelial clusters (**Fig. A1.3F** and **A1.3G**). However, more K8⁺K14⁺ basal-like cells were seen in the epithelial regions at the outer edge of the necrosis (**Fig. A1.3H** and **A1.3I**). K14⁺ basal cells (K8⁺K14⁺ & K8⁻K14⁺ cells) significantly increased in DDR1^{-/-} epithelial regions next to necrosis (**Fig. 2.2M** and **2.2N**), while K8⁺K14⁺ basal-like cells tended to increase (**Fig. A1.3J**).

We then determined which cell compartment proliferated in DDR1^{-/-} mammary tumors by staining tissues for K8, K14 and pH3. PhH3⁺ cells were localized mainly in K8⁺ luminal cells of the epithelial clusters (**Fig. A1.4A** and **A1.4B**). Moreover, K8⁺K14⁺ basal-like cells proliferated at

significantly higher rates, especially near the necrotic regions in DDR1^{-/-} mammary tumors (**Fig. A1.4C** and **A1.4D**). PhH3 positivity correlated with K14⁺ basal cell numbers (Correlation coefficient $r=0.75$) rather than K8⁺K14⁺ basal-like cell numbers ($r=0.07$) in epithelial clusters.

Finally, to examine whether DDR1 deletion alters the phenotype of K8⁺K14⁺ basal-like cells, we stained tumor tissues for K8, K14 and DDR2. K8⁺K14⁺ basal-like cells, which upregulated DDR2 expression, increased significantly in DDR1^{-/-} mammary tumors (**Fig. A1.5A** and **A1.5B**). Moreover, DDR1 deletion decreased branching in tumor organoids *in vitro* (**Fig. A1.5C** and **A1.5D**).

These data suggest that tumor growth correlates with K14⁺ basal cell numbers and that when DDR1 is knocked out, the tumors have a more basal phenotype and are more aggressive. Taken together these data suggest that loss of DDR1 may lead to breast cancers of poorer prognosis.

Hypoxic regions show increased hypoxia-inducible factor-1a (HIF1a) expression

Tumor necrosis is significantly associated with hypoxia and in basal-type breast cancer and is an independent predictor for early recurrence and death^{74,75}. Since reduced expression of DDR1 in primary tumors increased the amount of necrosis in tumors (**Fig. 2.2D**), we hypothesized that necrosis and hypoxia might be linked in the DDR1^{-/-} tumors. Using immunofluorescent staining for HIF1a in primary tumors, we observed that tumor necrosis was associated with hypoxia. HIF1a was highly increased in the PyMT/DDR1^{-/-} mammary tumor tissue and was expressed near necrotic regions (**Fig. 2.2O**).

PyMT/DDR1^{-/-} tumors have increased fibrosis and exhibit increased mechanochemical tension

Basal-like breast tumors often present as highly fibrotic, which contributes to disease aggression through enhanced tumor cell mechanosignaling and impaired vascularization leading

to hypoxia^{76,77}. Consistently, picrosirius red staining showed that the more basal-like DDR1^{-/-} tumors contain significantly more fibrillar collagen than the DDR1^{+/+} tumors (**Fig. 2.3A** and **2.3B**). Atomic force microscopy (AFM) further revealed that the DDR1^{-/-} tumors have a higher elastic modulus than the DDR1^{+/+} controls (**Fig 2.3C** and **2.3D**). To determine whether the stiffened, collagen-rich ECM of DDR1^{-/-} tumors corresponded to a higher level of mechanosignaling within the tumor, we analyzed levels of focal adhesion kinase (FAK) phosphorylation at tyrosine 397 in tumor lysates (**Fig 2.3E**). We observed increased FAK phosphorylation in the DDR1^{-/-} tumors, which is indicative of integrin-mediated signaling and focal adhesion formation that has been shown to promote tumor progression³⁵. Moreover, the loss of DDR1 resulted in more contractile tumors, as shown by increased pMLC2 staining in the DDR1^{-/-} tumors (**Fig. 2.3F** and **2.3G**). Given the reduction in cell contractility upon DDR1 knockdown *in vitro*, we asked whether the increased contractility in DDR1^{-/-} tumors could be attributed to the dramatic expansion of the basal/myoepithelial compartment in DDR1^{-/-} mammary glands. Indeed, using traction force microscopy on flow sorted luminal and basal/myoepithelial cells from the murine mammary glands we also showed that the basal/myoepithelial cells generated much higher traction forces (**Fig. 2.1F**). These data suggest that the aggressive, basal-like phenotype of the DDR1^{-/-} tumors may result from a competitive advantage of the already enriched basal population due to a DDR1-dependent impairment in luminal cell interactions with the ECM.

Loss of DDR1 results in increased lung metastases

Since basal tumors with increased basal markers have a poor outcome in breast cancer patients⁷⁸⁻⁸¹, we next determined whether DDR1 plays a role in lung metastasis. When we scored the macroscopic and microscopic metastatic burden, we found increased metastasis both in volume and in numbers of metastases in the lungs of PyMT/DDR1^{-/-} mice (**Fig. 2.4A-C**). When we

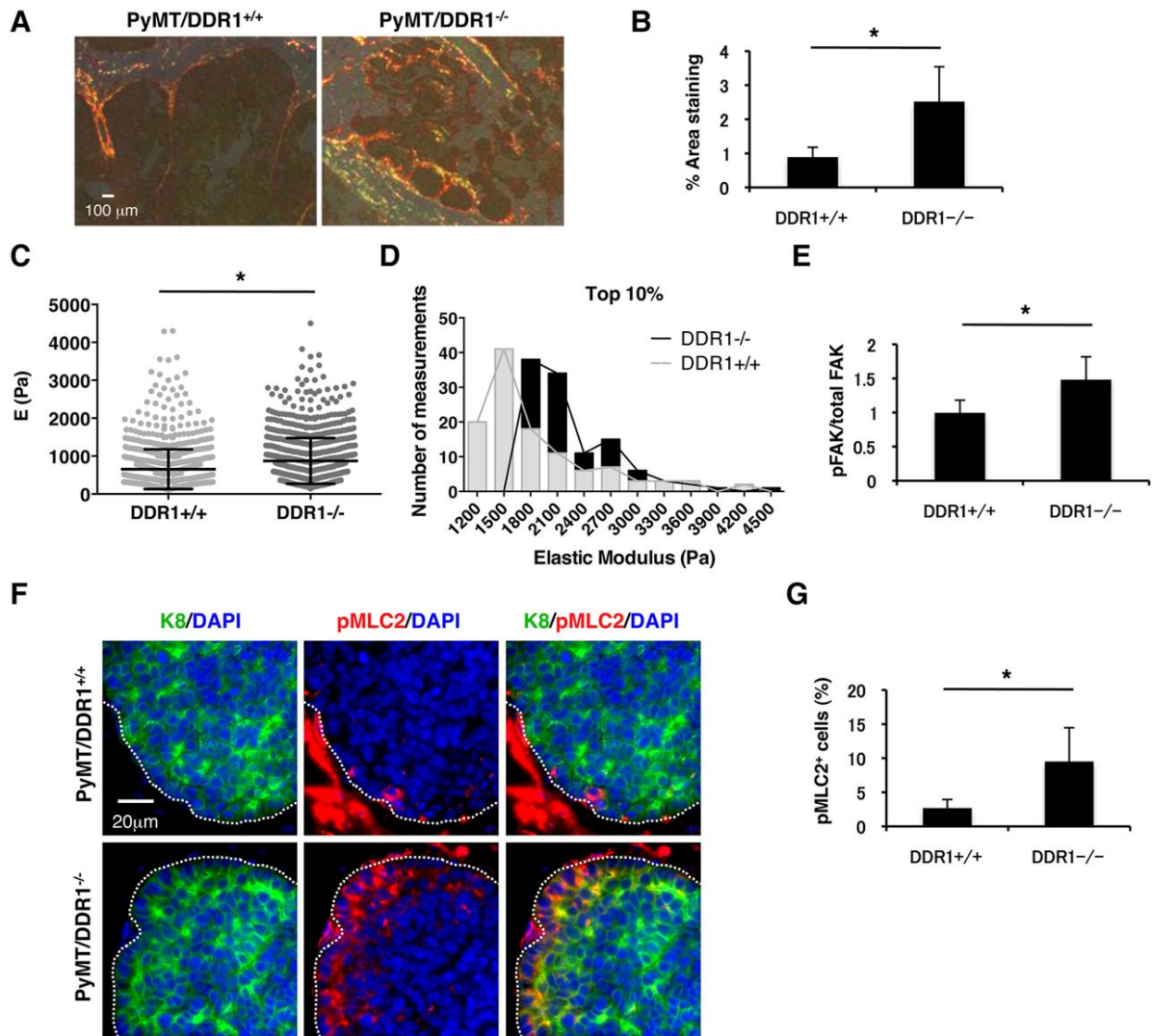


Figure 2.3: PyMT/DDR1^{-/-} tumors have increased fibrosis and exhibit increased mechanochemical tension. (A,B) Picosirius red staining of primary tumors (A) and quantification (B) by the percent area of birefringent signal in each image. Representative photographs are shown (A). DDR1^{-/-} tumors contain significantly more fibrillar collagen than DDR1^{+/+} tumors (B). Data are shown as mean \pm SD, $n=3$, $*p < 0.05$ (unpaired Student's t test). (C,D) Quantification of tissue elastic modulus measured by AFM. $*p < 0.0001$ (Mann-Whitney U-test) (C). The histogram shows the distribution of the top 10% of measurements for each group (D). DDR1^{-/-} tumors have a higher elastic modulus than DDR1^{+/+} tumors. (E) Quantification of Western blots for pFAK^{Y397} protein in wildtype and DDR1 knockout tumor tissue lysates normalized to total FAK protein levels. FAK phosphorylation increased in DDR1^{-/-} tumors. Data are shown as mean \pm SD, $n=6$, $*p < 0.02$ (unpaired Student's t test). (F,G) Immunofluorescence of the primary tumors was performed by using anti-keratin 8 (green) and anti-pMLC2 (red) antibodies. DAPI (blue) stained nuclei. Representative photographs are shown. The white dots represent a border between an epithelium and a stroma (F). The ratio of pMLC2⁺ cells per epithelial cell increased significantly in DDR1^{-/-} tumors (G). Data are shown as mean \pm SD, $n=3$, $*p < 0.05$ (unpaired Student's t test).

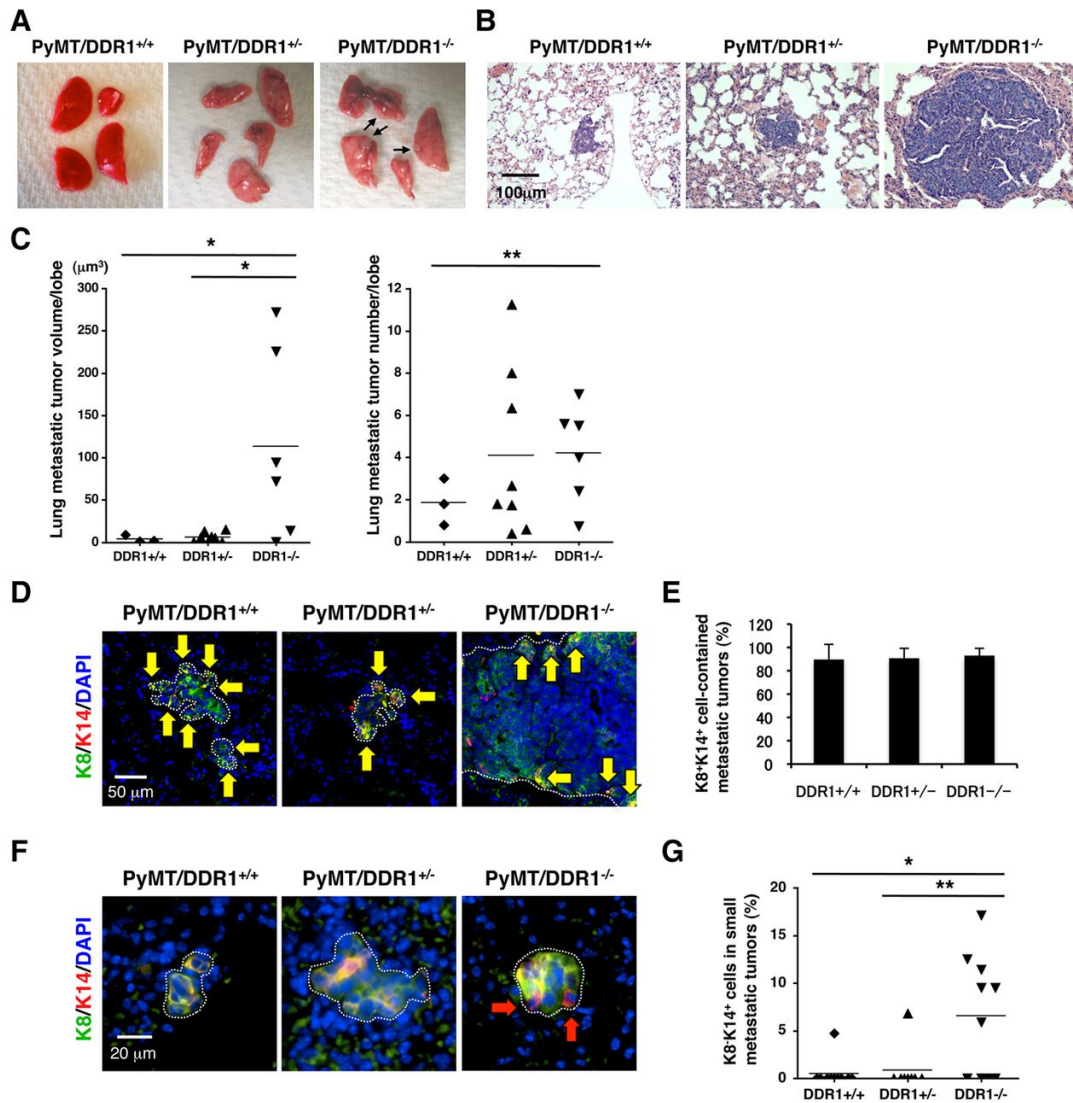


Figure 2.4: Loss of DDR1 results in increased lung metastases. (A) PyMT/DDR1^{-/-} mice show larger and increased lung metastatic tumors macroscopically. (B) PyMT/DDR1^{-/-} mice have larger and increased number of lung metastatic tumors by H&E staining. (C) Left panel indicates lung tumor volume. Right panel indicates lung tumor number/lobe. * $p < 0.05$ (one-way ANOVA and unpaired Student's t test), ** $p < 0.05$ (unpaired Student's t test). (D-G) Immunofluorescence of lung using anti-keratin 8 (green) and anti-keratin 14 (red) antibodies and DAPI (blue) stained nuclei. Metastatic tumor cells are located inside the dashed lines. K8⁺K14⁺ basal-like cells (yellow arrows) are detected in most of the metastatic tumors regardless of DDR1 genotype (Data shown as mean \pm SD, $n=3$, unpaired Student's t test) (D,E). K8⁺K14⁺ basal cells (red arrows) significantly increased in DDR1^{-/-} small (length $< 75 \mu\text{m}$) metastatic tumors ($n=8-10$, * $p < 0.01$, ** $p < 0.05$, one-way ANOVA and unpaired Student's t test) (F,G).

examined the epithelial differentiation state of metastatic tumors in the lungs, we found K8⁺K14⁺ basal-like cells in most of the metastatic tumors even with any small size regardless of DDR1 genotype (**Fig. 2.4D** and **2.4E**). Next, to examine whether DDR1 deletion is associated with the epithelial differentiation, we focused on the proportion of K8⁺K14⁺ basal cells in the small metastatic tumors and found that K8⁺K14⁺ basal cells significantly increased in DDR1^{-/-} metastases (**Fig. 2.4F** and **2.4G**). These results suggest that DDR1 deletion might induce basal differentiation.

CD90⁺CD24⁺ cells from PyMT/DDR1^{-/-} tumors transplanted into wild-type mice yield high-grade tumors resembling the PyMT/DDR1^{-/-} primary tumors

CD90⁺CD24⁺ cells are enriched for metastasis-initiating cells⁸². Based on the increased metastasis, we asked whether PyMT/DDR1^{-/-} tumors are enriched in CD90⁺CD24⁺ cells and found that the DDR1^{-/-} mammary tumor cell populations contained more CD90⁺CD24⁺ cells (**Fig. 2.5A** and **2.5B**). To understand the influence on epithelial differentiation by DDR1 deletion, we collected CD90⁺CD24⁺ cells from both PyMT/DDR1^{+/+} and PyMT/DDR1^{-/-} primary tumors by flow cytometry. We then transplanted 2000 CD90⁺CD24⁺ cells into the mammary glands of wild-type recipient mice. We observed sections of one grafted tumor from PyMT/DDR1^{+/+} CD90⁺CD24⁺ cells and two grafted tumors from PyMT/DDR1^{-/-} CD90⁺CD24⁺ cells. The grafted tumors from PyMT/DDR1^{+/+} mice had a more luminal morphology with large epithelial clusters (**Fig. 2.5C**). In contrast, one grafted mammary tumor from PyMT/DDR1^{-/-} cells was less differentiated and its size was larger (**Fig. 2.5C**). The other grafted tumor from PyMT/DDR1^{-/-} cells grew huge once but shrank later, had areas of hemorrhagic necrosis (**Fig. 2.5C**). These PyMT/DDR1^{-/-} CD90⁺CD24⁺ cell-derived tumors displayed decreased expression of E-cadherin, increased vimentin⁺ cells, and had increased numbers of K14⁺ basal cells and K8⁺K14⁺ basal-like cells near the necrotic areas (**Fig. 2.5D-F**). Tumor size correlated with increased K14⁺ basal cells in DDR1^{-/-} epithelial areas. These results indicate that, after transplantation with CD90⁺CD24⁺ cells from primary

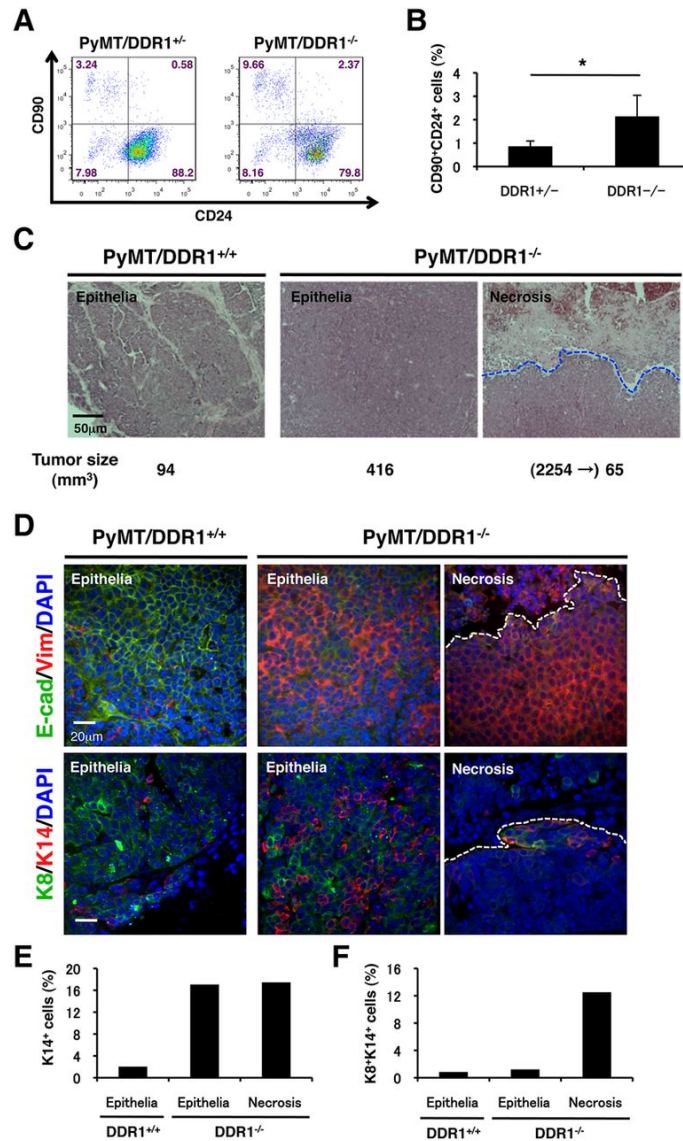


Figure 2.5: CD90⁺CD24⁺ cells from PyMT/DDR1^{-/-} tumors transplanted into wild-type mice yield high-grade tumors resembling the PyMT/DDR1^{-/-} primary tumors. (A,B) FACS analysis from DDR1^{+/+} and DDR1^{-/-} mammary tumor cells using anti-CD90 and anti-CD24 antibodies. DDR1^{-/-} mammary tumor cells have more CD90⁺CD24⁺ cancer cells than control tumors. Data shown as mean \pm SD, n=5-6, **p* < 0.02 (unpaired Student's t test). (C) 2000 CD90⁺CD24⁺ cancer cells from PyMT/DDR1^{+/+} and PyMT/DDR1^{-/-} tumors were transplanted into mammary glands. We observed sections of one grafted tumor from PyMT/DDR1^{+/+} cells and two grafted tumors from PyMT/DDR1^{-/-} cells. Mammary tumors from PyMT/DDR1^{+/+} cells showed large epithelial clusters by H&E staining whereas the mammary tumors from PyMT/DDR1^{-/-} cells showed non-cluster structures and hemorrhagic necrosis. The blue dots represent a border between an epithelium and a necrotic field. Tumor size (μm^3) is indicated in each tumor when the tumors were obtained at 8 weeks after transplantation. The largest tumor size is also indicated before the necrotic tumor from PyMT/DDR1^{-/-} cells shrank. (D) Immunofluorescence of CD90⁺CD24⁺ cell-derived mammary tumor tissues was conducted by using anti-E-cadherin (green) and anti-vimentin (red) antibodies in the upper panel and anti-keratin 8 (green) and anti-keratin 14 (red) antibodies in the lower

panel. DAPI (blue) stained nuclei. The dots represent a border between an epithelium and a necrotic field. The mammary tumor from PyMT/DDR1^{-/-} CD90⁺CD24⁺ cells shows decreased expression of E-cadherin, increased vimentin⁺ cells (D, upper panel) and increased K14⁺ basal cells (D, lower panel). (E,F) The ratio of K14⁺ basal cells (K8⁺K14⁺ and K8⁺K14⁺ cells) increased in DDR1^{-/-} epithelial areas (E). Increased K14⁺ (E) and K8⁺K14⁺ (F) cells were seen near the necrotic field.

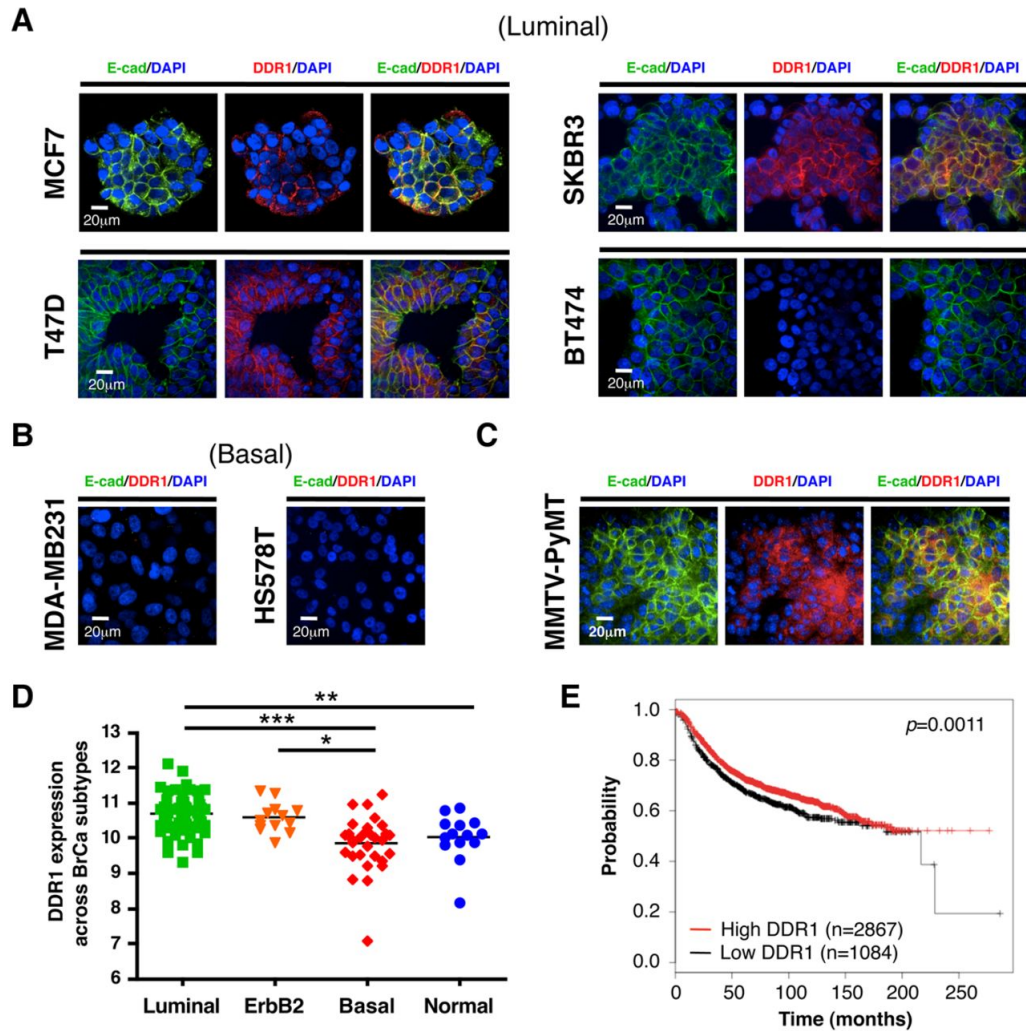


Figure 2.6: DDR1 expression predicts prognosis in breast cancer. (A) Immunofluorescence of MMTV-PyMT luminal-type tumor cells in 2D culture was conducted by using anti-DDR1 (red) and anti-E-cadherin (green) antibodies. DAPI (blue) stained nuclei. DDR1 and E-cadherin were expressed on the cells. (B) Clinical data of breast cancer patients. DDR1 expression was lower in basal type than luminal type. $*p < 0.05$, $**p < 0.01$, $***p < 0.001$ (Dunn's multiple comparison test). (C) Kaplan-Meier analysis of relapse-free survival for breast cancer patients. Low DDR1 expression was associated with worse relapse-free survival (Logrank Test). (D, E) Immunofluorescence of luminal-type (MCF7, T47D, SKBR3 and BT474) and basal-type (MDA-MB231 and HS578T) breast cancer cell lines was conducted by using anti-DDR1 (red) and anti-E-cadherin (green) antibodies. DAPI (blue) stained nuclei. DDR1 and E-cadherin were detected on luminal-type cells (except BT474) (D), but not on basal-type cells (E).

tumors, the phenotype of the transplanted tumors resembled that of the primary tumor from which they were derived and suggest that DDR1 deletion in CD90⁺CD24⁺ cells induces basal differentiation and that the resulting increase in K14⁺ basal cells in DDR1^{-/-} epithelium promotes tumor growth.

DDR1 expression predicts prognosis in breast cancer

DDR1 is overexpressed in some breast, lung, ovarian, brain, and esophageal cancers and leukemia^{37,52–57}, implicating DDR1 as a candidate oncogene. In breast cancer cell lines DDR1 expression was higher in luminal-type than basal-type human cell lines by microarray analysis⁷¹ (Supplemental Fig. S2C). When we stained the luminal-type (MCF7, T47D, SKBR3, BT474) and basal-type (MDA-MB231, HS578T) cell lines for DDR1 and E-cadherin by immunofluorescence, we observed staining on luminal-type cells (except in BT474), but not on basal-type cells (**Fig. 2.6A** and **2.6B**). Cultured MMTV-PyMT mouse luminal B-type tumor cells that expressed E-cadherin also expressed DDR1 (**Fig. 2.6C**).

We then analyzed clinical data from breast cancer patients and found that DDR1 expression was lower in basal-type than luminal-type tumors⁸³ (**Fig. 2.6D**). The relapse-free survival rate was lower in the patient group of low DDR1 expression by a Kaplan-Meier plot^{84,85} (**Fig. 2.6E**). These data suggest that DDR1 expression is prognostic of survival in breast cancer patients.

Discussion

In the present study, we discovered that luminal cells, but not basal/myoepithelial cells, express DDR1, and that after DDR1 deletion, luminal-type MMTV-PyMT mammary tumors exhibit basal-type characteristics, grow faster, and have enhanced lung metastasis. The mechanism underlying these results may derive from a reduced ability of luminal cells to interact with collagen leading to an enrichment of the basal cell population, basal differentiation of DDR1^{-/-} progenitor cells with primary tumor growth promoted by basal cells, and the enhanced tumor

necrosis/hypoxia seen in DDR1^{-/-} tumors, which, in turn, increases the number of K8⁺K14⁺ cells in the CD90⁺CD24⁺ population. Our data suggest that K8⁺K14⁺ progenitor cells, which increased in tumors deleted for DDR1, promote primary and metastatic tumor growth. Since DDR1 deletion resulted in increased necrosis in the primary tumors and increased rates of CSCs/MICs, it is likely that the absence of DDR1 alters the paracrine signaling and promotes an increase in CSCs/MICs. Our data suggest that DDR1 thwarts the development of poor prognosis tumors. Thus, elimination of DDR1 may result in a more aggressive basal-type breast cancer. In keeping with these results, DDR1 expression is lower in basal-type than luminal-type tumors. Since the basal phenotype promotes invasion/migration activity of mammary tumor cells^{73,86-88}, this provides a second mechanism by which loss of DDR1 acts. Correlating with the DDR1-deficient mammary tumor model, we found that basal/myoepithelial cells increased in adult DDR1^{-/-} mammary glands and facilitated mammary branching *in vitro*. This may be a mechanism underlying the mammary hyperbranching in adult mammary gland by DDR1 ablation, and this effect may reflect breast tumor progression promoted by DDR1 ablation. On the other hand, DDR1 deletion decreased branching in mammary organoids and tumor organoids *in vitro* and reduced mammary branches and ductal lengths in mammary development *in vivo* and luminal tumor cluster size in PyMT tumors (Table 1). These findings can be explained by impaired functions in collective cell migration and a collagen receptor by loss of DDR1.

Why does DDR1 deletion promote necrosis in luminal tumor epithelial cell regions? It is generally believed that central necrosis is caused by inadequate blood supply and hypoxia due to rapid tumor growth⁸⁹. Since DDR1^{-/-} mammary tumors grew more rapidly, there was an increase in fibrillar collagens, and they were comprised of a stiffer ECM, tumor necrosis can occur more frequently. Necrosis accretion, in turn, may increase numbers of tumor initiating cells and promote lung metastasis. These observations may explain the relationship between tumor necrosis and tumor aggressiveness.

The basal markers such as vimentin, K14 and DDR2 promote tumor cell invasion and correlate with poor prognosis^{45,65,93,94,72,73,86–88,90–92}. Since DDR1^{-/-} tumors had increased vimentin expression, K14⁺ cells and DDR2⁺ cells, we suggest that DDR1 ablation from the spontaneous luminal-type breast cancer model may lead to more basal-type characteristics and enhance tumor cell invasion as a mechanism of the tumor progression. However, DDR1 ablation upregulated DDR2 expression mainly on K8⁺ luminal cells and K8⁺K14⁺ progenitor cells rather than on basal cells or stromal cells, although previous reports indicated that DDR2 on basal cells or cancer-associated fibroblasts regulate tumor cell invasion^{72,73}. It has been reported that DDR1 switches to DDR2 expression by TGFβ-exposed or SLUG-transfected epithelial-to-mesenchymal transition (EMT)^{72,95}. Interestingly, ECM stiffness can also regulate DDR2 to promote tumor cell invasion through an EMT and is well known to contribute to tumor hypoxia^{96,97}. Hypoxia dramatically increases phosphorylation of DDR2 in breast cancer cell lines and DDR2 is involved in hypoxia-induced breast cancer cell invasion and EMT⁹⁸. Moreover, a DDR1^{Low}/DDR2^{High} protein profile is associated with triple-negative breast cancer and worse prognosis⁹⁹. More study is necessary to understand the mechanisms of the alteration from DDR1 to DDR2 on luminal cells and basal cells and determine whether the tumor cells can acquire invasive ability by upregulation of basal markers including DDR2.

Our data add to the concept that the effects of DDR1 are complex. In mammary development, its loss inhibits mammary development early in puberty, but increases epithelial branching later. Similarly, while our results find that knockout of DDR1 increased tumor progression in MMTV-PyMT tumors, knockdown of DDR1 decreased viability of luminal-type breast cancer cell lines⁶⁴, and interference with DDR1 function in a metastatic luminal-type breast cancer cell line decreased its ability to colonize lung tissue⁶³. Those results suggest that DDR1 may behave as an oncogene in some circumstances and as an anti-oncogene in others.

How could such diverse effects arise? Since DDR1 knockdown in luminal cells impairs collective cell migration, cell adhesion and contractility, this could reduce tumor growth⁶³. In addition, induction of DDR1 expression inhibits migration of a DDR1-deficient basal-type breast cancer cell line⁶⁶, which may be caused by enhanced cell adhesion through DDR1 induction. Therefore, the results with cell lines and/or *in vitro* experiments may be based on DDR1 functions in collective cell migration and cell adhesion, which is different from possible effects of enhanced necrosis and increased K8⁺K14⁺ progenitor cells and more basal-type characteristics by DDR1 deletion in our DDR1-deleted spontaneous model of luminal B-type breast cancer. In support of this hypothesis, our *in vitro* studies demonstrated that the tumor organoids derived from our PyMT/DDR1^{-/-} tumors showed decreased branching. In our study, we did not observe an increase in carcinogenesis rates of DDR1^{-/-} mice compared to DDR1^{+/+} mice, as described in a previous report, suggesting that *DDR1* is not a tumor suppressor gene⁴⁶.

Activation and proliferation of K14⁺ progenitor cells and their invasive activity are important for tumor growth and metastasis. Our DDR1 knockout spontaneous breast cancer model enriches a population of tumor initiating cells that form tumors with a more basal phenotype that may promote metastasis. Thus, our research provides new insights into the complicated DDR1 roles in breast cancer that will contribute importantly to understanding of cancer mechanisms in the future.

Methods

Mouse models

All animal protocols were reviewed and approved by the UCSF IACUC. Mice were maintained under specific pathogen-free conditions in the UCSF barrier facility. DDR1^{-/-} mice on a 129/Sv background were kindly provided by the late Wolfgang F. Vogel, University of Toronto⁴⁶. DDR1^{-/-} mice were then backcrossed to the FVB/n background for at least 6 generations.

For development studies mammary glands were harvested from DDR1^{-/-} mice on mixed 129/Sv and FVB/n backgrounds, and stained with carmine alum (Sigma). These mice were crossed with K14/GFP transgenic mice (CD1 background) in which GFP expression was controlled by a keratin 14 (K14) promoter-driven transgene cassette¹⁰⁰. For cancer studies, the DDR1^{-/-} mice on the FVB/n background were crossed with MMTV-PyMT mice on the FVB/n background. Tumor volumes (mm³) were calculated using the formula: $V = 0.52 \times W^2 \times L$. W=width (mm), L=length (mm).

Flow cytometry analysis and cell sorting

Mammary glands from DDR1^{-/-}, K14/DDR1^{-/-} and littermate control mice or mammary tumors from PyMT/DDR1 mice were digested with collagenase^{101,102}. Organoids were collected by brief centrifugation and digested with trypsin to dissociate into single cells. Cultured adherent cells were trypsinized for single-cell suspensions. The cells were stained with antibodies against CD49f, CD24, CD90.1 and lineage markers (CD45, CD31, Ter119) (eBioscience), as described previously^{82,103}. Cell sorting was performed on FACS Aria II (Becton Dickinson), and analyzed using FlowJo (TreeStar) or FACSDiva software (BD Biosciences).

Cell adhesion assay

Cells (2×10^5) were seeded onto collagen-coated 12 well plates and subsequently washed with PBS at the indicated timepoints. After washing, the adhered cells were fixed with 4% PFA for 10 minutes. The adhered cells were permeabilized and stained with DAPI. Images were taken at 4x and the number of nuclei per field of view was quantified.

Collagen Contraction Assay

Collagen I solution was prepared by neutralizing acid-solubilized rat tail collagen I (Corning #354236) with 1 N NaOH and 10X DMEM buffer. Cells (2×10^5) were seeded in 2 mg/mL collagen gels in 48-well plates. Gels solidified at 37 °C for one hour prior to addition of prewarmed

media. After one hour in medium, a pipet tip was used to gently detach the collagen gel from the wall and bottom of the well. The collagen gel diameter was measured in ImageJ.

Western blot

Homogenized tumor tissue or cells were lysed in 2% SDS containing protease inhibitor cocktail (Sigma p8340) and phosphatase inhibitor (GenDEPOT P3200). Equal amounts of protein per sample were subjected to SDS-PAGE and transferred to a PVDF membrane. The membranes were blocked in 5% skim milk in TBST (TBS containing 0.1% Tween 20) for 30 minutes. Primary antibodies were incubated overnight at 4 °C in 3% BSA in TBST. Membranes were incubated with horseradish peroxidase (HRP)-conjugated secondary antibodies diluted in 5% milk-TBST for 1 hour at room temperature. Bands were visualized using Pierce ECL Plus Western Blotting Substrate (ThermoFisher 32132). Protein expression was quantified by measuring the pixel intensity of each band using ImageJ. pFAK/FAK represents the ratio of the pFAK signal to the total FAK signal of each sample.

Antibodies used are as follows: Cell Signaling #5583 Rabbit anti-DDR1, BD Biosciences #610088 Mouse anti-FAK, Cell Signaling #8556 Rabbit anti-pFAK^{Y397}, and Sigma #A5441 Mouse anti- β -actin.

3D organoid branching assay

K14⁻ cells and K14⁺ cells with or without DDR1 were aggregated overnight on ultralow attachment plates (Corning). The aggregated cells or organoids were embedded into growth factor-reduced Matrigel (BD Biosciences) and grown in serum-free medium supplemented with insulin-transferrin (Invitrogen) and 2.5 nM EGF (Invitrogen) or 2.5 nM FGF2 (Sigma) as previously described¹⁰⁴.

Cell culture

MCF7, T47D, SKBR3, BT474, MDA-MB231 and HS578T cells were obtained from the ATCC, Lawrence Berkeley Laboratory or the UCSF Cell Culture Facility, and grown in DME H-21 medium supplemented with 10% FBS and 1 μ g/mL insulin. Organoids from MMTV-PyMT

mammary tumors (see flow cytometry analysis and cell sorting) were cultured in ACL4 + 5% FBS medium in a 3% O₂ incubator¹⁰⁵.

DDR1 Knockdown

HEK293T cells were transfected using polyethylenimine to generate a lentivirus titer used to transduce a PyMT tumor-derived cell line with an IPTG inducible lentivirus (pLKO.1) expressing short hairpin RNA (shRNA) against DDR1 (5'-CCGGGATTCCACTTACGATGGATATCTCGAGATATCCATCGTAAGTGGAAATCTTTTT-3') and luciferase as a control. Transduced cells were selected by treating with 400 µg/mL G418.

Immunostaining and histology

Tissues were fixed in 4% PFA overnight and paraffin processed. We cut 5 µm sections from paraffin-embedded blocks for H&E staining and immunohistochemistry. Adherent cells cultured in two-well chamber slides and sorted cells after cytopsin at 1000 rpm for 4 min were stained by immunocytochemistry.

The following antibodies were used for immunofluorescence at the indicated concentrations: DDR1 (Santa Cruz Biotechnology #sc-532, 1:50), E-cadherin (BD Biosciences #610181, 1:100), keratin 8 (Developmental Studies Hybridoma Bank TROMA-I, 1:50), keratin 14 (Convance #PRB-155P, 1:5000), alpha-smooth muscle actin (α-SMA) Cy3 conjugate (Sigma #C6198, 1:250), vimentin (Sigma V5255, 1:200), DDR2 (LifeSpan BioSciences LS-C164363, 1:50), phospho-histone H3 (Cell Signaling #9701, 1:100), HIF1α (Novus Biologicals NB100-479, 1:50), goat anti-mouse IgM µ chain Cy3 conjugate (Jackson ImmunoResearch #115-166-075, 1:200), Alexa 488 anti-rat, 488 anti-rabbit, 488 anti-mouse and 568 anti-rabbit secondary antibodies (Molecular Probes A11006, A24922, A24920, A21069, 1:500). Nuclei were stained with DAPI (Vector Laboratories H-1200). Confocal microscopy was performed on a Nikon C1si confocal microscope.

Picrosirius Red Quantification

Images were taken using polarized light such that only the birefringent collagen signal is visible. The amount of collagen was quantified as the percent area of the image with a positive signal using ImageJ. The threshold pixel value to determine a positive signal was held constant for each image analyzed.

qPCR

Total RNA was isolated from mouse mammary tumors using a Qiagen minikit. cDNA was synthesized using the Superscript III RT First Strand Kit (Invitrogen). qPCR was performed using the Sybgreen (Applied Biosystems) in an Eppendorf Mastercycler Realplex machine. Ct values were normalized to actin, and relative expression was calculated using the $2^{\Delta\Delta Ct}$ method (Slorach 2011). The forward and reverse primer sequences for mouse DDR1 were 5'-TCCATAGACCAGAGGGATC -3' and 5'-CAGGGCATAGCGGCACTTGG -3'.

Traction force microscopy

Primary murine mammary luminal and basal epithelial cells were sorted as previously described¹⁰³ and seeded overnight on collagen I-coated polyacrylamide gels with embedded 500 nm fluorescent red beads. Images of cells and beads were taken at 20 x magnification before adding 2% SDS to lyse the cells. A second picture of the beads was taken after lysis and aligned with the first image using the ImageJ (<http://rsb.info.nih.gov/ij>) registration plug-in Linear Stack Alignment with SIFT. To assess bead movement, a particle image velocimetry (PIV) program was implemented in ImageJ as described previously⁷. The iterative scheme included a first pass at 32/64 (i.e., interrogation and search window size in pixels), followed by a second pass at 20/40, all at a correlation threshold of 0.60. For PIV postprocessing, a normalized mean test (NMT) was performed as described⁷ with NMT noise of 0.2 and threshold of 2.0 as starting parameters. The traction force was calculated by the Fourier transform traction cytometry (FTTC) method with a Poisson ratio of 0.5. The maximum traction stress generated was calculated by averaging the five largest traction vectors generated by each cell. The PIV and FTTC microscopy software for

ImageJ was kindly made available by Qingzong Tseng (<https://sites.google.com/site/qingzongtseng/tfm>).

Atomic Force Microscopy

Tumor samples were frozen in OCT and cut into 30 μ m sections. Each section was thawed in room temperature PBS and maintained in 0.5% BSA with protease inhibitor (Sigma p8340) in PBS supplemented with propidium iodide (Sigma P4170, 20 μ g/mL) for no more than 90 minutes after thawing.

All AFM indentations were performed using an MFP3D-BIO inverted optical AFM (Asylum Research) mounted on a Nikon TE2000-U inverted fluorescent microscope. We used silicon nitride cantilever with an approximate spring constant of 0.06 N m⁻¹ with a 5 μ m spherical borosilicate glass tip (Novascan Tech). The exact cantilever spring constant was determined using its thermal oscillation prior to each experiment. Samples were indented at a 2 μ m/s loading rate until a maximum force of 1nN was achieved. Five 40 x 40 μ m indentation maps were typically obtained on each tissue section in ECM-rich regions as determined through picosirius red staining of serial tissue sections. The elastic modulus of the tissue was determined through fitting to the Hertz model using a Poisson's ratio of 0.5, which assumes the tissue samples are incompressible.

Transplantation

2 x 10³ cells (CD90⁺CD24⁺ CSCs from PyMT/DDR1^{+/+} or PyMT/DDR1^{-/-} tumors) were injected in a 10- μ l volume of 1:1 v/v Matrigel:DMEM/F12 medium into mammary glands of FVB/n mice by using a Hamilton syringe. Tumors were harvested 8 weeks after transplantation.

Lung metastasis analysis

To determine lung metastatic tumor volume and frequency, lung tissue blocks were sectioned into 5 μ m sections and stained by hematoxylin and eosin. For each mouse analyzed, one section was scored for size and number of metastases per lobe^{106,107}. Tumor volumes (μ m³) were calculated using the formula: $V = 0.52 \times W^2 \times L$. W=width (μ m), L=length (μ m).

Computational analysis

We compared DDR1 expression levels in 25 luminal and 26 basal (A+B) cell lines and in 61 luminal-type, 13 HER2-type and 30 basal-type human breast tumors and 14 normal human breast tissues using the published microarray datasets^{71,83}. Breast cancer patients (n=3951) were separated by high (n=2867) versus low (n=1084) DDR1 expression and analyzed for relapse-free survival by a Kaplan-Meier plot^{84,85}.

Statistical analysis

Statistical analysis was conducted using Prism 4 software (Graph Pad Software, Inc.). Kaplan-Meier survival curves were analyzed by log-rank tests to determine the significance of observed differences between the curves. All tests used and *P* values are specified in the figure legends. *p* <0.05 was considered significant.

Chapter 3: Collagen crosslinking and stiffening in breast tumors is primarily regulated by macrophage-stimulated fibroblasts and promotes tumor aggression

In collaboration with: Ori Maller*¹, Alexander S. Barrett*², Signe Borgquist^{3,4}, Brian Ruffell⁵, Pham T Thanh², Tina Gruosso⁶, Hellen Kuasne⁶, Johnathon N. Lakins¹, Irene Acerbi¹, J. Matthew Barnes¹, Travis Nemkov², Aastha Chauhan⁷, Jessica Gruenberg⁷, Aqsa Nasir⁷, Olof Bjarnadottir³, Zena Werb^{8,9}, Peter Kabos¹⁰, E. Shelley Hwang¹², Morag Park⁶, Lisa M. Coussens⁵, Andrew C. Nelson⁷, Kirk C. Hansen^{2,14} and Valerie M. Weaver^{9,13,14,15}

¹Department of Surgery, Center for Bioengineering and Tissue Regeneration, University of California, San Francisco, California, USA

²Department of Biochemistry and Molecular Genetics, University of Colorado Denver - Anschutz Medical Campus, Aurora, CO, USA

³Division of Oncology and Pathology, Department of Clinical Sciences, Lund, Lund University

⁴Clinical Trial Unit, Clinical Studies Sweden, Forum South, Skåne University Hospital, Lund, Sweden

⁵Cell, Developmental & Cancer Biology, Oregon Health & Science University; Knight Cancer Institute, Oregon Health & Science University, Portland, Oregon, USA

⁶Goodman Cancer Research Centre, McGill University, Montreal, QC, Canada; Department of Biochemistry, McGill University, Montreal, QC, Canada; Department of Oncology, McGill University, Montreal, QC, Canada

⁷Department of Laboratory Medicine and Pathology, University of Minnesota, Minneapolis, MN, USA

⁸Department of Anatomy and Biomedical Sciences Program, University of California, San Francisco CA, USA

⁹UCSF Helen Diller Comprehensive Cancer Center, University of California, San Francisco, San Francisco, CA, USA

¹⁰Department of Medicine, Division of Medical Oncology, University of Colorado Anschutz Medical Campus, Aurora, Colorado, USA

¹¹Department of Pathology, University of California, San Francisco, CA, USA

¹²Department of Surgery, Duke University Medical Center, Durham, NC, USA

¹³Departments of Bioengineering and Therapeutic Sciences, and Radiation Oncology, Eli and Edythe Broad Center of Regeneration Medicine and Stem Cell Research

Contribution from previously published work: Maller, O.*, Drain, A.P.*, Barret, A.S.*, *et al.* Inflammation promotes tumor aggression by stimulating stromal cell-dependent collagen crosslinking and stromal stiffening. *bioRxiv* 2020.02.13.948141 (2020). doi:10.1101/2020.02.13.948141¹⁰⁸

Introduction

Pathological accumulation of extracellular matrix (ECM) accompanies the formation of all solid tumors^{26,109,110}. The tumor ECM is composed primarily of interstitial collagen that is progressively reorganized and stiffened^{26,30}. The collagenous fibrotic tumor ECM compromises treatment and is linked to poor patient prognosis^{111–114}. Tumor biopsy analysis showed that a thick fibrous collagenous ECM associates with less differentiated tumors and that this phenotype predicts poor patient survival, emphasizing the relevance of collagen architecture^{30,109,115}. Patients with pancreatic ductal adenocarcinomas (PDACs) that are surrounded by stiff, thick fibrous collagens have a shorter survival, and invasive breast carcinomas with the stiffest ECM stroma at their invasive front are the most aggressive^{26,109}. These observations suggest that stromal stiffness reflects collagen organization may be an important prognostic variable. Consistently, preclinical studies using organotypic cultures and rodent models provide plausible evidence for a causal relationship between collagen organization, stromal stiffness, tumor cell invasion in culture, and metastasis *in vivo*^{33,35,116–118}. These findings underscore the clinical relevance of collagen architecture and stiffness to malignancy and emphasize the need to clarify the molecular nature of the collagenous ECM so that new biomarkers can be identified and anti-cancer therapeutics may be developed^{23,26,109,119}.

Interstitial fibrillar collagens assemble to form long, rod-like bundles are the ECM components that contribute most significantly to the tensile strength of tissue¹²⁰. Fibrillar collagen α chains are synthesized in the endoplasmic reticulum as pro- α chains, with long propeptide regions on either side of the triple helical domain. Prior to triple helix formation, the α chains can undergo extensive posttranslational modifications including proline and lysine hydroxylation, lysine and hydroxylysine glycosylation, and tyrosine sulfation^{121,122}. Proline hydroxylation by prolyl hydroxylases is particularly critical for the stability of the ensuing triple helix. Associations between pro- α chains begin with disulfide bonding among their C-terminal propeptides and initiate the

formation of the triple helix near the C-terminus^{123,124}. Triple helix formation then propagates toward the N-terminus like a zipper forming a procollagen molecule. Formation of the complete triple helix quenches further posttranslational modification of the triple helical region. The procollagen molecule is shuttled to the Golgi where it is packaged for secretion into the extracellular space.

Following their extracellular secretion, extracellular BMP1/tolloid-like proteinases and ADAMTS family proteinases cleave the C- and N- terminal propeptides, respectively yielding a mature collagen molecule. Mature collagen molecules undergo entropy-driven self-assembly into small microfibrils of about 20 nm diameter and 4-12 μm in length. The collagen molecules pack together in a longitudinally staggered pattern that form areas of high and low packing density. This causes the characteristic 67 nm periodic banding pattern observed in collagen fibrils. Immature microfibrils associate with each other and are organized into very long mature collagen fibrils that can be 20 – 500 nm in length¹²⁵.

In the final step of collagen maturation, fibrils undergo varying degrees of enzymatic and nonenzymatic covalent crosslinking. The mechanical properties of fibrillar collagens are highly dependent on these modifications. The lysyl oxidase (LOX) family enzymes catalyze the oxidative deamination of peptidyl lysine and hydroxylysine residues in the telopeptide region adjacent to the triple helix in the collagen molecule. The aldehyde produced by this reaction spontaneously reacts with another LOX-derived aldehyde or with the amine group in helical lysine or hydroxylysine residues to form covalent intra- and intermolecular crosslinks. These initial divalent crosslinks can mature further into multivalent crosslinks through incorporation of additional amino acids¹²⁶. The hydroxylation of telopeptide lysines by lysyl hydroxylase 2 (LH2; gene name procollagen-lysine, 2-oxoglutarate 5-dioxygenase or PLOD) during collagen synthesis in the endoplasmic reticulum gives rise to crosslinking maturation products with distinct mechanical properties and are enriched in bone, ligaments, tendons, and pathologically fibrotic tissues^{126,127}.

Collagen in softer connective tissues such as skin or cornea contain lower levels of hydroxylated telopeptide lysine residues and therefore contain a much different profile of mature collagen crosslinks. Tissues finely tune the quantity and quality of LOX-mediated collagen crosslinks to meet their structural needs. Although many of the crosslinking maturation products have been identified, the precise mechanisms by which they all form and are regulated are not fully understood. Recent advances in mass spectrometry methods have allowed quantification of specific LOX-mediated crosslinking products in tissues to understand their role in tissue structure and in the progression of fibrotic disease^{128,129}. LOX activity has traditionally been difficult to assay *in situ* because the posttranslational modifications and copper cofactor required for catalysis decouple extracellular LOX protein levels from its enzymatic activity.

Fibrotic human tumors express high levels of LOX and LH2 enzymes^{130,131}. Tumor grade and overall patient survival associate with total tissue LOX and PLOD2 mRNA^{130,132–134}. Pharmacological or antibody-mediated inhibition of LOX in MMTV-Her2/Neu mice or genetic reduction of PLOD2 in subcutaneously injected lung tumor epithelial cells reduce tissue fibrosis, stromal stiffening and collagen crosslinking and concomitantly decrease tumor incidence and aggression^{35,130}. Moreover, elevating LOX or LH2-mediated collagen crosslinking enhances fibrosis and stromal stiffness and promotes malignant transformation and tumor aggression in lung and mammary xenografted tumors^{35,130}. These observations suggest that the direct targeting of specific collagen crosslinking enzymes has clinical merit for the treatment of cancer. However, given caveats with recent clinical trials targeting ECM modifiers including suboptimal activity of inhibitory treatments and the risk of off-target effects, strategies designed to interfere with the induction and activation of these crosslinking enzymes offer an attractive alternative¹³⁵. Towards this goal, the identification and causal implication of additional factors that regulate the levels and/or activity of collagen crosslinking enzymes has the potential to identify new predictive biomarkers and alternative anti-tumor treatment targets.

Pre-neoplastic lesions are inflamed, and pathological fibrosis correlates with inflammation^{136,137}. Chronic inflammation and experimental manipulations that promote inflammation in rodent models induce fibrosis by secreting factors such as metalloproteinases and TGF β ^{118,136,138–140}. Furthermore, fibrotic tumors are frequently inflamed, and this inflammation promotes tumor aggression, whereas either inhibiting inflammation or decreasing macrophage infiltration reduce tumor metastasis and enhance anti-tumor treatment^{126,137,141–144}. Nevertheless, it remains unclear if inflammation promotes tumor progression and aggression by inducing stromal stiffening, and if so, whether this is regulated via epithelial and/or stromal fibroblast-mediated collagen remodeling and crosslinking.

Results

xAAA profiling identifies increased levels of collagen crosslinks and stromal stiffness as indicators of breast tumor aggression

To clarify the role of collagen crosslinking in tumor fibrosis we developed a crosslinked amino acid analysis (xAAA) method that enabled the characterization and quantification of specific collagen crosslinks in tissues across a wide range of collagen levels. We utilized solid phase extraction (SPE) enrichment followed by high pH amide hydrophilic chromatography (HILIC) coupled to a benchtop orbitrap (QExactive) mass spectrometer for these measurements. The validated method detected all known LOX-generated crosslinks including divalent (lysinonorleucine, dihydroxy lysinonorleucine), trivalent (pyridinoline and deoxy-pyridinoline) and tetravalent (desmosine and isodesmosine) crosslinked amino acids linearly over four orders of magnitude, with calculated limits of quantification (LLOQ) in the femtomolar range (**Fig. A2.1; Table A2.1**)¹⁴⁵. The technique revealed a positive correlation between collagen crosslinking and abundance in excised human clinical specimens with very low to very high collagen concentrations and varying mechanical properties (**Fig A2.2**). The method also identified a subset

of hydroxylysine aldehyde (Hyl^{ald})-derived collagen crosslinks (HLCCs) crucial for the mechanical strength of tissue^{120,146}.

We next obtained snap-frozen biospecimens of normal human breast tissue (N=10; age between 22 and 58) and human tumor biopsies representing early stage (stage 1-2) invasive breast cancers (IBC) excised from mastectomy specimens. Molecular subtyping that subdivides human breast tumors stratified by estrogen receptor (ER+) and human epidermal growth factor receptor two (HER2+) status and ER/PR/HER2-negative (triple negative; TN) is a key determinant used to direct the treatment of breast cancer patients. Accordingly, we chose human breast tumor biopsies that represented ER+ (N=8; age between 42 and 71); HER2+ (N=6; age between 40 and 76) and TN (N=6; age between 50 and 71). H&E stained tissue sections confirmed the presence of normal glandular structures in the normal controls and invasive breast cancer in the tumor specimens (**Fig. 3.1a; top panels**). Polarized light imaging of Picrosirius-stained (PS) tissue revealed that the normal breast tissue stroma had very little fibrillar collagen, whereas stromal tissue in all patients with IBCs contained abundant fibrillar collagen (**Fig. 3.1a; middle panels**) that second harmonic generation (SHG) imaging indicated was thicker and more linearized (**Fig. 3.1a; bottom panels**). Polarized light microscopy and two-photon imaging further revealed that the level of fibrosis in the tissue was higher in HER2+ as compared to the ER+ breast tumors, and was further increased in the TN tumors, consistent with our previous report that TN tumors contain a high density of aligned collagen fibers (**Fig. 3.1a; middle and bottom panels**)²⁶. AFM microindentation revealed a significant increase in the elastic modulus of the stroma associated with the invasive front of all the IBC tissues (**Fig. 3.1b**)^{26,30,35}. xAAA analysis revealed a significant increase in total collagen crosslinking in all the IBCs (**Fig. 3.1c, Fig. A2.5**). These findings are consistent with an association between collagen crosslinks, tissue fibrosis and stromal stiffness, as has been previously documented in experimental murine models of mammary cancer³⁵.

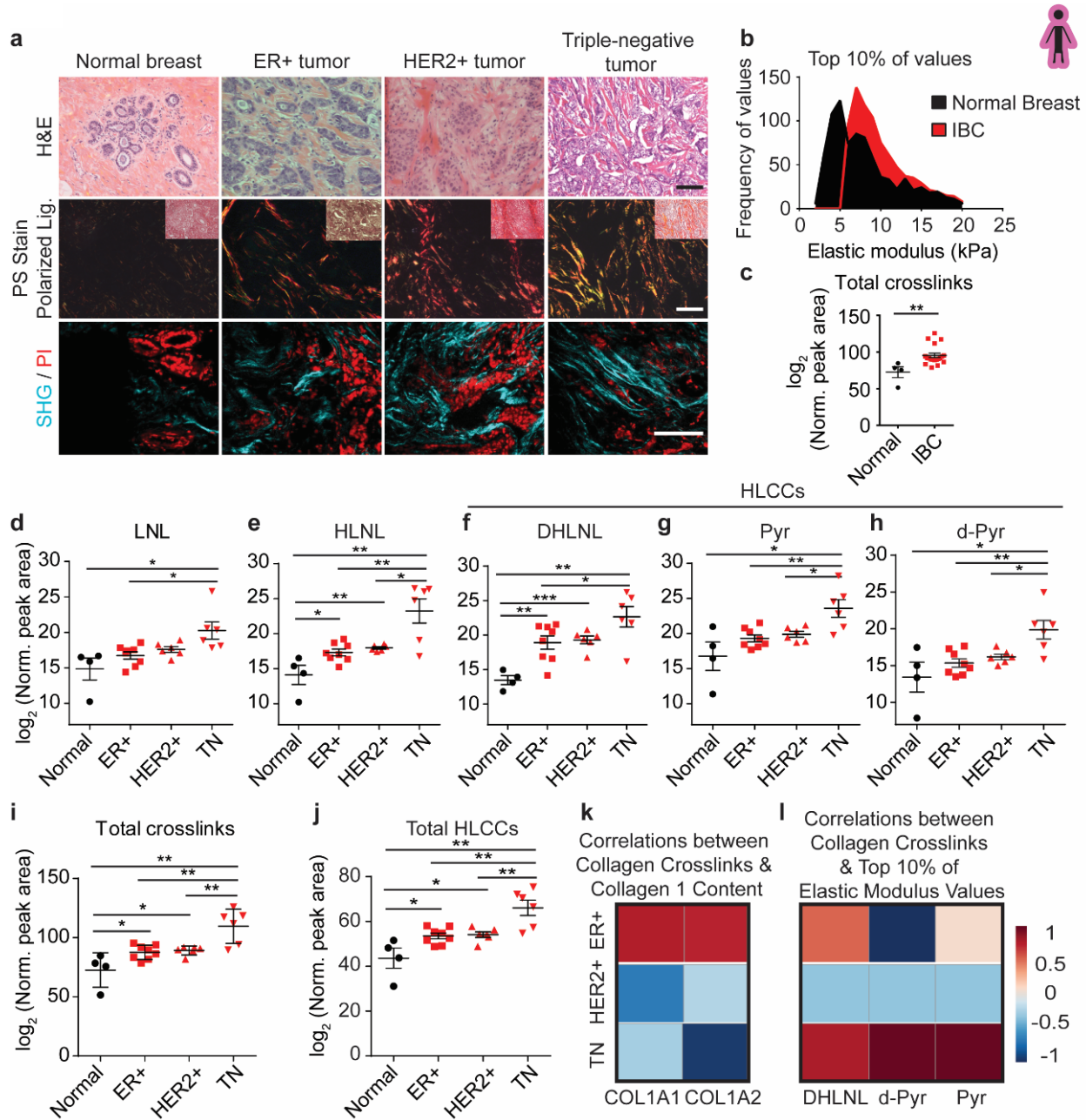


Figure 3.1: Hydroxylysine collagen crosslink abundance correlates with human breast cancer aggression. (a) Representative images of normal breast tissue (normal breast; $n = 4$) and invasive tumors diagnosed as estrogen receptor positive (ER+ tumor; $n = 8$), epidermal growth factor receptor two positive (HER2+ tumor; $n = 6$) and triple negative (TN tumor; $n = 6$). (Top row) Brightfield images of human breast tissue stained with hematoxylin and eosin (H&E). (Middle row) Polarized light images of picosirius red (PS) stained human breast tissue with an inset brightfield image shows relative levels of fibrillar collagen. (Bottom row) Two photon second harmonic generation (SHG) images of human breast tissue revealing collagen organization (turquoise) and propidium iodide (PI; red) stained nuclei. Scale bar, 100 μm . (b) The distribution of the top 10% of elastic modulus values of normal breast tissue ($n = 10$) and invasive breast

carcinoma (IBC; n = 10) measured by AFM microindentation. Statistical analysis was performing using Mann-Whitney U test ($****p < 0.0001$). **(c)** Quantification of the abundance of all detected collagen crosslinks in normal breast tissue (n = 4) and in IBC tissues (n = 19) plotted as a scatter plot of individual samples with mean \pm SEM. Statistical analysis was performed using Mann-Whitney U test ($**p < 0.01$). **(d-h)** Scatter plots showing individual and mean values \pm SEM of the levels of each LCC and HLCC crosslink measured in normal breast tissues, and in ER+, HER2+ and TN breast tumors. The total abundance of crosslinks **(i)** was calculated by summing all individual crosslinks and the total tissue HLCC abundance **(j)** was calculated by summing DHLNL, Pyr, and d-Pyr and plotted as individual and mean values \pm SEM. All crosslink values are normalized to total collagen content (i.e. hydroxyproline abundance) and wet tissue weight and are plotted as \log_2 transformed normalized peak areas from LC-MS data. Statistical analysis of crosslinks was performed using one-way ANOVA test for overall analysis and unpaired t-test was used for individual comparisons ($*p < 0.05$; $**p < 0.01$). **(k,l)** Heat maps of Spearman correlation coefficients indicating correlations between levels of total collagen crosslinks and collagen I content **(k)** and between levels of each HLCC and the top 10% of elastic modulus measurements **(l)** stratified by tumor subtype.

Interestingly, when we subdivided the IBC collagen crosslinking analysis into breast tumor subtype the most significant increase in total collagen crosslinks was calculated to be in the TN breast tumors (**Fig. 3.1i**). Furthermore, biochemical quantification of total tissue collagen 1A1 or 1A2 did not account for the higher total number of collagen crosslinks in the TN breast tumor tissue (**Fig. 3.1k**). Instead, molecular characterization of the isolated tissue collagen revealed that the TN tumors had a distinctive crosslink profile due to a strong preference for a combination of DHLNL, Pyr, and d-Pyr crosslinks (**Fig. 3.1d-j**). Subtype analysis further revealed that the level of hydroxylysine aldehyde-derived collagen crosslinks (HLCCs) in the TN subtype correlated significantly and positively with the stiffness of the stroma at the invasive front of the tumor tissue (**Fig. 3.1l**). These findings highlight the importance of HLCC collagen crosslinking in breast cancer aggression.

Increased collagen crosslinking correlates with high expression of stromal LOX and PLOD2 in aggressive tumor subtypes

To determine if the observed increase in collagen crosslinking and stromal stiffness in TN tumors was related to the expression levels of enzymes implicated in regulating collagen crosslinking, we analyzed publicly available human breast cancer gene expression array data (n = 1904) for the genes coding these enzymes and examined their correlation to breast cancer subtype. Bioinformatics analyses revealed a significant increase in the major collagen crosslinking enzyme LOX, but not lysyl oxidase like two (LOXL2), in the more aggressive HER2 and TN tumor subtypes and indicated that LOX levels were particularly high in TN tumors (**Fig. 3.2a-b**). The arrays also showed bulk gene expression of PLOD2, the major regulator of HLCC accumulation, to be highly upregulated in aggressive human TN breast cancers (**Fig. 3.2c**).

To gain insight into the cellular sources of LOX and LH2 in human tumors, we used laser capture microdissection to isolate regions of tumor epithelium and stroma to identify the origins of LOX and LH2 in invasive human breast cancers^{147,148}. Gene expression analysis of stromal and

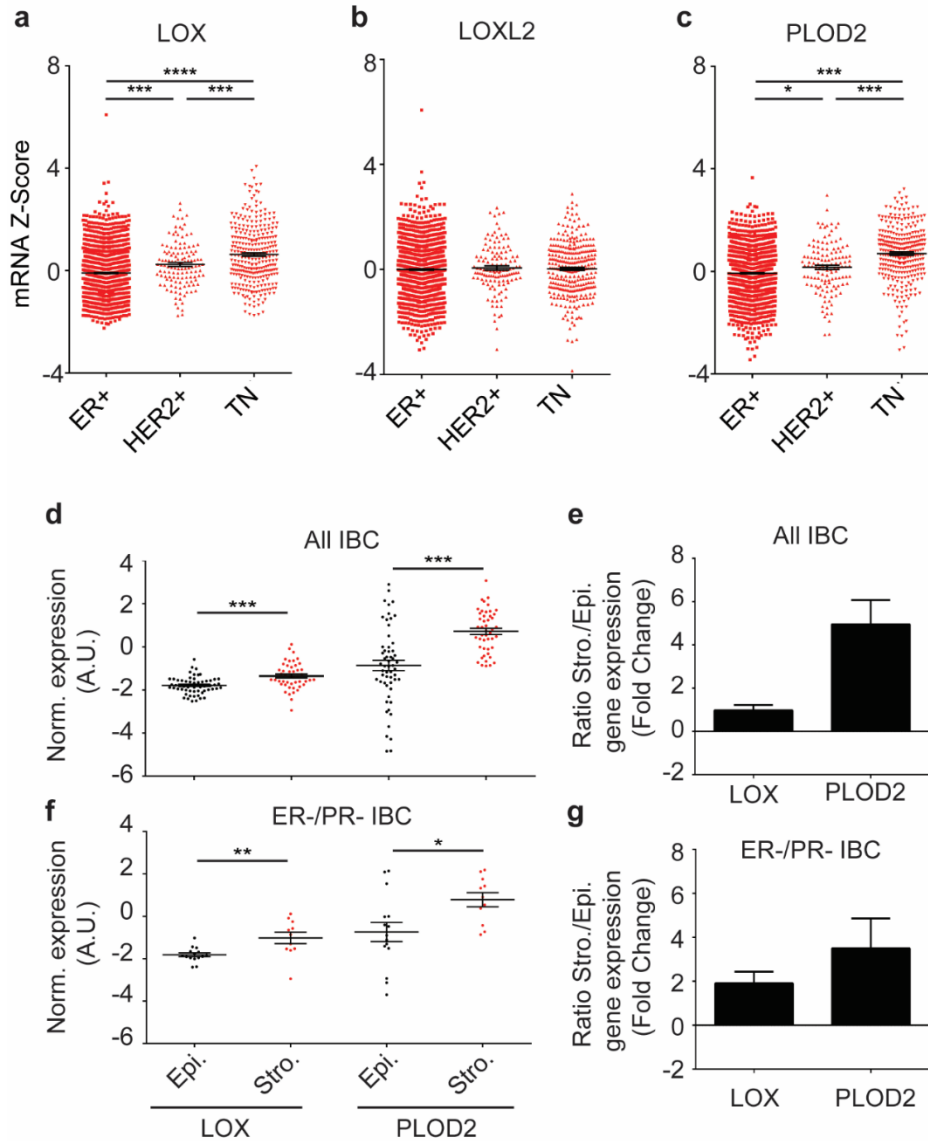


Figure 3.2: LOX and PLOD2 are enriched in TNBC and predominantly expressed by stromal cells. (a-c) Gene expression analysis of LOX (a), LOXL2 (b), and PLOD2 (c) stratified by ER⁺ (n = 1355), HER2⁺ (n = 127), and triple negative (TN; n = 299) subtypes. Gene expression is plotted as a scatter plot of mRNA z scores with the mean \pm SEM. Statistical analysis was performed using one-way ANOVA for overall analysis and unpaired t-test was used for individual comparisons (* p < 0.05, ** p < 0.01, *** p < 0.001, **** p < 0.0001). (d) Scatter plot of individual and mean values \pm SEM comparing LOX (n = 47) and PLOD2 (n = 57) gene expression in microdissected epithelial and stromal compartments of human invasive breast carcinomas. Statistical analysis was performed using Mann-Whitney U test (**** p < 0.0001). (e) Quantification of LOX and PLOD2 gene expression fold change from (d) in stromal cells relative to epithelial cells. (f-g) Restriction of the stromal/epithelial gene expression analysis in (d) and (e) to estrogen receptor (ER) negative and progesterone receptor (PR) negative samples. (LOX n = 11, PLOD2 n = 15). Statistical analysis was performed using Mann-Whitney U test (* p < 0.05, ** p < 0.01).

epithelial compartments revealed that the stromal cells in the tumor tissue expressed significantly more LOX and PLOD2 than the associated tumor epithelium. The data further indicated that this relationship was more evident in the breast tissue from women with ER-/PR- breast cancer that is frequently the more aggressive tumor subclass (**Fig. 3.2d-g**).

The findings implicate, but do not definitively demonstrate a role for LOX and PLOD2 in generating the increased level and greater complexity of collagen crosslinking we quantified in the more aggressive human breast tumors. Nevertheless, the combination of these gene expression data with our findings showing increased collagen crosslink abundance provide compelling evidence to suggest that increased expression of LOX and PLOD2, particularly from stromal cells, likely contribute to elevated levels of collagen crosslinks and HLCCs in TN tumors. Moreover, given that TN tumors are the most aggressive and lethal breast cancer, these data link human breast tumor aggression to increased levels of total and complex collagen crosslinks and higher stromal stiffness. Accordingly, the findings implicate the collagen crosslinking enzymes LOX and LH2, and by extension factors that regulate their expression, in breast cancer aggression.

Stromal — and not epithelial — crosslinking enzymes regulate tissue fibrosis and collagen crosslinking *in vivo*

Prior studies demonstrated that both cancer cell lines and stromal fibroblasts express LOX and LH2 to induce tissue stiffening and fibrosis implying they also drove collagen cross-linking. Seminal articles identified hypoxia-induced HIF1a as a key regulator of tumor epithelial LOX and LH2 expression and suggested epithelial secretion of these enzymes drives collagen remodeling, crosslinking and stiffening that foster tumor cell dissemination and primes the pre-metastatic niche to facilitate metastatic colonization^{133,134}. Our analysis of breast cancer clinical specimens showed that the stromal cells in the breast tissue express higher levels of LOX and PLOD2 as compared to the breast tumor epithelium. Moreover, our prior studies showed LOX is expressed in stromal

fibroblasts in a transgenic mouse model of ErbB2-induced mammary tumor malignancy. Furthermore, we demonstrated that fibroblasts expressing LOX injected into a cleared mammary fat pad not only induced ECM remodeling and stiffening but also potentiated the growth and malignant progression of pre-malignant tumor cells injected into the modified glands³⁵. Thus, the relative contribution of tumor- and stromal- derived collagen crosslinking enzymes to tumor fibrosis, ECM remodeling and collagen crosslinking remains unclear; particularly in the context of spontaneous tumors and patient tumors in which the ECM evolves concurrently with tumor progression.

To directly test the extent to which epithelial-derived LOX can crosslink collagen and induce tissue fibrosis and stromal stiffening in mammary tissue, we created a genetically engineered mouse model (GEMM) in which we targeted and controlled luminal epithelial-specific expression of mouse LOX using the MMTV-rtTA promoter (Epithelial LOX overexpression [OX]). (**Fig. 3.3a, Fig. A2.6a-b**). We crossed these mice into the PyMT spontaneous mammary tumor model to enhanced LOX expression in the mammary tumor epithelium (PyMT epithelial LOX OX) and assayed their stromal phenotype as compared to the mammary glands from age-matched PyMT control mice (PyMT). Again, despite confirming ectopic LOX expression and elevated levels of cleaved LOX protein in the mammary tumor epithelial compartment (**Fig A2.6c**), we were not able to detect any increase in the levels, nor any altered organization of the mammary gland interstitial collagen (**Fig 3.3b-c**). Moreover, xAAA crosslinking analysis revealed that the level of collagen crosslinks between the PyMT control and PyMT epithelial LOX OX mammary gland stroma were indistinguishable (**Fig. 3.3d-i**). Nevertheless and importantly, we could easily and consistently detect a significant increase in fibrillar collagens, collagen crosslinks and stromal stiffness in the PyMT mammary tumors as compared to age-matched FVB mammary glands lacking tumors (**Fig. 3.4c,f-k**). These studies both validate the sensitivity of our crosslinking assay and imply that tumor epithelial LOX is not the primary driver of collagen crosslinking and stiffening in endogenous mammary tumors.

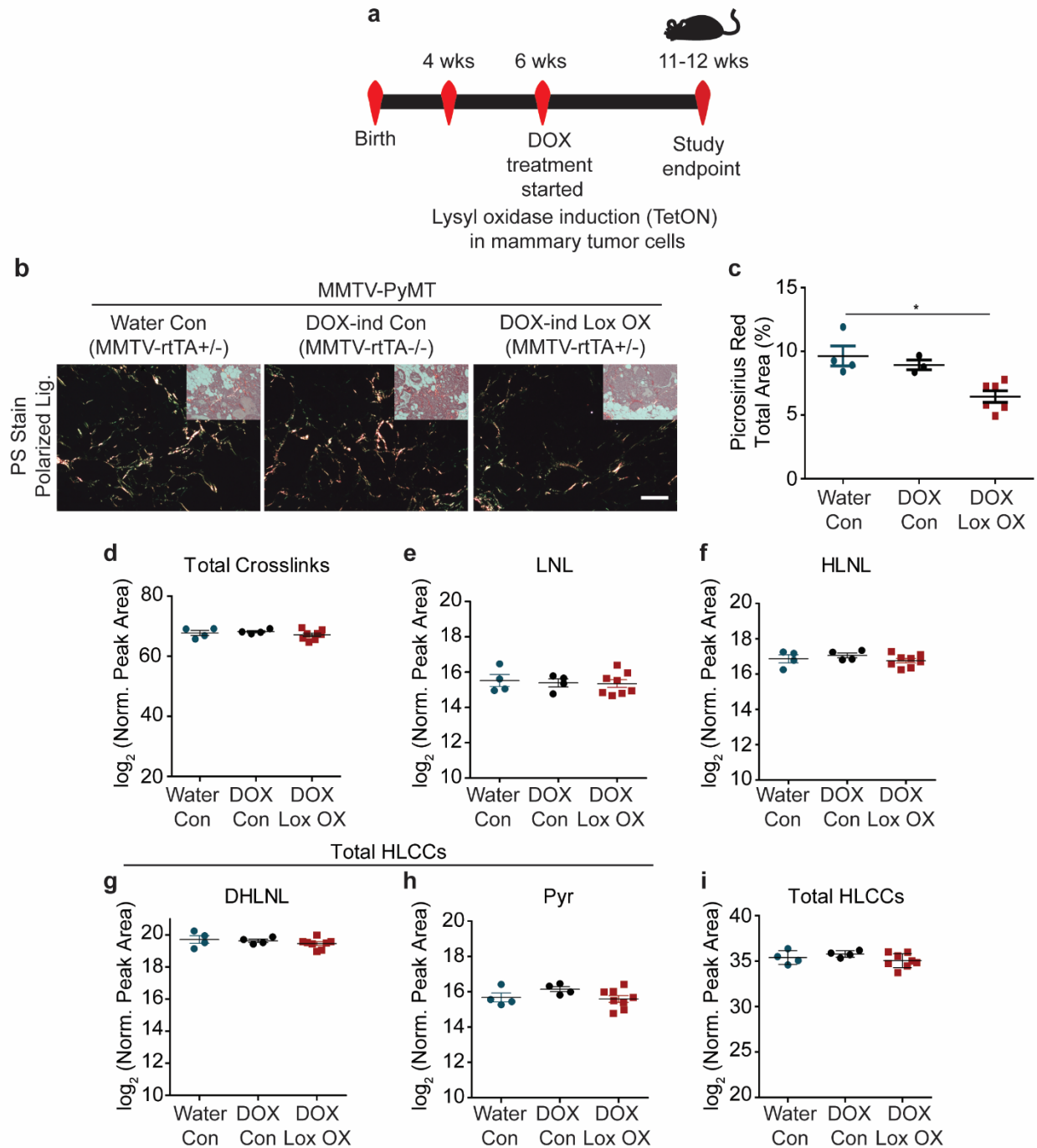


Figure 3.3: Epithelial-derived collagen crosslinking enzymes fail to induce collagen crosslinking. (a) Schematic depicting the experimental strategy used to induce epithelial Lox overexpression. (b) Polarized light images with brightfield inset of picrosirius red stained murine mammary tissues. (c) Quantification of percent area of picrosirius red staining per field of view, plotted as a scatter plot of the mean for each animal \pm SEM. Statistical analysis was performed using Kruskal-Wallis one-way ANOVA (* $p < 0.05$). (d) Scatter plot showing individual and mean values \pm SEM of total tissue collagen crosslinks in PyMT controls (Water $n = 4$, DOX $n = 4$) and

PyMT epithelial Lox overexpression (n = 8). **(e-h)** Scatter plots showing individual and mean values \pm SEM for each LCC and HLCC collagen crosslink measured in PyMT control and PyMT epithelial Lox overexpression tumor tissue. **(i)** Scatter plot showing individual and mean values \pm SEM of total HLCCs calculated as the sum of DHLNL and Pyr crosslinks. Quantity of crosslinks per tissue was calculated normalizing crosslinks to total collagen content (i.e., hydroxyproline abundance) and wet tissue weight. Values were plotted as \log_2 transformed normalized peak areas as quantified from LC-MS data. Statistical analyses for crosslinking data were performed using one-way ANOVA for overall comparison and unpaired t-test for individual comparisons (*p < 0.05, **p < 0.01, ***p < 0.001, ****p < 0.0001).

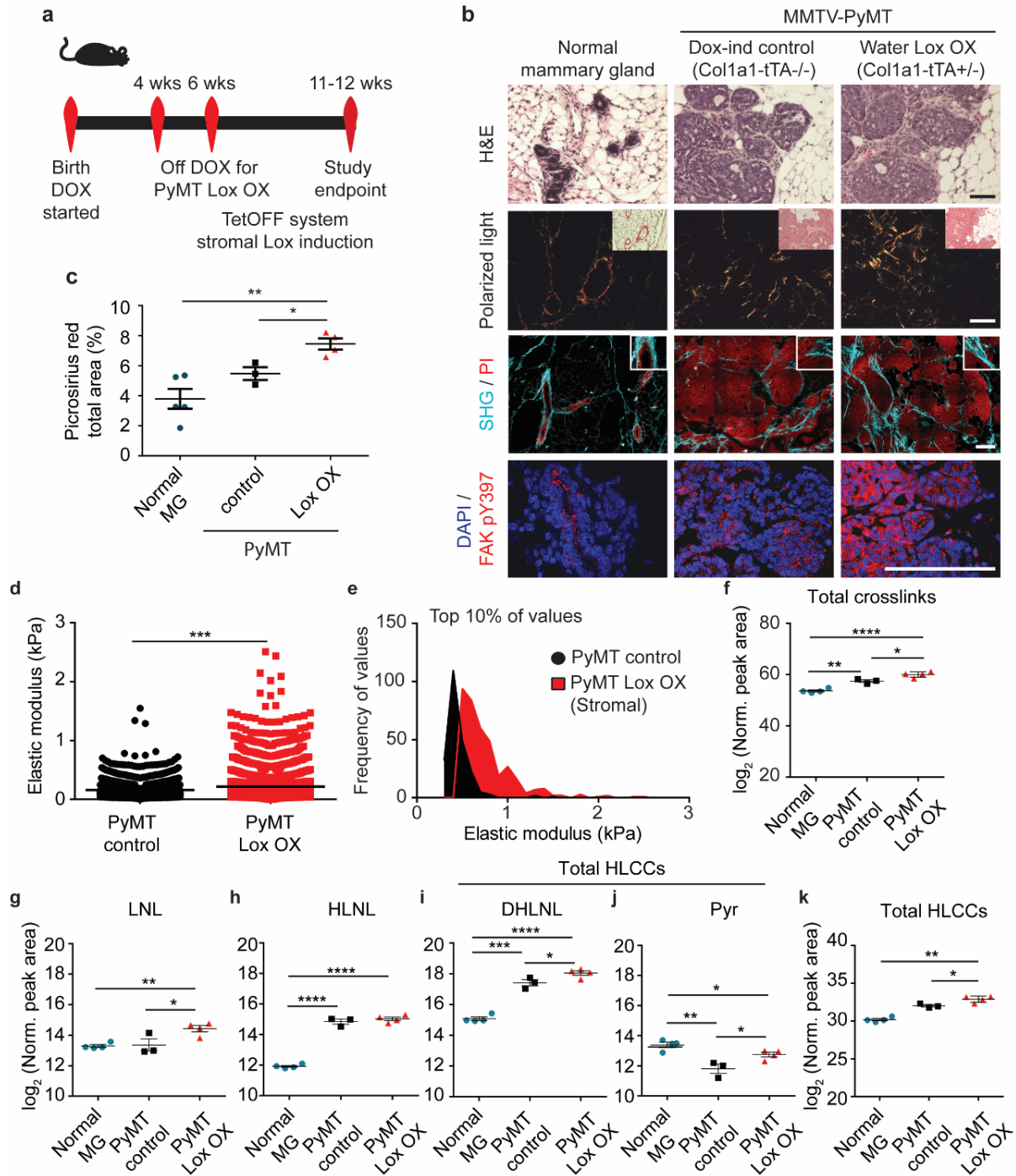


Figure 3.4: Stromal-derived LOX regulates collagen crosslinking and stiffening. (a) Schematic depicting the experimental strategy used to induce stromal Lox overexpression. (b) Representative images of normal murine mammary gland and PyMT control and stromal Lox overexpressing tumor tissues. (**Top row**) Brightfield images of H&E stained murine mammary tissues. (**Second row**) Polarized light images with brightfield inset of picrosirius red stained murine mammary tissues. (**Third row**) Two photon second harmonic generation (SHG) images of murine mammary tissues revealing collagen organization (turquoise) and propidium iodide (PI;

red) stained nuclei. **(Bottom row)** Confocal images of mammary tissue stained with anti-FAK pY397 monoclonal antibody (red) and DAPI (blue; nuclei). Scale bars are all 100 μm . **(c)** Quantification of fibrillar collagen by picrosirius red staining by percent area per field of view. The mean of 3-5 regions was calculated and plotted for each animal \pm SEM. Statistical analysis was performed using Kruskal-Wallis one-way ANOVA ($*p < 0.05$) for overall relationship and unpaired t-test for comparing individual groups ($*p < 0.05$, $**p < 0.005$). **(d)** Scatter plot showing individual values and mean of the top 10% of elastic modulus measurements performed by AFM microindentation on the mammary stroma from mice with PyMT-induced tumors (PyMT Control; $n = 3$ mice) as compared to the stroma in PyMT-induced tumors in which lysyl oxidase was elevated in stromal cells (PyMT Lox OX; $n = 4$ mice). Values reflect measurements taken from 3-5 individual force map regions per mammary gland. Statistical analyses were performed using Mann-Whitney U test ($***p < 0.001$). **(e)** Histogram showing the distribution of the top 10% of elastic modulus measurements by AFM microindentation in PyMT control and Lox OX tumors. Statistical analysis was performed using Mann-Whitney U test ($****p < 0.0001$). **(f)** Scatter plots showing individual and mean values \pm SEM of total collagen crosslink abundance in the normal murine mammary gland ($n = 4$) as compared to glands with doxycycline-induced PyMT tumors ($n = 3$ mice per control group) and PyMT tumors in which stromal lysyl oxidase was elevated ($n = 4$ mice per Lox OX group). **(g-j)** Scatter plots showing individual and mean values \pm SEM of LCC and HLCC crosslinks quantified in normal mammary gland, PyMT Control tumors and PyMT Lox OX tumors. **(k)** Scatter plot showing individual and mean values \pm SEM of total HLCCs calculated as the sum of DHLNL and Pyr crosslinks. Quantity of crosslinks per tissue was calculated normalizing crosslinks to total collagen content (i.e., hydroxyproline abundance) and wet tissue weight. Values were plotted as \log_2 transformed normalized peak areas as quantified from LC-MS data. Statistical analyses for crosslinking data were performed using one-way ANOVA for overall comparison and unpaired t-test for individual comparisons ($*p < 0.05$, $**p < 0.01$, $***p < 0.001$, $****p < 0.0001$).

We and others have implicated stromal fibroblast LOX as a key promoter of epithelial tumor progression and aggression^{35,118,149}. To directly test the functionality of the ectopically-expressed LOX and the relevance of fibroblast-specific expression of LOX, we next created mouse cohorts of PyMT GEMMs in which we restricted ectopic LOX expression to the stromal population using the Col1a1-tTA promoter (MMTV-PyMT+/-; Col1a1-tTA+/-;TetO_mLox+/-; herein denoted PyMT LOX OX) (**Fig. 3.4a, Fig. A2.7b**). To begin with, induction of LOX in the stromal cells markedly enhanced the amount of fibrillar collagen in the MMTV-PyMT LOX OX mammary glands, as revealed by quantification of polarized images of Picrosirius Red stained tissue (**Fig. 3.4b, second row images; quantified in c**). We also detected more and thicker linearized interstitial collagen when LOX was increased in the stromal cells by two-photon second harmonic generation imaging (**Fig. 3.4b, third row panels**). In addition, immunostaining revealed more phosphorylated tyrosine 397 focal adhesion kinase protein (^{pY397}FAK) in the mammary epithelium of the glands in which stromal LOX was elevated (**Fig. 3.4b, bottom panels**), likely reflecting the increase in elasticity that we measured in the tissue stroma using atomic force microscopy (AFM) indentation (12) (**Fig. 3.4d-e & Fig. A2.9b**). Consistently, we measured higher levels of total collagen crosslinks in the PyMT LOX OX mice as compared to the levels quantified in the MMTV-PyMT control glands (**Fig. 3.4f**). Furthermore, the most significant increases that we quantified in the PyMT LOX OX glands were dihydroxy lysinonorleucine (DHLNL) and pyridinoline (Pyr) crosslinks (**Fig. 3.4g-k**), which are the crosslinks generated through the HLCC pathway that promote mechanical stability and strength in skeletal tissue^{146,150}. Of note, we did not detect any increase in DHLNL or Pyr in the mammary glands in which ectopic LOX expression was elevated in the mammary epithelium using the MMTV promoter (**Fig. 3.3g-h**). These findings imply that stromal cells are the primary regulators of interstitial collagen crosslinking and stromal stiffening in mammary tumors.

Tissue inflammation regulates tissue fibrosis, collagen crosslinking and stromal stiffening

Cancer progression is accompanied by tissue inflammation and the most aggressive human breast tumors with the stiffest invasive stroma harbor the highest number of macrophages^{26,144}. Consistently, decreasing the number of tumor macrophages, either through genetic ablation of macrophage colony stimulating factor (CSF-1) or via pharmacological and inhibitory antibody treatment with anti-CSF1 antibody, reduces lung metastasis in the PyMT mouse model of mammary cancer^{142,143,151,152}. Interestingly, macrophage ablation was more effective at preventing lung metastasis when the treatment was initiated early, prior to malignant transformation and coincident with the onset of tissue fibrosis¹⁴². These findings raise the possibility that macrophage ablation may regulate tumor aggression, at least in part, by promoting collagen remodeling and inducing ECM crosslinking and stromal stiffening (**Fig. 3.3 & 3.4**).

To assess the possibility that there is a causal association between macrophage-mediated tissue inflammation, tumor fibrosis and ECM stiffening and mammary tumor aggression, PyMT mice were treated with anti-CSF-1 antibody or an IgG control antibody commencing at four weeks of age, prior to the onset of ductal hyperplasia⁷⁰. Mouse cohorts (6/treatment group/time point) were sacrificed at eight and eleven weeks of age. Immunostaining confirmed reduction of tumor macrophages at eight weeks of age, that was also evident in the eleven-week-old treated tissue (**Fig. 3.5a top panel, Fig. A2.8a**). The excised lungs from the eleven week mice confirmed reduced frequency of lung metastasis in the anti-CSF-1 antibody-treated group (**Fig. 3.5b**), consistent with prior work documenting a significant inhibition of lung metastasis when anti-CSF-1 treatment was initiated at four weeks¹⁴². The mammary glands from the eight and eleven week old mice were excised and analyzed for fibrosis and biomechanical properties (**Fig. 3.5a,c-i**). Despite confirming an equivalent number of fibroblasts in the treated and nontreated groups, polarized images of PS stained tissue revealed lower levels of total fibrillar collagen in the stroma of the eight-week anti-CSF1 antibody treated

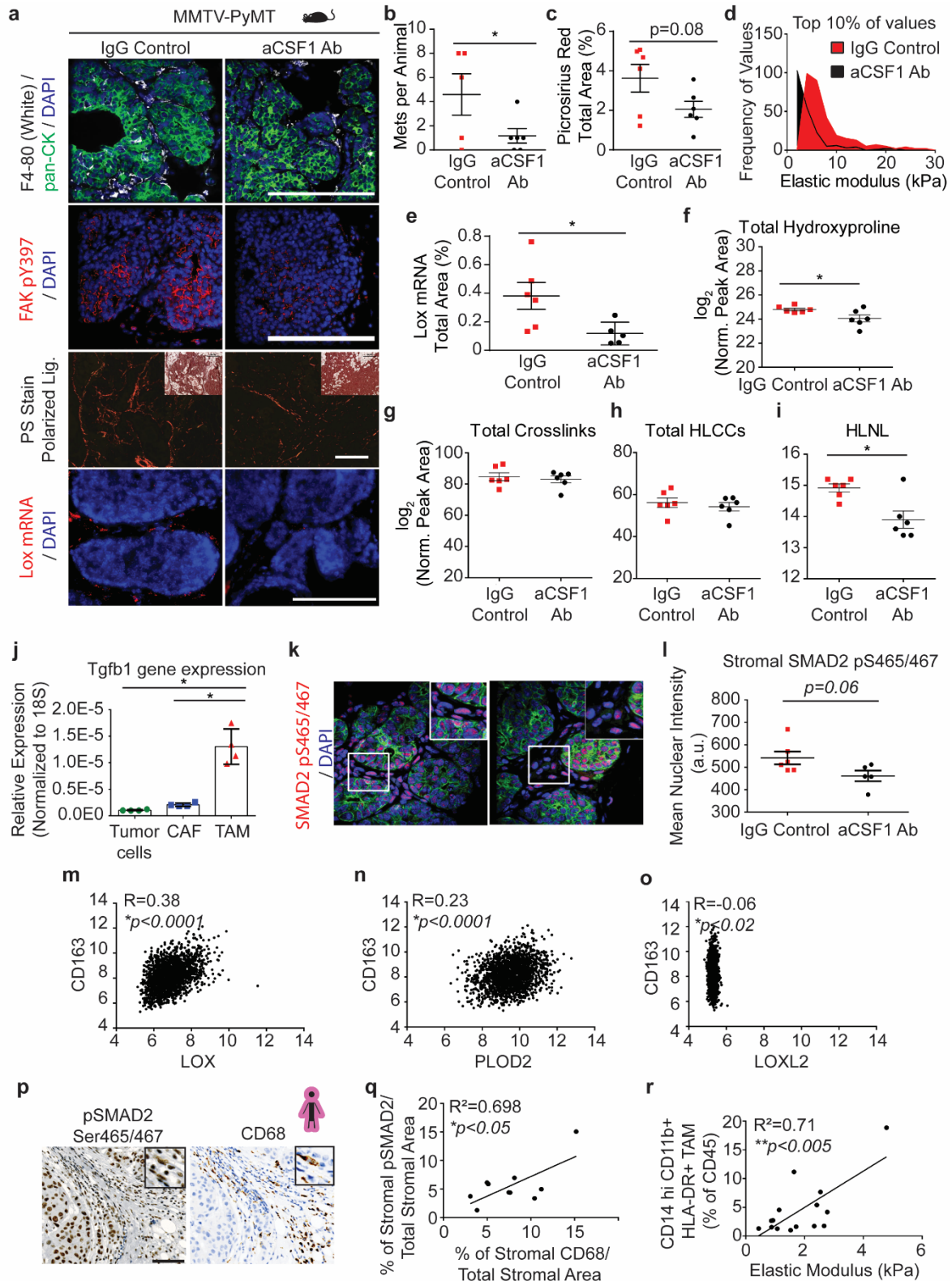


Figure 3.5: Tumor infiltrating macrophages secrete TGF β to activate stromal-mediated collagen crosslinking. (a) Representative images of PyMT tumor tissue from 8 weeks of age mice treated with anti-CSF1 blocking antibody or IgG1 control. (Top row) IgG1 treated (n = 6) and anti-CSF1 treated (n = 5) PyMT tumor tissue stained for pan-cytokeratin (green) marking

epithelial cells, F4/80 (white) marking tumor infiltrating macrophages, and DAPI marking nuclei (blue). **(Second row)** IgG1 treated (n = 6) and anti-CSF1 treated (n = 5) PyMT tumor tissue stained for tyrosine 397 phosphorylated focal adhesion kinase (red) indicative of mechanosignaling and DAPI marking nuclei (blue). **(Third row)** Polarized light images with brightfield inset of IgG1 treated (n = 6) and anti-CSF1 treated (n = 6) PyMT tumor tissue stained with picosirius red to visualize fibrillar collagen. **(Bottom row)** Lox mRNA in situ hybridization in IgG1 treated (n = 6) and anti-CSF1 treated (n = 5) PyMT tumor tissue and DAPI marking nuclei (blue). Scale bar for all images is 100 μ m. **(b)** Quantification of the number of metastatic colonies in the lung tissues from IgG1 treated (n = 5) and anti-CSF1 treated (n = 6) mice at 11 weeks of age via PyMT IHC assessing 5 layers (5 micron section; 5 sections per layer; 50-100 microns steps). Statistical analysis was performed using unpaired t-test (*p < 0.05). **(c)** Quantification of fibrillar collagen by picosirius red staining by percent area per field of view in 8-week-old mice treated with anti-CSF1 blocking antibody or IgG1 control. The mean of 3-4 regions was calculated and plotted for each animal \pm SEM. Statistical analysis was performed using unpaired t-test (p = 0.08). **(d)** Histogram showing the distribution of the top 10% of elastic modulus measurements by AFM microindentation in PyMT IgG1 treated (n = 6) and anti-CSF1 treated (n = 4) tumors. Statistical analysis was performed using Mann-Whitney U test (****p < 0.0001). **(e)** Quantification of Lox mRNA signal by percent area of signal per field of view in 8-week-old mice treated with anti-CSF1 blocking antibody (n = 5) or IgG1 control (n = 6). The mean of 5-6 regions was calculated and plotted for each animal \pm SEM. Statistical analysis was performed using an unpaired t-test (*p < 0.05). **(f-i)** Scatter plots showing individual and mean values \pm SEM of the levels of total hydroxyproline (collagen content) **(f)**, total collagen crosslinks **(g)**, HLCCs **(h)**, and HLNL crosslinks **(i)** in 8-week-old IgG1 treated and anti-CSF1 treated PyMT tumors. Quantity of crosslinks per tissue was calculated normalizing crosslinks to wet tissue weight. Values were plotted as log₂ transformed normalized peak areas as quantified from LC-MS data. Statistical analysis was performed using unpaired t-test (*p < 0.05). **(j)** Quantification of Tgfb1 gene expression by RT-qPCR in tumor cells, cancer-associated fibroblasts, and macrophages sorted out from PyMT tumors (n = 4). Gene expression was normalized to 18S. Statistical analysis was performed using Kruskal-Wallis one-way ANOVA for overall comparison and Mann-Whitney U test for individual comparisons (*p < 0.05, ***p < 0.001). **(k)** Representative images of PyMT tumor tissue from mice treated with IgG1 (n = 6) and anti-CSF1 (n = 5) stained for pan-cytokeratin (green) marking epithelial cells, SMAD2 pS465/467 (red), and DAPI marking nuclei (blue). **(l)** Scatter plot showing individual and mean values \pm SEM of the mean nuclear intensity of pSMAD^{S465/467} in stromal cells of IgG1 treated (n = 6) and anti-CSF1 treated (n = 5) PyMT mice. The mean for each animal was calculated from 4-7 regions within the tumor. Statistical analysis was performed using unpaired t-test (p = 0.06). **(m-o)** Scatter plot depicting the Spearman correlation of CD163 gene expression with LOX **(m)**, PLOD2 **(n)**, and LOXL2 **(o)** in human breast tumors (n = 1904). **(p)** Representative IHC images of serial human breast tumor sections stained for CD68 **(top)** and pSMAD2^{S465/467} **(bottom)** counterstained with hematoxylin to mark nuclei. **(q)** Scatter plot depicting the linear regression correlation of stromal pSMAD2 IHC staining with stromal CD68 IHC staining in human breast tumors (n = 10). **(r)** Scatter plot depicting the linear regression of CD14⁺ CD11b⁺ HLA-DR⁺ tumor associated macrophage infiltrate with tumor elastic modulus as measured by AFM microindentation in human breast tumors (n = 15).

group (**Fig. 3.5a, third row panel, Fig. A2.10b-c**). AFM microindentation additionally demonstrated that the tissue stroma from both the eight week old (**Fig. 3.5d**), and the eleven week old (not shown) mammary glands was softer, likely accounting for the reduced integrin mechanosignaling detected in the CSF1-antibody treated tissue, as revealed by less intense staining for p^{Y397} FAK (**Fig. 5a, second row panel**). Consistently, we also observed reduced levels of Lox mRNA in eight week, anti-CSF1 treated mice by in situ hybridization (**Fig. 3.5a, bottom panel, Fig. 3.5e**). In agreement with prior studies, nearly all the detected Lox mRNA was restricted to stromal cells (**Fig 3.5a, bottom panel**)¹¹⁸. These findings suggest that reducing the level of tumor-associated macrophages (TAMs) not only prevents lung metastasis but also concomitantly reduces tissue fibrosis and stiffening, likely by preventing stromal cell activation.

TAMs secrete abundant TGF β that stimulates fibroblast differentiation to a myofibroblast phenotype and induces expression of collagen crosslinking enzymes including LOX¹¹⁸. PCR analysis of flow activated cell sorted (FACS) cells from the transformed mammary glands of PyMT mice (11 weeks) confirmed that the TAMs expressed by far the highest levels of TGF β , as compared to neoplastic epithelium and the cancer-associated fibroblasts (**Fig. 5j**). These findings suggest that the tumor infiltrating macrophages could promote fibrosis and stromal stiffening through secreted TGF β ; a finding supported by a strong stromal pSMAD2 (SMAD2 pS465/467) in the IgG control antibody-treated PyMT mammary glands (**Fig. 3.5k-l**). To examine whether TAM recruitment could regulate collagen crosslinking in human tumors we queried a publicly available human breast tumor gene expression data set for TAM markers and collagen modifying enzymes. Consistent with a role for TAMs in stimulating expression of collagen modifying enzymes, gene expression of the TAM marker CD163 positively correlated with both LOX and PLOD2 but not LOXL2 in human breast tumors (n = 1904) (**Fig. 3.5m-o**). Moreover, co-staining of resected human breast tumors with the macrophage/monocyte marker CD68 and the downstream TGF β signaling molecule pSMAD2 Ser465/467 revealed a significant positive

correlation between pSMAD2 Ser465/467 and infiltrating tumor macrophages at the invasive front of human breast tumors (**Fig. 3.5p-q**). Furthermore, FACS analysis established a significant correlation between the infiltrating tumor associated macrophages, as demonstrated by CD14^{hi}CD11b⁺ HLA-DR⁺ cell surface markers normalized to total CD45 infiltrating cells, and the elastic modulus of the invasive front of human invasive breast cancers (**Fig. 3.5r**). These findings suggest that tumor inflammation and macrophage secreted factors such as TGF β could promote tissue fibrosis by enhancing fibroblast expression of the collagen crosslinking enzymes LOX and PLOD2, but not LOXL2, to induce collagen crosslinking and stromal stiffening.

LH2 inhibition reduces lung metastasis and stromal LH2 predicts poor prognosis in breast cancer patients

Using the data set generated from the micro-dissected tumors, we next explored the clinical relevance of epithelial vs. stromal LOX and PLOD2 expression by assessing their relative contribution to overall survival in breast cancer patients. Surprisingly, neither stromal cell nor epithelial LOX predicted overall patient survival in this cohort (**Fig. 3.6a-b**). However, the findings clearly showed that overexpression of stromal PLOD2, but not epithelial PLOD2, significantly correlated with poor breast cancer patient prognosis (**Fig. 3.6c-d**). The data provide further evidence that HLCCs, formed primarily through the activities of collagen crosslinking enzymes expressed by stromal cells, promote breast tumor aggression that contributes to poorer overall survival. The findings also highlight the importance of the collagen crosslinking profile and its potential impact on stromal stiffness in tumor aggression.

LH2 (the protein encoded by PLOD2) is a key enzyme that regulates the level of HLCC crosslinking of fibrillar collagen and consequently contributes substantially to the tensile properties of the tissue stroma^{130,153,154}. We quantified the highest level of HLCC crosslinking and the stiffest invasive front in the breast tissue from women with the most aggressive breast cancers (**Fig. 3.1j**). Consistently, when we analyzed the gene expression data from a published cohort of breast cancer patients we observed that ER-/HER2- (TN; n=133) breast cancers express the highest

level of the PLOD2 gene transcript as compared to the levels expressed in HER2+ (n=73) and ER+/HER2- (luminal, n=314) breast tumors (**Fig. A2.11a**)¹⁵⁵. Further analysis showed that high PLOD2 expression in breast cancer patients with HER2+ and TN tumors significantly predicts reduced distant metastasis-free survival (DMFS), as well as increased risk of relapse in TN tumors (**Fig. A2.11b-d**)^{84,155}. These findings implicate PLOD2/LH2 as a key regulator of breast tumor aggression through its ability to induce the HLCC crosslinking of fibrillar collagens that enhance the stiffness of the tumor stroma.

To evaluate whether LH2 does enhance stromal stiffness to promote breast tumor aggression, we systemically treated a cohort of PyMT mice with the LH2 inhibitor minoxidil or vehicle (PBS) from five weeks of age until sacrifice at either 11-12 weeks or 13-14 weeks of age (**Fig. 3.6e**). Consistent with its predicted role in enhancing stromal stiffness through modifying the nature of collagen crosslinks, AFM microindentation revealed that the phenotypically-similar collagen-rich ECM adjacent to tumors from the minoxidil treated mice (see polarized imaging of picosirius red stained tissue) was significantly softer when compared to the vehicle-treated age/stage-matched PyMT mice (**Fig. 3.6f-h**). Furthermore, inhibiting LH2 also significantly decreased lung metastasis, causally linking HLCC collagen crosslinking to stiffness-mediated breast tumor aggression (**Fig. 3.6i**). Our gene expression data from the epithelial and stromal microdissection cohort indicated that stromal PLOD2, but not epithelial PLOD2, strongly predicted poor survival in breast cancer patients. Therefore, we next sought to definitively assess the relative contribution of stromal versus neoplastic epithelial LH2 protein expression to human breast tumor aggression using a large tissue array of annotated human breast tumor biopsies. To accomplish this, we first developed an LH2 immunostaining protocol (IHC) and then we analyzed neoplastic epithelial and stromal expression of the LH2 enzyme in tissue biopsies from a large cohort of histopathologically classified breast cancer patients (N=505) with accompanying clinical

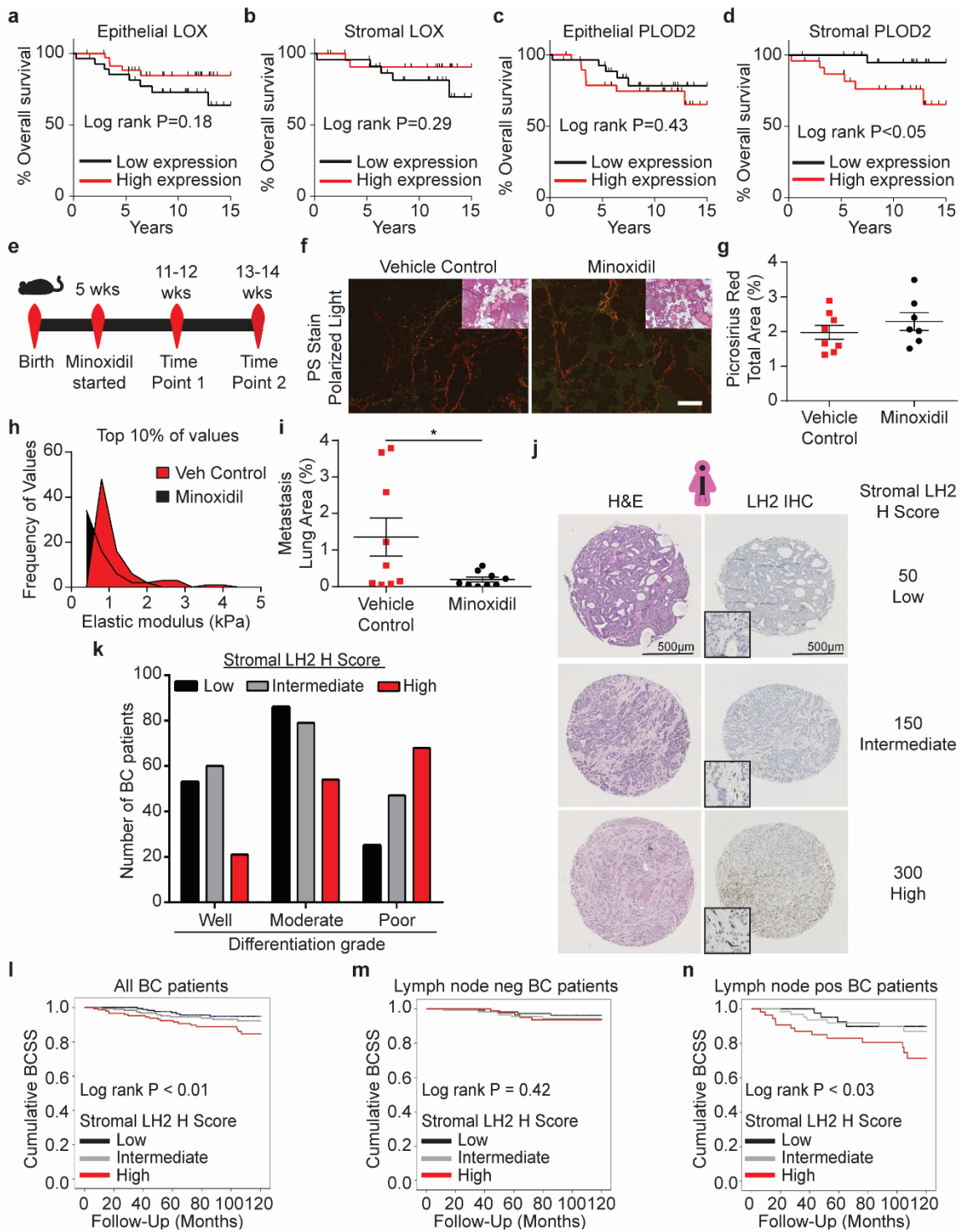


Figure 3.6: Stromal LH2 predicts poor patient outcomes. (a-b) Kaplan-Meier plots showing overall survival for patients based on levels of LOX expression in epithelial cells (low n = 28, high n = 36) (a) or stromal cells (low n = 23, high n = 24) (b). The median level of expression was defined as the cutoff for low and high expression. (c-d) Kaplan-Meier plots showing overall survival for patients based on levels PLOD2 expression in epithelial cells (low n = 28, high n = 29)

(c) or stromal cells (low n = 23, high n = 24) (d). The median level of expression was defined as the cutoff for low and high expression. (e) Schematic depicting the experimental timeline used to inhibit lysyl hydroxylase 2 in PyMT mice. (f) Representative polarized light images with brightfield insets of picrosirius red stained tumor tissue from PBS vehicle treated control (n = 8) and minoxidil treated (n = 7) PyMT mice. Scale bar is 100um. (g) Quantification of fibrillar collagen by picrosirius red staining by percent area per field of view. The mean was calculated and plotted for each animal \pm SEM. (h) Histogram showing the distribution of the top 10% of elastic modulus measurements by AFM microindentation in PyMT control and Lox OX tumors. Statistical analysis was performed using Mann-Whitney U test (****p < 0.0001). (i) Scatter plot quantifying the area of lung sections occupied by metastases from vehicle treated (n = 9) and minoxidil treated (n = 8) mice at 13 weeks of age via H&E staining and assessing 4 layers (5 micron section; 5 sections per layer; 50-100 microns steps). Statistical analysis was performed using a two-tailed unpaired t-test (*p < 0.05). (j) Representative phase contrast images of sections from tissue microarrays (TMAs) of human breast cancers representing incident breast cancer cases collected and arrayed as 1-mm cores from each tumor. Sections were stained with Hematoxylin and Eosin (H&E; top) and lysyl hydroxylase two (LH2; bottom) via immunohistochemistry. (k) Bar graphs showing clinical correlation between lysyl hydroxylase two (LH2) score as a function of tumor grade (see *Table 1 for number of patients*). LH2 IHC staining was assessed with the semi-quantitative stromal specific H-score from 0 to 300. The lowest tertile of LH2 H-scores was defined as H-scores between 0 and less or equal to 120, the intermediate H-score to above 120 and equal or less than 230, and the highest stromal LH2 score as above 230. For tumor grade and LH2 H score, statistical analysis was performed using a linear-by-linear association (***P<0.0001). (l) Kaplan-Meier curves indicating cumulative breast cancer specific survival (BCSS) based on stromal LH2 H score assessed in breast cancer patients up to 10 years after diagnosis (LH2 low n = 175, intermediate n = 188, high n = 146). (m) BCSS curves by stromal LH2 H score including only axillary lymph node negative patients (LH2 low n = 116, intermediate n = 116, high n = 90). (n) BCSS curves by stromal LH2 H score including only axillary lymph node positive patients (LH2 low n = 44, intermediate n = 63, high n = 54). For Kaplan-Meier curves, statistical analyses were performed by LogRank test.

information and follow up data (**Table A2.2** and **Table A2.3**). LH2 IHC staining in the epithelium and stromal cells was scored as low, intermediate and high and the relationship between epithelial versus stromal expression and breast cancer patient outcome was calculated (**Fig. 3.6j**; **Fig. A2.12a**). IHC scoring analysis revealed that only a modest number of patients with poorly differentiated breast tumors expressed moderate to high levels of epithelial LH2 (**Fig. A2.12b**); a finding that accords with prior links between tumor size, hypoxia and LH2-dependent tumor aggression^{130,133}. More strikingly however, we observed that a disproportionately high number of breast cancer patients with moderately and poorly differentiated breast tumors had high stromal cell LH2 (indicated by an H score of above 230; **Fig. 3.6k**). These data and our observation that even well differentiated breast tumors express intermediate levels of stromal cell LH2 (H score above 120 and equal or less than 230) imply that stromal cell LH2, rather than epithelial LH2, may be a more robust indicator of breast tumor aggression. Consistently, stratification of breast tumor patient analysis into ER+/HER2- (N=296); HER2+ (N=36) and TN (N=32) showed an enrichment for intermediate and high stromal LH2 H-score in the more aggressive cancer subtypes (**Table A2.2** and **Table A2.3**). Furthermore, we uncovered a significant correlation between high stromal cell LH2 H-score and shorter breast cancer patient-specific survival when adjusted for age at diagnosis (**Fig. 3.6l**). We also established a significant association between stromal cell but not epithelial LH2 levels and survival in lymph node positive breast cancer patients but not lymph node negative breast cancers (**Fig. 3.6m-n**; **Fig. A2.12d-e**). These clinical data identify stromal cell LH2 as a novel biomarker with potential to predict metastatic disease and poor patient survival among breast cancers overall, as well as within the highest risk TN breast cancer subtype.

Discussion

We identified infiltrating macrophages as key regulators of stromal cell-mediated collagen crosslinking, stromal stiffening and tumor metastasis. Our clinical findings corroborated our experimental results, revealing significant associations between macrophages and collagen

crosslinking enzymes providing evidence for a critical impact of inflammatory stromal cell-mediated collagen crosslinking and stromal stiffening in tumor aggression and patient outcome. Diverse subsets of myeloid cells account for adverse patient outcomes because they differentially promote angiogenesis, tumor cell intravasation, and suppress the anti-tumor immune response¹⁵⁶. Our results expand this perspective to include a key role for early infiltrating macrophages in initiating a collagen crosslinking and stiffening program that ultimately fosters tumor aggression and progression. We also determined that TN breast cancers contain much higher amounts of LH2- and LOX-derived collagen crosslinks. Specifically, we demonstrated that significantly higher levels of HLCC crosslinks could explain their higher stromal stiffness and aggressiveness²⁶. Intriguingly, in depth collagen analysis suggested that each breast tumor subtype exhibits a distinct collagen organization, stiffness and crosslinking profile, raising the possibility that distinct collagen architectures and crosslinking signatures may reflect differences in tissue pathobiology. Indeed, TN breast cancers often present with high macrophage infiltration; an observation that is consistent with our AFM, two photon and collagen crosslinking analysis data²⁶. Given that the immune cell infiltrate significantly influences treatment response it is tempting to speculate that distinct collagen architectures, crosslinking signatures and stiffnesses similarly regulate therapeutic efficacy.

We determined that stromal LH2 is a robust predictor of survival in breast cancer patients, especially in those that are lymph node positive, supporting a potentially important clinical link to stromal collagen crosslinking. Our data also revealed that both the upregulation of crosslinking enzymes and in turn, collagen crosslinking, occur at an early stage of malignancy that is concurrent with tumor cell invasion and coincident with the accumulation of infiltrating macrophages¹⁵⁷. In part, this may explain why therapeutics targeting LOX and LOXL2 have thus far failed to significantly prolong cancer patient survival. Substantial levels of collagen crosslinking are likely to have occurred prior to therapy administration, and while these agents may prevent further crosslinking activity, they are not capable of reversing crosslinks or collagen modifications

already present in the tissue. The early initiation of collagen crosslinking also suggests that a detectable increase in stromal LH2 may provide an early prognostic marker of disease progression and aggression that could inform treatment strategies. To that end, our results show for the first time that LH2-derived collagen crosslinks are not only a distinct feature of enhanced stromal stiffening in TN breast cancer but are able to predict distant metastasis-free survival. These results also suggest that the profile of collagen crosslinks, and not simply crosslink abundance alone, may play a role in promoting tumor aggression, thus warranting further investigations into the contributions of HLCCs to ECM mechanical properties and tumor aggression.

Our findings identify fibroblasts as the dominant cell population that promotes reorganization and crosslinking of interstitial collagen to stiffen the tissue stroma. Only stromal-targeted, and not epithelial-targeted, tissue-specific inducible LOX produced any measurable change in collagen architecture, stiffness or crosslink abundance in a spontaneous tumor^{134,158,159}. Our conclusion is consistent with earlier work in which we failed to detect any alterations in fibrosis, collagen organization or stiffness when LOXL2 was either genetically ablated, or ectopically-increased in the mammary epithelium of PyMT mouse tumors, despite documenting a significant impact on metastasis¹⁴⁹. Nevertheless, it is possible that our bulk assay would not detect any small increase in collagen crosslinking induced by invading tumor cells expressing high levels of LOX. To this end, immortalized tumor cells engineered to overexpress LOXL2 injected orthotopically as a bolus of cells were able to induce fibrosis and quantifiable changes in collagen remodeling and tissue stiffening; a finding we too confirmed using isolated PyMT tumor cells overexpressing the LOXL2 enzyme¹⁴⁹. Nevertheless, our data support the notion that in spontaneous tumors, the proximity of stromal cells to collagen and their significantly higher expression of crosslinking enzymes dictate the profile and extent of collagen crosslinking. Given that LH2 modifies collagen intracellularly and stromal cells secrete the vast majority of the interstitial fibrillar collagen, it is not surprising that this is the case^{127,160}. Moreover, our results

stress the necessity of choosing an appropriate model to study tumor associated ECM remodeling and suggest that orthotopic models may fail to accurately recapitulate the natural evolution of ECM in tumor progression.

Our findings not only underscore the importance of stromal stiffness and collagen crosslinking in cancer-associated fibrosis and disease aggression, but also define in more detail the molecular nature of collagen modifications that accompany pathological fibrosis. Clarifying the nature of collagen modifications and specific mechanisms regulating those alterations in fibrosis will assist in the strategic design of novel, efficacious strategies to combat progressive fibrosis and should prove instrumental in enabling further experimentation to understand pathological fibrosis. Indeed, defining the molecular regulators that stimulate collagen cross-linking, and mechanisms that distinguish resolvable from non-resolvable fibrosis would identify attractive therapeutic targets for several pathological fibrotic diseases with limited treatment options.

Methods

Human breast specimen acquisition and processing

Fresh human breast specimens from breast reduction, prophylaxis, or breast tumor mastectomy were either embedded in an optimum cutting temperature (OCT) aqueous embedding compound (Tissue-Plus, Scigen, Cat# 4583) within a disposable plastic base mold (Fisher, Cat# 22-363-554) and were snap frozen by direct immersion into liquid nitrogen and kept at -80°C freezer until cryo-sectioning for analysis, or specimens were formalin fixed and paraffin embedded (FFPE). All human breast specimens were collected from prospective patients undergoing surgical resection at UCSF or Duke University Medical Center between 2010 and 2014. The selected specimens were de-identified, stored, and analyzed according to the procedures described in Institutional Review Board (IRB) Protocol #10-03832 and #10-05046, approved by the UCSF Committee of Human Resources and the Duke's IRB (Pro00034242)²⁶.

Mouse studies

Macrophages were depleted in MMTV-PyMT mice by i.p. injections of 1 mg of anti-CSF1 antibody clone 5A1 or an IgG1 control every 7 days starting at 4 weeks of age. Mice were sacrificed at 8 and 11 weeks of age for tissue analysis.

Minoxidil and PBS vehicle was administered by i.p. injections of 3 mg/kg minoxidil in PBS three times per week starting at 6 weeks of age. Mice were sacrificed at 11-12 and 13-14 weeks of age for tissue analysis.

Generation of mice

All mouse studies were maintained under pathogen-free conditions and performed in accordance with the Institutional Animal Care and Use Committee and the Laboratory Animal Research Center at the University of California, San Francisco.

TetO-mLOX-eGFP construct and transgenic mouse generation

Full length mouse Lox (mLox) cDNA was purchased from OriGene. The full length ORF was amplified by PCR using forward and reverse primers respectively: GCAGGGATCCGCCACCATGCGTTTCGCCTGGGCTG and GGCGTCTAGAGCACCATGCGTTTCGCCTGGGCTGTGC. Following digestion with BamHI and XbaI, the PCR product was inserted into pSK TetO IRES 3xnlEGFP¹⁶¹ downstream of the Tet regulated minimal CMV promoter and a 5' UTR containing a chimeric intron of human β -globin and immunoglobulin heavy chain genes, which was expressed as a bicistronic mRNA via an internal ribosome entry site (IRES2) with eGFP targeted to the nucleus by a N terminal in frame fusion of 3 tandem repeats of the SV40 nuclear localization sequence (nlS). The fragment containing the expression cassette from Tet regulated promoter to SV40 polyadenylation signal (SV40pA) was agarose gel purified from XhoI–EagI digested donor plasmid and was used to generate TetO-mLox-eGFP transgenic mice by pronuclear injection into FVB/n oocyte (Mouse Biology Program at UC Davis; project number MBP-834; colony number PN663).

Generation of MMTV-PyMT/Col1a1(2.3)-tTA/TetO-mLox-eGFP mice

The MMTV-PyMT/Col1a1(2.3)-tTA/TetO-Rs1 triple transgenic mice were generated by heterozygote or homozygote crosses of mice carrying the TetO-mLox-eGFP transgene with mice carrying heterozygote of the Col1a1(2.3)-tTA transgene (line 139)¹⁶² or MMTV-rtTA and MMTV-PyMT transgene¹⁶³ to generate the experimental triple-transgenic genotype. In all breeding thereafter, MMTV-PyMT/Col11a1-tTA or MMTV-rtTA/TetO-mLox-eGFP male mice were crossed with TetO-mLox-eGFP female mice. Two mg/mL doxycycline hyclate (Alfa Aesar; Cat# J60579) was added to 5% sucrose water to modulate TetO-mLox-eGFP transgene expression.

Preparation of human breast specimens for hydrolysis

OCT was removed from tissue blocks by first transferring biospecimens to a conical tube and then performing 5X washes with 70% ethanol followed by 5X washes with 18 MΩ H₂O. Each wash consisted of vortexing the sample for 15 minutes at 4°C and then centrifuging at 18,000 x g for 15 minutes at 4°C. Between 1 and 3 milligrams of tissue was washed with 1X PBS buffer by vortexing for 15 minutes at 4°C and then sonicated on ice for 20 seconds using a Sonic Dismembrator M100 (ThermoFisher, San Jose, CA, USA). The homogenate was then centrifuged at 18,000 x g for 20 minutes at 4°C. The supernatant was removed and the pellet was re-suspended in 1mg/mL NaBH₄ (prepared in 0.1N NaOH) in 1X PBS for 1 hour at 4°C with vortexing. The reaction was neutralized by adding glacial acetic acid to a final concentration of 0.1% (pH ~ 3 -4)¹⁶⁴. The sample was then centrifuged at 18,000 x g for 20 minutes at 4°C. The supernatant was removed, and the pellet was washed three times with 18 MΩ H₂O to remove residual salt that could interfere with downstream LC-MS/MS analysis. The remaining pellet was dried under vacuum for further analysis.

Protein hydrolysis

The dried sample was placed in a glass hydrolysis vessel and hydrolyzed in 6N HCl, 0.1% phenol. The hydrolysis vessel is flushed with N₂ gas, sealed and placed in a 110°C oven for 24 hours. After hydrolysis, the sample was cooled to room temperature and then placed at -80°C for

30 minutes prior to lyophilization. The dried sample was re-hydrated in 100 μ L of 18 M Ω H₂O for 5 minutes, then 100 μ L of glacial acetic acid for 5 minutes and finally 400 μ L of butan-1-ol for 5 minutes. Importantly, 10 μ L of sample is removed after re-hydration in water and saved for determination of hydroxyproline content.

Preparation of crosslink enrichment column

CF-11 cellulose powder is loaded in a slurry of butan-1-ol: glacial acetic acid, water (4:1:1) solution onto a Nanosep MF GHP 0.45 μ m spin columns until a settled resin bed volume of approximately 5mm is achieved. The resin is washed with 1.5 mL 4:1:1 organic mixture using an in-house vacuum manifold set up. Re-hydrated samples are then loaded onto individual columns, the vacuum is turned on and the sample is pulled through the resin into glass collection vials. The flow through is again passed over the resin to ensure maximal binding of crosslinked amino acids and set aside. The column is then washed with 1.5 mL of fresh 4:1:1 organic mixture. A fresh collection vessel is placed under the column and 750 μ L of 18 M Ω H₂O is used to elute crosslinked amino acids off of the CF-11 resin. The eluent is then placed in a speed vac and run until complete dryness. Dried eluent is then reconstituted in a buffer appropriate for downstream MS analysis on amide HILIC UHPLC columns.

UHPLC analysis

Up to 20 μ L of tissue hydrolysates were analyzed on a Vanquish UPHLC system (ThermoFisher, San Jose, CA, USA) using an Acquity UHPLC BEH Amide column (2.1 x 100mm, 1.7 μ m particle size – Waters, Milford, MA, USA). Samples were separated using a 5 minute gradient elution (55% - 40% Mobile phase B) at 250 μ L/min (mobile phase: (A) 10 mM ammonium acetate adjusted to pH 10.2 with NH₄OH (B) 95% acetonitrile, 5% Mobile Phase A, pH 10.2, column temperature: 35°C.

MS data acquisition

The Vanquish UPHLC system (ThermoFisher, San Jose, CA, USA) was coupled online with a QExactive mass spectrometer (Thermo, San Jose, CA, USA), and operated in two different

modes – 1. Full MS mode (2 μ scans) at 70,000 resolution from 75 to 600 m/z operated in positive ion mode and 2. PRM mode at 17,500 resolution with an inclusion list of in-tact crosslinked amino acid masses (Supplementary Table 2), and an isolation window of 4 m/z. Both modes were operated with 4 kV spray voltage, 15 sheath gas and 5 auxiliary gas. Calibration was performed before each analysis using a positive calibration mix (Piercenet – Thermo Fisher, Rockford, IL, USA). Limits of detection (LOD) were characterized by determining the smallest injected crosslinked amino acids (LNL, DHLNL, d-Pyr,) amount required to provide a signal to noise (S/N) ratio greater than three using < 5 ppm error on the accurate intact mass. Based on a conservative definition for Limit of Quantification (LOQ), these values were calculated to be threefold higher than determined LODs.

MS data analysis

MS Data acquired from the QExactive were converted from a raw file format to .mzXML format using MassMatrix (Cleveland, OH, USA). Assignment of crosslinked amino acids was performed using MAVEN (Princeton, NJ, USA)¹⁶⁵. The MAVEN software platform provides the means to evaluate data acquired in Full MS and PRM modes and the import of in-house curated peak lists for rapid validation of features. Normalization of crosslinked amino acid peak areas was performed using two parameters, 1. Hydroxy proline content and 2. Tissue dry weight pre-hydrolysis (in milligrams)¹⁶⁴. Hydroxy proline content is determined by running a 1:10 dilution of the pre-enrichment sample through the Full MS mode (only) described above and exporting peak areas for each run.

Quantification of crosslinked amino acids

Relative quantification of crosslinked amino acids was performed by exporting peak areas from MAVEN into GraphPad (La Jolla, CA, USA) and normalizing based on the two parameters described above. Statistical analysis, including T test and ANOVA (significance threshold for P values <0.05) were performed on normalized peak areas. Total crosslink plots were generated by

summing normalized peak areas for all crosslinks in a given sample. Total HLCC plots were generated by summing normalized peak areas for all HLCC (DHLNL, Pyr, dPyr) for each sample.

Picrosirius red staining and quantification

FFPE tissue sections were stained using 0.1% Picrosirius red (Direct Red 80, Sigma-Aldrich, Cat# 365548 and picric acid solution, Sigma-Aldrich, Cat# P6744) and counterstained with Weigert's hematoxylin (Cancer Diagnostics, Cat# CM3951), as previously described²⁶. Polarized light images were acquired using an Olympus IX81 microscope fitted with an analyzer (U-ANT) and a polarizer (U-POT, Olympus) oriented parallel and orthogonal to each other. Images were quantified using an ImageJ macro to determine percentage area coverage per field of view. The ImageJ macro is available at <https://github.com/northcottj/picrosirius-red>.

Second harmonic generation image acquisition

Second harmonic generation (SHG) imaging was performed using a custom-built two-photon microscope setup equipped resonant-scanning instruments based on published designs containing a five-PMT array (Hamamatsu, C7950), as previously published²⁶. The setup was used with two channel simultaneous video rate acquisition via two PMT detectors and an excitation laser (2W MaiTai Ti-Sapphire laser, 710–920 nm excitation range). SHG imaging was performed on a Prairie Technology Ultima System attached to an Olympus BX-51 fixed stage microscope equipped with a 25X (NA 1.05) water immersion objective. Paraformaldehyde-fixed or FFPE tissue sections were exposed to polarized laser light at a wavelength of 830 nm and emitted light was separated using a filter set (short pass filter, 720 nm; dichroic mirror, 495 nm; band pass filter, 475/40 nm). Images of x–y planes at a resolution of 0.656 μm per pixel were captured using at open-source Micro-Magellan software suite.

Immunofluorescence/Immunohistochemistry

Immunofluorescence staining was performed as previously described²⁶. Briefly, mouse tissues were harvested and fixed with 10% buffered formalin phosphate (Fisher, Cat# 100-20) for 16-24 hours at room temperature and then further processed and paraffin-embedded. Five- μm

sections dried for 30 minutes in 60°C, follow by deparaffinization and rehydration. Antigen retrieval was perform using DAKO Target Retrieval Solution (DAKO, Cat# S1699) for five minutes in a pressure cooker set to high pressure. Tissue sections were incubated with anti-FAK pY397 antibody (Abcam, Cat# Ab39967, dilution 1:25) overnight at 4°C and with anti-rabbit IgG Alex Fluor 633 (ThermoFisher, Cat# A-21070, dilution 1:2000) for one hour at room temperature. Antigen retrieval for immunofluorescent staining of SMAD2 pS465/467, cytokeratin 8+18, cytokeratin 5, F4/80, vimentin, and PDGFR α was performed using Diva Decloaker (BioCare, Cat# DV2004MX) for five minutes in a pressure cooker set to high pressure. Tissue sections were incubated with anti-SMAD2 pS465/467 antibody (Millipore, Cat# AB3849-I, dilution 1:100), anti-F4/80 antibody (AbD Serotec, clone Cl:A3-1, Cat# MCA497GA, dilution 1:400), anti-cytokeratin 8+18 antibody (Fitzgerald, Cat# 20R-CP004, dilution 1:400), anti-cytokeratin 5 antibody (Fitzgerald, Cat# 20R-CP003, dilution 1:400), anti-vimentin antibody (Cell Signaling, Cat# 5741, dilution 1:100), and anti-PDGFR α (CD140a) antibody (Biolegend, Cat# 135901, dilution 1:100) overnight at 4°C and with anti-rat IgG Alex Fluor 488 (ThermoFisher, Cat# A-11006, dilution 1:1000), anti-guinea pig IgG Alex Fluor 568 (ThermoFisher, Cat# A-11075, dilution 1:1000), anti-rabbit IgG Alex Fluor 633 (ThermoFisher, Cat# A-21070, dilution 1:2000), anti-rabbit IgG Alex Fluor 633 (ThermoFisher, Cat# A-21070, dilution 1:1000) for one hour at room temperature.

Quantification of stromal nuclear SMAD2 pS465/467 was performed using Imaris 9. Surfaces were created around each nucleus and epithelial nuclei were manually excluded based on cytokeratin signal and cell morphology. The means of the mean nuclear signal intensity for all stromal nuclei were calculated for each field of view and averaged for every animal.

Lungs from 11-week-old IgG1 control and anti-CSF1 treated PyMT mice were cut into 5 micron sections from 5 layers with 100 microns between the first three layers and 50 microns between the last two layers. Sections were analyzed for metastases by PyMT staining. Antigen retrieval was performed in Tris-EDTA buffer at pH 9 for four minutes in a pressure cooker set to low pressure. Tissue sections were incubated with anti-PyMT antibody (Novus Biologicals, Cat#

NB-100-2749, dilution 1:250) overnight at 4°C and with a biotinylated anti-rat antibody for 1 hour at room temperature. Vectastain Elite ABC (Vector, Cat# PK6100) and ImmPACT DAB Peroxidase (Vector, Cat# SK-4105) were used for signal detection and nuclei were counterstained with methyl green.

mRNA In Situ Hybridization

Fresh, RNase-free FFPE sections were stained with RNAscope multiplex fluorescent reagent kit V2 according to standard manufacturer protocol. Target retrieval was performed using 8 minute incubation in a pressure cooker set to low pressure. Opal 520 and Opal 570 (PerkinElmer) were used at 1:1500 for target visualization.

Gene expression by RT-qPCR

Total RNA was reverse-transcribed using random primers (Amersham Biosciences) and results were normalized to 18S RNA to control for varying cDNA concentration between samples. The primer sequences used are 18s forward 5'-GGATGCGTGCATTTATCAGA-3' and reverse 5'-GGCGACTACCATCGAAAGTT-3', Lox forward 5'-CGGGAGACCGTACTGGAAGT-3' and reverse 5'-CCCAGCCACATAGATCGCAT-3', Loxl2 forward 5'-CACAGGCACTACCACAGCAT-3' and reverse 5'-CCAAAGTTGGCACACTCGTA-3', and Tgfb1 forward 5'-TCATGTCATGGATGGTGCCC-3' and reverse 5'-GTCACTGGAGTTGTACGGCA-3'.

Atomic force microscopy data acquisition

Atomic force microscopy (AFM) measurements were performed as previously described (2). Briefly, 20µm OCT-embedded frozen human breast tissue or 30µm mouse mammary gland sections were fast thawed by immersion in PBS at room temperature. Next, these sections were immersed in PBS containing phosphatase inhibitors (Roche, Cat# 04906845001), protease inhibitor (Roche, Cat# 04693124001), and propidium iodide (ACROS, Cat# 440300250) and placed on the stage for AFM measurements. AFM indentations were performed using an MFP3D-BIO inverted optical AFM (Asylum Research) mounted on a Nikon TE2000-U inverted fluorescent microscope. Silicon nitride cantilevers were used with a spring constant of 0.06 N m⁻¹ and a

borosilicate glass spherical tip with 5 μm diameter (Novascan Tech). The cantilever was calibrated using the thermal oscillation method prior to each experiment. The indentation rate was held constant within each study but varied between 2-20 μms^{-1} with a maximum force of 2 nN between studies. Force maps were obtained as a raster series of indentations utilizing the FMAP function of the IGOR PRO build supplied by Asylum Research. Elastic properties of ECM were reckoned using the Hertz model. A Poisson's ratio of 0.5 was used in the calculation of the Young's elastic modulus.

Western blotting

Snap frozen tissues were ground while frozen and lysed in 2% SDS containing protease and phosphatase inhibitor. Samples were boiled for 5 minutes (95°C) and loaded onto the SDS-polyacrylamide gel, and protein was separated at 110 constant volts.

The protein was transferred onto a pre-wet polyvinylidene difluoride (PVDF) membrane (100% methanol, 1 minute) at 250 mA for 2 hours. The PVDF membrane was rinsed with TBST and non-specific binding was blocked with 5% nonfat dry milk dissolved in TBST. The membrane was then incubated with the primary antibody overnight at 4°C, washed with TBST, incubated with horseradish-peroxidase conjugated secondary antibody (1 hour, room temperature; dilution 1:5000), washed with TBST, and detected with the chemiluminescence system Quantum HRP substrate (Advansta #K-12042). Quantification was performed using gel densitometry in ImageJ. Primary antibodies used are anti-LOX (1:1000, Abcam Cat# ab174316) and anti-E-cadherin (1:1000, Cell Signlaing Cat#3195).

Flow cytometry

Mouse tissue was harvested and chopped with a razor blade. Chopped tissue was digested in 100 U/mL Collagenase Type 1 (Worthington Biochemical Corporation, Cat# LS004196), 500 U/mL Collagenase Type 4 (Worthington Biochemical Corporation, Cat# LS004188), and 200 $\mu\text{g}/\text{mL}$ DNase I (Roche, Cat# 10104159001) while shaking at 37°C. Digested

tissue was filtered using a 100 µm filter to remove remaining pieces. Red blood cells were lysed in ammonium-chloride-potassium buffer and remaining cells were counted. Cells were stained with fluorophore-conjugated primary antibodies for 30 minutes on ice and subsequently stained with a viability marker. Antibodies used for staining were anti-mouse CD24-PE (BD Pharmingen, Cat# 553262), anti-mouse TER-119-APC (BioLegend, Cat# 116212), anti-mouse CD45-APC (BioLegend, Cat# 103112), anti-mouse CD29-AF700 (BioLegend, Cat# 102218), anti-mouse Ly6G-BV421 (BioLegend, Cat# 127628), anti-mouse F4/80-BV510 (BioLegend, Cat# 123135), anti-mouse CD29-AF488 (BioLegend, Cat# 102212), anti-mouse CD140a-PE (BioLegend, Cat# 135906), anti-mouse CD31-APC (BioLegend, Cat# 102410), anti-mouse CD11c-BV605 (BD Pharmingen, Cat# 563057), anti-mouse CD24-BV650 (BD Pharmingen, Cat# 563545), anti-mouse CD11b-PerCP-Cy5.5 (eBiosciences, Cat# 45-0112-82), anti-mouse CD45-AF700 (BioLegend, Cat# 103128), anti-mouse Ly6C-BV711 (BioLegend, Cat# 128037), anti-mouse MHCII-PE-Cy7 (BioLegend, Cat# 107630), and Zombie NIR Fixable Viability Dye (BioLegend, Cat# 423105). Cells were then analyzed on a flow cytometer.

Patient gene expression analysis

For the stroma and epithelium specific gene expression analysis, the breast cancer datasets from Finak *et al.* 2008 and Gruosso *et al.* 2019 have been used. Briefly, whole Human Genome 44 K arrays (Agilent Technologies, product G4112A) were used for stroma and epithelial expression profiles. Details of laser capture microdissection, RNA extraction, labeling, hybridization, scanning and quality filters are described in Finak *et al.*, 2006 and 2008. Briefly, the dataset was normalized using loess (within-array) and quantile (between-array) normalization. Probes were ranked by Inter-quartile range (IQR) values, and the most variable probe per gene across expression data were selected for further analysis. Replicate arrays with a concordance above 0.944 were averaged before assessing differential expression.

An association between PLOD2 and distant metastasis-free survival (DMFS) has been determined using an online tool (<http://xena.ucsc.edu>) to download GEO data (GSE2034, GSE5327, and GSE7390) from 683 patients analyzed on Affymetrix U133A platform as described in Yau et al. (46). Patients have been excluded from analyses if their molecular subtyping of ER/HER2 status and PAM50 did not align: ER+/HER2- must always be luminal, ER+ or-/HER2+ must be HER2+, and ER-/HER2- must always be basal-like. PLOD2 expression levels have been divided based on the median for each tumor subtype: ER+/HER2- (low n=157; high=157), ER- or +/HER2+ (low n=36; high=37), and ER-/HER2- (low n=66; high=67). All statistical analyses were done using GraphPad Prism Version 6.01: Kruskal-Wallis one-way ANOVA test was applied to assess the relationship in PLOD2 expression levels among tumor subtypes and log rank P value (Mantel-Cox) tests for DMFS curves.

An association between PLOD2 gene expression and relapse-free survival (RFS) has been determined using an online tool (<http://kmplot.com/analysis/>) from 1,809 patients analyzed on Affymetrix platform (HGU133A and HGU133+2 microarrays)⁸⁴. Affymetrix ID 202619 or 202620 were used for PLOD2 probes (2014 version) in these analyses. All breast cancer patients in this database were included regardless to lymph node status, TP53 status, or grade. No restrictions were placed in term of patient treatment. PLOD2 expression levels have been divided based on the median for each tumor subtype: ER+/PR+/HER2- (low n=170; high=169), ER-/PR-/HER2+ (low n=58; high=57), and ER-/PR-/HER- (low n=128; high=127). Hazard ratio (and 95% confidence intervals) and log rank P values were calculated and displayed once the data were plotted using the online tool.

The cBioPortal for Cancer Genomics was used to determine the levels of LOX, PLOD2, and LOXL2 gene expression in breast cancer patients segregated by ER and HER2 status^{166,167}. ER, PR, and HER2 status were determined by gene expression levels. Samples positive for both ER/PR and HER2 overexpression were excluded from subtype analysis. All data accessed via

cBioPortal are from the 1904 patients in the METABRIC dataset analyzed for gene expression by Illumina human v3 microarray¹⁶⁸. All 1904 samples were included in correlation analyses.

Statistical analysis

GraphPad Prism Version 6.01 was used to perform all statistical analyses with the exception of LH2 IHC and RFS correlations with PLOD2. Statistical significance was determined using the appropriate tests as noted in the figure legends or method section.

LH2 IHC and prognostic analyses:

Study population

The female Malmö Diet and Cancer Study (MDCS) cohort consists of women born 1923–1950)¹⁶⁹. Information on incident breast cancer is annually retrieved from the Swedish Cancer Registry and the South Swedish Regional Tumor Registry. Follow-up until December 31, 2010, identified a total of 910 women with incident breast cancer, the following conditions excluded patients: 1) with in situ only cancers (n=68), 2) who received neo-adjuvant treatments (n=4), 3) with distant metastasis at diagnosis (n=14), 4) those who died from breast cancer-related causes ≤ 0.3 years from diagnosis (n=2), and finally 5) patients with bilateral cancers (n=17). In addition, one patient who declined treatment for four years before accepting surgery was excluded. Patient characteristics at diagnosis and pathological tumor data were obtained from medical records. Information on cause of death and vital status was retrieved from the Swedish Causes of Death Registry, with last follow-up December 31st, 2014. Ethical permission was obtained from the Ethical Committee at Lund University (Dnr 472/2007). All participants originally signed a written informed consent form.

Tumor evaluation

Tumor samples from incident breast cancer cases in MDCS were collected, and a tissue microarray (TMA) including two 1-mm cores from each tumor was constructed (Beecher, WI, USA). Within the study population (N=910), tumor tissue cores were accessible from 718 patients. Four- μ m sections dried for one hour in 60°C were automatically pretreated using the Autostainer

plus, DAKO staining equipment with Dako kit K8010 (Dako, DK). A primary mouse monoclonal Lysyl Hydroxylase 2 (LH2) antibody (Origene; Cat# TA803224, dilution 1:150) was used for the immunohistochemical staining.

TMA cores were analyzed by a cohort of 4 anatomic pathologists (ACN, AC, JG, AN) using the PathXL digital pathology system (<http://www.pathxl.com>, PathXL Ltd., UK) blinded to all other clinical and pathologic variables. Immunohistochemistry for LH2 was assessed separately for stromal and neoplastic epithelial components of the tumors. Stromal LH2 staining was assessed with the semi-quantitative H-score which combines intensity and proportion positive assessments into a continuous variable from 0-300¹⁷⁰. Cellular stromal components were assessed (including fibroblasts, macrophages, endothelial cells, adipocytes, and other stromal cell types) while areas of significant lymphocytic infiltrate were specifically excluded from the percent positive estimation. Neoplastic epithelial LH2 staining intensity was scored 0-3+ based on the predominant intensity pattern in the tumor — invasive tumor cells did not display significant intra-tumoral heterogeneity of LH2 staining within each core. Verification of inter-observer reproducibility for the H-score was established in a training series of 16 cases evaluated by all study pathologists to harmonize scoring. Inter-observer agreement in the training set was very high, evaluating the IHC scores both as continuous variables (Pearson correlation coefficients ranging from 0.912-0.9566, all p values < 0.0001), and after transformation into categorical data (negative, low, and moderate/high; weighted kappa coefficients ranging from 0.673-0.786). In addition, 50 cases of the study cohort were evaluated blindly by two pathologists to confirm data fidelity; the Pearson correlation coefficient = 0.7507 (p = 5.7 E-05), considered a strong level of agreement.

After exclusion of cases for which LH2 was not evaluable on the TMA, H-scores for 505 patients were included for statistical associations with clinicopathologic features and patient outcome. Each patient was represented by two cores, and TMA core 1 and core 2 were merged into a joint variable favoring the highest stromal LH2 H-score or epithelial LH2 intensity because we predict that higher H-score would drive patient outcome in accordance with our gene

expression data demonstrating high LH2 expression correlated with poor outcome. The Pearson correlation coefficient between cores = 0.647, demonstrating moderate agreement among the stromal LH2 H-scores for the two cores. In cases with only one TMA core providing a LH2 score, the expression of this core was used. Further, the joint stromal LH2 variable was categorized into tertiles based on the study population with valid LH2 annotation (N=505). The lowest tertile of LH2 H-scores were defined as scores between 0 and less or equal to 120 (N=171), the intermediate H-score as above 120 and equal or less than 230 (N=188), and the highest stromal LH2 score as above 230 (N=146).

Statistical analyses for LH2 IHC analyses

Patient and tumor characteristics at diagnosis in relation to stromal LH2 expression were categorized and presented as percentages. Continuous variables are presented as the mean and min/max. The associations between LH2 expression and grade or tumor size, respectively, were analyzed through linear-by-linear association. The association between LH2 expression and prognosis was examined using breast cancer-specific mortality as endpoint, which was defined as the incidence of breast cancer-related death. Follow-up was calculated from the date of breast cancer diagnosis to the date of breast cancer-related death, date of death from another cause, date of emigration or the end of follow-up as of December 31st, 2014. Main analyses included the overall population; additional analyses were performed in subgroup analyses stratified by estrogen receptor (ER) or axillary lymph node involvement (ALNI) status. The prognostic impact of stromal LH2 expression was analyzed through Cox proportional hazards analyses, which yielded hazard ratios (HR) and 95% confidence intervals (CI) for crude models, and multivariate models adjusted for age at diagnosis (model 1) and tumor characteristics ER (dichotomized, cut-off 10% stained nuclei), ALNI (none or any positive lymph node involvement), histological grade (Nottingham grade I-III), and tumor size (dichotomized using cut-off 20 mm). Kaplan-Meier curves including the LogRank test indicated LH2 status to particularly impact the first 10 years after diagnosis and survival variables constructed to capture these effects were used in Cox regression

models investigating the effects during the first post-diagnostic decade. All statistical analyses were performed in SPSS version 22.0 (IBM).

Chapter 4: Extracellular matrix compliance drives treatment resistance in triple negative breast cancer through elevated NF- κ B signaling

In collaboration with: Nastaran Zahir³, Hui Zhang⁴, Po-Jui Huang¹, Ori Maller¹, Jason J. Northey¹, Johnathon N. Lakins¹, Jennifer L. Leight⁵, Brenda Alston-Mills⁶, E. Shelley Hwang⁷, Yunn-Yi Chen⁸, Catherine C. Park^{4,9}, and Valerie M. Weaver^{1,9,10}

¹Department of Surgery, Center for Bioengineering and Tissue Regeneration, University of California, San Francisco, San Francisco, CA, USA

²UC Berkeley – UCSF Graduate Program in Bioengineering, University of California, San Francisco, CA, USA

³Department of Bioengineering and Institute for Medicine and Engineering, University of Pennsylvania, Philadelphia, PA, USA. *Current address: Division of Cancer Biology, National Cancer Institute, Rockville, MD, USA

⁴Department of Radiation Oncology, Eli and Edythe Broad Center of Regeneration Medicine and Stem Cell Research, University of California, San Francisco, San Francisco, CA, USA

⁵Department of Bioengineering and Institute for Medicine and Engineering, University of Pennsylvania, Philadelphia, PA, USA. *Current address: Department of Biomedical Engineering, The Ohio State University, Columbus, OH, USA

⁶Department of Bioengineering and Institute for Medicine and Engineering, University of Pennsylvania, Philadelphia, PA, USA

⁷Department of Surgery, Duke University Medical Center, Durham, NC, USA

⁸Department of Pathology, University of California, San Francisco, San Francisco, CA, USA

⁹UCSF Helen Diller Comprehensive Cancer Center, University of California, San Francisco, San Francisco, CA, USA

¹⁰Department of Bioengineering and Therapeutic Sciences, University of California, San Francisco, San Francisco, CA, USA

Introduction

Neoadjuvant chemotherapy (NAC) is increasingly used in the treatment of invasive breast cancer providing the opportunity to understand the relative sensitivity or resistance of tumors while still in situ ¹⁷¹. Many studies have demonstrated the more aggressive nature of hormone receptor negative, HER-2 negative breast cancer (TNBC) compared to other phenotypes, and TNBCs have been repeatedly correlated with increased local recurrence, distant recurrence and worse overall survival ¹⁷². Despite significant advances in targeted therapies for hormone receptor positive and HER2 positive disease, cytotoxic chemotherapy remains the standard of care for most TNBC, followed by radiation in selected cases.

TNBC tumors that are completely eradicated in the breast with NAC, known as a pathologic complete response (pCR), are associated with an excellent patient prognosis, significantly better than for patients whose tumors lack such a response ¹⁷². However, this response is heterogeneous, and TNBC patients continue to have worse overall outcomes compared to breast tumors of other subtypes. Currently, there are no reliable methods to identify patients that are likely to respond well and those that are likely to be chemotherapy resistant. The ability to improve predicted response would improve personalization of treatment and patient outcomes. There is also an urgent need for a deeper understanding of the biological basis for chemotherapy response in TNBC that will inform treatment decisions and the development of effective strategies to overcome therapy resistance.

In addition to their highly aggressive phenotype, TNBC have a characteristically high degree of extracellular matrix (ECM) remodeling and stiffening. ECM stiffness is well known to heavily influence cell behavior and has been shown to extrinsically modulate drug responses via blood vessel occlusion that limits transport. ECM stiffness can also regulate cell intrinsic behaviors that affect therapy response including proliferation, survival, and growth factor signaling²³. Despite the important role the ECM plays in regulating cell behavior, it is unclear whether the stiffer ECM

measured in TNBC contributes to the underlying mechanisms whereby the evolving ECM may impact the development of therapy resistance.

NF- κ B signaling is critically important to ECM-mediated cell survival. The apoptosis resistance phenotype of 3D mammary epithelial tissue-like structures in a reconstituted basement membrane depended upon the activation of NF- κ B, but NF- κ B activity per se failed to protect mammary epithelial cells from apoptosis when cells were plated as 2D monolayers^{173,174}. Importantly, NF- κ B activity can drive resistance to chemo- and radiation therapy in many tumor types by modifying the expression and stability of apoptosis regulators including the stress-activated protein kinase, JNK¹⁷⁵⁻¹⁷⁹. JNK permits apoptosis induction in a variety of cell types in response to assorted cell stress stimuli, including paclitaxel, TRAIL, UV and ionizing radiation exposure¹⁸⁰⁻¹⁸². Recently, an *in vivo* screen also implicated JNK as a key mediator of chemotherapeutic efficacy¹⁸³. Importantly, JNK signaling is responsive to mechanical stimuli such as substrate strain and mediates mechanical stretch-induced apoptosis of renal epithelial cells^{17,184}. Moreover, Rho GTPases that are elevated in mammary epithelial cells cultured on stiff matrices also activate JNK^{27,185}. Thus, substrate stiffness could enhance JNK activation to sensitize mammary epithelial cells to anti-tumor treatment.

Here we show that residual disease from NAC treated tumors localizes within a soft, remodeled ECM niche. We then demonstrate that mammary epithelial cells and tumor cells assembled into organoid-like structures in soft ECMs can efficiently engage NF- κ B signaling to resist apoptosis induction. Conversely, cells interacting with a stiff substrate show reduced NF- κ B signaling and increased JNK activity that sensitize them to several apoptosis inducing agents. Consistent with this mechanism, we show human breast tumors that failed to achieve pCR in response to NAC were enriched for an NF- κ B gene expression signature, and NF- κ B levels were highly elevated in residual disease of NAC treated TNBC tumors. This study implicates ECM stiffness as an important mediator of response to chemotherapy and radiation in TNBC. It has

important clinical implications for understanding the heterogenous response to therapy in TNBC and for making rational, informed decisions in selecting effective therapies.

Results

Residual triple negative breast tumors are surrounded by a soft interstitial stroma

We first assessed the organization and biophysical properties of the ECM associated with primary human TNBCs and compared these stromal features with the ECM of residual tumor tissue of neoadjuvant chemotherapy-treated tumors. Histological analysis of a cohort of primary untreated TNBC biopsies demonstrated the presence of an interstitial stroma comprised of abundant ECM proteins that was infiltrated by numerous tumor epithelial cells (**Figure 4.1 A**). Picrosirius red staining (PS) and polarized light imaging revealed that the ECM in the primary, stage-matched, human TNBCs (N=9) contained abundant quantities of fibrillar type collagens (**Figure 4.1 B-C**), that atomic force microscopy (AFM) indentation showed was significantly stiffer than that measured previously in the normal human breast (**Figure 4.1 D-E**)²⁶. By contrast, hematoxylin and eosin staining indicated that the residual tumor epithelium in the neoadjuvant chemotherapy treated TNBCs (N=7) was dramatically reorganized into epithelial aggregates, many of which were reminiscent of tubular carcinoma (compare **Figure 4.1 A**). Polarized light imaging of picrosirius red stained tissue further revealed that the residual TNBC tumors were surrounded by large quantities of a remodeled collagenous-rich stroma (compare **Figure 4.1 B-C**). Nevertheless, AFM analysis revealed that the collagen-rich fibrillar stroma surrounding the residual tumor was significantly softer than that measured in the primary TNBCs (**Figure 4.1 D-E**). The findings indicate that chemotherapy treatment not only significantly reduces the density of the tumor epithelium but also induces substantial remodeling and reorganization of the ECM stroma that substantially decreases its stiffness. The data raise also the intriguing possibility that the softened, remodeled ECM might be causally linked to the pathogenesis of the treatment resistant residual tumor tissue.

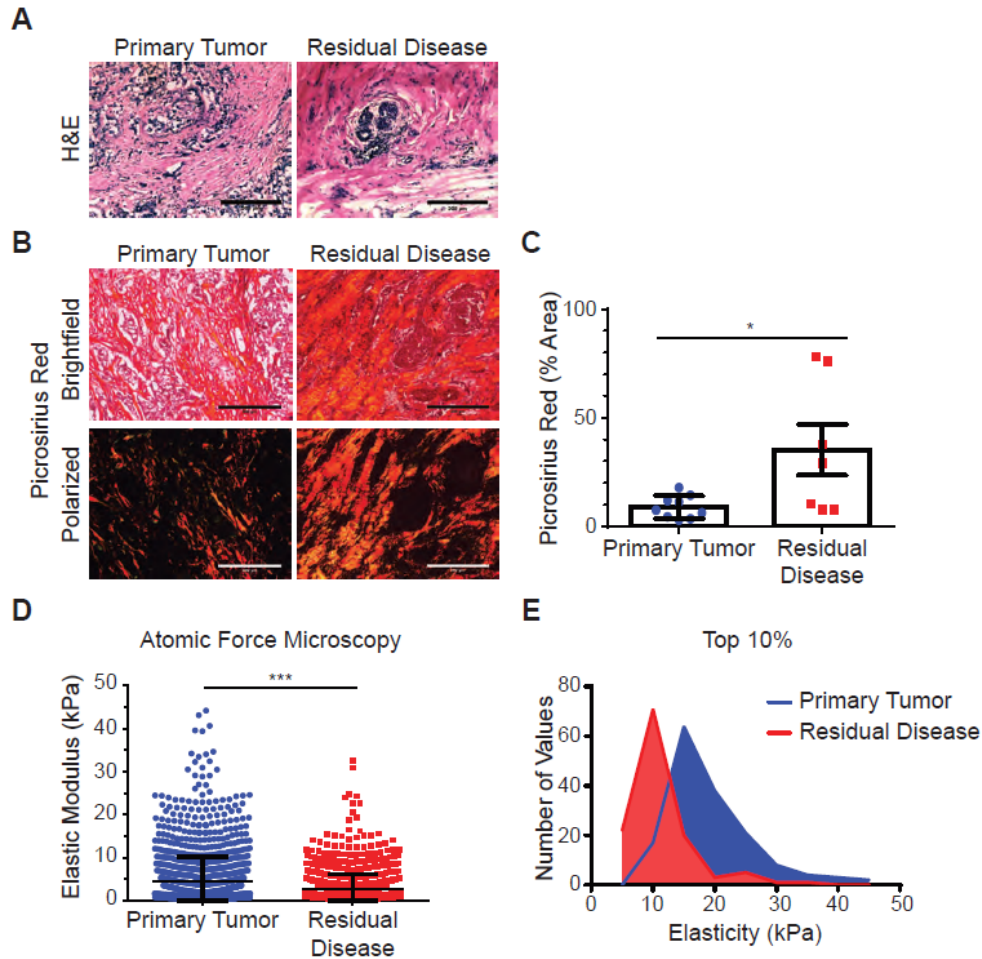


Figure 4.1: Treatment resistant residual disease localizes within a soft ECM niche. (A) Representative hematoxylin and eosin stained tissue sections of untreated human primary tumor or residual disease from neoadjuvant chemotherapy treated tumors. (B) Representative images of brightfield and polarized light picrosirius red stained primary tumor or residual disease tissue sections. (C) Bar graph showing mean and SEM of polarized light picrosirius red signal for primary tumor (n = 9) and residual disease (n = 7) from 3-5 fields of view per sample. (D) Scatter plot showing mean and SD of atomic force microscopy elasticity measurements of tumor cell adjacent extracellular matrix from primary tumor (n = 9) and residual disease (n = 7). Values reflect measurements from 3-5 elasticity maps per sample. (E) Histogram showing distribution of the top 10% of AFM elasticity measurements in each group. Statistical analyses were performed using two-tailed Mann-Whitney U test (*p < 0.05, **p < 0.01, ***p < 0.001). All scale bars are 200 μ m.

ECM stiffness regulates chemotherapy responsiveness of human mammary tumors

To determine if a remodeled, compliant ECM could compromise chemotherapy responsiveness of mammary tumors and whether any changes in response vary with tumor stage, we tested the impact of ECM stiffness on the apoptosis response of premalignant and malignant mammary epithelial organoids to a standard chemotherapy agent. We generated proliferating organoid structures of estrogen receptor (ER) and human epidermal growth factor receptor 2 (HER2) negative, premalignant human mammary epithelial (MEC) MCF10A and malignant HMT-3522 T4-2 cells to model early and late stage TNBCs. MCF10A and T4-2 mammary cells were plated on basement membrane (BM)-conjugated polyacrylamide (PA) substrates calibrated to recapitulate the low and high end of the elasticity we measured in the normal ($E = 150$ Pascals; Pa) and tumor stroma ($E = 5,000$ Pa)^{27,186}. The mammary tumor cells were overlaid with growth media containing two percent reconstituted basement membrane (rBM; Matrigel) to create a three-dimensional (3D) ECM microenvironment. The tumor cells were then grown for 5 days until they formed small uniformly proliferating tissue-like colonies (16-24 cells/colony)^{27,186}. The organoids were then treated with increasing dose of the chemotherapeutic drug paclitaxel. Intriguingly, the treated premalignant colonies cultured on the stiff PA substrate displayed a significant, dose-dependent loss of metabolic activity, as measured by the MTT assay, and a concomitant increase in apoptosis, as measured by positive staining for cleaved caspase 3 (Figure 2 A-C). By contrast, the premalignant structures cultured on the soft substrate showed only a modest reduction in metabolic activity and apoptosis levels were significantly lower than that quantified in the same proliferating structures plated on a stiff ECM substrate, despite exposure to the same dosages of paclitaxel (**Figure 4.2 A-C**). The malignant colonies plated on the compliant ECM substrates similarly displayed a striking apoptosis resistance in response to the paclitaxel chemotherapy, as indicated by significantly lower levels of cleaved caspase 3 following paclitaxel treatment, than those malignant colonies grown on the stiffer ECM substrate

(**Figure 4.2 D-E**). Importantly, malignant tumor colonies of T4-2 embedded within stiff ribose cross-linked collagen gels and injected into the fat pads of immunocompromised mice were also significantly more sensitive to chemotherapy treatment. Indeed, the xenografted tumor colonies shrunk significantly more (**Figure 4.3 A**) and displayed higher levels of apoptosis in response to paclitaxel treatment as compared to the orthotopically implanted tumors injected within the soft collagen ECM gels (**Figure 4.3 B**). The findings argue that a stiff ECM sensitizes breast tumors to chemotherapy both in culture and *in vivo*.

ECM stiffness modulates the radiation responsiveness of mammary tumors

To investigate whether ECM stiffness influences tumor treatment efficacy by modifying drug uptake or tumor cell accessibility we next examined the impact of ECM stiffness on ionizing radiation (IR) responsiveness, a standard therapeutic modality used to treat TNBCs that is not influenced by multidrug resistance pumps or drug diffusion through ECM. Interestingly, once again experiments showed that premalignant mammary organoids cultured on a stiff substrate exhibited a significant reduction in metabolic activity and displayed greater numbers of cells that stained positively for cleaved caspase 3, 48 hours following exposure to increasing dose of IR (**Figure 4.4 A-B, Figure A3.1**). Furthermore, a clonogenic survival assay revealed that a significantly higher proportion of the three-dimensional premalignant mammary cell colonies irradiated on a soft substrate not only survived better but were also able to regrow into viable colonies when plated on a soft ECM, as compared to parallel cultures of premalignant cell colonies irradiated and re-plated on stiff substrates (**Figure 4.4 C**). A stiff ECM similarly sensitized colonies of malignant T4-2 cells to increasing doses of IRs, whereas the same tumor colonies interacting with a soft ECM were protected, even when the malignant colonies were exposed to doses up to 12 Gy of IR (**Figure 4.4 D-E**). Thus, while a soft ECM apparently protects premalignant and malignant mammary tumor tissue from traditional anti-cancer treatments, this effect is not likely mediated through reducing drug accessibility or by elevating the activity of a drug efflux pump.

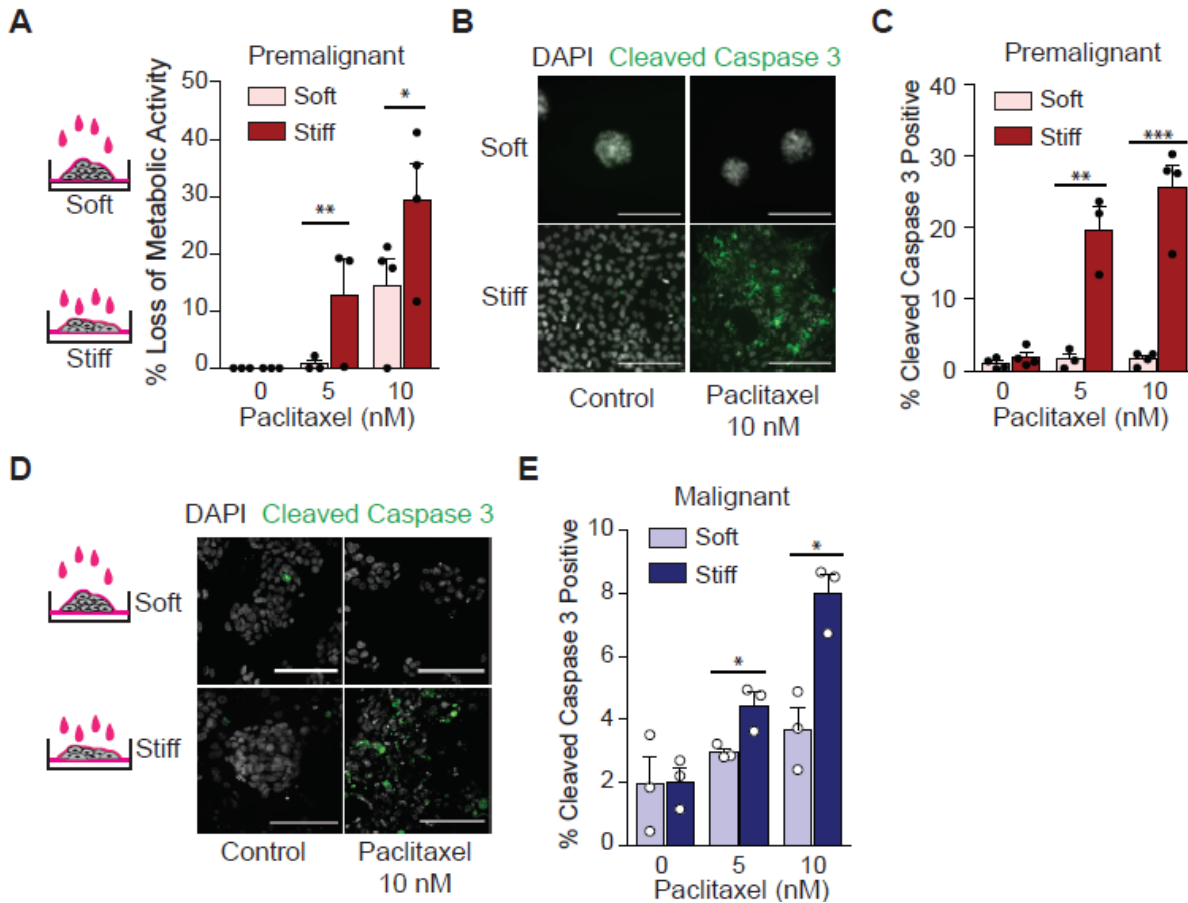


Figure 4.2: Stiff ECM enhances chemotherapeutic efficacy. (A) Bar graph with mean and SEM of loss of metabolic activity by MTT assay after paclitaxel treatment in MCF10A cells cultured on soft or stiff substrates. (B) Representative images of MCF10A cells cultured on soft and stiff substrates treated with 10 nM paclitaxel or DMSO vehicle stained for cleaved caspase 3 (green) and with DAPI (gray). (C) Bar graph with mean and SEM of the percentage of cleaved caspase 3 positive cells from MCF10A cultures on soft and stiff substrates with paclitaxel treatment. At least 300 cells on soft and 900 cells on stiff were counted in each experiment. (D) Representative images of T4-2 cells cultured on soft and stiff substrates and treated with 10 nM paclitaxel or DMSO vehicle stained for cleaved caspase 3 (green) and with DAPI (gray). (E) Bar graph showing mean and SEM of the percentage of cleaved caspase 3 positive cells from T4-2 cultures on soft and stiff substrates with paclitaxel treatment. At least 900 cells on soft and stiff were counted in each experiment. Statistical analyses were performed using two-tailed t test (* $p < 0.05$, ** $p < 0.01$, *** $p < 0.001$). Unless otherwise noted, $n = 3$ for all experiments. All scale bars are 100 μm .

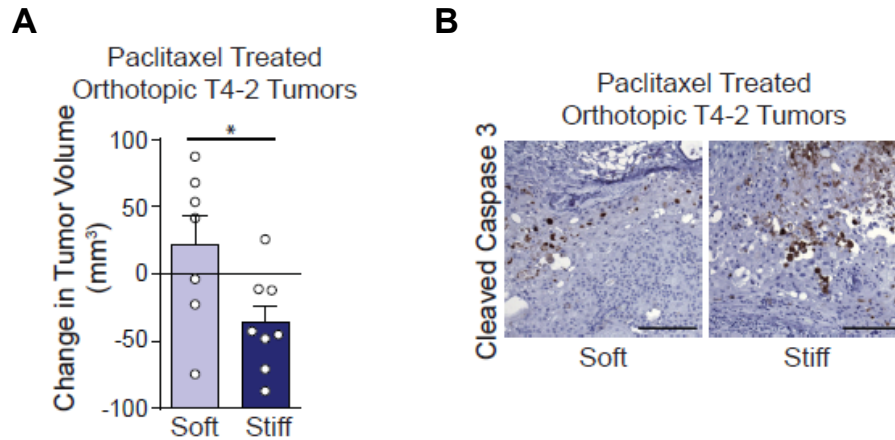


Figure 4.3: ECM stiffness sensitizes tumors to chemotherapy in mice. (A) Bar graph showing mean and SEM of the change in tumor volume after 14 days of paclitaxel treatment of animals with orthotopically injected T4-2 cells in soft ($n = 7$) or stiff ($n = 8$) collagen gels. **(B)** Representative images of FFPE tumor tissue sections stained for cleaved caspase 3 from orthotopically injected T4-2 tumors in soft or stiff collagen after 14 days of paclitaxel treatment. Statistical analyses were performed using two-tailed t test (* $p < 0.05$, ** $p < 0.01$, *** $p < 0.001$). Unless otherwise noted, $n = 3$ for all experiments. All scale bars are $100 \mu\text{m}$.

Apoptosis sensitivity cannot be explained by differences in cell proliferation

Chemotherapy and radiation efficacy are due in part to exploitation of the rapid division of cancer cells to induce apoptosis. A stiff ECM can enhance growth factor-dependent signaling and elevate cell growth^{23,27,187}. This enhanced growth phenotype raises the possibility that the differential tumor sensitivity incurred by interaction with a stiff ECM substrate to both the chemotherapy and the radiation treatment reflected an increased rate of cell proliferation. However, all culture and *in vivo* experiments were initiated when the tumor colonies were actively proliferating. Thus, all treatments were started at days 4-5 of culturing when the premalignant and malignant organoids were proliferating at similar levels on both the soft and stiff ECM substrates. Indeed, quantification of phosphorylated histone H3 (Ser10) staining confirmed that the level of proliferation was equally high in both the premalignant and malignant tumor three dimensional colonies plated on the soft and stiff substrates between days 4 and 5, when the anti-tumor treatments were initiated (**Figure 4.4 A-B**). Flow activated cell sorting (FACs) analysis of propidium iodide (PI) labeled cells further revealed that neither the doubling time nor the proportion of cells in G1, S and G2 of the cell cycle were significantly different on either soft or stiff ECM substrates at the time of treatment (**Figure 4.5 C-D**). Accordingly, the findings rule out the possibility that significant differences in cell proliferation or cell cycle status explain the differential apoptosis sensitivity exhibited by the premalignant and malignant tumor colonies on the soft versus the stiff ECM substrates.

Nonetheless, to provide further evidence to rule out the possibility that the stiffness-mediated sensitization of premalignant and malignant colonies to apoptosis inducing agents could simply be explained by differences in cell proliferation, we treated the two types of tumor colonies with TNF-related apoptosis-inducing ligand (TRAIL), a cytokine that binds to the death receptors DR4 and DR5. Importantly, TRAIL is induced in tumors in response to chemo and radiation

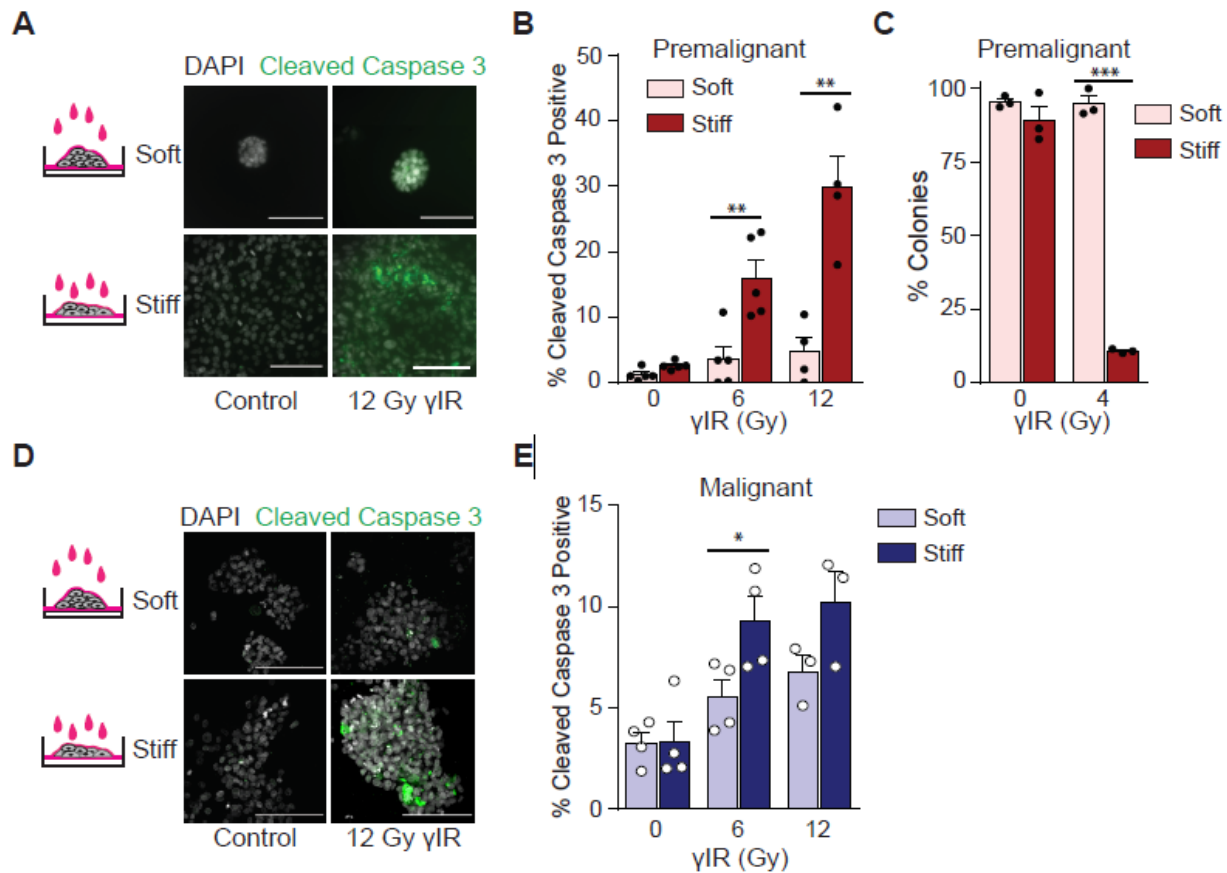


Figure 4.4: Stiff ECM enhances efficacy of radiation therapy. (A) Representative images of irradiated or nonirradiated MCF10A cells cultured on soft and stiff substrates stained for cleaved caspase 3 (green) and with DAPI (gray). (B) Bar graph showing mean and SEM of the percentage of cleaved caspase 3 positive cells from MCF10A cultures on soft and stiff substrates with increasing dose of γ -irradiation. At least 300 cells on soft and 500 cells on stiff were counted in each experiment ($n = 4-5$). (C) Bar graph showing mean and SEM of the percentage of MCF10A cells cultured on a soft or stiff substrate that are capable of reforming colonies after γ -irradiation ($n = 3$). (D) Representative images of irradiated or nonirradiated T4-2 cells cultured on soft and stiff substrates stained for cleaved caspase 3 (green) and with DAPI (gray). (E) Bar graph showing mean and SEM of the percentage of cleaved caspase 3 positive cells from T4-2 cultures on soft and stiff substrates with increasing dose of γ -irradiation. At least 800 T4-2 cells on soft and 1000 T4-2 cells on stiff were counted in each experiment ($n = 4$). All statistical analyses were performed using two-tailed t test (* $p < 0.05$, ** $p < 0.01$, *** $p < 0.001$). All scale bars are 100 μm .

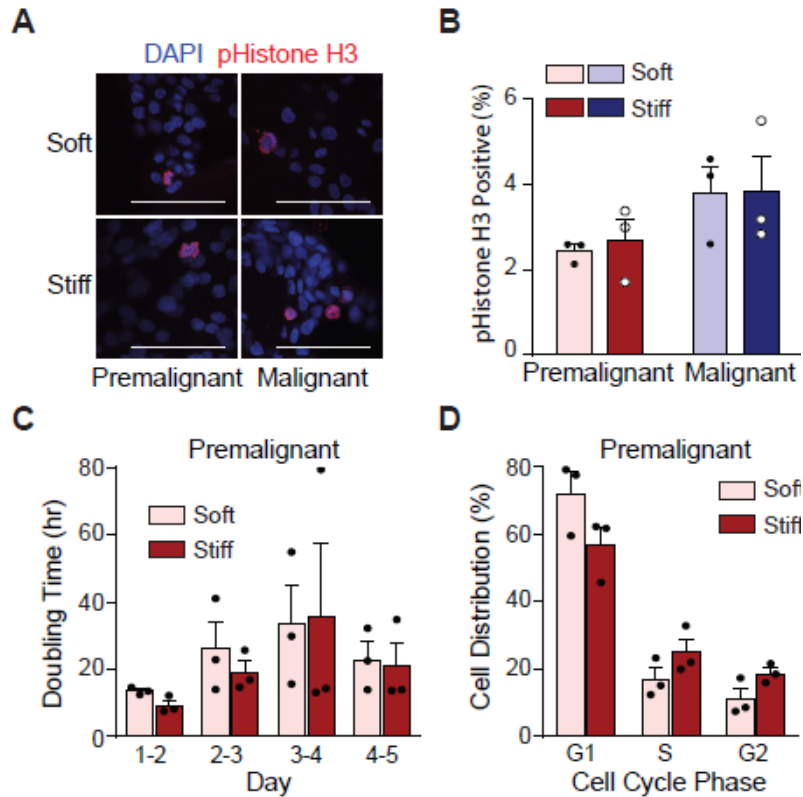


Figure 4.5: Proliferation cannot explain ECM stiffness-mediated sensitivity to apoptosis-inducing therapies. (A) Representative images of MCF10A and T4-2 cells at day 5 of culture on soft or stiff substrates stained for phosphorylated histone H3 (Ser10). (B) Bar graph showing mean and SEM of the percentage of phosphorylated histone H3 (Ser10) positive MCF10A and T4-2 cells on day 5 of culture on soft or stiff substrates. (C) Bar graph showing mean and SEM of the doubling time of MCF10A cells cultured on soft or stiff substrates each day over five days of culture. (D) Bar graph showing mean and SEM of the percentage of MCF10A cells in each cell cycle phase at day 5 of culture on soft or stiff substrates. At least 1000 T4-2 cells on soft and stiff were counted in each experiment. Statistical analyses were performed using two-tailed t test (* $p < 0.05$, ** $p < 0.01$, *** $p < 0.001$). Unless otherwise noted, $n = 3$ for all experiments. All scale bars are 100 μm .

treatment, and the cytokine induces tumor cell apoptosis through a pathway that is independent of cell growth^{188,189}. Consistent with our conclusion that the differential sensitivity of mammary tumors to anti-tumor treatment is independent of cell growth, we noted that the proliferating premalignant MCF10A and the malignant T4-2 colonies interacting with soft ECM substrate both were protected from TRAIL-induced apoptosis. Thus, we observed a dose-dependent increase in apoptosis, as indicated by cleaved caspase 3, in the TRAIL treated tumor colonies cultured on stiff as compared to soft ECM substrates (**Figure 4.4 E-H**). Accordingly, these data demonstrate that the sensitivity of the tumors to these anti-cancer treatments is likely not due to differences in cell proliferation. Instead the findings suggest that differences in tumor treatment sensitivity likely reflect a cell intrinsic phenotype conferred on the tumors by the compliance of the ECM substrate.

A stiff ECM sensitizes tumor colonies to anti-tumor treatment by enhancing JNK activation

Cell survival in response to an anti-tumor treatment is regulated by stress response pathways whose activity is controlled by a comparatively small number of key molecular regulators or signaling nodes^{159,190}. Jun N-terminal kinases (JNKs) comprise one major signaling node that can dictate whether a cell survives or undergoes apoptosis in response to an exogenous stress^{191,192}. JNKs phosphorylate c-Jun, which is a component of the Fos/Jun AP-1 transcriptional complex that regulates the expression of key cell growth and survival genes¹⁹¹. AP-1 levels and transcriptional activity can be induced by a stiff ECM, possibly because a stiff ECM increases RhoA-ROCK signaling¹⁸⁵. Elevated JNK activity has also been implicated in both the intrinsic apoptosis pathway triggered in response to stress-inducing stimuli such as UV radiation or chemotherapeutic agents, as well as via the extrinsic apoptosis pathway stimulated in response to death receptor signaling¹⁹¹. Accordingly, we reasoned that a stiff ECM substrate could sensitize mammary tumors to anti-tumor treatment by enhancing JNK activity. Consistently, we observed a significant and sustained increase in JNK activity following paclitaxel treatment in both the premalignant and malignant tumor colonies when they were cultured on the stiff as

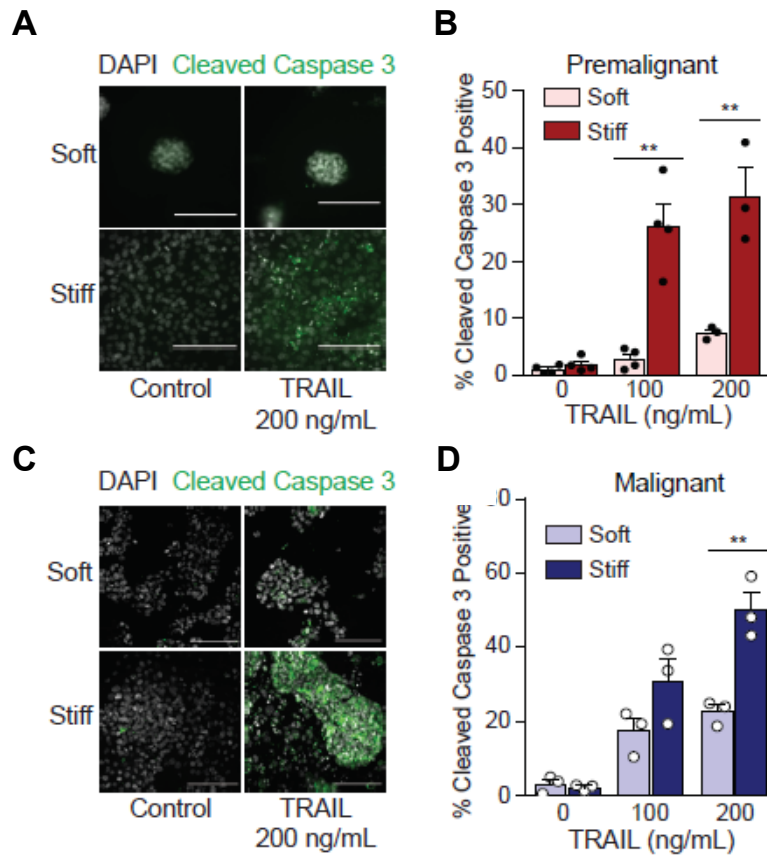


Figure 4.6: ECM stiffness broadly sensitizes cells to apoptosis through proliferation-independent pathways. (A) Representative images of vehicle and TRAIL treated MCF10A cells cultured on soft and stiff substrates stained for cleaved caspase 3 (green) and with DAPI (gray). (B) Bar graph showing mean and SEM of the percentage of cleaved caspase 3 positive cells from MCF10A cultures on soft and stiff substrates with increasing dose of TRAIL. At least 300 cells on soft and 700 cells on stiff were counted in each experiment (n = 3-4). (C) Representative images of vehicle and TRAIL treated T4-2 cells cultured on soft and stiff substrates stained for cleaved caspase 3 (green) and with DAPI (gray). (D) Bar graph showing mean and SEM of the percentage of cleaved caspase 3 positive cells from T4-2 cultures on soft and stiff substrates with increasing dose of TRAIL (n = 4). At least 1000 T4-2 cells on soft and stiff were counted in each experiment. Statistical analyses were performed using two-tailed t test (*p < 0.05, **p < 0.01, ***p < 0.001). Unless otherwise noted, n = 3 for all experiments. All scale bars are 100 μ m.

compared to the soft ECM substrate (**Figure 4.5 A, Figure A3.3**). Furthermore, and importantly, treating tumor cells with a pharmacological inhibitor of JNK activity, SP600125, significantly protected the premalignant tumor colonies plated on the stiff ECM substrate from apoptosis induction. Indeed, inhibiting JNK reduced apoptosis as indicated by the percentage of activated caspase 3 positive cells, induced in the tumor colonies in response to paclitaxel treatment when they were cultured on the stiff ECM substrates, as compared to those cultured on a soft ECM substrate that were treated with the same doses (**Figure 4.5 B**). Furthermore, to more directly implicate JNK in the stiffness-mediated sensitization of tumor tissue to anti-cancer treatment, we engineered the MCF10A MECs to express either a dominant negative JNK1 or JNK2 construct that were designed to prevent kinase activation ¹⁹³. Consistent with our hyper JNK activation hypothesis, both dominant negative JNK constructs rendered the MCF10A MECs interacting with the stiff ECM substrates resistant to apoptosis induction following treatment with either paclitaxel or TRAIL (**Figure 5.5 C**). Moreover, to further implicate stiffness-mediated modulation of JNK activity in tumor treatment responsiveness, we next tested whether a gain of JNK activity could sensitize the tumor tissue interacting with a soft ECM substrate to anti-tumor treatment. The MCF10A MECs were engineered to constitutively activate JNK by expressing a MKK7-JNK1 fusion protein that renders the JNK1 protein constitutively active ^{194,195}. Importantly, increasing JNK activity sensitized the tumor tissue to paclitaxel treatment and enhanced the level of apoptosis induced, as indicated by greater numbers of activated caspase 3 positive cells, even when the cells were cultured on a soft ECM substrate (**Figure 5 D**). Notably, the level of apoptosis induced in the MKK7-JNK1 expressing premalignant tumor cells cultured on the soft ECM substrate was virtually identical to that observed in the vector expressing tumor tissue cultured on the stiff ECM substrate. The data functionally implicate JNK activity as one key mechanism whereby a stiff ECM substrate can sensitize mammary tumors to anti-cancer apoptosis inducing agents.

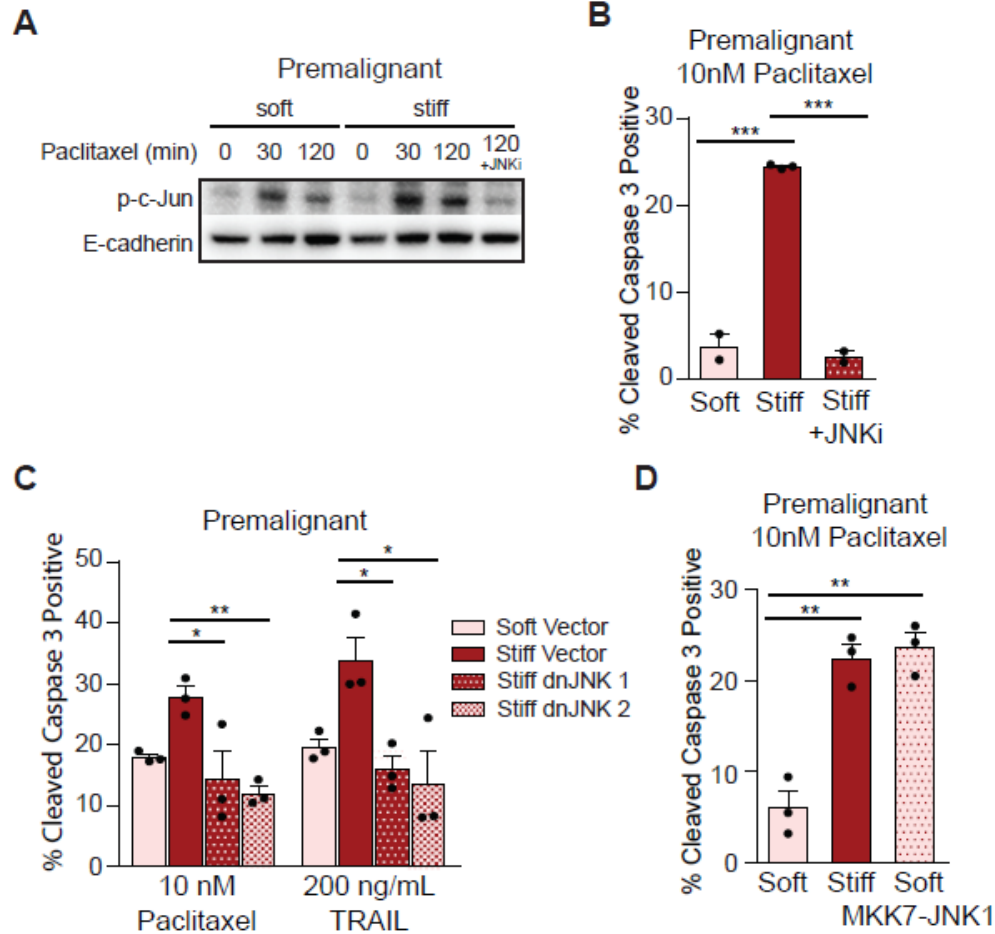


Figure 4.7: Enhanced JNK activity in cells on stiff ECM sensitizes cells to chemotherapy. (A) Representative Western blot bands for phosphorylated c-Jun (Ser63) in MCF10A cultured on soft or stiff substrates after 10nM paclitaxel treatment or paclitaxel with 5 μ M JNK inhibitor SP600125. (B) Bar graph showing mean and SEM of the percentage of cleaved caspase 3 positive cells from MCF10A cultured on soft and stiff substrates treated with 10nM paclitaxel or paclitaxel plus 5 μ M JNK inhibitor SP600125 (n = 2-3). (C) Bar graph showing mean and SEM of the percentage of cleaved caspase 3 positive cells from MCF10A cultured on soft and stiff substrates and stably transduced with dominant negative JNK1 or JNK2 or the vector control and treated with 10nM paclitaxel. (D) Bar graph showing mean and SEM of the percentage of cleaved caspase 3 positive cells from MCF10A cultured on soft and stiff substrates and transduced with a constitutively active MKK7-JNK1 fusion protein and treated with 10nM paclitaxel. Unless otherwise noted, n = 3 for all experiments. Statistical analyses were performed using two-tailed t test (*p < 0.05, **p < 0.01, ***p < 0.001).

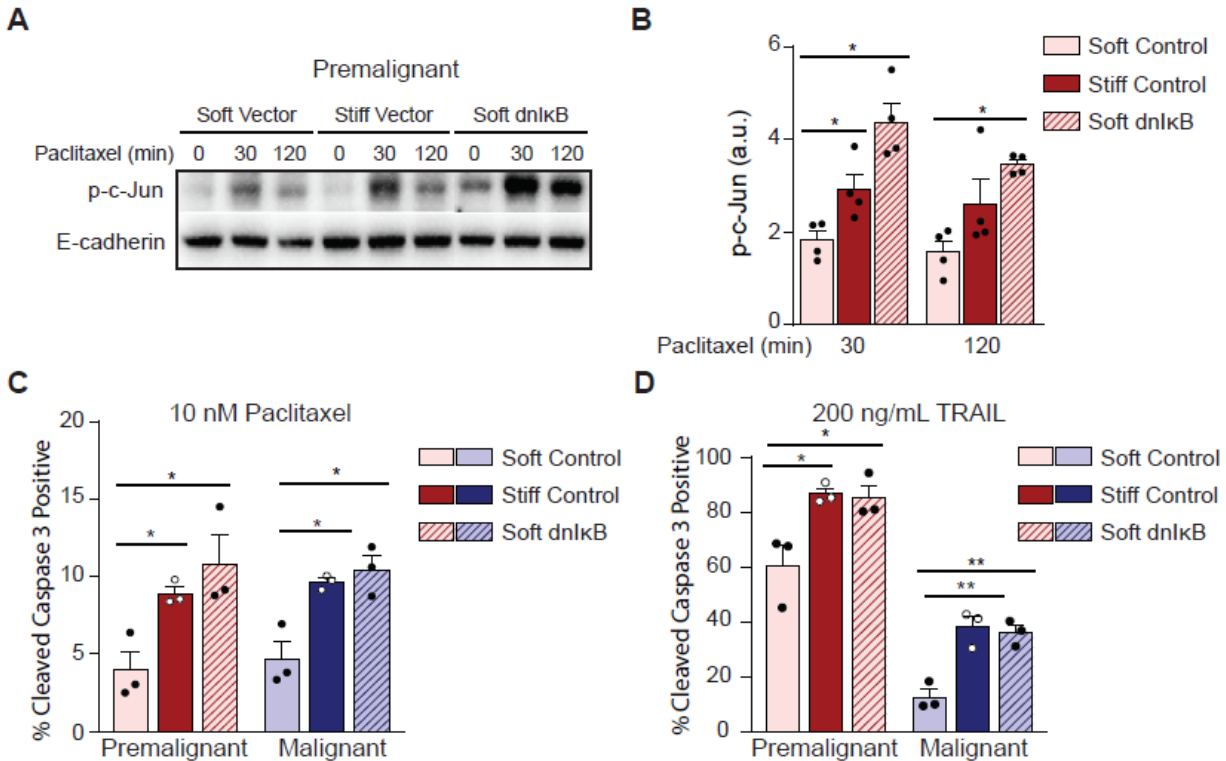


Figure 4.8: A soft ECM increases NF- κ B signaling to regulate JNK activity and apoptosis. (A) Western blot showing bands for phosphorylated c-Jun (Ser63) in MCF10A cells stably transduced with a dominant negative I κ B α M mutant (dnIkB) or the vector backbone and cultured on soft or stiff substrates at indicated timepoints after 10nM paclitaxel treatment. (B) Bar graph showing mean and SEM of Western blot quantifications of phosphorylated c-Jun (Ser63) by pixel density normalized to E-cadherin loading control (n = 4). (C) Bar graph showing mean and SEM of the percentage of cleaved caspase 3 positive cells from MCF10A or T4-2 cells expressing a dominant negative I κ B α M mutant cultured on soft or stiff substrates and treated with 10nM paclitaxel. At least 400 MCF10A cells or 600 T4-2 cells were counted in each experiment. (D) Bar graph showing mean and SEM of the percentage of cleaved caspase 3 positive cells from MCF10A or T4-2 cells expressing a dominant negative I κ B α M mutant cultured on soft or stiff substrates and treated with 200 ng/mL TRAIL. Unless otherwise noted, n = 3 for all experiments. Statistical analyses were performed using two-tailed t test (*p < 0.05, **p < 0.01, ***p < 0.001).

NF-κB represses JNK activity to promote tumor treatment resistance

We next assessed whether ECM stiffness could modulate the levels and/or activity of JNK regulators previously implicated in tumor treatment resistance. Elevated tumor levels of nuclear NF-κB have been implicated in cancer aggression and poor patient outcome^{196,197}. Experimental models have also shown that NF-κB activity enhances tumor cell survival and resistance to anti-tumor treatment both in culture and *in vivo*^{173,174,198–200}. We therefore tested whether ablating NF-κB activity could sensitize mammary tumor organoids to anti-tumor treatment and if this was linked to enhanced JNK activation. We engineered premalignant MCF10A mammary tumor cells with a dominant negative IκBαM mutant that sequesters NF-κB in the cytosol. Consistent with prior studies, we noted that ablating NF-κB activity significantly increased JNK activity, even in tumor organoids cultured on the soft ECM substrate (**Figure 4.6 A-B**). Furthermore, and importantly, inhibiting NF-κB significantly sensitized both the MCF10A and T4-2 colonies to both paclitaxel and TRAIL treatment, even when they were grown on a soft ECM substrate (**Figure 4.6 C-D**). These findings not only implicate NF-κB activity as a key regulator of JNK-dependent apoptosis signaling, but they also revealed an unappreciated potential link between ECM stiffness, NF-κB and JNK activity in the pathogenesis of treatment resistant breast tumors.

NF-κB activity predicts pathological response to neoadjuvant chemotherapy, modulates anti-tumor treatment response, and is elevated in residual TNBCs

We next explored the relevance of NF-κB activity in breast cancer patient response to therapy. Analysis of I-SPY patient data sets from neoadjuvant chemotherapy treated patients showed that patients who failed to achieve a pCR had primary tumors that were significantly enriched for an NF-κB dependent gene signature with a normalized enrichment score (NES) of 1.799 (**Figure 4.7 A**)²⁰¹. The findings are consistent with prior studies suggesting NF-κB target genes modulate tumor response to chemotherapy.

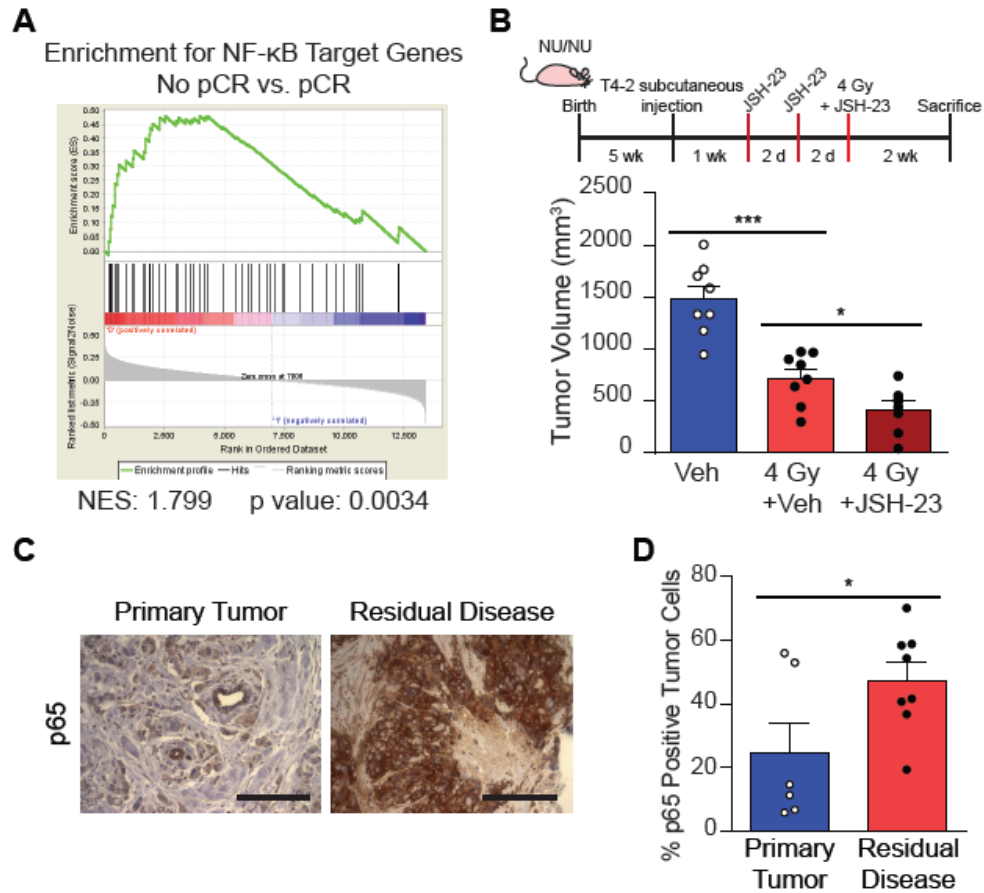


Figure 4.9: NF- κ B activity antagonizes tumor therapy. (A) Gene set enrichment analysis for NF- κ B target genes in human breast cancer samples prior to treatment that failed to achieve a pathological complete response ($n = 138$ total patients). Normalized enrichment score (NES) is 1.799. (B) Bar graph showing mean and SEM of tumor volume of subcutaneously injected T4-2 tumors treated with radiation or radiation in combination with NF- κ B inhibitor JSH-23 ($n = 7-8$ animals per group). Cartoon shows experimental design. (C) Representative images of p65 IHC in untreated primary human triple negative breast tumors or in residual disease of chemotherapy treated human triple negative breast tumors ($n = 6$ primary, $n = 8$ residual disease). (D) Bar graph showing mean and SEM of the percent of p65 positive cells in primary human triple negative breast tumors or in residual disease of chemotherapy treated human triple negative breast tumors ($n = 6$ primary, $n = 8$ residual disease). Statistical analyses were performed using two-tailed t test (B) or two-tailed Mann-Whitney U test (D) (* $p < 0.05$, ** $p < 0.01$, *** $p < 0.001$). Scale bars are 100 μm .

Nonetheless, to directly test whether NF- κ B activity could antagonize anti-tumor treatment responsiveness, we injected malignant T4-2 cells subcutaneously into the rear flanks of immunocompromised nude mice. After two weeks the mice were injected either with vehicle or the NF- κ B inhibitor JSH-23 and thereafter the tumors were subjected to ionizing radiation (4 Gy) treatment. Tumor response rates were assessed by monitoring changes in tumor growth. We observed that NF- κ B inhibition potentiated therapy response, and those tumors whose NF- κ B activity had been inhibited with JSH-23, grew significantly slower following radiation treatment as compared to the vehicle treated tumors (**Figure 4.7 B**). These findings further implicate elevated NF- κ B activity in the treatment resistance phenotype of mammary tumors.

To explore the clinical relevance of links between ECM substrate stiffness, elevated NF- κ B activity and treatment resistance, we next examined NF- κ B levels in the neoadjuvant treated, residual TNBCs surrounded by the highly compliant, remodeled ECM stroma. Consistent with a compliant ECM enhancing NF- κ B activity to potentially impair the response of TNBCs to anti-cancer treatment, we quantified a significant increase in NF- κ B (p65) in the residual epithelium in the chemotherapy treated TNBC patients that were surrounded by the remodeled, soft stroma. In contrast, the level of NF- κ B was markedly lower in the tumor epithelium in a cohort of untreated TNBC patients in which the associated and surrounding ECM was significantly stiffer (**Figures 4.1 D-E, 4.7 C-D**). These studies imply that a remodeled, compliant ECM could contribute to the treatment resistance of TNBCs to preclude a pathological complete response. The data also implicate anti-apoptotic NF- κ B activity in the pathogenesis of this residual tumor phenotype.

Discussion

In this study, we identified ECM stiffness as a critical modulator of anti-tumor treatment response. Using cultured 3D organoids of premalignant and malignant tumors and xenografted malignant tumors, we determined that a stiff ECM substrate broadly sensitizes tumor cells to the chemotherapeutic agent paclitaxel and to ionizing radiation and did so irrespective of cell cycle

status or level of cell proliferation. Surprisingly, we found that the tumor tissue interacting with a soft ECM was able to efficiently activate NF- κ B to resist even high doses of chemotherapy, ionizing radiation and even death receptor signaling. By contrast, we observed that a stiff ECM substrate sensitized tumor organoids to anti-tumor therapies by promoting therapy-induced stress signaling through JNK to abrogate pro-survival NF- κ B signaling. Critically, we determined that breast cancer patients whose primary tumors had high NF- κ B activity also had a higher rate of treatment resistance and post-treatment were enriched for NF- κ B activity. Consistently, residual chemotherapy resistant TNBC tissue that was surrounded by a highly remodeled, soft ECM also showed high levels of nuclear NF- κ B. These findings are consistent with prior studies implicating NF- κ B activity in the treatment resistance of tumors and highlight the importance of tissue context in regulating anti-tumor treatment response. These data also suggest therapies designed to inhibit NF- κ B could be used to improve the treatment response of TNBCs to enhance the long-term survival of these patients.

Consistent with an association between a soft ECM and treatment resistance, we observed a profoundly remodeled ECM in post-treatment human TNBCs and showed that this modified ECM was softer than that measured in primary TNBCs. Manipulations using 3D organoid models in which the substrate biomechanical properties could be precisely manipulated provided direct evidence to show that a soft ECM protects whereas a stiff ECM sensitizes tumor cells to anti-tumor treatment. The findings are consistent with prior studies which showed that 3D mammary organoids grown within soft reconstituted basement membrane gels (Matrigel) exhibit improved survival following chemotherapy and radiation by activating NF- κ B^{174,198,199}. Critically these and other reports established a link between the 3D culture format and multicellularity in generating the treatment resistance phenotype of tumors^{173,174,202,203}. Our experiments, which rigorously controlled for confounding variables including hypoxia, proliferation and drug accessibility not only confirmed those results, but also extended those earlier observations to

unequivocally demonstrate a role for ECM stiffness and multicellular architecture in modulating the treatment response of tumors ²⁰⁴. Our studies also imply that the organoid models used to study treatment resistance in culture and to screen for novel anti-tumor agents need to consider the biophysical properties of the matrix when interpreting data and designing assays.

A stiff ECM promotes epidermal growth factor receptor (EGFR) signaling to increase the activity of PI3K and ERK that in turn enhance tumor cell growth and survival ^{23,187}. Not surprisingly, a stiff tissue microenvironment was shown to promote the resistance of melanomas to targeted kinase inhibitors both in culture and *in vivo*, presumably by potentiating receptor tyrosine kinase activity to increase net pro survival signaling ²⁰⁵. Those prior studies addressed the impact of therapies that target a specific defined receptor tyrosine kinase signaling pathway whose activity is significantly potentiated by ECM stiffness. However, our studies addressed the impact of ECM stiffness on agents and treatments that trigger apoptosis by inducing a general cellular stress response. To this end we found that a stiff ECM permits an unencumbered chronic elevation in JNK activity in response to an exogenous stress such as chemotherapy, and we provided evidence that this effect compromised tumor cell survival. Consistent with a reduced stress response in cells interacting with a soft ECM, we showed that premalignant MECs treated with 6-12 Gy ionizing radiation not only failed to die but showed a significantly enhanced clonogenic survival only when re-plated on a soft ECM; an observation also observed with chemotherapy treated hepatic cancer cells ²⁰⁴. Intriguingly, a set of studies conducted in monolayer 2D cultures implicated higher stress signaling through JNK as a protective mechanism whereby cultured breast and hepatic cancer cells plated on a stiffer ECM substrate acquired greater resistance to the multikinase inhibitor sorafenib ²⁰⁶. In marked contrast to these monolayer culture studies, our work was conducted in cancer organoids in which we recapitulated the 3D tissue-like structures of *in vivo* tumor tissue. Moreover, unlike many 2D studies our culture studies were faithfully reproduced in mouse models and patient samples ^{207,208}. Indeed, while cells grown as 2D

monolayers show an absolute requirement for PI3 kinase for survival and for ERK activation to progress through G1, cells grown as 3D organoids depend less upon PI3 kinase and ERK and instead require Rac GTPase for both their growth and survival ^{174,209}.

We and others have identified NF- κ B as a key regulator of treatment resistance ^{173,174,199,210}. NF- κ B directly mediates the transcription of several anti-apoptotic genes and alters angiogenesis, metabolism, immune cell interactions, and metastasis ^{210,211}. We noted an increase in NF- κ B in the residual tumor of chemotherapy treated patients and mechanistically, we determined that the failure of tumor organoids in a stiff 3D ECM to robustly activate NF- κ B in response to therapy permitted a high degree of JNK activation, which induced apoptosis in these cells. These findings are consistent with work from others showing JNK stress signaling reduces tumor viability and compromises survival in response to therapy ¹⁸². Conversely, JNK activation in some contexts, such as cells plated on a stiff 2D substrate, prevents apoptosis to promote drug resistance, consistent with its pleiotropic role in apoptosis and stress response ^{191,206}. Nevertheless, compelling *in vivo* evidence identified JNK as a key mediator of chemotherapy sensitivity, and furthermore, human TNBC data sets linked a high JNK activity gene expression signature with improved chemotherapy response implicating JNK in chemosensitivity ¹⁸³. Our findings further support the physiological relevance of JNK in chemotherapy response and demonstrate that the soft, remodeled ECM niche contributes to the ability of residual tumor cells to resist apoptosis via NF- κ B-JNK signaling. These data suggest that the targeting of additional pathways, such as the NF- κ B-JNK axis, may sensitize or potentially re-sensitize chemotherapy resistant tumor cells to enhance treatment efficacy and eradicate residual tumor cells.

Resistance to chemotherapy and radiation continue to be significant barriers to overcome, particularly in TNBC. Many TNBC patients respond only partially to neoadjuvant chemotherapy with as much as 60-70% of these cancers showing some level of residual disease ¹⁷². Importantly, an incomplete pathological response to therapy associates with worse overall patient survival ¹⁷².

Indeed, primary TNBCs that fail to respond well to chemotherapy frequently recur with metastatic disease that is refractory to nearly all therapies with fewer than 30% of patients surviving beyond five years. Targeting the pro-survival molecular effectors activated in cells within a soft ECM niche will very likely be a more tractable and efficacious strategy to improve chemotherapy response than modulating ECM mechanics directly. Unfortunately, despite promise in many tumor types, systemic NF- κ B inhibitors have proven immensely toxic due to lack of tumor cell selectivity and immune suppression ²¹². Targeting NF- κ B regulated anti-apoptotic proteins has shown more promise. A recent clinical trial using LCL161, an antagonist of inhibitor of apoptosis proteins (IAPs), in combination with paclitaxel found the rate of pCR more than doubled in this group when patients had a high TNF α gene expression signature ²¹³. However, this combination treatment was also associated with higher incidence of serious adverse events. Recently, a small molecule selectively targeting NF- κ B-JNK signaling by disruption of an inactivating interaction between NF- κ B-regulated GADD45 β and MKK7 in multiple myeloma enabled MKK7 to phosphorylate JNK and sensitized these cells to apoptosis ²¹⁴. While this mechanism has not been demonstrated in breast cancer, it serves as a proof of principle that selective targeting of the NF- κ B-JNK pathway may be of considerable benefit to patients. Other approaches to indirectly modulate NF- κ B activity may also mitigate therapy resistance. For example, chemotherapy administered at the maximum tolerated dose can activate NF- κ B in stromal fibroblasts, triggering the secretion of potent cytokines that induce the formation of highly drug resistant tumor initiating cells. Low dose metronomic chemotherapy abrogated stromal NF- κ B activation, thus potentiating tumor response to systemic chemotherapy ²¹⁵. Clearly more work is needed to clarify the nature of the mechanisms that mediate treatment resistance, and develop effective, selective, and safe therapeutics.

Methods

Human breast tissue acquisition and processing

Human breast tumor specimens were either embedded in an optimum cutting temperature (OCT) aqueous embedding compound (Tissue-Plus, Scigen, Cat# 4583) within a disposable plastic base mold (Fisher, Cat# 22-363-554) and were snap frozen by direct immersion into liquid nitrogen and kept at -80°C freezer until cryo-sectioning for analysis, or specimens were formalin fixed and paraffin-embedded (FFPE). All human breast specimens were collected from prospective patients undergoing surgical resection at UCSF or Duke University Medical Center between 2010 and 2014. The selected specimens were de-identified, stored, and analyzed according to the procedures described in Institutional Review Board (IRB) Protocol #10-03832 and #10-05046, approved by the UCSF Committee of Human Resources and the Duke's IRB (Pro00034242)²⁶.

Cell culture

Human mammary epithelial cell lines MCF10A and HMT-3522 T4-2 were grown and maintained as previously described²⁷. Growth medium was supplemented with 2% rBM at the time of plating. Growth medium was changed one day after plating and every two days thereafter. All assays were performed between days 4 and 5 after seeding.

Lentiviral infection and vectors

MCF10A cells were transduced with the dominant negative forms of JNK: HA-JNK1-APF and HA-JNK2-APF and used as previously described (L. Heasley, University of Colorado, Denver)¹⁹³. MCF10A cells were transduced with the constitutively active JNK1, the MKK7-JNK1 α fusion protein as previously described^{194,195}.

MCF10A and T4-2 cells were electroporated to introduce a transposon (PiggyBac) expressing a doxycycline inducible I κ B α M and PiggyBac transposase ²¹⁶. Cells were selected in G418 (500 μ g/mL) for purity. Cells containing I κ B α M are denoted as dnI κ B.

Polyacrylamide gel preparation

Basement-membrane conjugated polyacrylamide gels were prepared as described ²¹⁷. Soft gels with measured elastic moduli of 140 Pascal were prepared with 3% (w/v) acrylamide and 0.04% (w/v) bis-acrylamide, and stiff gels with elastic moduli of 5000 Pascal were prepared with 5.5% (w/v) acrylamide and 0.15% (w/v) bis-acrylamide.

Apoptosis assays

MECs grown on soft or stiff polyacrylamide gels for 96 hours were treated with either paclitaxel (5 or 10 nM), TRAIL (100 or 200 ng/ml), or gamma irradiation (4 – 12 Gy). Apoptosis was directly assayed at 24 hours post-treatment via immunofluorescent staining of cleaved caspase 3. Percent apoptosis was calculated as the number of cells positive for activated caspase 3 expressed as a percentage of the total number of cells. A minimum of 300 cells per condition were counted from several fields of view. Maximum intensity projections of z-stacks were used for analysis of cleaved caspase 3 positive cells.

Immunofluorescence and immunohistochemistry

Cells were briefly rinsed in PBS and directly fixed using 2-4% paraformaldehyde for 20 minutes at room temperature. Cells were washed with IF buffer (32.5 mM NaCl, 3.3 mM Na₂HPO₄, 76 μ M KH₂PO₄, 1.92 mM NaN₃, 0.1% (w/v) BSA, 0.2% (v/v) Triton-X 100, 0.05% (v/v) Tween 20) and then incubated with the blocking solution (10% goat serum in IF buffer; 1 hour, room temperature). Cells were incubated with primary antibodies in a humidified chamber overnight at 4°C. Samples were washed with IF buffer (3 X 10 minutes while rocking) and incubated with Alexa-488- or Alexa 555-conjugated secondary antibodies (1 hour, room temperature). Samples

were washed again with IF buffer (3 X 15 minutes while rocking) and nuclei were counterstained with DAPI (1 µg/ml in PBS; 5 minutes, room temperature). Cells on gels were inverted onto a number 1 coverglass immediately prior to imaging.

Fluorescent images were acquired on a spinning disk confocal Nikon Eclipse Ti microscope at 20x magnification with a 0.75 NA objective. Cells on polyacrylamide gels were inverted directly onto a No. 1 coverslip and imaged immediately at room temperature. The images were acquired using an Andor Zyla sCMOS camera and MetaMorph acquisition software. Images were processed in ImageJ.

FFPE slides were deparaffinized in xylene and rehydrated in graded ethanol solutions. Heat-mediated antigen retrieval was performed in 10mM citrate buffer pH = 6.0 and endogenous peroxidase activity blocked by incubation with 3% hydrogen peroxide. Tissues were incubated with primary antibody overnight at 4°C and biotin-conjugated secondary antibody 1 hour at room temperature. Vectastain Elite ABC (Vector Laboratories PK-6100) and DAB Peroxidase substrate kit (Vector Laboratories SK-4100) were used for signal detection according to manufacturer instructions.

IHC images were acquired on a Nikon Eclipse TE2000-U inverted microscope at 20x magnification with a 0.75 NA objective. Images were acquired with a Hamamatsu ORCA-Flash4.0 LT camera using NIS-Elements software.

Protein lysates

Protein lysates were prepared using RIPA (50 mM Tris-HCl, 150 mM NaCl, 0.25% Na-deoxycholate, 0.1% SDS, and 1.0 % IGPAL CA-630 (NP-40); pH 7.4 at room temperature) or Laemmli lysis buffer (50 mM Tris-HCl, 2% SDS, and 5mM EDTA; pH 7.4 at room temperature). Immediately prior to cell lysis, a cocktail of protease inhibitors was added to the buffer (1.2 µg Leupeptin, 1.2 µg Pepstatin, 2.4 µg Aprotinin, 12 µg E-64, 0.5 mM Benzamidine, 50 mM NaF, and 1.2 µg Pefabloc), and the phosphatase inhibitor Na Orthovanadate (1mM activated with 1.5%

H₂O₂). RIPA lysates were done on ice, while Laemmli lysates were performed at room temperature due to SDS precipitation at cold temperatures. After rinsing the dishes with PBS, lysis buffer was added and cells were scraped off the dish with a cell scraper. RIPA lysates were sonicated 3 times, each for 10 seconds, while Laemmli lysates were passed through a fine pipet tip (p200) several times. Both were centrifuged for 10 minutes at 20,817 rcf to pellet any internal organelles and cellular debris. Supernatant was collected and fast frozen on dry ice. Protein concentration was determined using the BCA assay kit (Promega), following the manufacturer's protocol.

Cytoplasmic and nuclear protein extracts were obtained with a kit using manufacturer instructions (ThermoFisher #78833).

Western blotting

Cells were lysed as described above and equal amounts of protein were separated on reducing SDS-polyacrylamide gels, immunoblotted and detected with an ECL-Plus system. Samples were boiled for 5 minutes (95°C) and loaded onto the SDS-polyacrylamide gel, and protein was separated at 120 constant volts.

The protein was transferred onto a pre-wet polyvinylidene difluoride (PVDF) membrane (100% methanol, 1 minute), either at 300 mA for 2 hours or at 25 constant volts overnight (4°C). The PVDF membrane was rinsed with TBST and non-specific binding was blocked with 5% nonfat dry milk dissolved in TBST. The membrane was then incubated with the primary antibody overnight at 4°C, washed with TBST, incubated with horseradish-peroxidase conjugated secondary antibody (1 hour, room temperature; dilution 1:5000), washed with TBST, and detected with the chemiluminescence system Quantum HRP substrate (Advansta #K-12042). Quantification was performed using ImageJ.

Metabolic activity assay

MECs were washed with 1X PBS and incubated with MTT working solution (a 5 mg/ml (w/v) MTT stock solution in PBS, diluted tenfold in DMEM/F12 for a final MTT concentration of 500 µg/ml) for 2 hours at 37°C. MTT was solubilized with DMSO for 10 minutes at 37°C. The plate was tapped vigorously to extract all of the MTT from the cells and once the solution was an even purple color and 100 µl was transferred to a 96-well plate. The absorbance was measured directly using a plate reader set at 550 nm and background subtraction set at 630 nm. Absorbance values were normalized to the untreated controls to determine relative metabolic activity.

Irradiation

All cell culture and mouse experiments used a J L Shepherd Mark I model-20 ¹³⁷Cesium source irradiator.

Proliferation assay

To measure the proliferation rate of MECs in log phase of growth on soft (E=140 Pa) and stiff (E=5000 Pa) polyacrylamide gels, cells were trypsinized and counted at 24 hour intervals. The growth rate constant, k , was derived using the equation: $N/N_0 = e^{kt}$, where N_0 is the initial absorbance or cell number, and N is the absorbance or cell number at time t . The doubling time, t_d , was calculated using the derived k and setting $N/N_0 = 2$ in the following equation: $t_d = (\ln 2)/k$.

To assess the proliferation rate of MECs in 3D rBM, cultures was fixed and stained at different time points with anti-phosphorylated histone H3. Proliferating cells or colonies (positive pH3 staining) were scored using a fluorescence microscope. A minimum of 250 cells per condition were scored from several fields of view.

Colony size was determined by measuring the diameter of MEC colonies after 10-14 days in 3D rBM or 3D collagen/rBM. The colony diameters were measured using a pre-calibrated

eyepiece on a light microscope. At least 50 colonies per sample were scored from different fields of view in the center of each gel.

Cell cycle analysis

The percentage of cells in each stage of the cell cycle was determined by propidium iodide (PI) staining and FACS analysis for DNA content (FACS Calibur, Becton Dickinson, San Jose, CA). MECs were grown on soft and stiff polyacrylamide gels and processed on days 4 and 5 in order to determine cell cycle status. Briefly, MECs were trypsinized, counted, and washed with ice-cold 1% BSA/DPBS. MECs were fixed with a 1:4 dilution of 1% BSA/DPBS in 96% ethanol. Fixed MECs were centrifuged at 259 rcf, washed with ice-cold PBS, and incubated in PI staining solution (50 µg/ml PI in PBS supplemented with 3.8 mM sodium citrate and 500 µg/ml RNase A; 500 µl per 2×10^6 cells; 3 hours on ice). DNA content was determined using the FACS Calibur set to low flow and data was acquired for 20,000 cells within the gated region of cells in G0/G1, S and G2/M phases of the cell cycle.

Clonogenic survival assay

MECs were grown for 4 days on soft and stiff polyacrylamide gels and treated with apoptosis inducers on day 4 as described. Cells were trypsinized and replated on soft or stiff polyacrylamide gels at low density on day 4 (500 cells in a 60 mm gel; triplicates), grown for 7-10 days, and assayed for colony formation. Briefly, cells were rinsed with 1X PBS, fixed (ice-cold 100% methanol, 10 minutes, -20°C), rinsed with 1X PBS, stained with crystal violet (0.5% (w/v) solution, 10 minutes, room temperature), rinsed with 1X PBS, rinsed with ddH₂O, and air dried by inverting onto a paper towel (overnight).

Plates were scanned with a conventional flatbed scanner (grayscale, 150 dpi, tif). Colonies were counted using a MATLAB script (K. Tsai, Weaver Lab). First a representative positive colony was chosen for calibration, where a positive colony contained 50-100 cells (about 10 square

pixels). The program output was the number of colonies greater than or equal to the size indicated for a positive colony. Any fused colonies in the program output were accounted for by adding one to the final colony number for each fusion.

Mouse experiments

Five-week-old nude mice were orthotopically injected with 10^6 T4-2 cells in soft or stiff, ribose crosslinked collagen gels. Collagen gels were prepared as previously described¹⁸⁷. Briefly, collagen was incubated with 500mM L-ribose for at least 4 weeks at 4 °C prior to neutralization and gelation. Intraperitoneal paclitaxel injections (10 mg/kg) were given every two days starting seven weeks after tumor cell injection, coinciding with the emergence of measurable tumors. Mice were sacrificed, and tissue was harvested 14 days following the start of paclitaxel injections.

Five-week-old nude mice were injected with 5 million T4-2 cells subcutaneously in collagen gels. Mice were given three intraperitoneal injections with NF- κ B inhibitor JSH-23 (4.8 mg/kg) or DMSO vehicle with the final injection coinciding with 4 Gy ionizing irradiation of the tumor. Mice were sacrificed and tissue harvested two weeks after irradiation.

All mouse studies were maintained under specific pathogen-free conditions and performed in accordance with the Institutional Animal Care and Use Committee and the Laboratory Animal Research Center at the University of California, San Francisco.

Picrosirius red staining and quantification

FFPE tissue sections were stained using 0.1% Picrosirius red (Direct Red 80, Sigma-Aldrich, Cat# 365548 and picric acid solution, Sigma-Aldrich, Cat# P6744) and counterstained with Weigert's hematoxylin (Cancer Diagnostics, Cat# CM3951). Brightfield and polarized light images were acquired using an Olympus IX81 microscope fitted with an analyzer (U-ANT) and a polarizer (U-POT, Olympus) oriented parallel or orthogonal to each other, respectively. The

percentage of picosirius red signal per field of view was quantified in polarized light images using ImageJ.

Atomic force microscopy data acquisition

Atomic force microscopy (AFM) measurements were performed using 30 μm thick OCT-embedded frozen human breast tumor tissue sections were thawed by immersion in room temperature PBS. Thawed sections were immersed in PBS containing phosphatase inhibitor (GenDEPOT Xpert #P3200-001), protease inhibitor cocktail (GenDEPOT Xpert # P3100-001), and propidium iodide (ACROS, Cat# 440300250) and placed on the stage for AFM measurements. AFM indentations were performed using an MFP3D-BIO inverted optical AFM (Asylum Research) mounted on a Nikon TE2000-U inverted fluorescent microscope. Silicon nitride cantilevers were used with an approximate spring constant of 0.06 N m^{-1} and a borosilicate glass spherical tip with 5 μm diameter (Novascan Tech). The cantilever was calibrated using the thermal oscillation method prior to each experiment. Specimens were indented at $1 \mu\text{ms}^{-1}$ loading rate. Force maps were obtained in tumor adjacent ECM as a raster series of indentations utilizing the FMAP function of the IGOR PRO build supplied by Asylum Research. Elastic properties of ECM were determined by fitting data with the Hertz model. A Poisson's ratio of 0.5 was used in the calculation of the Young's elastic modulus.

Antibodies and reagents

We used commercial extracellular matrix (Matrigel™; Collaborative Research) for the reconstituted basement membrane (rBM) assays. Primary antibodies used were: cleaved caspase-3 (1:400, Cell Signaling #9661), phospho-c-Jun (serine 63) (1:1000, Cell Signaling #3270), JNK1/JNK2 (1:1000, BD PharMingen #554285), E-cadherin (1:1000, Cell Signaling #3195), phospho-JNK (G-7) mAb (1:100, Santa Cruz Biotechnology #sc-6254), and HA.11 clone 16B12 (1:2000, BabCO, Richmond, CA), p65 (1:1000 Western blot, 1:800 IHC, Cell Signaling

#8242). The secondary antibodies used were: horseradish peroxidase-conjugated anti-rabbit and mouse (Amersham Biosciences, Piscataway, NJ); and Alexa Fluor 488- and 555-conjugated anti-mouse and rabbit IgGs (Molecular Probes, Carlsbad, CA). The following reagents were used in these studies: propidium iodide, diaminophenylindole (DAPI), 3-(4,5-dimethyl thiazol-2-yl)-2,5-diphenyl tetrazolium bromide (MTT), Trichrome Masson Stain, and Weigert's Iron Hematoxylin (all from Sigma, St. Louis, MO); N-Tetra-methyl-ethylenediamine (TEMED), 30% acrylamide/bis solution (37.5:1, 2.6% C), 40% acrylamide solution and 2% bis solution (Bio-Rad Laboratories, Hercules, CA); TRAIL (100-200 ng/ml), paxlitaxel (5-10 nM), and the JNK inhibitor SP600125 (5 μ M, ApexBio #A4604), recombinant human TNF α (20 ng/ml, Invitrogen #68-8786-63), and NF- κ B inhibitor JSH-23 (Millipore #481408).

Gene set enrichment analysis

GSEA was performed to assess differential expression of NF- κ B target genes in patients that achieved or failed to achieve a pathological complete response to neoadjuvant chemotherapy using publicly available software maintained by the Broad Institute²¹⁸. Publicly available gene expression and treatment response data from the ISPY-1 trial were used (GSE32603)²⁰¹. The NF- κ B gene signature gene set was taken from publicly available CHIP-Seq data from the Cistrome data browser. The gene set consisted of the top 100 targets from a p65 (RELA) CHIP-Seq experiment in the MCF-7 mammary epithelial cell line treated with TNF α compared with vehicle treated cells²¹⁹.

Statistics

Unless otherwise noted, all tests for statistical significance were done using an unpaired student's t-test, assuming unequal variances and a two-tailed distribution, with a significance level of 0.05. Data were analyzed using GraphPad Prism. All data reported herein displays one star denoting a p-value \leq 0.05, two stars denoting $p \leq$ 0.01, and three stars denoting $p \leq$ 0.001.

For all data presented, the number of biological replicate experiments conducted is denoted as n.

Study approval

All human breast specimens were collected from prospective patients undergoing surgical resection at UCSF or Duke University Medical Center between 2010 and 2014. Informed consent was received from patients prior to tissue collection. The selected specimens were de-identified, stored, and analyzed according to the procedures described in Institutional Review Board (IRB) Protocol #10-03832 and #10-05046, approved by the UCSF Committee of Human Resources and the Duke's IRB (Pro00034242)²⁶. All mouse studies were maintained under specific pathogen-free conditions and performed in accordance with the Institutional Animal Care and Use Committee and the Laboratory Animal Research Center at the University of California, San Francisco.

Chapter 5: LOX-mediated ECM stiffening reshapes immune cell populations and regulates tumor metastasis

In collaboration with: Ori Maller¹, Connor Stashko^{1,2}, Jason Northey¹, and Valerie M. Weaver^{1,3,4}

¹Department of Surgery, Center for Bioengineering and Tissue Regeneration, University of California, San Francisco, San Francisco, CA, USA

²UC Berkeley-UCSF Graduate Program in Bioengineering, University of California, San Francisco, CA USA

³UCSF Helen Diller Comprehensive Cancer Center, University of California, San Francisco, San Francisco, CA, USA

⁴Department of Bioengineering and Therapeutic Sciences, University of California, San Francisco, San Francisco, CA, USA

Introduction

As breast tumors grow, they recruit several types of innate immune cells to the tumor microenvironment that promote continued growth, immune evasion, and metastasis. The Weaver lab has shown that the most fibrotic subtypes of human breast tumors also contain the highest level of immune cell infiltration, particularly macrophages²⁶. We have also shown that infiltrating immune cells recruited early in tumor development are key activators of tumor fibrosis through secretion of TGF β (Chapter 3). However, it is unclear whether ECM stiffness can in turn alter the recruitment of phenotype of tumor associated-immune cells. Many myeloid cells including macrophages and neutrophils react to substrate stiffness *in vitro*, but how ECM stiffness may regulate their behavior in the tumor microenvironment has not been investigated²²⁰⁻²²⁴.

One of the most abundant immune cell types in breast tumor stroma is the tumor-associated macrophage (TAM)²²⁵. Macrophages are a diverse population of myeloid cells that, depending on tissue context, can phagocytose infectious bacteria and cell debris, orchestrate stromal behavior in wound healing, and present antigens to T cells. TAMs consist of distinct populations of tissue resident macrophages and bone marrow derived macrophages, which are recruited to the tumor as circulating monocytes and differentiate into macrophages after extravasation. Macrophages polarize into different activated phenotypes upon encountering specific cytokine signals that instruct their differentiation. Breast tumors contain multiple subpopulations of differentially polarized macrophages, but in general, early in tumor initiation these cells may be phagocytic and immune activating, but inevitably become immunosuppressive and support tumor cell invasion as tumors progress^{144,226,227}. Much attention and effort has been given to understand the mechanisms by which TAMs promote metastasis and to therapeutically target these cells²²⁸.

Until recently, neutrophils have been ignored as insignificant relative to macrophages, but mounting evidence over the last ten years argues that neutrophils also play a key role in shaping

the tumor microenvironment and promoting metastasis. Neutrophils are exceptionally unique cells. Like the other granulocytes/polymorphonuclear leukocytes basophils and eosinophils, they have a characteristic lobed nucleus that becomes hyper-segmented upon activation²²⁹. Neutrophils are produced in massive quantities in the bone marrow in response to G-CSF. Unless neutrophils are stimulated, they circulate for a short time and return to bone marrow to die. In humans, 60-70% of circulating leukocytes are neutrophils, and they have an average half life of 13-19 hours^{230,231}. To maintain their place as the most abundant leukocytes, humans produce an average of 10^{11} neutrophils per day. Canonically, neutrophils perform critical functions as the first responders to sites of injury or infection. Within minutes neutrophils are recruited to sites of acute injury through adhesion to activated endothelium and chemotaxis toward damage associated molecular patterns (DAMPs), pathogen associated molecular patterns (PAMPs) such as formylated peptides, and chemokines such as CXCL8^{229,232}. The first wave of recruited neutrophils release potent secondary chemoattractants like leukotriene B₄ (LTB₄) that initiate the recruitment of large number of neutrophils from long distances^{233,234}. They perform three main effector functions in response to infection and tissue injury: phagocytosis, degranulation to release antimicrobial molecules and proteases, and forming neutrophil extracellular traps (NETs). Because neutrophils are required to respond immediately upon stimulation, they likely do not rely on *de novo* transcription to synthesize materials needed to carry out their effector functions²³⁵. Instead, they presynthesize the necessary proteins and store them within different types of cytoplasmic granules that are released upon a variety of stimuli.

Multiple lines of evidence exist suggesting that neutrophils play a prometastatic role in breast cancer. Neutrophil production is upregulated in many breast tumor models including the highly metastatic 4T1 and PyMT models^{236,237}. This is primarily due to elevated G-CSF that stimulates granulopoiesis in the bone marrow. Neutrophils in mouse tumors have been shown to be potently immunosuppressive and often make up a large portion of the ambiguous population

of immunosuppressive myeloid cells called myeloid-derived suppressor cells (MDSCs). Neutrophils suppress T cell function through high arginase activity, which depletes arginine required for cytotoxic T cell proliferation, and ROS production, which also dampens T cell effector function^{238,239}. Neutrophils also secrete protumor cytokines such as TGF β , PDGF, and VEGF²⁴⁰. Depletion of neutrophils in orthotopic and spontaneous murine tumor models significantly reduces metastatic burden in the lung^{241–243}. Furthermore, interfering with neutrophil recruitment using CXCR2 inhibitors or blocking antibodies also inhibits tumor metastasis^{239,244,245}.

In addition to the prometastatic role of neutrophils found within the primary tumor, neutrophils that populate future sites of tumor metastasis modify this environment to become hospitable to tumor cells upon their arrival. Neutrophils arrive to organ sites prior to tumor cells and condition the premetastatic niche through the release of ECM proteases such as MMPs, cathepsins, and neutrophil elastase as well as immunosuppressive signaling^{246,247}. Neutrophils have also been implicated in arousing dormant tumor cells via NET-mediated ECM protease release that exposes laminin binding sites to tumor cells²⁴⁸.

Despite the wealth of evidence implicating neutrophils in prometastatic functions, some reports demonstrate neutrophils may also restrict tumor growth and metastasis. Neutrophils have been shown to release cytotoxic factors like nitric oxide in mice and humans that mediate tumor cell killing^{249,250}. Another study harvested neutrophils from the lungs of 4T1 tumor-bearing mice and when injected into the tail vein following 4T1 cells, inhibited the formation of metastatic foci²⁵¹. Antibody depletion of neutrophils had no effect on tumor growth in this model but potently reduced metastasis. Interestingly, G-CSF conditioned neutrophils failed to inhibit metastasis when injected following tumor cells suggesting that similar to macrophages, neutrophils can adopt different phenotypic states, an idea that only recently has become broadly accepted. In support of this view, studies in mice receiving a systemic TGF β inhibitor revealed distinct populations of neutrophils with those receiving the inhibitor exhibiting more tumor cytotoxicity²⁴².

Much of our knowledge of neutrophil biology, including their role in cancer, has been gained through mouse models; however, key differences in mouse and human neutrophil biology present important caveats to keep in mind when interpreting these studies. Neutrophils make up only 10-20% of circulating neutrophils in mice, compared to 60-70% in humans. Moreover, mice lack orthologs to many important neutrophil chemokines, including CXCL8, as well as Fc α RI, an Fc receptor that triggers neutrophil effector functions²⁵². Human neutrophils are also identified using different markers and contain different material within their granules, which complicates comparisons of these cells between mouse and human.

In these preliminary studies, we manipulated stromal LOX activity and ECM stiffness in *in vivo* breast tumor models to understand how tumor-associated ECM remodeling affected the tumor immune landscape. We observed that neutrophil abundance in the primary tumor and in premetastatic lung was regulated by ECM stiffness but varied between tumor contexts. These preliminary studies pave the way forward for more focused mechanistic studies regarding how the ECM influences neutrophil recruitment and phenotype to alter metastasis.

Results

In order to understand how ECM stiffness may regulate tumor immunity, we used the stromal LOX overexpressing mouse model, MMTV-PyMT; Col1a1-tTA; TetO-mLox, introduced in Chapter 3, which stiffens the tumor ECM by increasing LOX-mediated collagen crosslinking. We used flow cytometry to analyze the immune cell compartment in control and LOX overexpressing tumors, particularly focusing on myeloid cells. We focused on myeloid cells because of their abundance in the tumor stroma, the critical contribution of myeloid cells in orchestrating tumor immunity, and technical limitations on the number of channels we could successfully resolve²⁵³. We observed a modest reduction in TAMs and a significant expansion of the neutrophil population in the stromal LOX overexpressing tumors to near double that of control mice (**Figure 5.1 A**). The total abundance of CD45⁺ cells and the relative abundance of dendritic cells (DCs) and monocytes

remained about the same. Because the Col1a1 promoter used is expressed in osteoblasts and osteocytes, we profiled circulating immune cell populations in PyMT negative mice to confirm that LOX overexpression did not cause altered bone marrow hematopoiesis (Peng et al Endocrinology 2008). Indeed, all major circulating immune cell populations remained nearly identical between wildtype FVB, TetO-mLOX, and Col1a1-tTA; TetO-mLOX mice (**Figure 5.1 B**).

Neutrophils have been widely reported to play a prometastatic role in breast tumor progression in the PyMT model^{236,241}. Therefore, we focused on characterizing these neutrophils, understanding how LOX regulated their abundance, and how they affected tumor metastasis. We sought to establish whether the increase in neutrophils occurred exclusively in the primary tumor or whether neutrophil numbers were elevated systemically. We profiled neutrophils in lungs and in blood of control and stromal LOX overexpressing tumor bearing mice. The number of neutrophils remained unchanged in the lungs of control and LOX overexpressing mice, while the neutrophil population appeared slightly larger in blood of LOX overexpressing animals (**Figure 5.1 C,D**). Given that the population of neutrophils nearly doubled in the tumors of LOX overexpressing mice, it is unlikely that this modest increase in circulating neutrophils is the primary driver of the increase within the tumor.

We next looked to determine how stiffness might regulate the size of the neutrophil population in the primary tumor. Neutrophils could accumulate via one or a combination of three possible mechanisms: increased production and release from bone marrow, increased chemotaxis, or increased survival in the tumor bed. Upon activation and recruitment to peripheral tissues, neutrophils are thought to die there and be phagocytosed by macrophages²³⁵. However, recent evidence suggests that neutrophils recruited to the site of sterile injury may reverse migrate back into circulation²⁵⁴. The fate of tumor associated neutrophils is unknown and it could also be possible that that the rate of reverse migration from the tumor back into circulation may influence neutrophil.

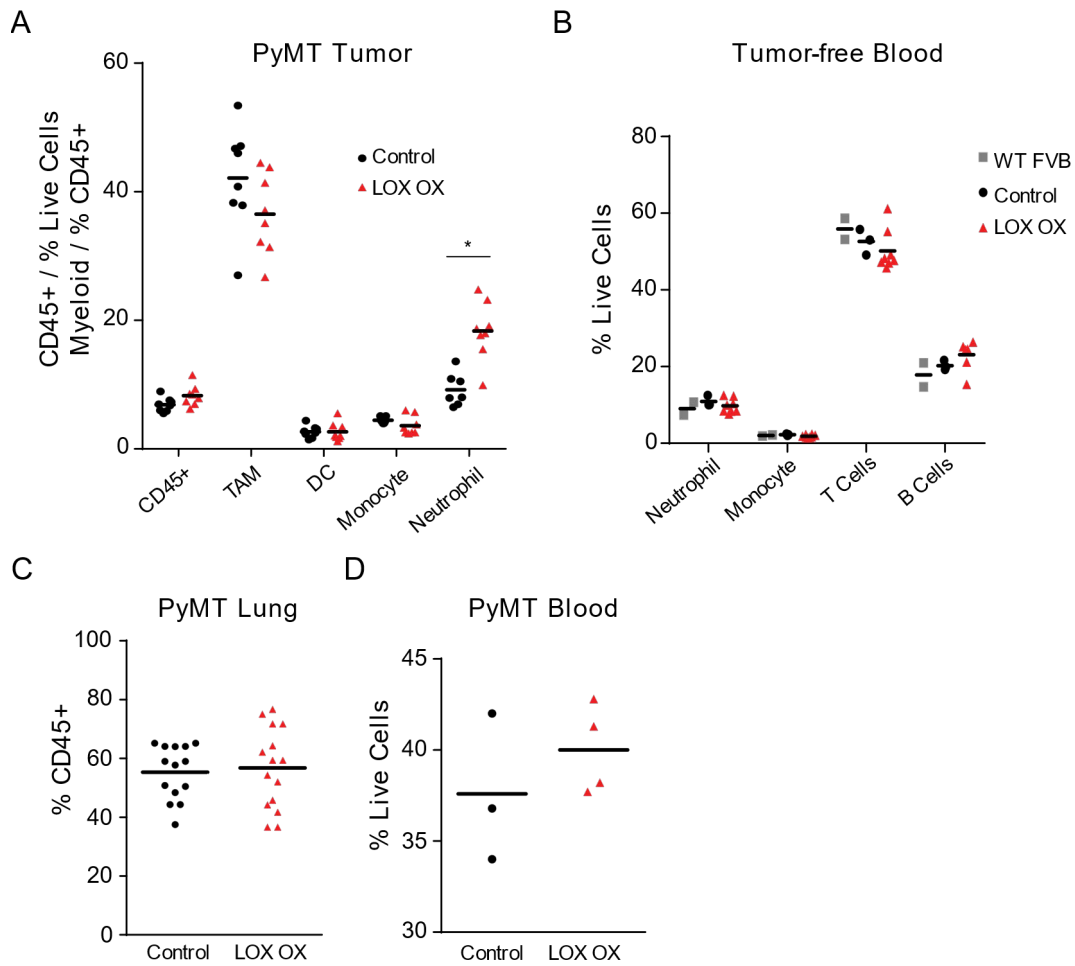


Figure 5.1: Stromal LOX overexpression causes neutrophil accumulation in tumors. (A) Scatter plot showing mean and individual values of immune cell abundance by flow cytometry from primary tumor. CD45⁺ population is plotted as percentage of live cells and remaining populations are plotted as percentage of CD45⁺ cells. **(B)** Scatter plot showing mean and individual values of abundance of immune cell populations circulating in peripheral blood of non-tumor bearing mice plotted as a percentage of live cells. **(C)** Scatter plot showing mean and individual values of neutrophil abundance by flow cytometry from lungs of tumor-bearing mice plotted as percentage of CD45⁺ cells. **(D)** Scatter plot showing mean and individual values of neutrophil abundance by flow cytometry from peripheral blood of tumor-bearing mice plotted as percentage of live cells. Statistical analysis was performed using Mann-Whitney U-test *p < 0.05.

Both chemotaxis and neutrophil production are regulated by cytokines. We analyzed the cytokines produced from PyMT tumor cells on 400 Pa and 60 kPa polyacrylamide gels using a cytokine array and found that three cytokines related to neutrophil production or chemotaxis were upregulated in cells cultured on a stiffer substrate (**Figure 5.2 A**). G-CSF is the primary cytokine that triggers neutrophil production in the bone marrow. IL-23 stimulates $\gamma\delta$ T cells to produce IL-17, which leads to increased G-CSF production by bone marrow stromal cells, ultimately increasing neutrophil production²³⁸. CXCL5 binds the chemokine receptor CXCR2 and can recruit neutrophils into tissues. Interestingly, CXCL5 is a YAP target, and high YAP activity in prostate cancer has been shown to induce CXCL5 expression to recruit polymorphonuclear MDSCs to the tumor²⁴⁴. This would be consistent with CXCL5 being regulated by stiffness. However, when we profiled cytokine levels in the PyMT control and stromal LOX overexpressing tumors, we did not detect significant changes in any of these three cytokines (**Figure 5.2 B,F**). Levels of G-CSF increased slightly in LOX overexpressing tumors, but the trend did not approach statistical significance (**Figure 5.2 B**). Notably, IL23 was not measured in these tumors, but given the modest change in G-CSF and its role in promoting G-CSF expression, it seems unlikely to be playing a major role in neutrophil production in the LOX overexpression model. We detected a trend toward increased levels of GM-CSF in LOX overexpressing tumors, which can stimulate production of both granulocytes and monocytes (**Figure 5.2 C**). GM-CSF also promotes neutrophil recruitment, degranulation, cytotoxicity, and survival²⁵⁵. The three canonical chemokines that signal through CXCR2 to recruit neutrophils into tissue in mice, CXCL1, CXCL2, and CXCL5, all showed no change or a slight decrease in abundance in LOX overexpressing tumors (**Figure 5.2 D-F**). CCL3, which can recruit neutrophils, was higher in LOX overexpressing tumors, but the difference did not achieve statistical significance (**Figure 5.2 G**). Taken together, these data suggest that both enhanced neutrophil production and increased neutrophil recruitment may contribute to the increase in neutrophils within the primary tumor. However, given

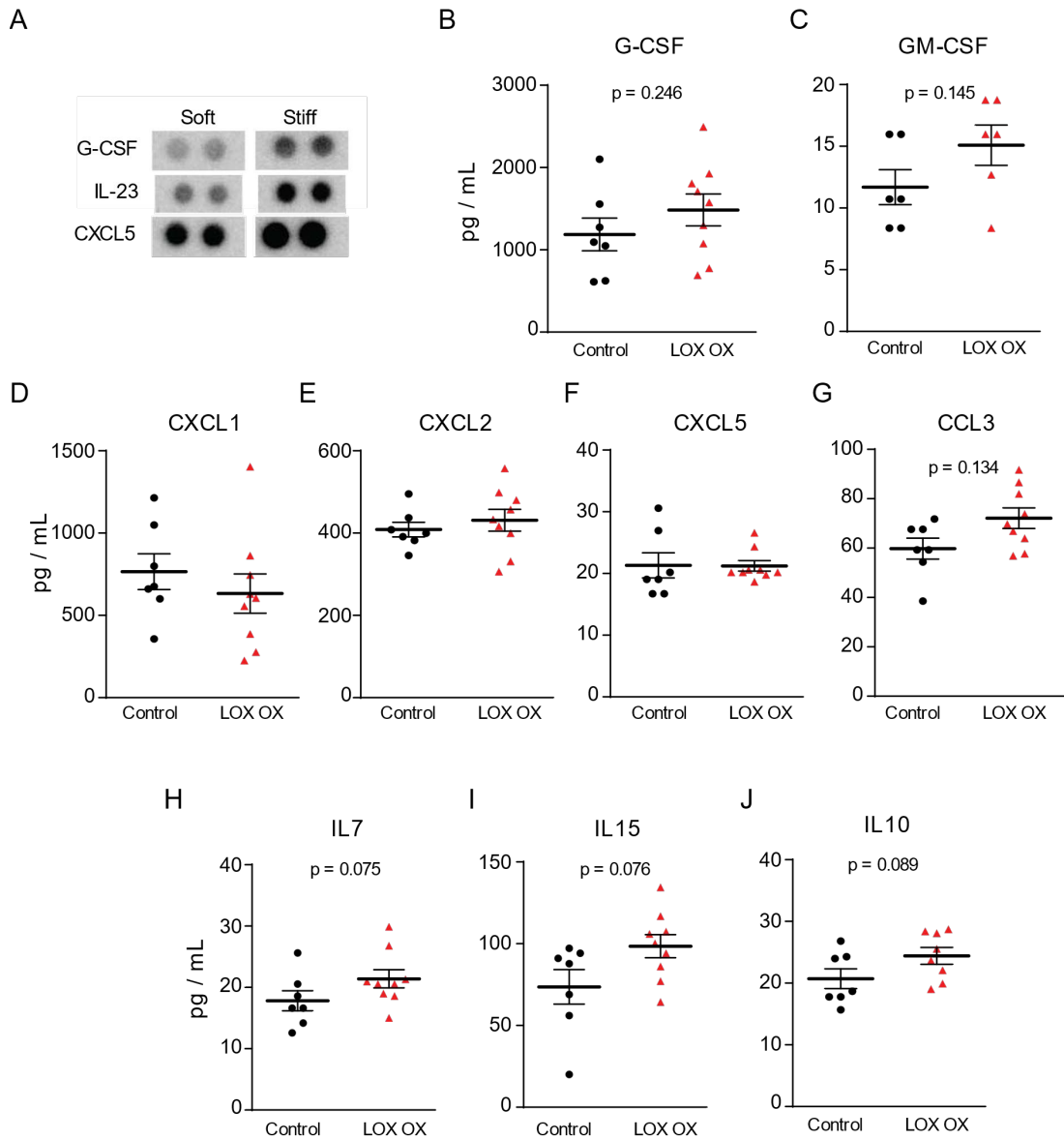


Figure 5.2: Stromal LOX overexpression modulates some cytokines related to neutrophil production and chemotaxis. (A) Protein blots from cytokine array of cell culture media from PyMT tumor cells cultured on 400 Pa (soft) and 60 kPa (stiff) fibronectin coated polyacrylamide gels. **(B-J)** Scatter plots showing mean \pm SEM and individual values of cytokine levels from whole tumor lysates ($n = 7$ Control, $n = 9$ LOX OX). Statistical analyses were performed using Mann-Whitney U-test.

the modest differences and lack of statistical significance, it is difficult to draw a confident conclusion from these data regarding the magnitude of the contributions of each.

In addition to understanding what might be regulating neutrophils, cytokine levels also provide information about the general status of the immune microenvironment within the tumor. Three of the most significantly altered cytokines were IL7, IL15, and IL10 with all three higher in the LOX overexpressing mice (**Figure 5.2 H-J**). IL7 enhances production and proliferation of lymphocytes, and IL15 promotes the formation of CD8⁺ memory T cells. Both have been linked to an anti-tumor T cell response and are clinically relevant cytokines with potential to enhance the anti-tumor immune response^{256–259}. Interestingly, IL10 is an anti-inflammatory cytokine that generally acts to suppress the anti-tumor immune response. However, IL10 can elicit several pleiotropic effects and has been shown to stimulate anti-tumor immunity in some tumor contexts^{260–264}. Taken together, these cytokines would indicate LOX overexpressing tumors may support a more robust anti-tumor T cell response compared to control tumors.

We also investigated whether neutrophils were retained longer in LOX overexpressing tumors. Mouse bone marrow progenitors proliferate rapidly to generate approximately 10⁷ neutrophils per day, but once released into circulation, neutrophils cease to proliferate. We labelled proliferating stem and progenitors using 3 i.p. BrdU injections 72, 48, and 24 hours prior to sacrificing mice^{265–267}. We then used flow cytometry to analyze the fraction of BrdU positive neutrophils in the primary tumor, lung, and blood. Neutrophils older than 72 hours will remain BrdU negative, while most neutrophils younger than 72 hours should be BrdU positive. We observed a slight increase in BrdU positive neutrophils in both lung and blood of LOX overexpressing mice (**Figure 5.3 B-C**). This is consistent with a slight increase in neutrophil production in LOX overexpressing mice. However, the primary tumors of LOX overexpressing mice showed a considerably lower percentage of BrdU positive neutrophils compared to control tumors (**Figure 5.3 A**). This suggests that the neutrophils found within LOX overexpressing

tumors are older and survive longer than neutrophils populating control tumors; although more mice should be analyzed to confirm these findings. Also of note, the percentage of BrdU positive neutrophils in blood much lower than expected in both conditions²⁶⁶. This could be due to strain-specific or tumor-specific differences in the kinetics of neutrophil production, incomplete BrdU labelling, or poor permeabilization and anti-BrdU accessibility in these samples. Circulating neutrophils in tumor bearing mice often display an immature morphology suggesting that they are released from bone marrow prior to full maturation, which would alter production and release kinetics. Therefore, it is possible that some circulating BrdU negative neutrophils could have been released from the bone marrow following the last BrdU pulse.

Interestingly, aged neutrophils have been reported to highly reactive to inflammatory stimuli and more phagocytic than non-aged neutrophils²⁶⁸. It is still unclear whether neutrophils from LOX overexpressing tumors are phenotypically distinct from those within control tumors. In order to gain some insight into whether these neutrophils were pro- or anti-tumor and into the influence of stromal LOX overexpression, we measured the abundance of circulating tumor cells and the number of metastatic foci in the lungs. Both the levels of circulating tumor cells and metastatic foci were the same between the two groups (**Figure 5.3 D-E**). This contradicts data from the Weaver lab in which tumor-bearing mice treated systemically with LOX inhibitor β -aminopropionitrile (BAPN) had significantly reduced levels of circulating tumor cells and lung metastasis (data not shown). The reasons for this discrepancy are unclear. It is tempting to speculate that the effects of a more robust anti-tumor immune response in the LOX overexpressing mice competes with prometastatic collagen crosslinking negate each other, but there is not enough evidence to draw such a conclusion.

To overcome some technical limitations with the Col1a1 LOX overexpression mouse model, we generated a new stromal LOX overexpressing tumor model: MMTV-PyMT; Pdgfrb-

rtTA; TetO-mLox. This is a Tet on model that overexpresses Lox in cells that express Pdgfrb including fibroblasts, mural cells, adipocytes, and some neurons of the brain. We expected this promoter to be more robustly expressed than the Col1a1 promoter with the caveat of being expressed by stromal cells other than fibroblasts in the tumor microenvironment and in the metastatic site. After backcrossing to achieve a $\geq 99\%$ FVB background, we profiled the immune cell populations within primary tumors and lungs. Unexpectedly, we have not observed an increase in neutrophils within the primary tumor, although not enough tumors have yet been profiled (**Figure 5.4 A**). In contrast, lungs of LOX overexpressing mice contain higher abundance of neutrophils relative to control mice (**Figure 5.4 B**). LOX overexpressing mice also have a higher prevalence of metastatic foci in the lungs (**Figure 5.4 C**). Surprisingly, pilot experiments performed in mixed background mice while backcrossing from the C57BL6/J to FVB yielded the opposite trend in metastasis with LOX overexpressing mice containing fewer metastatic foci than control mice (**Figure 5.4 D**). The two pilot studies displayed are from the first backcross (F1, 50% C57BL6/J, gray/blue) and the second backcross (N2, 25% C57BL6/J, black/red). Notably, the F1 cohort, although small, had an extraordinarily large difference in metastasis. While it is admittedly difficult to interpret mixed background studies, these data would suggest that LOX overexpression on the C57BL6/J background is anti-metastatic while LOX overexpression on the FVB background is pro-metastatic.

To better understand the role of stiffness in regulating immunity and conditioning of the premetastatic niche, we used two patient derived xenograft (PDX) models with higher and lower metastatic capacity: HCI-001 and HCI-002, respectively. We orthotopically implanted these tumors in NOD-SCID mice in soft or ribose-crosslinked stiffened collagen. Flow cytometry analysis revealed no differences in the size of immune cell populations in the lung in mice bearing HCI-001 tumors (**Figure 5.5 A**). However, in contrast with the LOX overexpressing models, mice

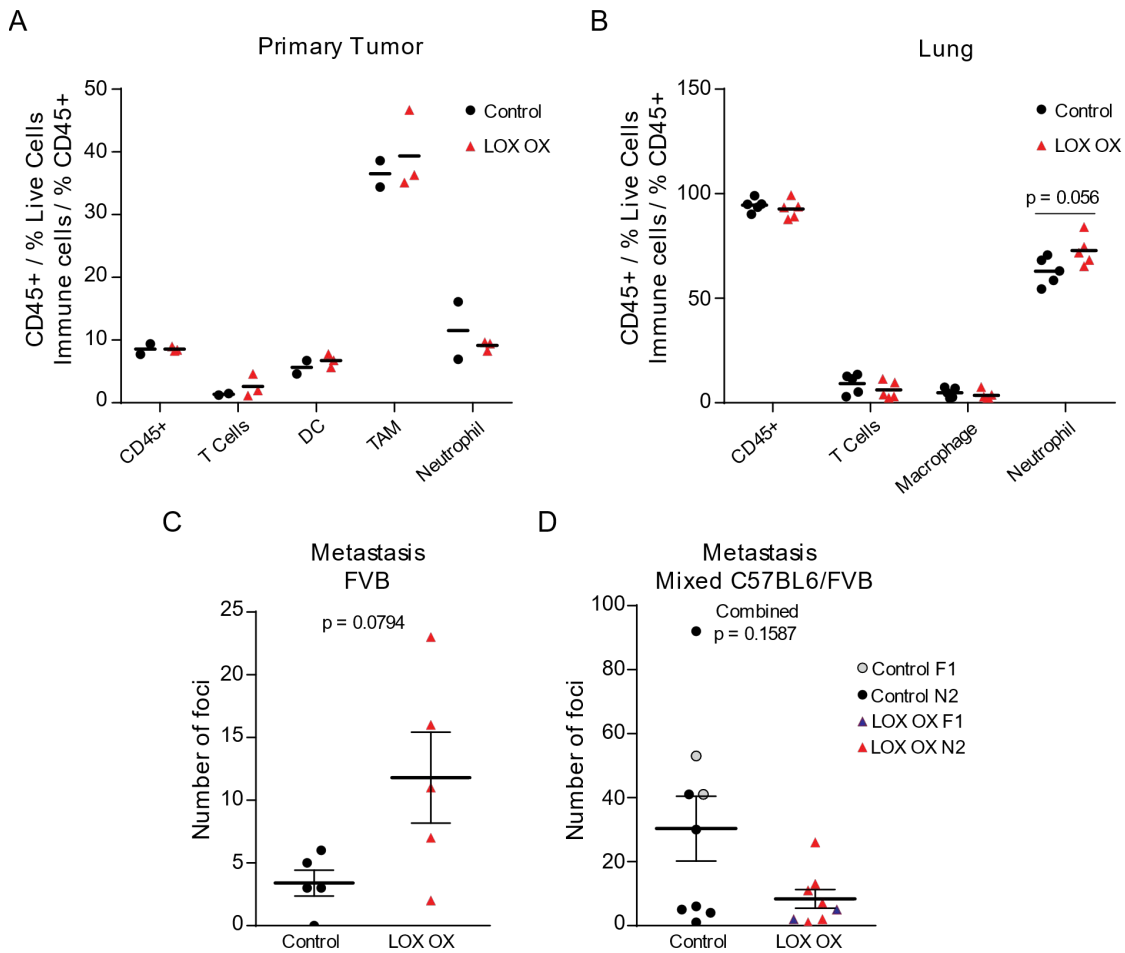


Figure 5.4: Stromal LOX overexpression using the Pdgfrb promoter increases lung neutrophil abundance and modulates metastasis. (A) Scatter plot showing mean and individual values of immune cell abundance by flow cytometry from primary tumor in control and LOX overexpressing tumors (Pdgfrb-rtTA promoter). CD45⁺ population is plotted as percentage of live cells and remaining populations are plotted as percentage of CD45⁺ cells. (B) Scatter plot showing mean and individual values of immune cell abundance by flow cytometry from lung in control and LOX overexpressing tumors (Pdgfrb-rtTA promoter). CD45⁺ population is plotted as percentage of live cells and remaining populations are plotted as percentage of CD45⁺ cells. (C) Scatter plot showing mean \pm SEM and individual values of number of metastatic foci in control and LOX overexpressing lungs from the FVB/N strain. (D) Scatter plot showing mean \pm SEM and individual values of number of metastatic foci in control and LOX overexpressing lungs from mixed background C57BL6/J:FVB/N mice. F1 generation (gray/blue) is pure C57BL6/J crossed with pure FVB/N and N2 generation (black/red) is F1 crossed with FVB/N.

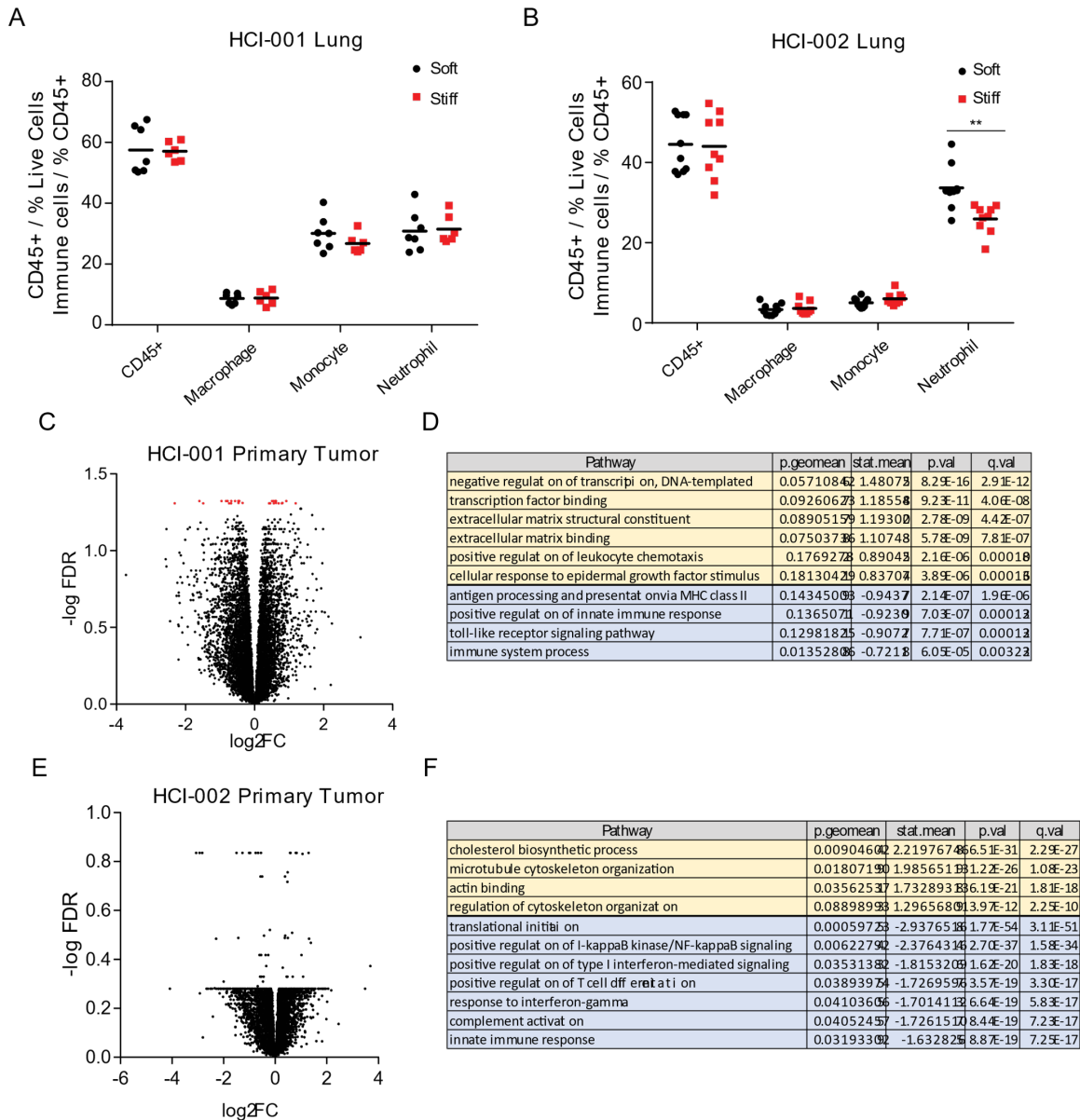


Figure 5.5: PDXs with soft ECM have more lung neutrophils and increased proinflammatory signaling. (A) Scatter plot showing mean and individual values of immune cell abundance by flow cytometry from lung in soft and stiff HCI-001 tumors. CD45⁺ population is plotted as percentage of live cells and remaining populations are plotted as percentage of CD45⁺ cells. (B) Scatter plot showing mean and individual values of immune cell abundance by flow cytometry from lung in soft and stiff HCI-002 tumors. CD45⁺ population is plotted as percentage of live cells and remaining populations are plotted as percentage of CD45⁺ cells. (C) Volcano plot showing differentially regulated genes between soft and stiff HCI-001 tumors. Significantly altered genes are colored in red. (D) Differentially regulated gene ontology pathways from primary tumor RNA-seq in soft and stiff HCI-001 tumors. Pathways upregulated in stiff are colored in orange and those upregulated in soft are colored in blue. (E) Volcano plot showing differentially regulated genes between soft and stiff HCI-002 tumors. (F) Differentially regulated gene ontology pathways

from primary tumor RNA-seq in soft and stiff HCI-002 tumors. Pathways upregulated in stiff are colored in orange and those upregulated in soft are colored in blue.

injected with the less metastatic HCI-002 tumors in soft collagen had a significant increase in the number of neutrophils in lungs (**Figure 5.5 B**). It is still unclear whether these neutrophils are phenotypically distinct and whether this difference in neutrophils has any influence on metastasis. The neutrophils were sorted out of the lungs from each condition in both PDX models and will be analyzed by RNA-seq to assess any potential phenotypic differences. Immune cell profiling was limited to major myeloid populations because these mice lack lymphocytes and NK cells.

Whole tumor mRNA of soft and stiff tumors from HCI-001 and HCI-002 was analyzed using RNA-seq to uncover any differential regulation of stiffness on tumor phenotype or immune regulation at the primary tumor. Only 29 genes were found to be differentially regulated (FDR < 0.05) between soft and stiff in HCI-001 tumors, and zero differentially regulated genes met the FDR threshold for significance between soft and stiff in HCI-001 (**Figure 5.5 C,E**). However, gene ontology analysis of these RNA-seq data suggest that in both PDXs, cytoskeletal and ECM binding pathways are upregulated in the stiff condition (**Figure 5.5 D,F**, orange). Interestingly, the soft conditions in both PDXs upregulate pathways associate with immune and inflammatory processes such as antigen processing, toll-like receptor signaling, response to interferon gamma, and innate immune response (**Figure 5.5 D,F blue**). These data would suggest that the soft tumors elicit a more proinflammatory immune response and that the increase in lung neutrophils in soft HCI-002 tumors may have a cytotoxic, anti-tumor phenotype. Further studies are necessary to test these hypotheses.

Discussion

These studies demonstrate a potential role for LOX in regulating tumor immunity via neutrophil abundance and phenotypes within primary tumors and metastatic sites. However, these studies are highly exploratory and additional experiments are required to understand unexpected discrepancies between models and to generate data that coalesce to support a mechanistic understanding of LOX-mediated regulation of tumor associated neutrophils.

These studies explored how ECM stiffness may regulate tumor immunity. Profiling of immune cell types in LOX overexpressing PyMT tumors revealed a near twofold increase in neutrophil abundance. Neutrophil count in blood appeared slightly higher and unchanged in lung. Because LOX-mediated crosslinking of collagen stiffens the ECM and promotes metastasis, these data fueled the hypothesis that ECM stiffness may promote metastasis through regulating the neutrophil population in tumors. Interestingly, studies utilizing a similar but stronger stromal LOX overexpressing tumor model show an increase in neutrophils in lung. Many possibilities could explain this observation including that this model causes a more robust systemic increase in neutrophil levels, higher LOX overexpression in the lung directly recruits or activates neutrophils, or increased ECM stiffness modulates levels of tumor secreted factors that promote neutrophil recruitment to the premetastatic site. This model also had higher levels of lung metastasis, which may be attributable to the increase in neutrophil population.

Cytokine analysis within the tumors of LOX overexpressing mice suggest chemotaxis may play a role in the increased abundance of neutrophils but likely is not the main driver. These analyses also did not implicate increased neutrophil production, although we would also need to profile serum cytokines to better assess this. Bone marrow progenitor labelling indicate prolonged survival or retention may account for neutrophil accumulation. This would be consistent with a higher degree of neutrophil activation, which prolongs neutrophil lifespan, or it could be indicative of a population of aged neutrophils reported to support tumor growth and metastasis. Interestingly, the general cytokine profile of LOX overexpressing tumors reflected a robust T cell response with elevated levels of IL7 and IL15. This could indicate that stiffness primes a more robust immune response and would be consistent with a report showing constitutively active YAP enhances T cell response to tumors²⁶⁹. More in depth characterization of lymphocytes in this model is necessary to understand this observation. An enhanced anti-tumor immune response could explain why tumor metastasis does not change with LOX overexpression, when in other models

LOX inhibition drastically reduces metastasis and injecting tumors orthotopically in stiffened collagen increases metastasis.

In a different PyMT model using the *Pdgfrb* promoter to overexpress LOX instead of *Col1a1*, we also observed changes in the neutrophil population. Not enough animals have been profiled to draw conclusions about the primary tumor, but the premetastatic lungs had an increase in neutrophils with LOX overexpression. Interestingly, this model also had an increase in lung metastasis with LOX overexpression, consistent with reports of neutrophils playing a critical role in remodeling the lung to permit metastatic colonization. The source of increased neutrophils in this model is unclear. This phenotype could depend on altered interactions within the primary tumors, or stronger expression of this promoter in the lung could be fueling the rise in neutrophils independent of stiffness of the primary tumor. This could be experimentally tested by conditioning the lungs by inducing LOX overexpression with doxycycline and injecting tumor cells by tail vein to assess metastatic seeding and outgrowth.

Surprisingly, pilot experiments performed in mixed background mice while backcrossing to a pure FVB background indicate that the metastasis phenotype observed in this model is strain specific. The higher the percentage of C57BL6, the more LOX overexpression inhibited metastasis. If these observations hold true on a pure C57BL6 background, it could yield tremendous insight into how tumors respond to LOX and ECM stiffness and how the same perturbation in different contexts can lead to drastically different outcomes. One of the key differences between FVB and C57BL6 mice is how their immune systems react to early transformation events. C57BL6 mice mount a more active and robust antitumor immune response leading to a much longer latency period for MMTV-PyMT tumors. Based on the results from this model, it is plausible that LOX overexpression boosts this response even further to inhibit metastasis, whereas the more subdued FVB tumor immune response is overcome by known prometastatic effects of LOX activity such as increased invasion and intravasation. Alternatively,

the increased latency and thus duration of LOX overexpression in C57BL6 could induce such a high level of crosslinking that tips the balance toward fibrosis that blocks cell invasion and intravasation. Our previous studies demonstrate the importance of using a spontaneous tumor model rather than orthotopic models to study LOX and ECM remodeling, but this observation suggests appropriate model choice may be more complex. Human tumors grow and develop much slower than many commonly used spontaneous tumor models including PyMT, and time could be an important factor governing ECM evolution in tumors. Collagen crosslinking is catalyzed by LOX but then proceeds in a spontaneous fashion that requires time for crosslinks to mature into higher valency products. It will be important for additional studies to clarify whether slower growing tumor models more accurately recapitulate the evolution and biological consequences of LOX activity and tumor fibrosis in human patients.

In contrast, PDX tumors injected orthotopically in soft or stiffened collagen show an increase in inflammatory signaling and neutrophil abundance when injected in soft tumors. Mice with soft HCI-002 tumors had higher numbers of neutrophils in lung and soft HCI-001 upregulated transcripts associated with inflammatory signaling. These data are interesting in that they suggest that LOX may play a role in regulating tumor immunity that is independent of ECM stiffness and that the role of ECM stiffness is clearly context dependent. Xenograft hosts lack T cells, B cells, and NK cells, which may also be essential to the phenotype observed in LOX overexpressing PyMT tumors. ECM stiffness also clearly has a stronger influence on some tumors more than others as HCI-002 had zero differentially expressed transcripts between the soft and stiff conditions, whereas HCI-001 had 29. It is unclear what factors cause some tumors to respond more to ECM stiffness than others.

Neutrophils play a critical role in cultivating the premetastatic niche to permit metastatic colonization. Multiple models used in these studies show ECM stiffness of the primary tumor may modulate neutrophil levels in the lung, where the vast majority of breast tumor metastasis occurs

in mice. Additional studies are needed to explore the possibility that ECM stiffness affects the formation of the premetastatic niche by regulating neutrophils. Neutrophils from the lungs of PDX tumor-bearing mice were sorted and will be analyzed by RNAseq to assess any changes in phenotype between the soft and stiff conditions. Moreover, frozen lung was harvested from all tumor models and could be subjected to proteomic analysis of ECM components as well as matrisome associated proteins. Comprehensive proteomic analysis of the ECM and matrisome associated proteins has never been reported from a spontaneous murine mammary tumor model and will likely yield novel, impactful insights into mechanisms promoting tumor metastasis in addition to understand how the stiffness of the primary tumor may influence this process.

These preliminary results have inspired the generation of several hypotheses regarding ECM regulation of tumor immunity and metastasis that require thoughtful follow up. Further analysis of the interplay between tumor immunity and ECM stiffness may benefit from more extensive use of syngeneic C57NL6 orthotopic tumor models that are less variable than spontaneous models. This approach could incorporate the stromal LOX overexpression to condition the stiffness of the mammary gland prior to tumor cell injection as well as other useful tools such as OT-I ovalbumin restricted T cells and a multitude of genetic manipulations. Understanding how ECM stiffness regulates immune cell populations and phenotypes in tumors may shed light on novel strategies to enhance the efficacy of immunotherapy to improve outcomes of breast cancer patients.

Methods

Mice

MMTV-PyMT; Col1a1-tTA; TetO-mLox mice were generated as previously described (Chapter 4). MMTV-PyMT; Pdgfrb-rtTA; TetO-mLox mice were generated using Pdgfrb-rtTA mice purchased from JAX Laboratories (Stock no. 028570). These mice were backcrossed to FVB

TetO-mLox mice for 5 generations and then screened for strain purity by SNP analysis. Mice with 98% FVB background or higher were backcrossed for 2 more generations and then used for tumor studies.

HCI-001 and HCI-002 were revived in NSG mice from Charles River and passaged into NOD-SCID mice for experimentation. Equal sized tumor pieces were placed in the inguinal mammary gland in 4 mg/mL rat tail collagen I that had previously been incubated with or without 2.5M L-ribose to glycate and stiffen the matrix. The collagen was supplemented with 20 % Matrigel.

All mouse studies were maintained under pathogen-free conditions and performed in accordance with the Institutional Animal Care and Use Committee and the Laboratory Animal Research Center at the University of California, San Francisco.

Flow cytometry

Mice were perfused with ice cold PBS and tissue was harvested and chopped with a razor blade. Chopped tissue was digested in 100 U/mL Collagenase Type 1 (Worthington Biochemical Corporation, Cat# LS004196), 500 U/mL Collagenase Type 4 (Worthington Biochemical Corporation, Cat# LS004188), and 200 µg/mL DNase I (Roche, Cat# 10104159001) while shaking at 37°C. Digested tissue was filtered using a 100 µm filter to remove remaining pieces. Red blood cells were lysed in ammonium-chloride-potassium buffer and remaining cells were counted. Cells were stained with fluorophore-conjugated primary antibodies for 30 minutes on ice and subsequently stained with a viability marker. Antibodies used for staining were anti-mouse CD45-APC-R700 (BD, Cat# 565478), anti-mouse Ly6G-BV421 (BioLegend, Cat# 127628), anti-mouse F4/80-BV510 (BioLegend, Cat# 123135), anti-mouse CD140a-PE (BioLegend, Cat# 135906), anti-mouse CD140b-APC (BioLegend, Cat# 136006), anti-mouse CD11c-BV605 (BD Pharmingen, Cat# 563057), anti-mouse CD24-BV650 (BD Pharmingen, Cat# 563545), anti-

mouse CD11b-PerCP-Cy5.5 (eBiosciences, Cat# 45-0112-82), anti-mouse CD45-AF700 (BioLegend, Cat# 103128), anti-mouse Ly6C-BV711 (BioLegend, Cat# 128037), anti-mouse MHCII-PE-Cy7 (BioLegend, Cat# 107630), anti-mouse CD3 ϵ -BV605 (BioLegend, Cat# 100351), anti-mouse CD4-PE/Cy7 (BioLegend, Cat# 116015), anti-mouse CD8a-BV711 (BioLegend, Cat# 100747), and Zombie NIR Fixable Viability Dye (BioLegend, Cat# 423105). Cells were then analyzed on a flow cytometer.

BrdU assay

Mice were injected i.p. with 100 μ L BrdU (10 mg/mL) 72 h, 48 h, and 24 h prior to tissue collection. A subset of cells stained for flow cytometry analysis were stained for BrdU using the BD FITC BrdU Flow Kit (BD Pharmingen #559619) according to the manufacturer's instructions.

Cytokine analysis

A PyMT-derived tumor cell line was seeded on 400 Pa or 6 kPa polyacrylamide gels coated with 10 μ g/mL fibronectin. Equal numbers of cells were seeded on gels and cultured for 48 hours and conditioned media was analyzed with the Proteome Profiler Mouse XL Cytokine Array (R&D Systems #ARY028). Cells cultured on the cells were trypsinized and counted. Conditioned media from cells on stiff gels was diluted with PBS by the factor in which cells on the stiff gel outnumbered cells on the soft gel at the study endpoint to control for differences in cell proliferation.

Whole tumor tissues were homogenized in RIPA buffer containing protease inhibitor. Homogenates were centrifuged at 10,000 xg for 10 minutes at 4 degrees and the supernatant was collected. BCA assay was used to quantify protein and equalize protein concentration in each sample. Samples were sent to Eve Technologies for cytokine analysis.

Cell culture

PyMT cells (Flox3) were obtained from the Hal Moses laboratory at Vanderbilt University and grown in DMEM/F12 medium supplemented with 10% FBS and antibiotic/antimycotic.

Circulating tumor cell analysis

PyMT mRNA is used as a measurement for circulating tumor cells in blood. Whole blood was collected in RNALater and stored at -80C until further processing. Blood was processed using Mouse RiboPure Blood RNA Isolation Kit (Invitrogen #AM1951) according to manufacturer's instructions. Genomic DNA was digested with DNase (Invitrogen #AM2238). RNA quality was verified using NanoDrop, reversed transcribed, and analyzed for PyMT transcripts by quantitative real-time PCR. PyMT expression was normalized to 18s in each sample.

Metastasis Analysis

Lungs were inflated with 10% formalin and fixed for 24 hours. Tissues were processed, paraffin embedded, and sections. Four sections 50 µm apart were stained with hematoxylin and eosin to visualize metastatic foci. All foci were summed and plotted as number of metastatic foci per mouse.

RNASeq

mRNA from Trizol preps was sent to the UC Berkeley – QB3 Genomics core. The core prepared libraries and sequences the samples on a NovaSeq 6000. Data were analyzed in R and pathway analysis was performed using the GAGE package.

Statistical analysis

GraphPad Prism Version 6.01 was used to perform all statistical analyses with the exception of LH2 IHC and RFS correlations with PLOD2. Statistical significance was determined using the appropriate tests as noted in the figure legends or method section.

Chapter 6: Conclusions and Future Directions

This thesis advances our understanding of ECM signaling in breast tumor progression, therapy response, and metastasis. It builds upon the prior work of many groups that implicates chemical and mechanical ECM cues in regulating breast tumor biology by enhancing tumor cell proliferation, survival, invasion, and escape from dormancy as well as by tuning tumor cell metabolism and inflammatory cell phenotypes^{23,25,76}. Thus, tumor-ECM interactions have grown to be broadly appreciated as a key factor orchestrating events in the tumor microenvironment. While many studies demonstrate integrins are critical mechanosensors of ECM stiffness and their interactions with remodeled tumor ECM drive a malignant phenotype, they are by no means the only receptors transducing signals from the ECM. Moreover, many of the far-reaching effects of ECM signaling remain underexplored and poorly understood. In light of these shortcomings, this thesis specifically addressed the following unanswered questions:

1. How does the loss of DDR1 signaling in luminal epithelial cells affect mammary gland homeostasis and the emergent breast tumor phenotype?
2. What regulates LOX-mediated collagen crosslinking breast tumor initiation and progression, and how does it correlate with tumor phenotype and patient outcome?
3. How does ECM stiffness influence therapy response of triple negative breast cancers and can targeting molecular mechanisms associated with prosurvival ECM signaling enhance therapeutic efficacy?
4. Does ECM stiffness regulate breast tumor metastasis through coordinating neutrophil phenotypes and abundance in the primary tumor and/or premetastatic niche?

This thesis addressed each of these questions through four independent research projects to test the overarching hypothesis that evolving chemical and mechanical ECM cues control breast tumor phenotype and regulate metastasis. The results of these studies yielded novel insights into mechanisms of cell-ECM interactions that govern tumor initiation, metastasis, and therapy response and expanded our mechanistic understanding of ECM remodeling over the

course of breast tumor progression. Each of these projects has also opened exciting avenues of future follow up work to uncover further mechanistic details of pro-metastatic ECM remodeling and signaling and to validate the efficacy of potential therapeutic strategies and targets designed to antagonize pro-tumor ECM signaling. The conclusions and future directions of each project are summarized in the following sections.

Loss of DDR1 biases mammary epithelial homeostasis and fosters a basal-like tumor phenotype

Previous studies of DDR1 in tumor development have produced seemingly conflicting results regarding whether DDR1 serves to promote or restrain tumor progression. DDR1 is overexpressed in many tumors and cell lines but low expression is correlated with worse relapse-free survival^{45,57,60}. We confirmed that DDR1 signaling occurs exclusively in luminal epithelial cells and that its loss compromises cell adhesion and disrupts ductal morphogenesis resulting in an expansion of basal/myoepithelial cells. Similarly, DDR1^{-/-} tumors also present with a more basal-like phenotype with a higher abundance of vimentin, K14, and DDR2 expressing cells. These tumors also exhibit traits characteristic of basal-like tumors including faster growth, increased fibrosis, and more lung metastases. Moreover, DDR1^{-/-} are enriched for K8⁺ K14⁺ progenitor cells and CD90⁺ CD24⁺ cells known to be enriched for tumor initiating cells. When injected into wildtype mammary glands, CD90⁺ CD24⁺ tumor initiating cells formed tumors that recapitulated the basal-like phenotype of DDR1^{-/-} tumors and contained higher levels of K14⁺ basal/myoepithelial cells. These data suggest that while DDR1 signaling may independently promote cell proliferation, its loss fundamentally alters the mammary epithelial cell population to favor the basal/myoepithelial lineage resulting in highly aggressive and metastatic tumors.

These results have implications both for understanding the role of DDR1 in mammary gland biology. The precise molecular mechanism leading to basal/myoepithelial expansion remains unclear. Loss of DDR1 compromises adhesion in luminal cells, so it is possible that the

loss of adhesion could impair migration or proliferation thus imparting basal/myoepithelial cells with a competitive advantage. In this case basal/myoepithelial cells would grow out to compensate for the crippled luminal cells. However, it is also possible that DDR1 plays a direct role in luminal cell differentiation and maintenance of the luminal cell phenotype. It would be interesting to observe whether basal/myoepithelial cells also expand in an inducible DDR1 knockout model in which the knockout doesn't occur until after puberty when the mammary ductal network has been established.

These data also have implications for understanding the role of DDR1 in breast cancer. Given that basal tumor cell lines have significantly lower levels of DDR1 and the loss of DDR1 in mice leads to an aggressive, basal-like tumor phenotype, DDR1 may play a role in thwarting the development of aggressive tumors. Further elucidation of this molecular mechanism may yield promising targets for the treatment of basal-like breast cancers. It's unclear whether the altered phenotype of DDR1^{-/-} tumors results directly from the increased number of basal/myoepithelial cells present at tumor initiation that then shape the behavior of the tumor or whether the cell type of origin in DDR1^{-/-} tumors is more often a basal/myoepithelial cell. Furthermore, because loss of DDR1 compromises adhesion and migration, it is likely that extrinsic effects of the loss of DDR1 on cell-cell communication within the tumor microenvironment play a major role in facilitating tumor metastasis. DDR1^{-/-} tumors are much more fibrotic than their wildtype counterparts indicating that signaling to fibroblasts is likely different in this context. Consistently DDR1^{-/-} tumors are more hypoxic and necrotic, which likely serve to enhance metastasis. Understanding these cell-cell interactions in more depth may also yield important insights and actionable targets for tumor therapeutics.

Collagen crosslinking in breast tumors is primarily regulated by macrophage-stimulated fibroblasts and predicts poor survival

The Weaver lab and others have demonstrated that collagen deposition and stiffening accompany malignancy, compromise treatment and promote tumor aggression. This study sought to clarify the molecular nature of the tumor-associated collagen matrix and the factors that regulate remodeling. Using an optimized, analytical method to profile lysyl oxidase-mediated LCCs and HLCCs. We quantified the greatest number of collagen crosslinks in biopsies of the more aggressive HER2+ and triple negative human breast cancer subtypes with the stiffest stroma. Using publicly available gene expression data, we confirmed that triple negative and HER2+ subtypes also have higher expression of LOX and PLOD2, which may explain their elevated levels of collagen crosslinks. When gene expression from tumor epithelium and tumor stroma are analyzed separately, we found the tumor stroma expressed much higher levels of both LOX and PLOD2.

LOX is produced by both tumor cells and stromal cells, but the relative contribution of each to collagen crosslinking is unknown. To address this knowledge gap, we generated two mouse models to directly assess the degree of crosslinking occurring with conditional LOX overexpression in either the epithelial or stromal compartments. Surprisingly, while we measured a significant increase in crosslink abundance with stromal LOX overexpression, we were unable to detect changes in crosslink abundance with epithelial LOX overexpression. These data indicate that despite synthesizing LOX, tumor cells contribute very little toward collagen crosslinking, particularly in the early stages of tumor development. Instead, we identify macrophages as key activators of fibroblasts in neoplastic lesions that initiate collagen crosslinking. Consistently, we found macrophage depletion was associated with low stromal levels of LOX and PLOD2 expression. Macrophage depletion also reduced collagen crosslinking, stromal stiffening, and tumor metastasis. We found high levels of stromal PLOD2 correlated with poor survival.

Immunohistochemical analysis of a large cohort of breast cancer patient biopsies confirmed that stromal LH2, the enzyme that enables high valency collagen crosslinks, correlated significantly with poor patient outcome and disease specific mortality. The findings provide a compelling link between tissue inflammation, stromal cell-mediated collagen crosslinking and stiffening and tumor aggression.

These results clearly and directly demonstrate that epithelial derived LOX does not contribute significantly to collagen crosslinking in breast tumors, and understanding the mechanism behind the failure of epithelial-derived LOX to crosslink collagen is an essential unanswered question. Many potential causes could explain this lack of observed catalytic activity by epithelial-derived LOX, and more studies are needed to fully understand the biological basis of this finding. One possibility is that epithelial cells fail to produce an enzyme with the necessary posttranslational modifications for catalytic activity. LOX enzymatic activity requires a copper cofactor, a lysine tyrosylquinone cofactor formed through a self-processing, intramolecular reaction, and protease cleavage of the LOX propeptide. However, another group has shown that LOXL2 overexpressing mammary tumor cells injected orthotopically into mice do alter ECM organization, so it is likely that epithelial cells are competent to produce a catalytically active enzyme¹⁴⁹. Yet it remains possible that in spontaneous tumor formation, LOX secreted from tumor cells does not encounter sufficient levels of BMP1 to efficiently cleave the propeptide. Similarly, it is also possible that epithelial LOX is retained within epithelial clusters and relatively little enzyme reaches the collagen-rich stroma. This could be particularly true for the PyMT model, which forms characteristic epithelial-dense tumor cell clusters. Many human tumors appear much more diffuse, and it is possible that LOX secreted from these cells may prove more active than we have observed. Future work should carefully characterize the catalytic activity of epithelial-derived versus stromal-derived LOX and identify if spatial localization plays a role in the failure of epithelial LOX-mediated crosslinking. If so, it will be important to validate this finding tumor models with

varying histologies to verify whether this phenomenon is universal among breast tumors or morphology-specific.

These studies also open broader questions relevant to understanding basic LOX biology in homeostasis and disease. Breast tumor epithelium produce abundant levels of LOX protein, especially in hypoxic environments, but if epithelial-derived LOX does not function efficiently for crosslinking, then what does it do? Recent works are discovering that multiple enzymes, particularly metabolic enzymes, have unexpected noncanonical activities that are independent of their primary functions^{270,271}. LOX has been implicated in regulating transcription mediated by both the cleaved propeptide and by enzymatic histone modification^{272,273}. Amazingly, nuclear LOX lacks its propeptide suggesting it is released into the extracellular space where it is cleaved by BMP, then endocytosed and transported into the nucleus. If this is the case, then administration of BAPN, a commonly used irreversible LOX family inhibitor, would be preventing this epigenetic function of LOX in addition to suppressing collagen crosslinking. This phenomenon should be studied more in depth and may yield insights that enable more accurate reinterpretation of seminal experiments in the LOX field.

We also identified stromal LH2 as a potential biomarker that could be useful to stratify patients for therapy. Particularly in lymph node positive patients, which are likely to be more metastatic, stromal LH2 levels correlated with significantly worse breast cancer specific survival. When speculating around tumor aggression to make treatment decisions, most of the information used comes from analysis of the tumor cells themselves. However, our findings and previous reports demonstrate that the stroma may also be an important consideration in these decisions and could help improve treatment decisions¹⁴⁸. This result also suggests a potentially important implication for understanding the role of ECM remodeling in breast tumor aggression. Most studies of tumor-associated collagen remodeling focus on the LOX family of enzymes that act immediately prior to crosslink formation, yet our data indicate stromal LH2 may be a much more

powerful predictor of poor outcomes than epithelial or stromal LOX. This implies that the type or profile of collagen crosslinks formed may be equally if not more important than the total abundance of crosslinks. Future work should further characterize the role of different LOX-mediated collagen crosslinks on ECM material properties and tumor phenotype.

Furthermore, these studies have significant implications for the development of ECM normalization strategies for breast tumor therapy. Despite much excitement and promise, strategies designed to normalize fibrotic tumor-associated ECM have largely failed. The LOXL2 antibody simtuzumab failed to add clinical benefit in phase II pancreatic cancer trials. It is difficult to understand exactly why this drug failed with publicly available data. Our data indicate that crosslinking is initiated very early on in tumor progression, and inhibiting further crosslinking does not act to reverse the crosslinks already formed. Thus, if LOX or LOXL2 inhibitors are administered following extensive crosslinking, they will have little effect on stromal stiffness. Our data would suggest inhibition of crosslinking enzymes is not a viable strategy for ECM normalization. It would likely be more effective to target profibrotic fibroblasts and disrupt signaling that upregulates collagen production and crosslinking enzymes, including lysyl hydroxylases.

ECM compliance drives treatment resistance in triple negative breast cancer by regulating the NF- κ B-JNK signaling axis

Triple negative breast cancers are highly fibrotic and have much higher rates of chemotherapy response than hormone receptor positive tumors. In this study we characterized the ECM of chemotherapy treated breast tumors and assessed the role of ECM stiffness in regulating tumor cell response to apoptosis-inducing tumor therapeutics. We found that following neoadjuvant chemotherapy, treatment resistant triple negative breast cancers have a high degree of fibrillar collagen deposition but are surrounded by softer ECM compared to that of untreated primary tumors. 3D organoid cultures and xenograft studies further demonstrated that a soft ECM protects tumor cells from undergoing apoptosis in response to commonly used therapeutics

paclitaxel and radiation. We found this phenotype was not caused by proliferation rate but rather cells cultured on soft substrates resisted treatment by elevating pro-survival NF- κ B activity that silenced pro-apoptotic JNK activity. We observed elevated JNK activity in cells cultured on stiff substrates and activating JNK in cells grown on soft substrates was sufficient to induce apoptosis upon paclitaxel or radiation treatment. Critically, treatment resistant residual human TNBCs residing within soft stroma had elevated NF- κ B levels, and disengaging NF- κ B activity sensitized tumors in a soft matrix to therapy. Accordingly, the biophysical properties of the ECM modify treatment response, and ancillary agents that modulate stiffness-dependent NF- κ B or JNK activity could enhance chemotherapeutic efficacy in patients with TNBC.

Future directions of this work will further explore the mechanistic interactions between NF- κ B and JNK and the transcriptional responses that mediate cell survival. RNA sequencing of cells cultured on soft or stiff substrates with and without chemotherapy would provide useful insight. NF- κ B has also been shown to enhance cell survival in a transcriptionally independent manner, but the precise molecular mechanism has not been elucidated. Greater clarity into the molecular effectors of this phenotype have much higher potential to identify actionable targets to augment chemotherapy in breast cancer treatment. This will likely be necessary given the difficulty of targeting NF- κ B.

Future work will also incorporate these findings into ongoing projects within the lab exploring how a soft ECM may upregulate nuclear repressor coreceptor 2 (NCoR2) to enable chemotherapy resistance and tumor recurrence. NCoR2 is a powerful epigenetic transcriptional repressor known to associate with treatment resistance and poor prognosis. NCoR2 has also been reported to suppress the JNK pathway and thus may act alongside NF- κ B.

LOX-mediated ECM stiffening reshapes immune cell populations and regulates tumor metastasis

Immunotherapy holds immense promise for curing cancers but is currently only effective in a minority of tumor types. Consequently, a considerable amount of funding and effort has been devoted to understanding how immune function is regulated in tumors and how to translate that information to improve immunotherapy. Unravelling the complex interactions influencing tumor immunity has proven to be a difficult task. Not only do breast tumor microenvironments contain a multitude of immune cell types, but also many can also assume a variety of distinct phenotypes. Their interactions with each other and with tumor and stromal cells dictate their response to the tumor that evolves as the tumor progresses. The immune response to tumors is commonly described as progressing through three phases: elimination, equilibrium, and escape. These phases describe the process in which the immune system initially responds by attacking the tumor but will be reprogrammed to support tumor growth and metastasis if the tumor persists.

In this project, we explored how ECM stiffness altered tumor immunity. We profiled immune cell types present in mammary gland tumors of LOX overexpressing mice and found that LOX overexpression increased the abundance of neutrophils in the primary tumor nearly twofold. In this model, the increase in neutrophils occurred exclusively in the primary tumor. Neutrophil count remained unchanged in the premetastatic lungs and may be slightly elevated in peripheral blood, but more animals need to be profiled to draw this conclusion. These data fueled the hypothesis that ECM stiffness may regulate the neutrophil population in tumors. Further characterization of this model revealed an upregulation of cytokines that have been reported to induce chemotaxis as well as a general cytokine profile indicative of a productive anti-tumor immune response. A progenitor labelling experiment suggested that neutrophils present in the primary tumors of LOX overexpressing mice were older than those of control tumors. While a wealth of data support an immunosuppressive role of neutrophils in PyMT tumors, it is plausible

that neutrophils recruited to LOX overexpressing tumors maintain an anti-tumor phenotype. Additional experiments directly profiling these cells are needed to confirm this hypothesis. Given the wealth of data indicating that LOX activity and ECM stiffness promote metastasis, it is tempting to speculate that metastasis does not increase in the LOX overexpressing tumors due to a counteracting anti-tumor immune response. Future work should explore this hypothesis.

Additional *in vivo* models modulating ECM stiffness produced varied results with regards to neutrophil infiltration. One of two triple negative PDX models, HCI-002, showed an increase in neutrophil abundance in lung in mice injected with tumors in soft collagen. Neutrophil abundance was not measured in the primary tumor; however, RNA-seq data from whole tumor mRNA showed indications of altered inflammatory signaling. In fact, HCI-001 may have higher inflammatory cell recruitment in the soft condition. However, these PDX studies are performed in immune compromised mice, which may be an important caveat to consider when drawing conclusions about innate immune cell behaviors in these models. In a PyMT model with stromal LOX overexpression using a different stromal promoter to drive LOX, the lungs have more neutrophils, but it is still unclear whether the primary tumors have more neutrophils. Interestingly, this model showed a strain dependent metastasis phenotype in which LOX overexpression on the FVB background promoted metastasis but seemed to inhibit metastasis on the C57BL6/J background. These two strains have characteristically different immune responses to tumors with FVB more type 2-like and C57BL6 more type 1-like. It is interesting to speculate that LOX overexpression interacts differently with these drastically different immune responses to promote or inhibit metastasis. Because of their more robust anti-tumor immune response, C57BL6 PyMT tumors take longer to develop, and it is also possible that increased crosslinking in this time prohibit tumor cells from entering or exiting circulation. Future work should characterize potential differences in crosslinking and in immune cell phenotypes in these two strains to understand how LOX may impart both prometastatic and antimetastatic qualities.

One of the key roles of tumor promoting neutrophils in mice is to condition the premetastatic niche to create a receptive environment for incoming tumor cells. Neutrophils secrete proteases and ECM proteins to create a hospitable niche for tumor cell survival and outgrowth. Future directions of this work should also include characterizing changes in the premetastatic niche both to understand how modulating neutrophil levels and phenotype alter the niche and to discover potent prometastatic mediators. The matrisome and matrisome associated proteins have never been profiled in the context of a spontaneously forming mouse mammary gland tumor and these studies could yield important and interesting insights into how metastatic sites are remodeled to promote tumor colonization. These studies could be expanded into mouse models with other organ-specific metastases such as bone or brain to characterize differences occurring in these tissues prior to tumor cell arrival. Studies of this nature have high potential for yielding impactful insights into mechanisms of tumor metastasis and organotropism.

Broad Implications and Final Comments

While the work discussed here focused only on breast cancer, these findings have broader implications for other tumor types and fibrotic pathologies. Fibrosis correlates with poor outcomes in many carcinomas including those of pancreas, lung, liver, prostate, and ovary^{23,25,76,274}. Thus, our results with respect to understanding stromal activation early in tumorigenesis, weighing the relative contributions of stromal cells and tumor epithelium to matrix remodeling, and understanding how ECM stiffness modulates chemotherapy response may be directly applicable to other fibrotic tumors. It will be important to keep in mind however, that ECM is highly tissue specific and the unique features of each of these local environments should be considered when designing experiments and interpreting results. These tissues also have unique stromal cell populations and tissue resident immune cells, which may alter how tumors in these tissues respond to a fibrotic environment.

This thesis sought to understand tumor associated ECM remodeling and fibrosis in greater detail and how signals from the tumor ECM influenced tumor pathology and therapy response. This work occurred across length scales from *in vitro* cell culture manipulations to several orthotopic and genetically engineered mouse models to carefully dissect the roles of DDR1 signaling and ECM stiffness on specific cell behaviors and demonstrate their relevance in the mouse tumor microenvironment. Human tissues and datasets validate that our observations translate to human disease and both provide LH2 as a potentially useful biomarker to stratify patients for therapy and inform treatment strategies that antagonize ECM-mediated tumor promoting signaling pathways. These studies have also launched several exciting new avenues of study to more precisely understand the role of stromal LOX in ECM remodeling and how ECM regulation of tumor immunity influences metastasis. This ongoing work has tremendous potential to further our understanding of how ECM remodeling and stiffening occur in cancer, how these activities regulate tumor biology, and how we might improve therapeutics to treat cancer and improve patient outcomes.

References

1. Female Breast Cancer - Cancer Stat Facts. Available at: <https://seer.cancer.gov/statfacts/html/breast.html>. (Accessed: 27th February 2020)
2. Yanagishita, M. Function of proteoglycans in the extracellular matrix. *Pathol. Int.* **43**, 283–293 (1993).
3. Evanko, S. P., Tammi, M. I., Tammi, R. H. & Wight, T. N. Hyaluronan-Dependent Pericellular Matrix. *Adv. Drug Deliv. Rev.* **59**, 1351–1356 (2007).
4. Iozzo, R. V. & Sanderson, R. D. Proteoglycans in cancer biology, tumour microenvironment and angiogenesis. *Journal of Cellular and Molecular Medicine* **15**, 1013–1031 (2011).
5. Nam, S., Hu, K. H., Butte, M. J. & Chaudhuri, O. Strain-enhanced stress relaxation impacts nonlinear elasticity in collagen gels. *Proc. Natl. Acad. Sci. U. S. A.* **113**, 5492–5497 (2016).
6. Miri, A. K., Heris, H. K., Mongeau, L. & Javid, F. Nanoscale viscoelasticity of extracellular matrix proteins in soft tissues: A multiscale approach. *J. Mech. Behav. Biomed. Mater.* **30**, 196–204 (2014).
7. Tseng, Q. *et al.* Spatial organization of the extracellular matrix regulates cell-cell junction positioning. *Proc. Natl. Acad. Sci. U. S. A.* **109**, 1506–1511 (2012).
8. Frantz, C., Stewart, K. M. & Weaver, V. M. The extracellular matrix at a glance. *Journal of Cell Science* **123**, 4195–4200 (2010).
9. Weaver, V. M. *et al.* Reversion of the malignant phenotype of human breast cells in three-dimensional culture and in vivo by integrin blocking antibodies. *J. Cell Biol.* **137**, 231–245 (1997).
10. Tozluoğlu, M. *et al.* Matrix geometry determines optimal cancer cell migration strategy and modulates response to interventions. *Nat. Cell Biol.* **15**, 751–62 (2013).

11. Lee, B. L.-P. *et al.* Synovial stem cells and their responses to the porosity of microfibrinous scaffold. *Acta Biomater.* **9**, 7264–75 (2013).
12. McGregor, A. L., Hsia, C.-R. & Lammerding, J. Squish and squeeze—the nucleus as a physical barrier during migration in confined environments. *Curr. Opin. Cell Biol.* **40**, 32–40 (2016).
13. Hynes, R. O. Integrins: Bidirectional, allosteric signaling machines. *Cell* **110**, 673–687 (2002).
14. Barczyk, M., Carracedo, S. & Gullberg, D. Integrins. *Cell Tissue Res.* **339**, 269–280 (2010).
15. Jansen, K. A. *et al.* A guide to mechanobiology: Where biology and physics meet. *Biochim. Biophys. Acta - Mol. Cell Res.* **1853**, 3043–3052 (2015).
16. Mammoto, T. & Ingber, D. E. Mechanical control of tissue and organ development. *Development* **137**, 1407–1420 (2010).
17. Katsumi, A., Naoe, T., Matsushita, T., Kaibuchi, K. & Schwartz, M. A. Integrin activation and matrix binding mediate cellular responses to mechanical stretch. *J. Biol. Chem.* **280**, 16546–16549 (2005).
18. Zhang, H. *et al.* A tension-induced mechanotransduction pathway promotes epithelial morphogenesis. *Nature* **471**, 99–103 (2011).
19. Yurchenco, P. D. Basement membranes: Cell scaffoldings and signaling platforms. *Cold Spring Harb. Perspect. Biol.* **3**, a004911 (2011).
20. Exposito, J. Y., Valcourt, U., Cluzel, C. & Lethias, C. The fibrillar collagen family. *Int. J. Mol. Sci.* **11**, 407–426 (2010).
21. Mouw, J. K., Ou, G. & Weaver, V. M. Extracellular matrix assembly: A multiscale deconstruction. *Nat. Rev. Mol. Cell Biol.* **15**, 771–785 (2014).
22. Kadler, K. E., Hill, A. & Canty-Laird, E. G. Collagen fibrillogenesis: fibronectin, integrins, and minor collagens as organizers and nucleators. *Curr. Opin. Cell Biol.* **20**, 495–501

- (2008).
23. Pickup, M. W., Mouw, J. K. & Weaver, V. M. The extracellular matrix modulates the hallmarks of cancer. *EMBO Rep.* **15**, 1243–1253 (2014).
 24. Jain, R. K., Martin, J. D. & Stylianopoulos, T. The role of mechanical forces in tumor growth and therapy. *Annu Rev Biomed Eng* **16**, 321–346 (2014).
 25. Kai, F., Drain, A. P. & Weaver, V. M. The Extracellular Matrix Modulates the Metastatic Journey. *Dev. Cell* **49**, 332–346 (2019).
 26. Acerbi, I. *et al.* Human breast cancer invasion and aggression correlates with ECM stiffening and immune cell infiltration. *Integr. Biol. (Camb)*. **7**, 1120–34 (2015).
 27. Paszek, M. J. *et al.* Tensional homeostasis and the malignant phenotype. *Cancer Cell* **8**, 241–254 (2005).
 28. Rubashkin, M. G. *et al.* Force engages vinculin and promotes tumor progression by enhancing PI3K activation of phosphatidylinositol (3,4,5)-triphosphate. *Cancer Res.* **74**, 4597–611 (2014).
 29. Kai, F., Laklai, H. & Weaver, V. M. Force Matters: Biomechanical Regulation of Cell Invasion and Migration in Disease. *Trends Cell Biol.* **26**, 486–497 (2016).
 30. Conklin, M. W. *et al.* Aligned collagen is a prognostic signature for survival in human breast carcinoma. *Am. J. Pathol.* **178**, 1221–1232 (2011).
 31. Provenzano, P. P. *et al.* Collagen reorganization at the tumor-stromal interface facilitates local invasion. *BMC Med.* **4**, 38 (2006).
 32. Chambard, J. C., Lefloch, R., Pouysségur, J. & Lenormand, P. ERK implication in cell cycle regulation. *Biochim. Biophys. Acta - Mol. Cell Res.* **1773**, 1299–1310 (2007).
 33. Provenzano, P. P., Inman, D. R., Eliceiri, K. W. & Keely, P. J. Matrix density-induced mechanoregulation of breast cell phenotype, signaling and gene expression through a FAK-ERK linkage. *Oncogene* **28**, 4326–4343 (2009).
 34. Lim, Y. *et al.* PyK2 and FAK connections to p190Rho guanine nucleotide exchange factor

- regulate RhoA activity, focal adhesion formation, and cell motility. *J. Cell Biol.* **180**, 187–203 (2008).
35. Levental, K. R. *et al.* Matrix Crosslinking Forces Tumor Progression by Enhancing Integrin Signaling. *Cell* **139**, 891–906 (2009).
 36. Takai, K. *et al.* Discoidin domain receptor 1 (DDR1) ablation promotes tissue fibrosis and hypoxia to induce aggressive basal-like breast cancers. *Genes Dev.* **32**, 244–257 (2018).
 37. Alves, F. *et al.* Distinct structural characteristics of discoidin I subfamily receptor tyrosine kinases and complementary expression in human cancer. *Oncogene* **10**, 609–618 (1995).
 38. Leitinger, B. Molecular analysis of collagen binding by the human discoidin domain receptors, DDR1 and DDR2. Identification of collagen binding sites in DDR2. *J. Biol. Chem.* **278**, 16761–16769 (2003).
 39. Leitinger, B. & Kwan, A. P. L. The discoidin domain receptor DDR2 is a receptor for type X collagen. *Matrix Biol.* **25**, 355–364 (2006).
 40. Vogel, W., Gish, G. D., Alves, F. & Pawson, T. The discoidin domain receptor tyrosine kinases are activated by collagen. *Mol. Cell* **1**, 13–23 (1997).
 41. Mihai, C., Chotani, M., Elton, T. S. & Agarwal, G. Mapping of DDR1 Distribution and Oligomerization on the Cell Surface by FRET Microscopy. *J. Mol. Biol.* **385**, 432–445 (2009).
 42. Noordeen, N. A., Carafoli, F., Hohenester, E., Horton, M. A. & Leitinger, B. A transmembrane leucine zipper is required for activation of the dimeric receptor tyrosine kinase DDR1. *J. Biol. Chem.* **281**, 22744–22751 (2006).
 43. Xu, H. *et al.* Normal activation of discoidin domain receptor 1 mutants with disulfide cross-links, insertions, or deletions in the extracellular juxtamembrane region: Mechanistic implications. *J. Biol. Chem.* **289**, 13565–13574 (2014).
 44. Juskaite, V., Corcoran, D. S. & Leitinger, B. Collagen induces activation of DDR1 through

- lateral dimer association and phosphorylation between dimers. *Elife* **6**, e25716 (2017).
45. Leitinger, B. *Discoidin domain receptor functions in physiological and pathological conditions. International Review of Cell and Molecular Biology* **310**, (Elsevier Inc., 2014).
 46. Vogel, W. F., Aszódi, A., Alves, F. & Pawson, T. Discoidin domain receptor 1 tyrosine kinase has an essential role in mammary gland development. *Mol. Cell. Biol.* **21**, 2906–17 (2001).
 47. Hou, G., Vogel, W. & Bendeck, M. P. The discoidin domain receptor tyrosine kinase DDR1 in arterial wound repair. *J. Clin. Invest.* **107**, 727–735 (2001).
 48. Ferri, N., Carragher, N. O. & Raines, E. W. Role of Discoidin Domain Receptors 1 and 2 in Human Smooth Muscle Cell-Mediated Collagen Remodeling: Potential Implications in Atherosclerosis and Lymphangiomyomatosis. *Am. J. Pathol.* **164**, 1575–1585 (2004).
 49. Neuhaus, B. *et al.* Migration inhibition of mammary epithelial cells by Syk is blocked in the presence of DDR1 receptors. *Cell. Mol. Life Sci.* **68**, 3757–3770 (2011).
 50. Roberts, M. E., Magowan, L., Hall, I. P. & Johnson, S. R. Discoidin domain receptor 1 regulates bronchial epithelial repair and matrix metalloproteinase production. *Eur. Respir. J.* **37**, 1482–1493 (2011).
 51. Yeh, Y. C., Wu, C. C., Wang, Y. K. & Tang, M. J. DDR1 triggers epithelial cell differentiation by promoting cell adhesion through stabilization of E-cadherin. *Mol. Biol. Cell* **22**, 940–953 (2011).
 52. Johnson, J. D., Edman, J. C. & Rutter, W. J. A receptor tyrosine kinase found in breast carcinoma cells has an extracellular discoidin I-like domain. *Proc. Natl. Acad. Sci. U. S. A.* **90**, 5677–5681 (1993).
 53. Zerlin, M., Julius, M. A. & Goldfarb, M. NEP: A novel receptor-like tyrosine kinase expressed in proliferating neuroepithelia. *Oncogene* **8**, 2731–2739 (1993).
 54. Laval, S. *et al.* Isolation and characterization of an epithelial-specific receptor tyrosine kinase from an ovarian cancer cell line. *Cell Growth Differ.* **5**, 1173–1183 (1994).

55. Barker, K. T. *et al.* Expression patterns of the novel receptor-like tyrosine kinase, DDR, in human breast tumours. *Oncogene* **10**, 569–75 (1995).
56. Perez, J. L., Jing, S. Q. & Wong, T. W. Identification of two isoforms of the Cak receptor kinase that are co-expressed in breast tumor cell lines. *Oncogene* **12**, 1469–1477 (1996).
57. Ford, C. E. *et al.* Expression and mutation analysis of the discoidin domain receptors 1 and 2 in non-small cell lung carcinoma. *Br. J. Cancer* **96**, 808–814 (2007).
58. Quan, J., Yahata, T., Adachi, S., Yoshihara, K. & Tanaka, K. Identification of receptor tyrosine kinase, discoidin domain receptor 1 (DDR1), as a potential biomarker for serous ovarian cancer. *Int. J. Mol. Sci.* **12**, 971–982 (2011).
59. Valencia, K. *et al.* Inhibition of collagen receptor discoidin domain receptor-1 (DDR1) reduces cell survival, homing, and colonization in lung cancer bone metastasis. *Clin. Cancer Res.* **18**, 969–980 (2012).
60. Gao, H. *et al.* Multi-organ Site Metastatic Reactivation Mediated by Non-canonical Discoidin Domain Receptor 1 Signaling. *Cell* **166**, 47–62 (2016).
61. Hou, G., Vogel, W. F. & Bendeck, M. P. Tyrosine kinase activity of discoidin domain receptor 1 is necessary for smooth muscle cell migration and matrix metalloproteinase expression. *Circ. Res.* **90**, 1147–9 (2002).
62. Eswaramoorthy, R. *et al.* DDR1 regulates the stabilization of cell surface E-cadherin and E-cadherin-mediated cell aggregation. *J. Cell. Physiol.* **224**, 387–397 (2010).
63. Hidalgo-Carcedo, C. *et al.* Collective cell migration requires suppression of actomyosin at cell-cell contacts mediated by DDR1 and the cell polarity regulators Par3 and Par6. *Nat. Cell Biol.* **13**, 49–58 (2011).
64. Marcotte, R. *et al.* Essential gene profiles in breast, pancreatic, and ovarian cancer cells. *Cancer Discov.* **2**, 172–189 (2012).
65. Ren, T., Zhang, J., Zhang, J., Liu, X. & Yao, L. Increased expression of discoidin domain receptor 2 (DDR2): A novel independent prognostic marker of worse outcome in breast

- cancer patients. *Med. Oncol.* **30**, 397 (2013).
66. Hansen, C., Greengard, P., Nairn, A. C., Andersson, T. & Vogel, W. F. Phosphorylation of DARPP-32 regulates breast cancer cell migration downstream of the receptor tyrosine kinase DDR1. *Exp. Cell Res.* **312**, 4011–4018 (2006).
 67. Lee, R., Eidman, K. E., Kren, S. M., Hostetter, T. H. & Segal, Y. Localization of discoidin domain receptors in rat kidney. *Nephron - Exp. Nephrol.* **97**, e62-70 (2004).
 68. Ram, R. *et al.* Discoidin domain receptor-1a (DDR1a) promotes glioma cell invasion and adhesion in association with matrix metalloproteinase-2. *J. Neurooncol.* **76**, 239–248 (2006).
 69. Xu, H. *et al.* Discoidin Domain Receptors Promote $\alpha 1\beta 1$ - and $\alpha 2\beta 1$ -Integrin Mediated Cell Adhesion to Collagen by Enhancing Integrin Activation. *PLoS One* **7**, e52209 (2012).
 70. Lin, E. Y. *et al.* Progression to Malignancy in the Polyoma Middle T Oncoprotein Mouse Breast Cancer Model Provides a Reliable Model for Human Diseases. *Am. J. Pathol.* **163**, 2113–2126 (2003).
 71. Neve, R. M. *et al.* A collection of breast cancer cell lines for the study of functionally distinct cancer subtypes. *Cancer Cell* **10**, 515–527 (2006).
 72. Zhang, K. *et al.* The collagen receptor discoidin domain receptor 2 stabilizes SNAIL1 to facilitate breast cancer metastasis. *Nat. Cell Biol.* **15**, 677–687 (2013).
 73. Corsa, C. A. S. *et al.* The Action of Discoidin Domain Receptor 2 in Basal Tumor Cells and Stromal Cancer-Associated Fibroblasts Is Critical for Breast Cancer Metastasis. *Cell Rep.* **15**, 2510–2523 (2016).
 74. Gilchrist, K. W., Gray, R., Fowble, B., Tormey, D. C. & Taylor IV, S. G. Tumor necrosis is a prognostic predictor for early recurrence and death in lymph node-positive breast cancer: A 10-year follow-up study of 728 eastern cooperative oncology group patients. *J. Clin. Oncol.* **11**, 1929–1935 (1993).
 75. Fulford, L. G. *et al.* Specific morphological features predictive for the basal phenotype in

- grade 3 invasive ductal carcinoma of breast. *Histopathology* **49**, 22–34 (2006).
76. Leight, J. L., Drain, A. P. & Weaver, V. M. Extracellular Matrix Remodeling and Stiffening Modulate Tumor Phenotype and Treatment Response. *Annu. Rev. Cancer Biol.* **1**, 313–334 (2017).
 77. Northey, J. J., Przybyla, L. & Weaver, V. M. Tissue force programs cell fate and tumor aggression. *Cancer Discovery* **7**, 1224–1237 (2017).
 78. Perou, C. M. *et al.* Molecular portraits of human breast tumours. *Nature* **406**, 747–752 (2000).
 79. Sørlie, T. *et al.* Gene expression patterns of breast carcinomas distinguish tumor subclasses with clinical implications. *Proc. Natl. Acad. Sci. U. S. A.* **98**, 10869–10874 (2001).
 80. Van de Rijn, M. *et al.* Expression of cytokeratins 17 and 5 identifies a group of breast carcinomas with poor clinical outcome. *Am. J. Pathol.* **161**, 1991–1996 (2002).
 81. Sørlie, T. *et al.* Repeated observation of breast tumor subtypes in independent gene expression data sets. *Proc. Natl. Acad. Sci. U. S. A.* **100**, 8418–8423 (2003).
 82. Malanchi, I. *et al.* Interactions between cancer stem cells and their niche govern metastatic colonization. *Nature* **481**, 85–91 (2012).
 83. Chin, K. *et al.* Genomic and transcriptional aberrations linked to breast cancer pathophysiologies. *Cancer Cell* **10**, 529–541 (2006).
 84. Györfy, B. *et al.* An online survival analysis tool to rapidly assess the effect of 22,277 genes on breast cancer prognosis using microarray data of 1,809 patients. *Breast Cancer Research and Treatment* **123**, 725–731 (2010).
 85. Szász, A. M. *et al.* Cross-validation of survival associated biomarkers in gastric cancer using transcriptomic data of 1,065 patients. *Oncotarget* **7**, 49322–49333 (2016).
 86. Hendrix, M. J. C., Seftor, E. A., Seftor, R. E. B. & Trevor, K. T. Experimental co-expression of vimentin and keratin intermediate filaments in human breast cancer cells

- results in phenotypic interconversion and increased invasive behavior. *Am. J. Pathol.* **150**, 483–495 (1997).
87. McInroy, L. & Määttä, A. Down-regulation of vimentin expression inhibits carcinoma cell migration and adhesion. *Biochem. Biophys. Res. Commun.* **360**, 109–114 (2007).
 88. Cheung, K. J., Gabrielson, E., Werb, Z. & Ewald, A. J. Collective Invasion in Breast Cancer Requires a Conserved Basal Epithelial Program. *Cell* **155**, 1639–1651 (2013).
 89. Brown, J. M. Tumor Hypoxia in Cancer Therapy. *Methods in Enzymology* **435**, 297–321 (2007).
 90. Thomas, P. A. *et al.* Association between keratin and vimentin expression, malignant phenotype, and survival in postmenopausal breast cancer patients. *Clin. Cancer Res.* **5**, 2698–2703 (1999).
 91. Abd El-Rehim, D. M. *et al.* Expression of luminal and basal cytokeratins in human breast carcinoma. *J. Pathol.* **203**, 661–671 (2004).
 92. Karantza, V. Keratins in health and cancer: More than mere epithelial cell markers. *Oncogene* **30**, 127–138 (2011).
 93. Valiathan, R. R., Marco, M., Leitinger, B., Kleer, C. G. & Fridman, R. Discoidin domain receptor tyrosine kinases: New players in cancer progression. *Cancer and Metastasis Reviews* **31**, 295–321 (2012).
 94. Zelenko, Z. *et al.* Silencing vimentin expression decreases pulmonary metastases in a pre-diabetic mouse model of mammary tumor progression. *Oncogene* **36**, 1394–1403 (2017).
 95. Maeyama, M. *et al.* Switching in discoid domain receptor expressions in SLUG-induced epithelial-mesenchymal transition. *Cancer* **113**, 2823–2831 (2008).
 96. Kim, D. *et al.* DDR2 controls the epithelial-mesenchymal-transition-related gene expression via c-Myb acetylation upon matrix stiffening. *Sci. Rep.* **7**, 6847 (2017).
 97. Jain, R. K., Martin, J. D. & Stylianopoulos, T. The Role of Mechanical Forces in Tumor

- Growth and Therapy. *Annu. Rev. Biomed. Eng.* **16**, 321–346 (2014).
98. Ren, T. *et al.* Discoidin domain receptor 2 (DDR2) promotes breast cancer cell metastasis and the mechanism implicates epithelial-mesenchymal transition programme under hypoxia. *J. Pathol.* **234**, 526–537 (2014).
 99. Toy, K. A. *et al.* Tyrosine kinase discoidin domain receptors DDR1 and DDR2 are coordinately deregulated in triple-negative breast cancer. *Breast Cancer Res. Treat.* **150**, 9–18 (2015).
 100. Hirakawa, S. *et al.* VEGF-A induces tumor and sentinel lymph node lymphangiogenesis and promotes lymphatic metastasis. *J. Exp. Med.* **201**, 1089–1099 (2005).
 101. Fata, J. E. *et al.* The MAPKERK-1,2 pathway integrates distinct and antagonistic signals from TGF α and FGF7 in morphogenesis of mouse mammary epithelium. *Dev. Biol.* **306**, 193–207 (2007).
 102. Ewald, A. J., Brenot, A., Duong, M., Chan, B. S. & Werb, Z. Collective Epithelial Migration and Cell Rearrangements Drive Mammary Branching Morphogenesis. *Dev. Cell* **14**, 570–581 (2008).
 103. Stingl, J. *et al.* Purification and unique properties of mammary epithelial stem cells. *Nature* **439**, 993–997 (2006).
 104. Chou, J. *et al.* GATA3 suppresses metastasis and modulates the tumour microenvironment by regulating microRNA-29b expression. *Nat. Cell Biol.* **15**, 201–213 (2013).
 105. Brower, M., Carney, D. N., Oie, H. K., Gazdar, A. F. & Minna, J. D. Growth of cell lines and clinical specimens of human non-small cell lung cancer in a serum-free defined medium. *Cancer Res.* **46**, 798–806 (1986).
 106. Littlepage, L. E. *et al.* The transcription factor ZNF217 Is a prognostic biomarker and therapeutic target during breast cancer progression. *Cancer Discov.* **2**, 638–651 (2012).
 107. Littlepage, L. E. *et al.* Matrix metalloproteinases contribute distinct roles in

- neuroendocrine prostate carcinogenesis, metastasis, and angiogenesis progression. *Cancer Res.* **70**, 2224–2234 (2010).
108. Maller, O. *et al.* Inflammation promotes tumor aggression by stimulating stromal cell-dependent collagen crosslinking and stromal stiffening. *bioRxiv* 2020.02.13.948141 (2020). doi:10.1101/2020.02.13.948141
 109. Laklai, H. *et al.* Genotype tunes pancreatic ductal adenocarcinoma tissue tension to induce matricellular fibrosis and tumor progression. *Nat. Med.* **22**, 497–505 (2016).
 110. Flier, J. S., Underhill, L. H. & Dvorak, H. F. Tumors: Wounds That Do Not Heal. *New England Journal of Medicine* **315**, 1650–1659 (1986).
 111. Olive, K. P. *et al.* Inhibition of Hedgehog signaling enhances delivery of chemotherapy in a mouse model of pancreatic cancer. *Science (80-.).* **324**, 1457–1461 (2009).
 112. Provenzano, P. P. *et al.* Enzymatic Targeting of the Stroma Ablates Physical Barriers to Treatment of Pancreatic Ductal Adenocarcinoma. *Cancer Cell* **21**, 418–429 (2012).
 113. Netti, P. A., Berk, D. A., Swartz, M. A., Grodzinsky, A. J. & Jain, R. K. Role of extracellular matrix assembly in interstitial transport in solid tumors. *Cancer Res.* **60**, 2497–2503 (2000).
 114. Jain, R. K., Lee, J. J., Hong, D. & Kurzrock, R. Reply to A. Levy *et al.* *Journal of Clinical Oncology* **31**, 396 (2013).
 115. Egeblad, M., Rasch, M. G. & Weaver, V. M. Dynamic interplay between the collagen scaffold and tumor evolution. *Curr. Opin. Cell Biol.* **22**, 697–706 (2010).
 116. Chaudhuri, O. *et al.* Extracellular matrix stiffness and composition jointly regulate the induction of malignant phenotypes in mammary epithelium. *Nat. Mater.* **13**, 1–35 (2014).
 117. Mekhdjian, A. H. *et al.* Integrin-mediated traction force enhances paxillin molecular associations and adhesion dynamics that increase the invasiveness of tumor cells into a three-dimensional extracellular matrix. *Mol. Biol. Cell* **28**, 1467–1488 (2017).
 118. Pickup, M. W. *et al.* Stromally derived lysyl oxidase promotes metastasis of transforming

- growth factor- β -deficient mouse mammary carcinomas. *Cancer Res.* **73**, 5336–5346 (2013).
119. Provenzano, P. P. *et al.* Collagen density promotes mammary tumor initiation and progression. *BMC Med.* **6**, 11 (2008).
 120. Eyre, D. R., Weis, M. A. & Wu, J. J. Advances in collagen cross-link analysis. *Methods* **45**, 65–74 (2008).
 121. Ricard, S. The Collagen Family. *Cold Spring Harb. Perspect. Biol.* **3**, 1–19 (2011).
 122. Myllyharju, J. & Kivirikko, K. I. Collagens, modifying enzymes and their mutations in humans, flies and worms. *Trends in Genetics* **20**, 33–43 (2004).
 123. McAlinden, A. *et al.* α -Helical Coiled-coil Oligomerization Domains Are Almost Ubiquitous in the Collagen Superfamily. *J. Biol. Chem.* **278**, 42200–42207 (2003).
 124. Bourhis, J., Mariano, N., Zhao, Y. & Harlos, K. Structural Basis of Fibrillar Collagen Trimerization and Related Genetic Disorders. **19**, 1031–1036 (2013).
 125. Chen, S. & Birk, D. E. The regulatory roles of small leucine-rich proteoglycans in extracellular matrix assembly. *FEBS J.* **280**, 2120–2137 (2013).
 126. Yamauchi, M. & Sricholpech, M. Lysine post-translational modifications of collagen. *Essays Biochem.* **52**, 113–133 (2012).
 127. Van der Slot, A. J. *et al.* Identification of PLOD2 as Telopeptide Lysyl Hydroxylase, an Important Enzyme in Fibrosis. *J. Biol. Chem.* **278**, 40967–40972 (2003).
 128. Sims, T. J., Avery, N. C., Grant, M., Bailey, A. J. & Streuli, C. Quantitative Determination of Collagen Crosslinks. *Extracell. Matrix Protoc.* **139**, 11–26 (2003).
 129. Yoshida, K. *et al.* Quantitative Evaluation of Collagen Crosslinks and Corresponding Tensile Mechanical Properties in Mouse Cervical Tissue during Normal Pregnancy. *PLoS One* **9**, e112391 (2014).
 130. Chen, Y. *et al.* Lysyl hydroxylase 2 induces a collagen cross-link switch in tumor stroma. *J. Clin. Invest.* **125**, 1147–1162 (2015).

131. Wang, T. H., Hsia, S. M. & Shieh, T. M. Lysyl oxidase and the tumor microenvironment. *Int. J. Mol. Sci.* **18**, 1–12 (2017).
132. Miller, B. W. *et al.* Targeting the LOX / hypoxia axis reverses many of the features that make pancreatic cancer deadly: inhibition of LOX abrogates metastasis and enhances drug efficacy . *EMBO Mol. Med.* **7**, 1063–1076 (2015).
133. Gilkes, D. M. *et al.* Procollagen Lysyl Hydroxylase 2 Is Essential for Hypoxia-Induced Breast Cancer Metastasis. *Mol. Cancer Res.* **11**, 456–466 (2013).
134. Erler, J. T. *et al.* Lysyl oxidase is essential for hypoxia-induced metastasis. *Nature* **440**, 1222–1226 (2006).
135. Lampi, M. C. & Reinhart-King, C. A. Targeting extracellular matrix stiffness to attenuate disease: From molecular mechanisms to clinical trials. *Science Translational Medicine* **10**, (2018).
136. Mack, M. Inflammation and fibrosis. *Matrix Biology* **68–69**, 106–121 (2018).
137. Grivennikov, S. I., Greten, F. R. & Karin, M. Immunity, Inflammation, and Cancer. *Cell* **140**, 883–899 (2010).
138. Sun, X. *et al.* CCL2-driven inflammation increases mammary gland stromal density and cancer susceptibility in a transgenic mouse model. *Breast Cancer Res.* **19**, 1–15 (2017).
139. Wick, G. *et al.* The Immunology of Fibrosis. *Annu. Rev. Immunol.* **31**, 107–135 (2013).
140. Ueha, S., Shand, F. H. W. & Matsushima, K. Cellular and molecular mechanisms of chronic inflammation-associated organ fibrosis. *Frontiers in Immunology* **3**, 71 (2012).
141. Qian, B.-Z. *et al.* CCL2 recruits inflammatory monocytes to facilitate breast-tumour metastasis. *Nature* **475**, (2011).
142. Lohela, M. *et al.* Intravital imaging reveals distinct responses of depleting dynamic tumor-associated macrophage and dendritic cell subpopulations. *Proc. Natl. Acad. Sci. U. S. A.* **111**, E5086-95 (2014).
143. Ruffell, B. *et al.* Macrophage IL-10 Blocks CD8+ T Cell-Dependent Responses to

- Chemotherapy by Suppressing IL-12 Expression in Intratumoral Dendritic Cells. *Cancer Cell* **26**, 623–637 (2014).
144. DeNardo, D. G. *et al.* Leukocyte complexity predicts breast cancer survival and functionally regulates response to chemotherapy. *Cancer Discov.* **1**, 54–67 (2011).
 145. Nemkov, T., D'Alessandro, A. & Hansen, K. C. Three-minute method for amino acid analysis by UHPLC and high-resolution quadrupole orbitrap mass spectrometry. *Amino Acids* **47**, 2345–2357 (2015).
 146. Oxlund, H., Barckman, M., Ortoft, G. & Andreassen, T. T. Reduced concentrations of collagen cross-links are associated with reduced strength of bone. *Bone* **17**, 365S-371S (1995).
 147. Gruosso, T. *et al.* Spatially distinct tumor immune microenvironments stratify triple-negative breast cancers. *J. Clin. Invest.* **129**, 1785–1800 (2019).
 148. Finak, G. *et al.* Stromal gene expression predicts clinical outcome in breast cancer. *Nat. Med.* **14**, 518–527 (2008).
 149. Salvador, F. *et al.* Lysyl oxidase-like protein LOXL2 promotes lung metastasis of breast cancer. *Cancer Res.* **77**, 5846–5859 (2017).
 150. Eyre, D. R., Paz, M. A. & Gallop, P. M. Cross-Linking in Collagen and Elastin. *Annu. Rev. Biochem.* **53**, 717–748 (1984).
 151. Lin, E. Y., Nguyen, A. V., Russell, R. G. & Pollard, J. W. Colony-stimulating factor 1 promotes progression of mammary tumors to malignancy. *J. Exp. Med.* **193**, 727–739 (2001).
 152. Strachan, D. C. *et al.* CSF1R inhibition delays cervical and mammary tumor growth in murine models by attenuating the turnover of tumor-associated macrophages and enhancing infiltration by CD8+ T cells. *Oncoimmunology* **2**, (2013).
 153. Yamauchi, M. & Shiiba, M. Lysine Hydroxylation and Cross-linking of Collagen BT - Post-translational Modifications of Proteins: Tools for Functional Proteomics. in *Methods*

- in molecular biology* (Clifton, N.J.) (ed. Kannicht, C.) **446**, 95–108 (Humana Press, 2008).
154. Takaluoma, K., Lantto, J. & Myllyharju, J. Lysyl hydroxylase 2 is a specific telopeptide hydroxylase, while all three isoenzymes hydroxylate collagenous sequences. *Matrix Biol.* **26**, 396–403 (2007).
 155. Yau, C. *et al.* A multigene predictor of metastatic outcome in early stage hormone receptor-negative and triple-negative breast cancer. *Breast Cancer Res.* **12**, R85 (2010).
 156. Noy, R. & Pollard, J. W. Tumor-Associated Macrophages: From Mechanisms to Therapy. *Immunity* **41**, 49–61 (2014).
 157. Lin, E. Y. *et al.* Macrophages regulate the angiogenic switch in a mouse model of breast cancer. *Cancer Res.* **66**, 11238–11246 (2006).
 158. Gilkes, D. M., Bajpai, S., Chaturvedi, P., Wirtz, D. & Semenza, G. L. HIF-1 Promotes Extracellular Matrix Remodeling under Hypoxic Conditions by Inducing P4HA1, P4HA2, and PLOD2 Expression in Fibroblasts. *J. Biol. Chem.* (2013).
 159. Wong, R. S. Y. Apoptosis in cancer: From pathogenesis to treatment. *J. Exp. Clin. Cancer Res.* **30**, 87 (2011).
 160. Lu, P., Takai, K., Weaver, V. M. & Werb, Z. Extracellular Matrix degradation and remodeling in development and disease. *Cold Spring Harb. Perspect. Biol.* **3**, (2011).
 161. Ahn, Y., Sanderson, B. W., Klein, O. D. & Krumlauf, R. Inhibition of Wnt signaling by wise (Sostdc1) and negative feedback from Shh controls tooth number and patterning. *Development* **137**, 3221–3231 (2010).
 162. Hsiao, E. C. *et al.* Osteoblast expression of an engineered Gs-coupled receptor dramatically increases bone mass. *Proc. Natl. Acad. Sci. U. S. A.* **105**, 1209–1214 (2008).
 163. Guy, C. T., Cardiff, R. D. & Muller, W. J. Induction of mammary tumors by expression of polyomavirus middle T oncogene: a transgenic mouse model for metastatic disease. *Mol. Cell. Biol.* **12**, 954–961 (1992).

164. Avery, N. C., Sims, T. J. & Bailey, A. J. Quantitative Determination of Collagen Cross-links. in *Methods in molecular biology (Clifton, N.J.)* **522**, 103–121 (2009).
165. Clasquin, M. F., Melamud, E. & Rabinowitz, J. D. LC-MS data processing with MAVEN: A metabolomic analysis and visualization engine. *Curr. Protoc. Bioinforma.* **Chapter 14**, Unit14.11 (2012).
166. Cerami, E. *et al.* The cBio Cancer Genomics Portal: An open platform for exploring multidimensional cancer genomics data. *Cancer Discov.* **2**, 401–404 (2012).
167. Gao, J. *et al.* Integrative analysis of complex cancer genomics and clinical profiles using the cBioPortal. *Sci. Signal.* **6**, (2013).
168. Curtis, C. *et al.* The genomic and transcriptomic architecture of 2,000 breast tumours reveals novel subgroups. *Nature* **486**, 346–352 (2012).
169. Manjer, J. *et al.* The Malmö Diet and Cancer Study: Representativity, cancer incidence and mortality in participants and non-participants. *Eur. J. Cancer Prev.* **10**, 489–499 (2001).
170. Cohen, D. A. *et al.* Interobserver agreement among pathologists for semiquantitative hormone receptor scoring in breast carcinoma. *Am. J. Clin. Pathol.* **138**, 796–802 (2012).
171. Abt, N. B. *et al.* Neoadjuvant chemotherapy and short-term morbidity in patients undergoing mastectomy with and without breast reconstruction. *JAMA Surg.* **149**, 1068–1076 (2014).
172. Von Minckwitz, G. *et al.* Definition and impact of pathologic complete response on prognosis after neoadjuvant chemotherapy in various intrinsic breast cancer subtypes. *J. Clin. Oncol.* **30**, 1796–1804 (2012).
173. Weaver, V. M. *et al.* B4 integrin-dependent formation of polarized three-dimensional architecture confers resistance to apoptosis in normal and malignant mammary epithelium. *Cancer Cell* **2**, 205–216 (2002).
174. Zahir, N. *et al.* Autocrine laminin-5 ligates $\alpha 6\beta 4$ integrin and activates RAC and NF κ B to

- mediate anchorage-independent survival of mammary tumors. *J. Cell Biol.* **163**, 1397–1407 (2003).
175. Baldwin, A. S. Series Introduction: The transcription factor NF- κ B and human disease. *J. Clin. Invest.* **107**, 3–6 (2001).
176. Baeuerle, P. A. & Baltimore, D. NF-kappa B: ten years after. *Cell* **87**, 13–20 (1996).
177. Tergaonkar, V., Pando, M., Vafa, O., Wahl, G. & Verma, I. p53 stabilization is decreased upon NF κ B activation. *Cancer Cell* **1**, 493–503 (2002).
178. Javelaud, D. & Besançon, F. NF- κ B activation results in rapid inactivation of JNK in TNF α -treated Ewing sarcoma cells: A mechanism for the anti-apoptotic effect of NF- κ B. *Oncogene* **20**, 4365–4372 (2001).
179. Tang, G. *et al.* Inhibition of JNK activation through NF- κ B target genes. *Nature* **414**, 313–317 (2001).
180. Sunters, A. *et al.* Paclitaxel-induced nuclear translocation of FOXO3a in breast cancer cells is mediated by c-Jun NH2-terminal kinase and Akt. *Cancer Res.* **66**, 212–220 (2006).
181. Hu, Y.-L., Li, S., Shyy, J. Y.-J. & Chien, S. Sustained JNK activation induces endothelial apoptosis: studies with colchicine and shear stress. *Am. J. Physiol. Circ. Physiol.* **277**, H1593–H1599 (1999).
182. Chen, Y.-R., Wang, X., Templeton, D., Davis, R. J. & Tan, T.-H. The Role of c-Jun N-terminal Kinase (JNK) in Apoptosis Induced by Ultraviolet C and γ Radiation. *J. Biol. Chem.* **271**, 31929–31936 (1996).
183. Ashenden, M. *et al.* An In Vivo Functional Screen Identifies JNK Signaling As a Modulator of Chemotherapeutic Response in Breast Cancer. *Mol. Cancer Ther.* **16**, 1967–1978 (2017).
184. Nguyen, H. T. *et al.* JNK/SAPK and p38 SAPK-2 mediate mechanical stretch-induced apoptosis via caspase-3 and -9 in NRK-52E renal epithelial cells. *Nephron - Exp.*

- Nephrol.* **102**, 49–61 (2006).
185. Marinissen, M. J. *et al.* The small GTP-binding protein RhoA regulates c-jun by a ROCK-JNK signaling axis. *Mol. Cell* **14**, 29–41 (2004).
 186. Johnson, K. R., Leight, J. L. & Weaver, V. M. Demystifying the Effects of a Three-Dimensional Microenvironment in Tissue Morphogenesis. *Methods in Cell Biology* **83**, 547–583 (2007).
 187. Levental, K. R. *et al.* Matrix Crosslinking Forces Tumor Progression by Enhancing Integrin Signaling. *Cell* **139**, 891–906
 188. Srivastava, R. K. TRAIL/Apo-2L: Mechanisms and clinical applications in cancer. *Neoplasia* **3**, 535–546 (2001).
 189. Nagane, M., Huang, H. J. S. & Cavenee, W. K. The potential of TRAIL for cancer chemotherapy. *Apoptosis* **6**, 191–197 (2001).
 190. Fulda, S. & Debatin, K. M. Extrinsic versus intrinsic apoptosis pathways in anticancer chemotherapy. *Oncogene* **25**, 4798–4811 (2006).
 191. Dhanasekaran, D. N. & Reddy, E. P. JNK signaling in apoptosis. *Oncogene* **27**, 6245–6251 (2008).
 192. Sui, X. *et al.* P38 and JNK MAPK pathways control the balance of apoptosis and autophagy in response to chemotherapeutic agents. *Cancer Lett.* **344**, 174–179 (2014).
 193. Wojtaszek, P. A., Heasley, L. E., Siriwardana, G. & Berl, T. Dominant-negative c-Jun NH2-terminal kinase 2 sensitizes renal inner medullary collecting duct cells to hypertonicity-induced lethality independent of organic osmolyte transport. *J. Biol. Chem.* **273**, 800–804 (1998).
 194. Takada, E. *et al.* Interferon- β -induced activation of c-Jun NH2-terminal kinase mediates apoptosis through up-regulation of CD95 in CH31 B lymphoma cells. *Exp. Cell Res.* **304**, 518–530 (2005).
 195. Han, S. Y., Kim, S. H. & Heasley, L. E. Differential gene regulation by specific gain-of-

- function JNK1 proteins expressed in swiss 3T3 fibroblasts. *J. Biol. Chem.* **277**, 47167–47174 (2002).
196. Yamamoto, Y. & Gaynor, R. B. Therapeutic potential of inhibition of the NF- κ B pathway in the treatment of inflammation and cancer. *J. Clin. Invest.* **107**, 135–142 (2001).
 197. Zeligs, K. P., Neuman, M. K. & Annunziata, C. M. Molecular pathways: The Balance between cancer and the immune system challenges the therapeutic specificity of targeting nuclear Factor- κ B Signaling for cancer treatment. *Clin. Cancer Res.* **22**, 4302–4308 (2016).
 198. Friedland, J. C. *et al.* α 6 β 4 integrin activates Rac-dependent p21-activated kinase 1 to drive NF- κ B-dependent resistance to apoptosis in 3D mammary acini. *J. Cell Sci.* **120**, 3700–3712 (2007).
 199. Ahmed, K. M., Zhang, H. & Park, C. C. NF- κ B regulates radioresistance mediated by β 1-integrin in three-dimensional culture of breast cancer cells. *Cancer Res.* **73**, 3737–3748 (2013).
 200. Murray, S., Briasoulis, E., Linardou, H., Bafaloukos, D. & Papadimitriou, C. Taxane resistance in breast cancer: Mechanisms, predictive biomarkers and circumvention strategies. *Cancer Treat. Rev.* **38**, 890–903 (2012).
 201. Magbanua, M. J. M. *et al.* Serial expression analysis of breast tumors during neoadjuvant chemotherapy reveals changes in cell cycle and immune pathways associated with recurrence and response. *Breast Cancer Res.* **17**, 1–13 (2015).
 202. Sutherland, R. Cell and environment interactions in tumor microregions: the multicell spheroid model. *Science (80-.)*. **240**, 177–185 (1988).
 203. Durand, R. E. & Sutherland, R. M. Effects of intercellular contact on repair of radiation damage. *Exp. Cell Res.* **71**, 75–80 (1972).
 204. Schrader, J. *et al.* Matrix stiffness modulates proliferation, chemotherapeutic response, and dormancy in hepatocellular carcinoma cells. *Hepatology* **53**, 1192–1205 (2011).

205. Hirata, E. *et al.* Intravital imaging reveals how BRAF inhibition generates drug-tolerant microenvironments with high integrin $\alpha 1$ /FAK Signaling. *Cancer Cell* **27**, 574–588 (2015).
206. Nguyen, T. V., Sleiman, M., Moriarty, T., Herrick, W. G. & Peyton, S. R. Sorafenib resistance and JNK signaling in carcinoma during extracellular matrix stiffening. *Biomaterials* **35**, 5749–5759 (2014).
207. Lee, J. Y. *et al.* YAP-independent mechanotransduction drives breast cancer progression. *Nat. Commun.* **10**, 1–9 (2019).
208. Riedl, A. *et al.* Comparison of cancer cells in 2D vs 3D culture reveals differences in AKT–mTOR–S6K signaling and drug responses. *J. Cell Sci.* **130**, 203–218 (2017).
209. Fournier, A. K. *et al.* Rac-dependent cyclin D1 gene expression regulated by cadherin- and integrin-mediated adhesion. *J. Cell Sci.* **121**, 226–233 (2008).
210. Xia, Y., Shen, S. & Verma, I. M. NF- κ B, an Active Player in Human Cancers. *Cancer Immunol. Res.* **2**, 823–830 (2014).
211. Lin, Y., Bai, L., Chen, W. & Xu, S. The NF- κ B activation pathways, emerging molecular targets for cancer prevention and therapy. *Expert Opin. Ther. Targets* **14**, 45–55 (2009).
212. Baud, V. & Karin, M. Is NF- κ B a good target for cancer therapy? Hopes and pitfalls. *Nat. Rev. Drug Discov.* (2009). doi:10.1177/140349487800600105
213. Bardia, A. *et al.* Paclitaxel With Inhibitor of Apoptosis Antagonist, LCL161, for Localized Triple-Negative Breast Cancer, Prospectively Stratified by Gene Signature in a Biomarker-Driven Neoadjuvant Trial. *J. Clin. Oncol.* **36**, 3126–3133 (2018).
214. Tornatore, L. *et al.* Cancer-Selective Targeting of the Nf-KB Survival Pathway With Gadd45B/Mkk7 Inhibitors. *Cancer Cell* **26**, 495–508 (2014).
215. Chan, T.-S. *et al.* Metronomic chemotherapy prevents therapy-induced stromal activation and induction of tumor-initiating cells. *J. Exp. Med.* **213**, 2967–2988 (2016).
216. Van Antwerp, D. J., Martin, S. J., Kafri, T., Green, D. R. & Verma, I. M. Suppression of

- TNF- α -Induced Apoptosis by NF- κ B. *Science* (80-.). **274**, 787–789 (1996).
217. Przybyla, L., Lakins, J. N., Sunyer, R., Trepap, X. & Weaver, V. M. Monitoring developmental force distributions in reconstituted embryonic epithelia. *Methods* **94**, 101–113 (2016).
218. Subramanian, A. *et al.* Gene set enrichment analysis: a knowledge-based approach for interpreting genome-wide expression profiles. *Proc. Natl. Acad. Sci. U. S. A.* **102**, 15545–50 (2005).
219. Stender, J. D. *et al.* Structural and Molecular Mechanisms of Cytokine-Mediated Endocrine Resistance in Human Breast Cancer Cells. *Mol. Cell* **65**, 1122-1135.e5 (2017).
220. Flavell, R. A., Sanjabi, S., Wrzesinski, S. H. & Licona-Limón, P. The polarization of immune cells in the tumour environment by TGF β . *Nat. Rev. Immunol.* **10**, 554–567 (2010).
221. Oakes, P. W. *et al.* Neutrophil morphology and migration are affected by substrate elasticity. *Blood* **114**, 1387–1395 (2009).
222. Jannat, R. A., Robbins, G. P., Ricart, B. G., Dembo, M. & Hammer, D. A. Neutrophil adhesion and chemotaxis depend on substrate mechanics. *J. Phys. Condens. Matter* **22**, 194117 (2010).
223. McWhorter, F. Y., Wang, T., Nguyen, P., Chung, T. & Liu, W. F. Modulation of macrophage phenotype by cell shape. *Proc. Natl. Acad. Sci. U. S. A.* **110**, 17253–8 (2013).
224. Afik, R. *et al.* Tumor macrophages are pivotal constructors of tumor collagenous matrix. *J. Exp. Med.* **213**, jem.20151193 (2016).
225. Lewis, C. E. & Pollard, J. W. Distinct role of macrophages in different tumor microenvironments. *Cancer Res.* **66**, 605–612 (2006).
226. Ruffell, B., Affara, N. I. & Coussens, L. M. Differential macrophage programming in the tumor microenvironment. *Trends Immunol.* **33**, 119–126 (2012).

227. Qian, B.-Z. & Pollard, J. W. Macrophage diversity enhances tumor progression and metastasis. *Cell* **141**, 39–51 (2010).
228. Cassetta, L. & Pollard, J. W. Targeting macrophages: Therapeutic approaches in cancer. *Nat. Rev. Drug Discov.* **17**, 887–904 (2018).
229. Kolaczkowska, E. & Kubes, P. Neutrophil recruitment and function in health and inflammation. *Nat. Rev. Immunol.* **13**, 159–175 (2013).
230. Mestas, J. & Hughes, C. C. W. Of Mice and Not Men: Differences between Mouse and Human Immunology. *J. Immunol.* **172**, 2731–2738 (2004).
231. Lahoz-Beneytez, J. *et al.* Human neutrophil kinetics: Modeling of stable isotope labeling data supports short blood neutrophil half-lives. *Blood* **127**, 3431–3438 (2016).
232. Kovtun, A., Messerer, D. A. C., Scharffetter-Kochanek, K., Huber-Lang, M. & Ignatius, A. Neutrophils in Tissue Trauma of the Skin, Bone, and Lung: Two Sides of the Same Coin. *J. Immunol. Res.* **2018**, 8173983 (2018).
233. McDonald, B. *et al.* Intravascular danger signals guide neutrophils to sites of sterile inflammation. *Science (80-.)*. **330**, 362–366 (2010).
234. Afonso, P. V. *et al.* LTB₄ Is a Signal-Relay Molecule during Neutrophil Chemotaxis. *Dev. Cell* **22**, 1079–1091 (2012).
235. Kubes, P. The enigmatic neutrophil: what we do not know. *Cell Tissue Res.* **371**, 399–406 (2018).
236. Casbon, A.-J. *et al.* Invasive breast cancer reprograms early myeloid differentiation in the bone marrow to generate immunosuppressive neutrophils. *Proc. Natl. Acad. Sci. U. S. A.* **112**, E566-75 (2015).
237. Tabariès, S. *et al.* Granulocytic immune infiltrates are essential for the efficient formation of breast cancer liver metastases. *Breast Cancer Res.* **17**, 45 (2015).
238. Coffelt, S. B. *et al.* IL-17-producing $\gamma\delta$ T cells and neutrophils conspire to promote breast cancer metastasis. *Nature* **522**, 345–8 (2015).

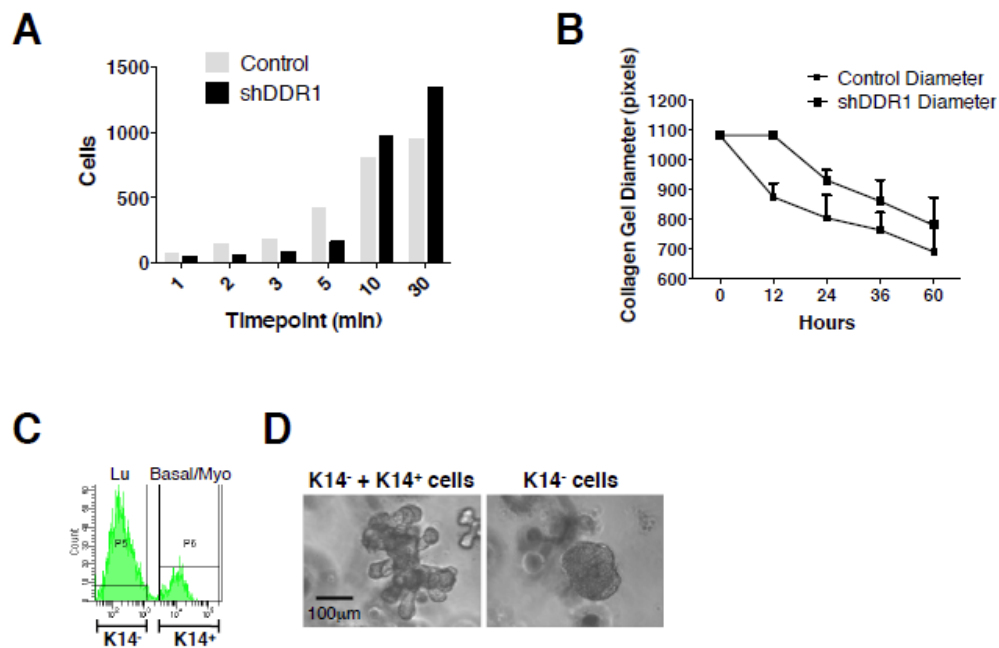
239. Coffelt, S. B., Wellenstein, M. D. & de Visser, K. E. Neutrophils in cancer: neutral no more. *Nat. Rev. Cancer* **16**, 431–46 (2016).
240. Granot, Z. & Jablonska, J. Distinct Functions of Neutrophil in Cancer and Its Regulation. *Mediators Inflamm.* **2015**, (2015).
241. Wculek, S. K. & Malanchi, I. Neutrophils support lung colonization of metastasis-initiating breast cancer cells. *Nature* **528**, 1–3 (2015).
242. Fridlender, Z. G. *et al.* Polarization of Tumor-Associated Neutrophil Phenotype by TGF- β : 'N1' versus 'N2' TAN. *Cancer Cell* **16**, 183–194 (2009).
243. Spiegel, A. *et al.* Neutrophils suppress intraluminal NK cell-mediated tumor cell clearance and enhance extravasation of disseminated carcinoma cells. *Cancer Discov.* **6**, 630–649 (2016).
244. Wang, G. *et al.* Targeting YAP-dependent MDSC infiltration impairs tumor progression. *Cancer Discov.* **6**, 80–95 (2016).
245. Acharyya, S. *et al.* A CXCL1 paracrine network links cancer chemoresistance and metastasis. *Cell* **150**, 165–178 (2012).
246. Doglioni, G., Parik, S. & Fendt, S. M. Interactions in the (pre)metastatic niche support metastasis formation. *Frontiers in Oncology* **9**, (2019).
247. Jablonska, J. & Granot, Z. Neutrophil, quo vadis? *J. Leukoc. Biol.* **102**, 685–688 (2017).
248. Albregues, J. *et al.* Neutrophil extracellular traps produced during inflammation awaken dormant cancer cells in mice. *Science (80-.).* **361**, (2018).
249. Finisguerra, V. *et al.* MET is required for the recruitment of anti-tumoural neutrophils. *Nature* **522**, 349–353 (2015).
250. Comen, E. *et al.* TNF is a key cytokine mediating neutrophil cytotoxic activity in breast cancer patients. *npj Breast Cancer* **2**, 16009 (2016).
251. Granot, Z. *et al.* Tumor entrained neutrophils inhibit seeding in the premetastatic lung. *Cancer Cell* **20**, 300–314 (2011).

252. Eruslanov, E. B., Singhal, S. & Albelda, S. M. Mouse versus human neutrophils in cancer: a major knowledge gap. *Trends in Cancer* (2017).
253. Gabrilovich, D. I., Ostrand-Rosenberg, S. & Bronte, V. Coordinated regulation of myeloid cells by tumours. *Nat. Rev. Immunol.* **12**, 253–68 (2012).
254. Wang, J. *et al.* Visualizing the function and fate of neutrophils in sterile injury and repair. *Science* (80-.). **358**, 111–116 (2017).
255. Gasson, J. C. Molecular physiology of granulocyte-macrophage colony-stimulating factor. *Blood* **77**, 1131–1145 (1991).
256. Song, Y. *et al.* In vivo antitumor activity of a recombinant IL7/IL15 hybrid cytokine in mice. *Mol. Cancer Ther.* **15**, 2413–2421 (2016).
257. Li, B., VanRoey, M. J. & Jooss, K. Recombinant IL-7 enhances the potency of GM-CSF-secreting tumor cell immunotherapy. *Clin. Immunol.* **123**, 155–165 (2007).
258. Klebanoff, C. A. *et al.* IL-15 enhances the in vivo antitumor activity of tumor-reactive CD8 + T Cells. *Proc. Natl. Acad. Sci. U. S. A.* **101**, 1969–1974 (2004).
259. Teague, R. M. *et al.* Interleukin-15 rescues tolerant CD8+ T cells for use in adoptive immunotherapy of established tumors. *Nat. Med.* **12**, 335–341 (2006).
260. Zheng, L. M. *et al.* Interleukin-10 inhibits tumor metastasis through an NK cell-dependent mechanism. *J. Exp. Med.* **184**, 579–584 (1996).
261. Fujii, S. I., Shimizu, K., Shimizu, T. & Lotze, M. T. Interleukin-10 promotes the maintenance of antitumor CD8 + T-cell effector function in situ. *Blood* **98**, 2143–2151 (2001).
262. Berman, R. M. *et al.* Systemic administration of cellular IL-10 induces an effective, specific, and long-lived immune response against established tumors in mice. *J. Immunol.* **157**, 231–8 (1996).
263. Emmerich, J. *et al.* IL-10 directly activates and expands tumor-resident CD8+ T cells without De Novo infiltration from secondary lymphoid organs. *Cancer Res.* **72**, 3570–

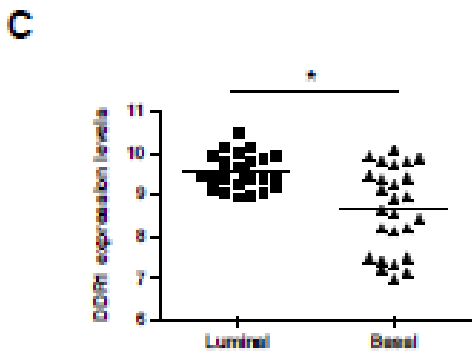
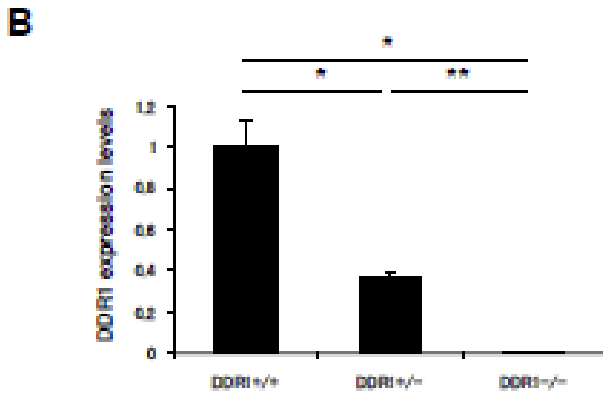
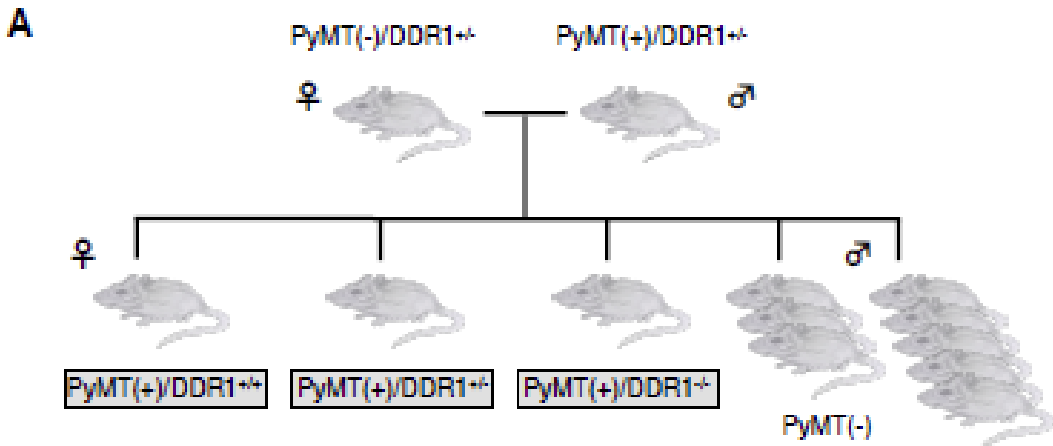
- 3581 (2012).
264. Mumm, J. B. *et al.* IL-10 Elicits IFN γ -Dependent tumor immune surveillance. *Cancer Cell* **20**, 781–796 (2011).
265. Guglietta, S. *et al.* Coagulation induced by C3aR-dependent NETosis drives protumorigenic neutrophils during small intestinal tumorigenesis. *Nat. Commun.* **7**, 11037 (2016).
266. Evrard, M. *et al.* Developmental Analysis of Bone Marrow Neutrophils Reveals Populations Specialized in Expansion, Trafficking, and Effector Functions. *Immunity* **48**, 364-379.e8 (2018).
267. Kim, J. H. *et al.* Aged polymorphonuclear leukocytes cause fibrotic interstitial lung disease in the absence of regulation by B cells article. *Nat. Immunol.* **19**, 192–201 (2018).
268. Uhl, B. *et al.* Aged neutrophils contribute to the first line of defense in the acute inflammatory response. *Blood* **128**, 2327–2337 (2016).
269. Moroishi, T. *et al.* The Hippo Pathway Kinases LATS1/2 Suppress Cancer Immunity. *Cell* **167**, 1525-1539.e17 (2016).
270. Gao, X., Wang, H., Yang, J. J., Liu, X. & Liu, Z. R. Pyruvate Kinase M2 Regulates Gene Transcription by Acting as a Protein Kinase. *Mol. Cell* **45**, 598–609 (2012).
271. Snaebjornsson, M. T. & Schulze, A. Non-canonical functions of enzymes facilitate cross-talk between cell metabolic and regulatory pathways. *Experimental and Molecular Medicine* **50**, 1–16 (2018).
272. Barker, H. E., Cox, T. R. & Erler, J. T. The rationale for targeting the LOX family in cancer. *Nat. Rev. Cancer* **12**, 540–552 (2012).
273. Iturbide, A., García De Herreros, A. & Peiró, S. A new role for LOX and LOXL2 proteins in transcription regulation. *FEBS J.* **282**, 1768–1773 (2015).
274. Gocheva, V. *et al.* Quantitative proteomics identify Tenascin-C as a promoter of lung cancer progression and contributor to a signature prognostic of patient survival. *Proc.*

Natl. Acad. Sci. **114**, E5625–E5634 (2017).

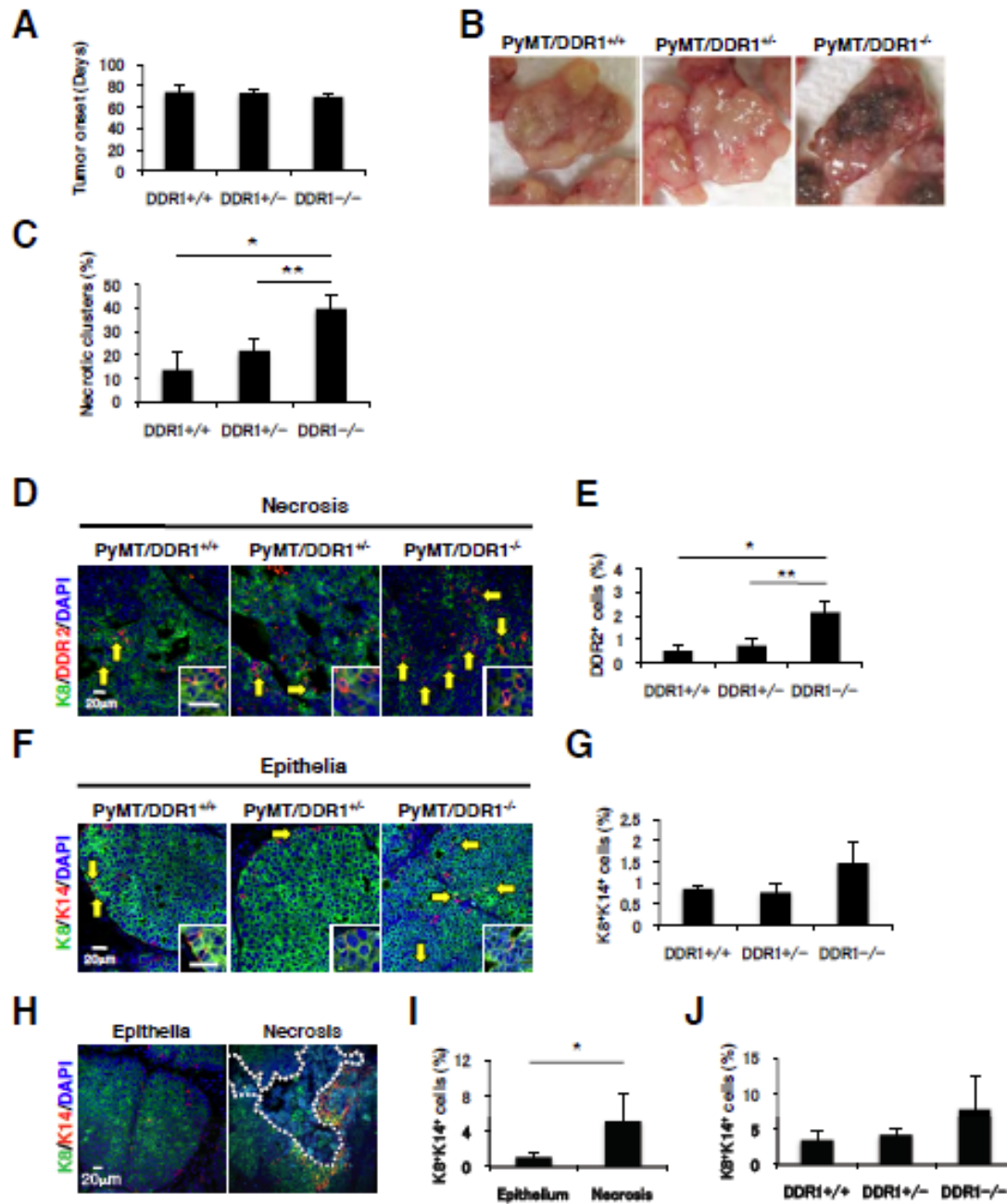
Appendix 1: Supplementary Material for Chapter 2



Supplementary Figure A1.1: (A) Quantification of the number of cells adhered to collagen coated tissue culture polystyrene at the indicated time point. Measurements were taken by imaging the culture wells and counting the number of cells per field of view. (B) Quantification of collagen gel contraction by cells seeded in free-floating collagen gels. Data are shown as the change in collagen gel diameter over time. (C, D) K14⁻ and K14⁺ mammary epithelial cells were isolated by flow cytometry from K14-GFP mice (C). K14⁻ luminal cells with or without K14⁺ basal/myoepithelial cells were aggregated overnight *in vitro* and then used in a 3D branching assay in Matrigel. K14⁺ basal/myoepithelial cells promoted mammary branching (D).

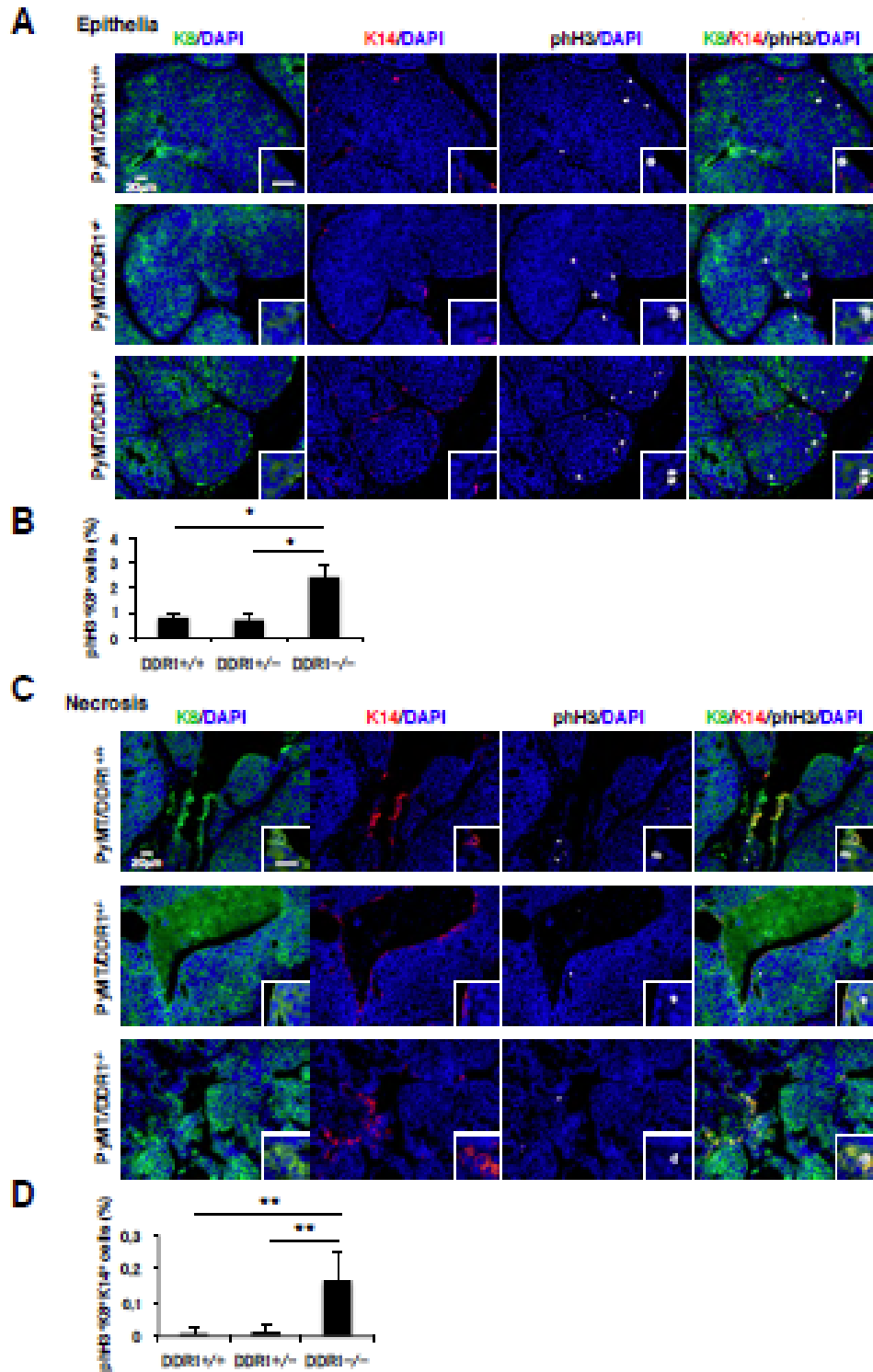


Supplementary Figure A1.2: (A) We crossed DDR1^{-/-} mice with MMTV-PyMT to determine the effects of DDR1 deletion in mammary tumorigenesis. (B) DDR1 expression levels of primary tumors from PyMT/DDR1^{+/+}, PyMT/DDR1^{+/-} and PyMT/DDR1^{-/-} mice by qPCR. PyMT/DDR1^{-/-} tumor did not express DDR1 and DDR1 expression level of PyMT/DDR1^{+/-} tumor was ~ 40% of PyMT/DDR1^{+/+} tumors. Data are shown as mean ± SD, n=2-4, **p* < 0.001, ***p* < 0.01 (one-way ANOVA and unpaired Student's t test). (C) DNA microarray datasets (Neve et al. 2006) were used to determine DDR1 expression in breast cancer cell lines. DDR1 expression was higher in luminal-type than basal-type (Basal A+B) cell lines. **p* < 0.001 (unpaired Student's t test).



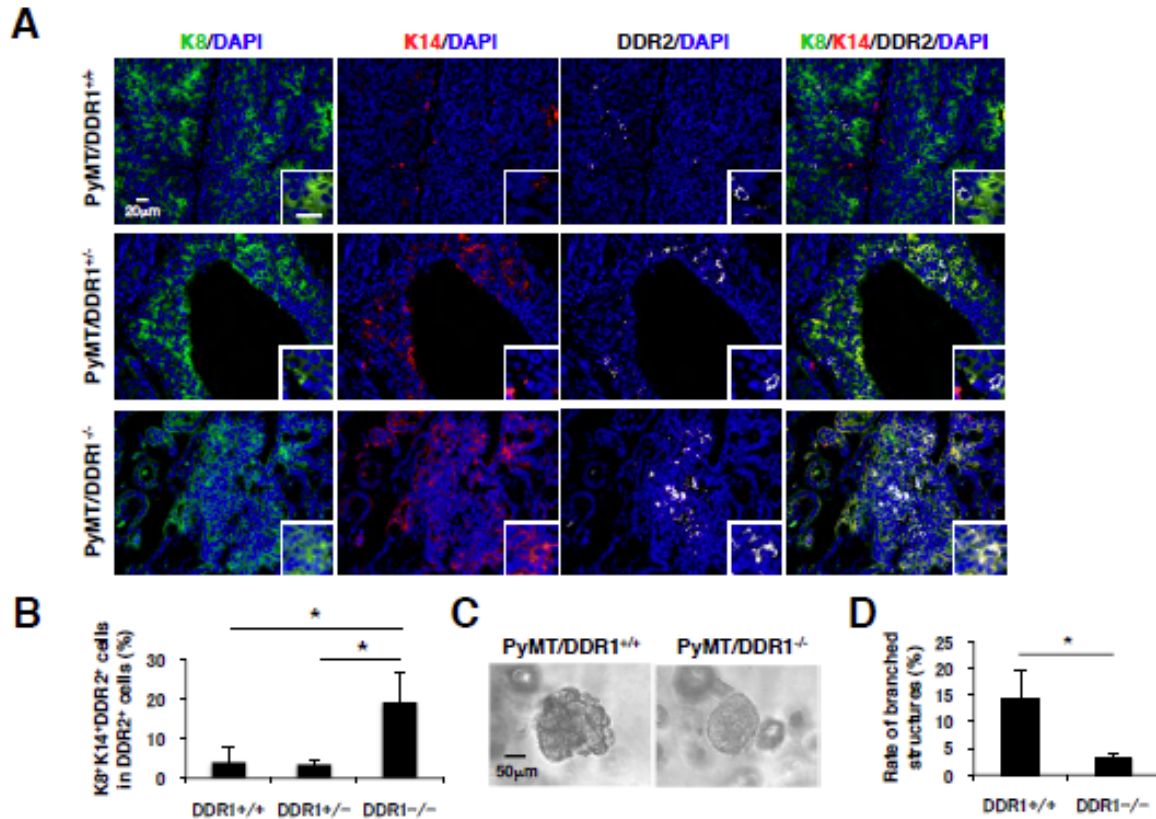
Supplementary Figure A1.3: (A) Day of primary tumor onset were not statistically significantly different in DDR1^{+/+}, DDR1^{+/-} and DDR1^{-/-} mice (Data shown as mean \pm SD, n=4-7, unpaired Student's t test). (B) Representative photographs show that hemorrhagic necrosis was characteristic of DDR1^{-/-} mammary tumors (13 weeks). n=3-7. (C) Rate of necrotic clusters out of small clusters (200-300 μ m length) was measured. Necrotic small clusters increased in DDR1^{-/-} tumors. Data are shown as mean \pm SD, n=3, **p* < 0.01, ***p* < 0.02 (one-way ANOVA and unpaired Student's t test). (D, E) Immunofluorescence of the primary tumors was performed by using anti-keratin 8 (green) and anti-DDR2 (red) antibodies. DAPI (blue) stained nuclei. Representative photographs of tumor necrosis are shown (D). The ratio of DDR2⁺ cells per epithelial cells increased significantly near necrotic fields of DDR1^{-/-} mammary tumor tissues. Data are shown as mean \pm SD, n=3, **p* < 0.01, ***p* < 0.02 (one-way ANOVA and unpaired Student's t test) (E). (F-J)

Immunofluorescence of the primary tumors was performed by using anti-keratin 8 (green) and anti-keratin 14 (red) antibodies. DAPI (blue) stained nuclei. K8⁺K14⁺ basal-like cells (yellow) showed an increased trend in DDR1^{-/-} epithelial clusters (**F**, **G**), which was not statistically significant (Data shown as mean \pm SD, n=3, unpaired Student's t test). Representative photos of tumor epithelial clusters (DDR1^{+/-}, **H left panel**) and necrosis (DDR1^{-/-}, **H right panel**) are shown. The white dots represent a border between an epithelium and a necrotic field (**H right panel**). The ratios of K8⁺K14⁺ basal-like cells per epithelial (K8⁺ and K14⁺) cell increased significantly near necrotic fields (**I**). Data are shown as mean \pm SD, n=9, **p* <0.01 (unpaired Student's t test). K8⁺K14⁺ cells showed an increased trend near necrotic fields of DDR1^{-/-} mammary tumor tissues (**J**), which was not statistically significant (Data shown as mean \pm SD, n=3, unpaired Student's t test).



Supplementary Figure A1.4: (A-D) Immunofluorescence of the primary tumors was performed by using anti-keratin 8 (green), anti-keratin 14 (red) and anti-phospho-histone H3 (white) antibodies. DAPI (blue) stained nuclei. K8⁺ luminal cells were mainly proliferating in the epithelial clusters of DDR1^{-/-} mammary tumors (**A**, **B**). K8⁺K14⁺ basal-like cells were proliferating slightly

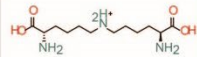
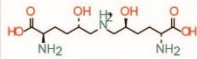
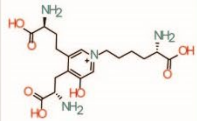
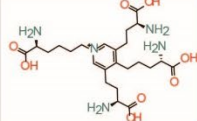
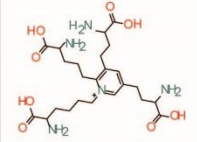
but significantly near the necrotic regions in DDR1^{-/-} tumors (**C**, **D**). Data are shown as mean ± SD, n=3, **p* <0.01, ***p* <0.05 (one-way ANOVA and unpaired Student's t test).



Supplementary Figure A1.5: (A, B) Immunofluorescence of the primary tumors was performed by using anti-keratin 8 (green), anti-keratin 14 (red) and DDR2 (white) antibodies. DAPI (blue) stained nuclei. Rate of K8⁺K14⁺ basal-like cells in DDR2⁺ cells increased significantly in DDR1^{-/-} tumors. Data are shown as mean \pm SD, $n=3$, $*p < 0.05$ (one-way ANOVA and unpaired Student's t test). **(C, D)** Primary tumors from 10-week-old PyMT/DDR1^{+/+} or PyMT/DDR1^{-/-} mice were digested with collagenase into organoids. The 3D assay of the organoids was performed in Matrigel in duplicate. Representative photographs were shown **(C)**. DDR1^{-/-} tumor organoids showed decreased branching structures (Data shown as mean \pm SD, $n=2$, $*p < 0.05$, unpaired Student's t test) **(D)**.

Appendix 2: Supplementary Material for Chapter 3

Supplementary Table A2.1: Serial dilutions of crosslinked amino acid standards were prepared in the background of *E. coli* hydrolysates and the lowest limit of detection (LLOD) and the lowest limit of quantification (LLOQ) were determined on a QExactive mass spectrometer. The LLOD is defined here as the concentration that is required to produce a signal that is three times the noise level. The LLOQ is the analyte concentration that is required to produce a signal that is three times that of the LLOD. *Denotes isomers that were not resolved.

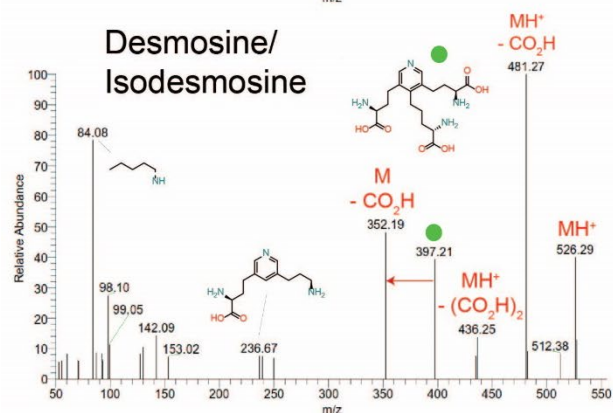
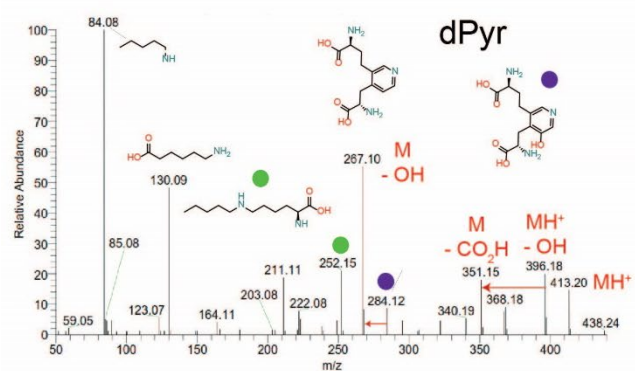
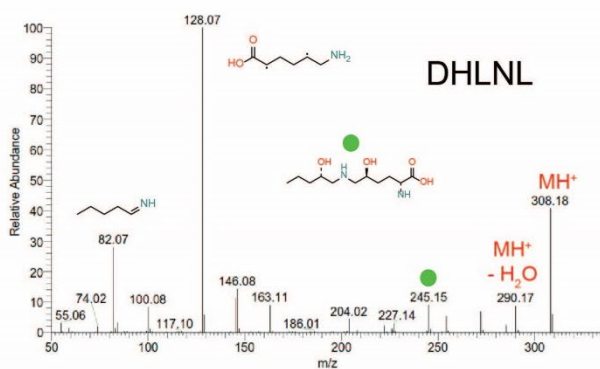
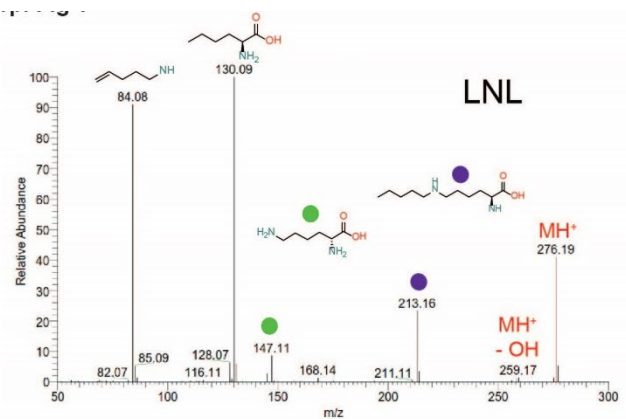
xAA Standard	Letter Code	Elemental Composition	RT (min)	Mass (Da)	Accuracy (ppm)	LLOD (fmole)	R ²	LLOQ (fmole)	Structure
Lysinonorleucine	LNL	C ₁₂ H ₂₆ N ₃ O ₄ ⁺	5.69	276.19	1.5	75	0.96	225	
Dihydroxy lysinonorleucine	DHLNL	C ₁₂ H ₂₆ N ₃ O ₆ ⁺	7.16	308.18	2	125	0.95	375	
deoxy Lysyl pyridinoline	dPyr	C ₁₈ H ₂₉ N ₄ O ₇ ⁺	8.14	413.2	4.5	250	0.98	750	
Desmosine*	Des	C ₂₄ H ₄₀ N ₅ O ₈ ⁺	10.14	526.29	0.9	156	0.92	468	
Isodesmosine*	iDes	C ₂₄ H ₄₀ N ₅ O ₈ ⁺	10.14	526.29	0.9	156	0.92	468	

Supplementary Table A2.2: Characterization of breast cancer patients used to develop neoplastic epithelial LH2 H-score.

Distribution of patient and tumor characteristics				
All n=910				
Tumor in tissue microarray, n (%)			Yes 718/910 (78.9)	
Lysyl hydroxylase 2 (LH2) epithelial expression assessable, n (%)			Yes, 468/718 (65.2%)	
LH2 neg/weak/moderate/strong		LH2 negative	LH2 weak	LH2 moderate/strong
		279 (59.6%)	112 (23.9%)	77 (16.5%)
Factor	n (%) or mean (min-max)	n (%) or mean (min-max)	n (%) or mean (min-max)	n (%) or mean (min-max)
Age at diagnosis	65.5 (45.7-87.3)	63.9 (48.4-84.7)	61.7 (46.4-85.6)	63.9 (45.7-87.3)
years (n= 910)				
BMI at baseline (n=910)				
<25	466 (51)	154 (56.8)	64 (57.1)	36 (46.8)
≥25 and <30	310 (34)	77 (28.4)	36 (32.1)	27 (35.1)
>30	134 (15)	40 (14.8)	12 (10.7)	14 (18.2)
Tumor size (n= 887)				
≤20 mm	637 (72)	190 (70.6)	77 (68.8)	43 (55.8)
>20 mm	250 (28)	79 (29.4)	35 (31.3)	34 (44.2)
ALNI (n=859)				
Negative	588 (68.5)	175 (67.6)	67 (61.5)	50 (65.8)
Positive (≥1 metastatic node)	271 (31.5)	84 (32.4)	42 (38.5)	26 (34.2)
Grade, NHG (n=860)				
I	233 (27.1)	84 (31.7)	21 (18.9)	12 (15.8)
II	405 (47.1)	138 (52.1)	52 (46.8)	14 (18.4)
III	222 (25.8)	43 (16.2)	38 (34.2)	50 (65.8)
ER status (n=784)				
Positive (>10%)	690 (88.0)	230 (93.5)	93 (87.7)	44 (63.8)
Negative (<10%)	94 (12.0)	16 (6.5)	13 (12.3)	25 (36.2)
HER2 status (n=609)				
Negative	556 (91.3)	161 (89.9)	71 (86.6)	50 (89.3)
Positive	53 (8.7)	18 (10.1)	11 (13.4)	6 (10.7)
Ki67 (n=655)				
Low (≤10%)	434 (66.3)	143 (71.5)	58 (61.7)	18 (32.7)
High (>10%)	221(33.7)	57 (28.5)	36 (38.3)	37 (67.3)
Molecular subtypes (n=639)				
ER+/HER2-	536 (83.9)	169 (88.0)	76 (80.9)	29 (53.7)
HER2+	53 (8.3)	5 (4.4)	11 (11.7)	6 (11.1)
TNBC	50 (7.8)	3 (2.7)	7 (7.4)	19 (35.2)

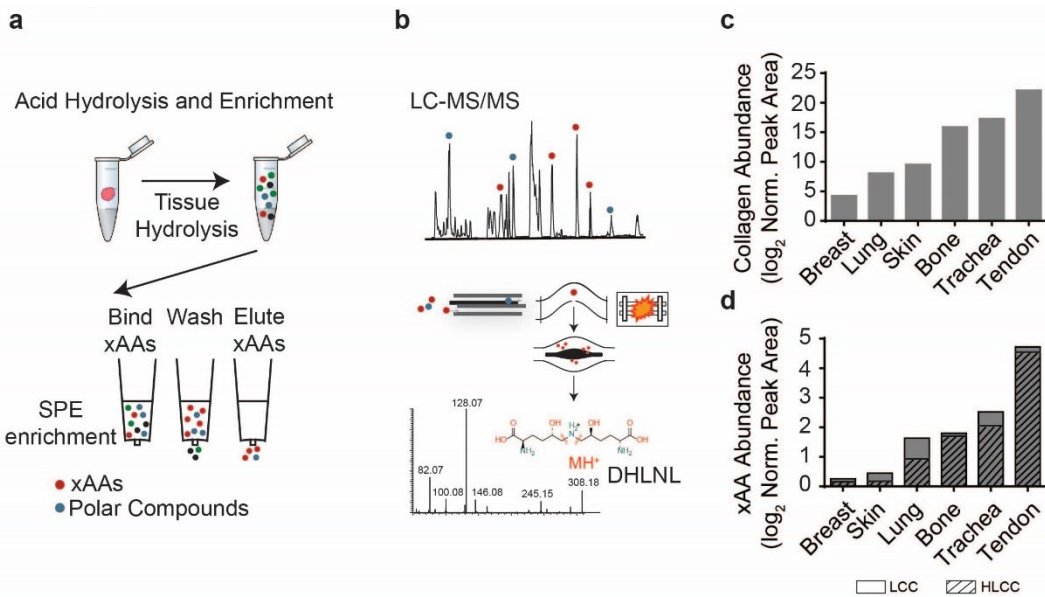
Supplementary Table A2.3: Characterization of breast cancer patients used to develop stromal LH2 H-score.

Distribution of patient and tumor characteristics				
All n=910				
Tumor in tissue microarray, n (%)			Yes 718/910 (78.9)	
Lysyl hydroxylase 2 (LH2) stromal expression assessable, n (%)			Yes, 505/718 (70.3%)	
LH2 low/intermediate/high		LH2 low	LH2 intermediate	LH2 high
		171 (33.9%)	188 (37.2%)	146 (28.9%)
Factor	n (%) or mean (min-max)	n (%) or mean (min-max)	n (%) or mean (min-max)	n (%) or mean (min-max)
Age at baseline	56.4 (44.7-73.0)	53.7 (44.9-73.0)	54.2 (44.7-72.7)	53.6 (45.0-72.8)
years (n= 910)				
Age at diagnosis	65.5 (45.7-87.3)	62.6 (48.5-84.7)	63.4 (45.7-87.3)	63.7 (46.4-85.6)
years (n= 910)				
BMI at baseline (n=910)				
<25	466 (51)	98 (57.3)	110 (58.5)	73 (50.0)
≥25 and <30	310 (34)	52 (30.4)	55 (29.3)	47 (32.2)
>30	134 (15)	20 (11.7)	23 (12.2)	26 (17.8)
Tumor size (n= 887)				
≤20 mm	637 (72)	118 (69.8)	131 (70.1)	95 (65.1)
>20 mm	250 (28)	51 (30.2)	56 (29.9)	51 (34.9)
ALNI (n=859)				
Negative	588 (68.5)	116 (72.5)	116 (64.8)	90 (62.5)
Positive (≥1 metastatic node)	271 (31.5)	44 (27.5)	63 (35.2)	54 (37.5)
Grade, NHG (n=860)				
I	233 (27.1)	53 (32.3)	60 (32.3)	21 (14.7)
II	405 (47.1)	86 (52.4)	79 (42.5)	54 (37.8)
III	222 (25.8)	25 (15.2)	47 (25.3)	68 (47.6)
ER status (n=784)				
Positive (>10%)	690 (88.0)	133 (94.3)	155 (89.1)	106 (77.9)
Negative (<10%)	94 (12.0)	8 (5.7)	19 (10.9)	30 (22.1)
HER2 status (n=609)				
Negative	556 (91.3)	104 (95.4)	120 (88.9)	85 (84.2)
Positive	53 (8.7)	5 (4.6)	15 (11.1)	16 (15.8)
Ki67 (n=655)				
Low (≤10%)	434 (66.3)	83 (72.2)	98 (66.7)	54 (48.2)
High (>10%)	221(33.7)	32 (27.8)	49 (26.1)	58 (51.8)
Molecular subtypes (n=639)				
ER+/HER2-	536 (83.9)	105 (92.9)	118 (81.9)	73 (68.2)
HER2+	53 (8.3)	5 (4.4)	15 (10.4)	16 (15.0)
TNBC	50 (7.8)	3 (2.7)	11 (7.6)	18 (16.8)

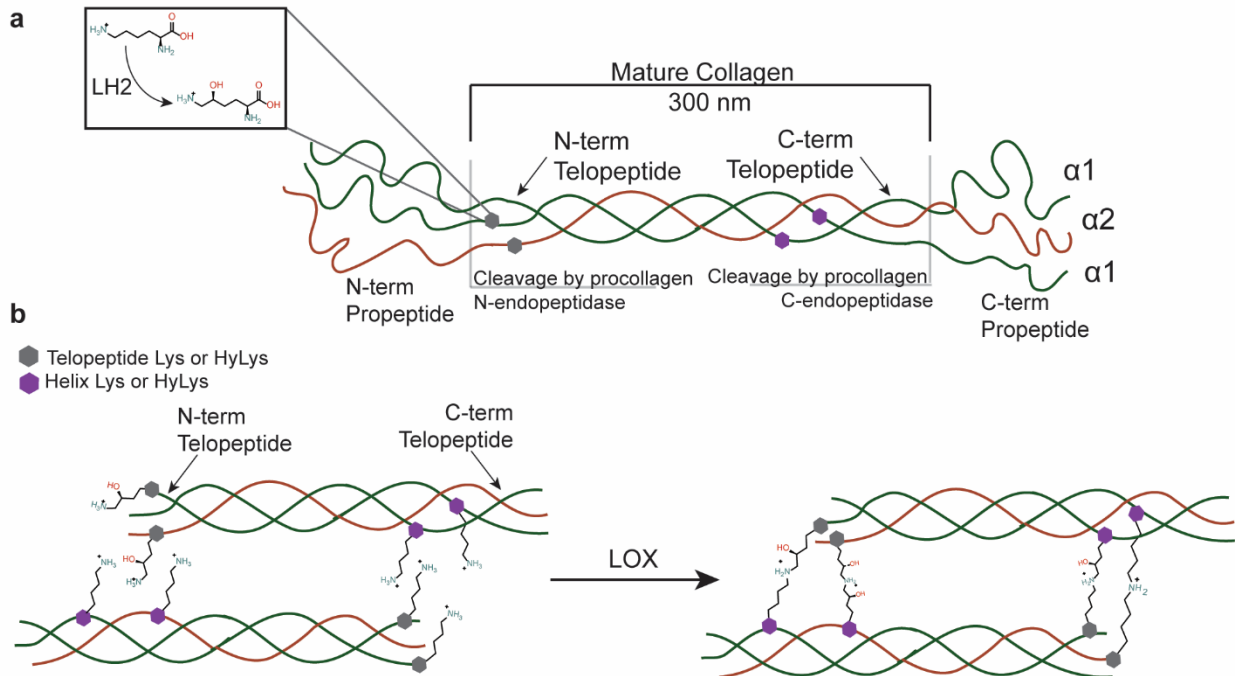


Supplementary Figure A2.1: Partial assignment of MS² fragmentation spectra of crosslinked amino acid standards. MS² fragmentation spectra of commercially available crosslinked amino

acid standards with partial assignment of MS² fragmentation spectra (LNL, **top**; DHLNL, **middle**; dPyr, **bottom**). Protonated forms of precursor ions are denoted by MH⁺ labels. Colored circles above fragment ions are matched to their suggested fragment ion structure above the full spectra or are listed above the ion if space permits.

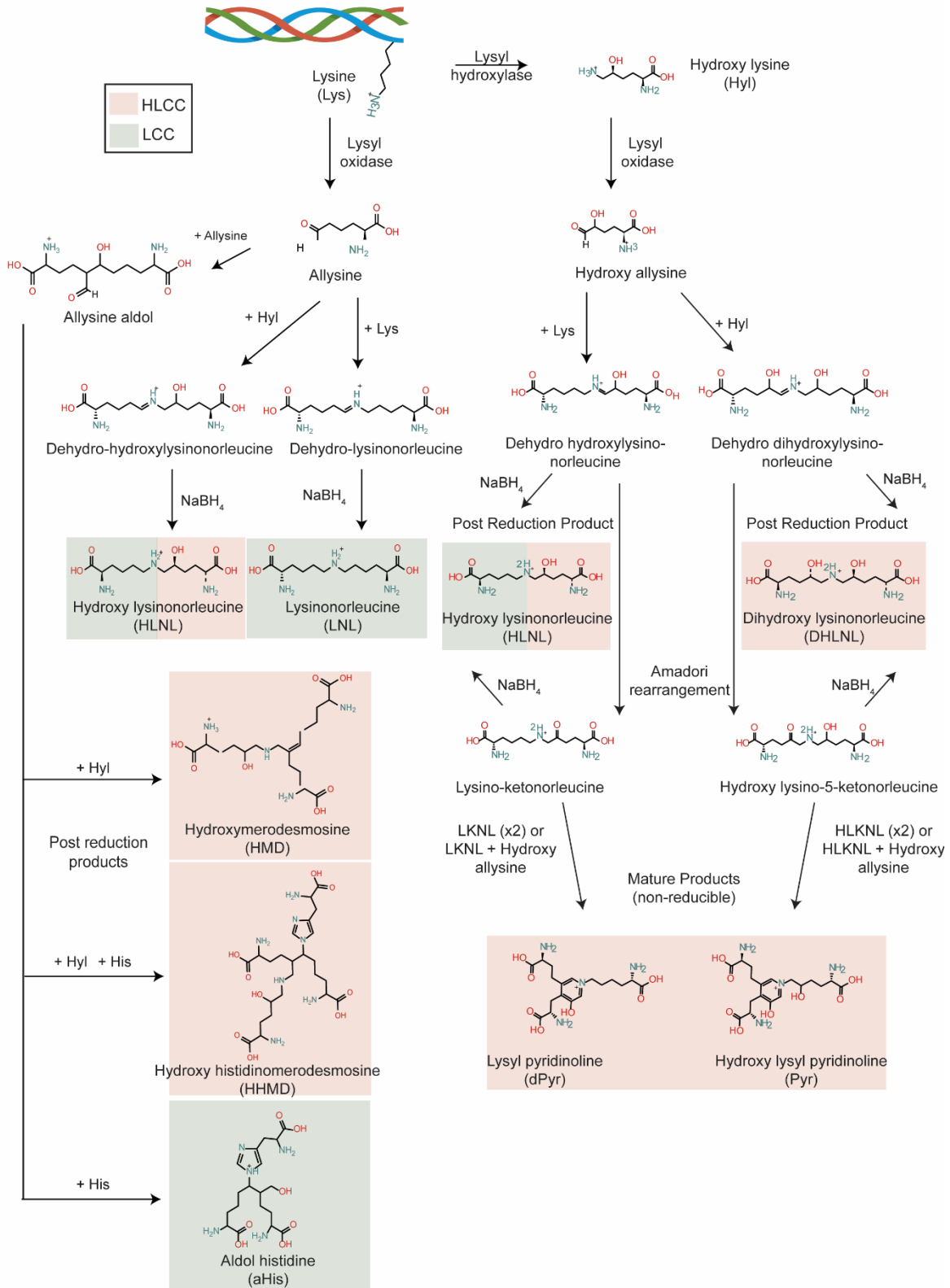


Supplementary Figure A2.2: (a) xAAA workflow schematic. Clinical specimens are hydrolyzed and enriched by solid phase extraction (SPE). (b) The enriched hydrolysate is analyzed by LC-SRM on a hybrid quadrupole orbitrap instrument. MS² spectra is used to accurately identify xAAs such as dihydroxy lysinonorleucine (DHLNL) (c) Bar graphs showing quantification of tissue collagen and (d) total crosslinked amino acids (xAA) measured in human breast, lung, skin, bone, trachea and tendon (pooled $n = 3$ each tissue). The calculated amino acid crosslink values are normalized to total tissue collagen content (hydroxyproline abundance) which is calculated based on wet tissue weight. The final values have been plotted as relative abundance based on peak area. Bar graphs depict relative abundance of Lysine derived-collagen crosslink (LCC) and hydroxylysine-derived collagen crosslink (HLCC) species.



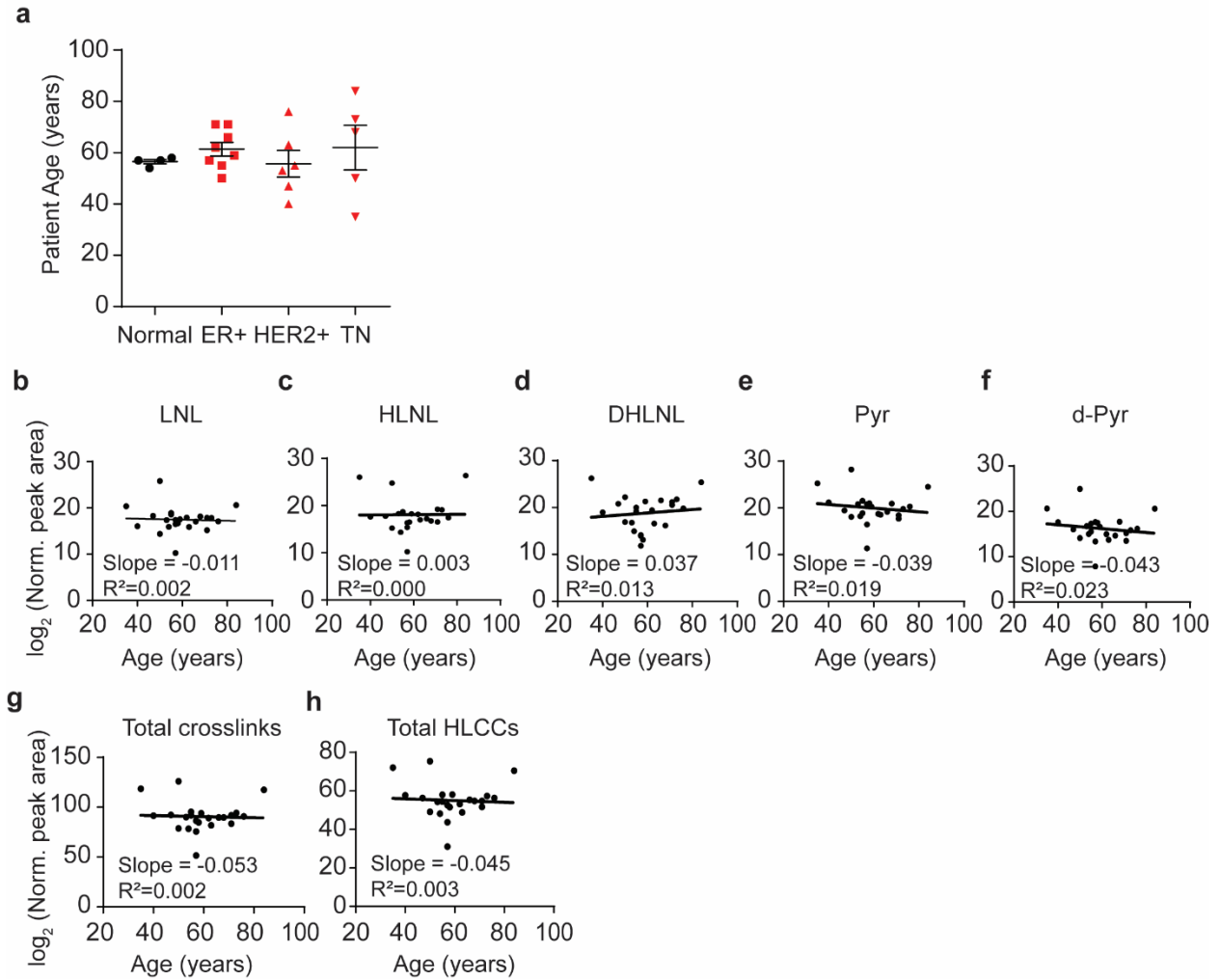
Supplementary Figure A2.3: (a) Schematic of a mature fibrillar collagen fiber. N- and C- terminal telopeptides are hydroxylated by lysyl hydroxylase 2 (LH2). N- and C- terminal propeptides are cleaved by procollagen endopeptidases to form the mature collagen fiber (300 nm). (b) Lysine (Lys) and the hydroxylysine (Hyl) residues in the telopeptide region of mature collagen are targeted by the crosslinking enzyme lysyl oxidase (LOX), which forms reactive aldehyde groups that spontaneously undergo aldol condensation reactions to form covalent collagen crosslinks.

Lysine aldehyde (Lys^{ald}) and hydroxylysine aldehyde (Hyl^{ald}) collagen crosslinking pathways

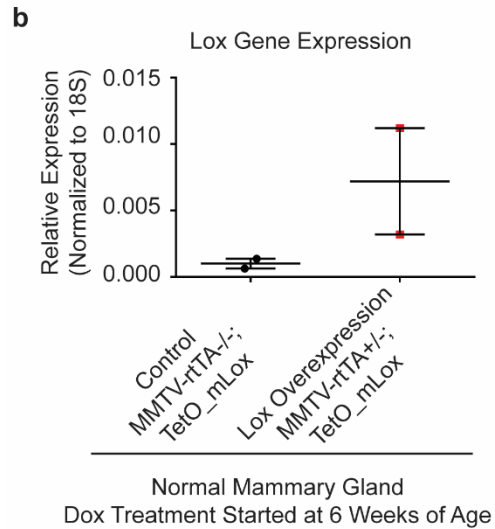
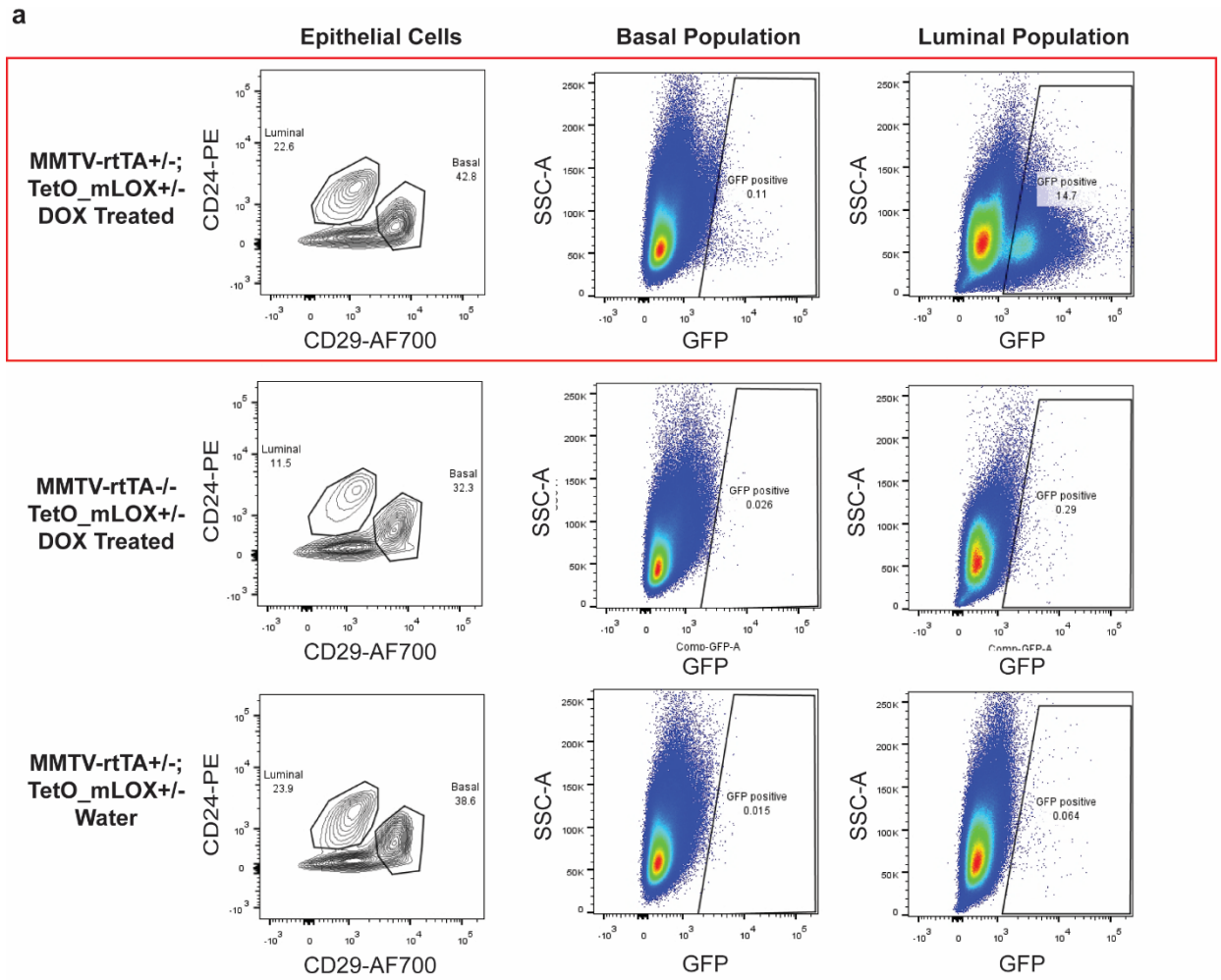


Supplementary Figure A2.4: Lysine aldehyde (Lys^{ald}) and hydroxylysine aldehyde (Hyl^{ald}) collagen crosslinking pathway. Lysyl oxidase modifies Lys residues to form allysine (Lys^{ald}), which spontaneously reacts with Lys and Hyl residues in the helical region to form the Schiff bases

dehydro-hydroxylysinonorleucine (deH-HLNL) dehydro-lysinonorleucine (deh-HLNL). These crosslinks can be reduced with NaBH_4 to form LNL and HLNL. The mature products of these crosslinks are currently unknown. Allysine can combine with an additional allysine residue to form allysine aldol. Allysine aldol can form the trivalent crosslink hydroxyl merodesmosine, aldol histidine, or the tetravalent crosslink histidino-hydroxymerodesmosine (HHMD) (only post-reduction products shown) through aldol condensation reactions with Hyl or histidine (His), or a combination of the two. Red and green shading denotes lysine-derived collagen crosslinks (LCC) or hydroxyl lysine-derived collagen crosslinks (HLCC). Telopeptide lysine residues are modified by lysyl hydroxylase. Lysyl oxidase modifies Hyl residues to hydroxyl allysine (Hyl^{ald}), which spontaneously reacts with Lys and Hyl residues to form the Schiff bases dehydro-dihydroxylysinonorleucine (deH-DHLNL) and dehydro-hydroxylysinonorleucine (deh-HLNL). They then undergo Amadori rearrangements to form hydroxylysino-keto-norleucine (HLKNL) or lysine-keto-norleucine (LKNL), respectively. These crosslinks can be reduced with NaBH_4 to form LNL and DHLNL. Mature crosslink products (Pyr and dPyr) are formed from the reaction of lysine ketonorleucine (LKNL) or hydroxyl lysinoketonorleucine (HKLNL) with hydroxyl allysine. Red and green shading denotes lysine-derived collagen crosslinks (LCC) or hydroxyl lysine-derived collagen crosslinks (HLCC).

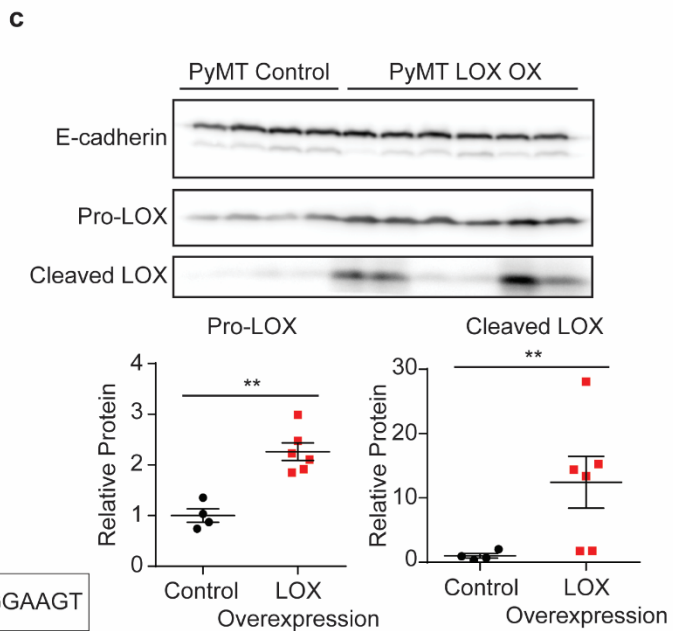


Supplementary Figure A2.5: (a) Scatter plot showing the mean and SEM of patient age for normal and tumor tissue samples by subtype. (b-f) Scatter plots showing the levels of each LCC and HLCC crosslink measured in normal and tumor breast tissues versus patient age. The total abundance of crosslinks (g) was calculated by summing all individual crosslinks and the total tissue HLCC abundance (h) was calculated by summing DHLNL, Pyr, and d-Pyr. All crosslink values are normalized to total collagen content (i.e. hydroxyproline abundance) and wet tissue weight and are plotted as \log_2 transformed normalized peak areas from LC-MS data. The best fit line and its slope and r^2 value are displayed on each plot.

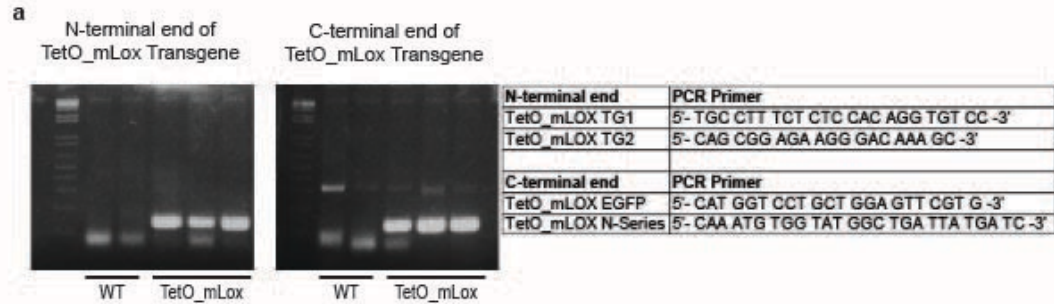


Lox Primers for qPCR:

Mouse	Rev	CGGGAGACCGTACTGGAAGT
Mouse	For	CCCAGCCACATAGATCGCAT

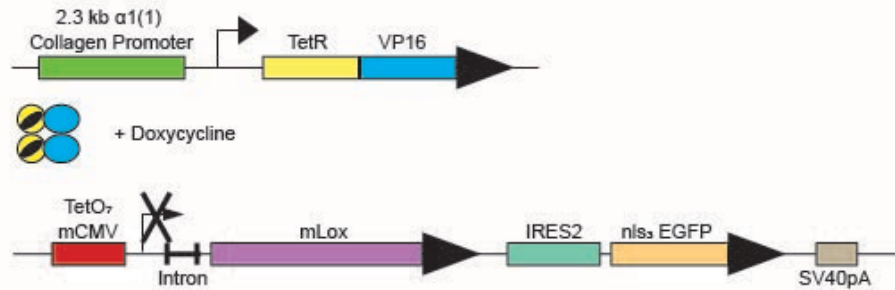


Supplementary Figure A2.6: (a) Representative dot plots (n = 2) of GFP expression in mouse mammary epithelial cells analyzed by flow cytometry. GFP and mLOX are encoded on the same mRNA transcript with independent translation initiation sites. **(Top panel)** GFP expression is induced in DOX treated MMTV-rtTA^{+/-}; TetO_mLox^{+/-} mice. **(Middle and Bottom panels)** GFP expression is not induced in control mice lacking the MMTV-rtTA promoter **(Middle)** or control mice not treated with DOX **(Bottom)**. To select for mammary epithelial cells were gated out cells positive for anti-mouse CD45-APC, anti-mouse CD31-APC, anti-mouse Ter119-APC antibodies. **(b)** Quantification of Lox gene expression in whole mouse mammary gland by RT-qPCR in control MMTV-rtTA^{-/-}; TetO_mLox^{+/-} mice (n = 2) and Lox overexpressing MMTV-rtTA^{+/-}; TetO_mLox^{+/-} (n = 2) mice. **(c)** Western blot of whole tumor lysate from control and epithelial LOX overexpressing PyMT tumors. Scatter plots with mean ± SEM quantify optical density of each band normalized to E-cadherin. Statistical analyses were performed using Mann-Whitney U test (**p < 0.01).

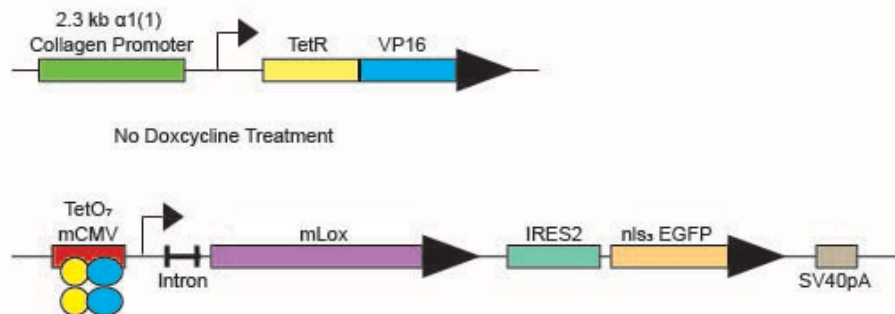


b Inducible lysyl oxidase model using TetOFF system in the background of MMTV-PyMT:

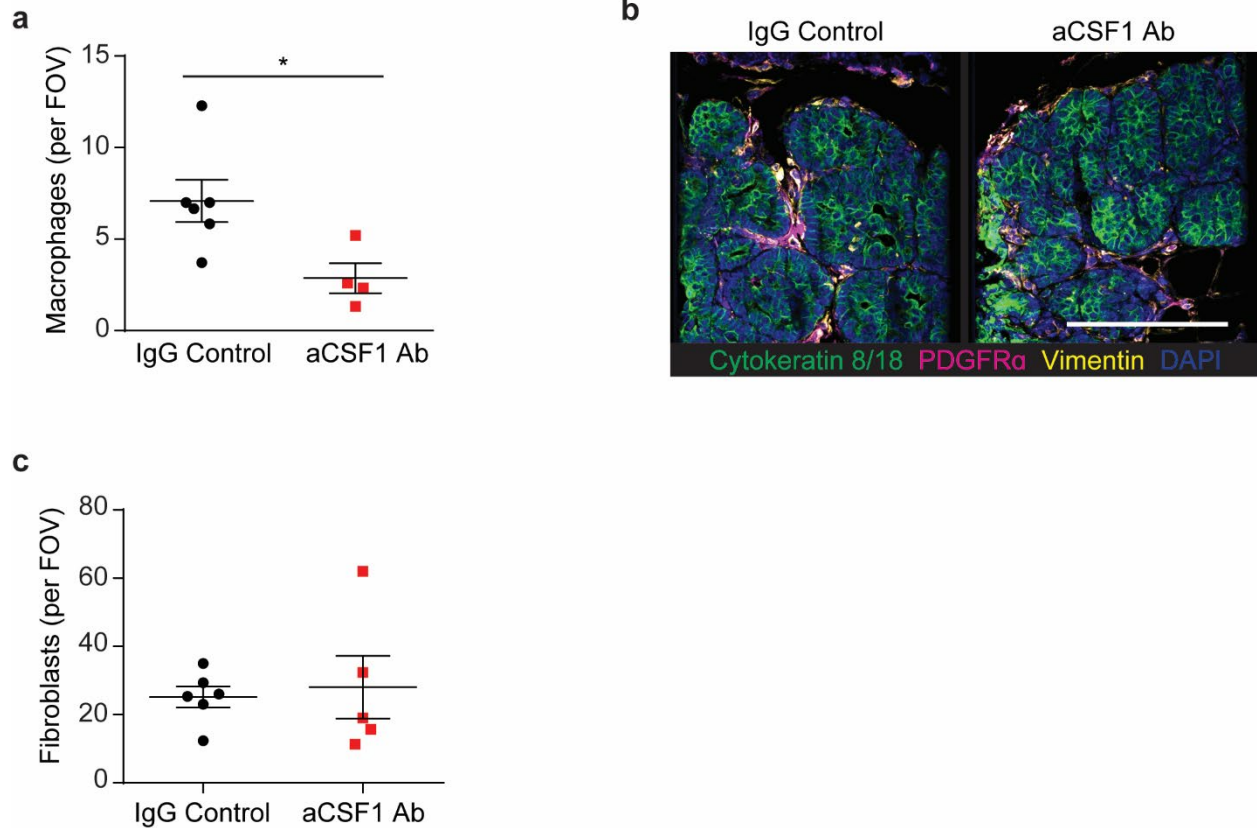
In the presence of Doxycycline:



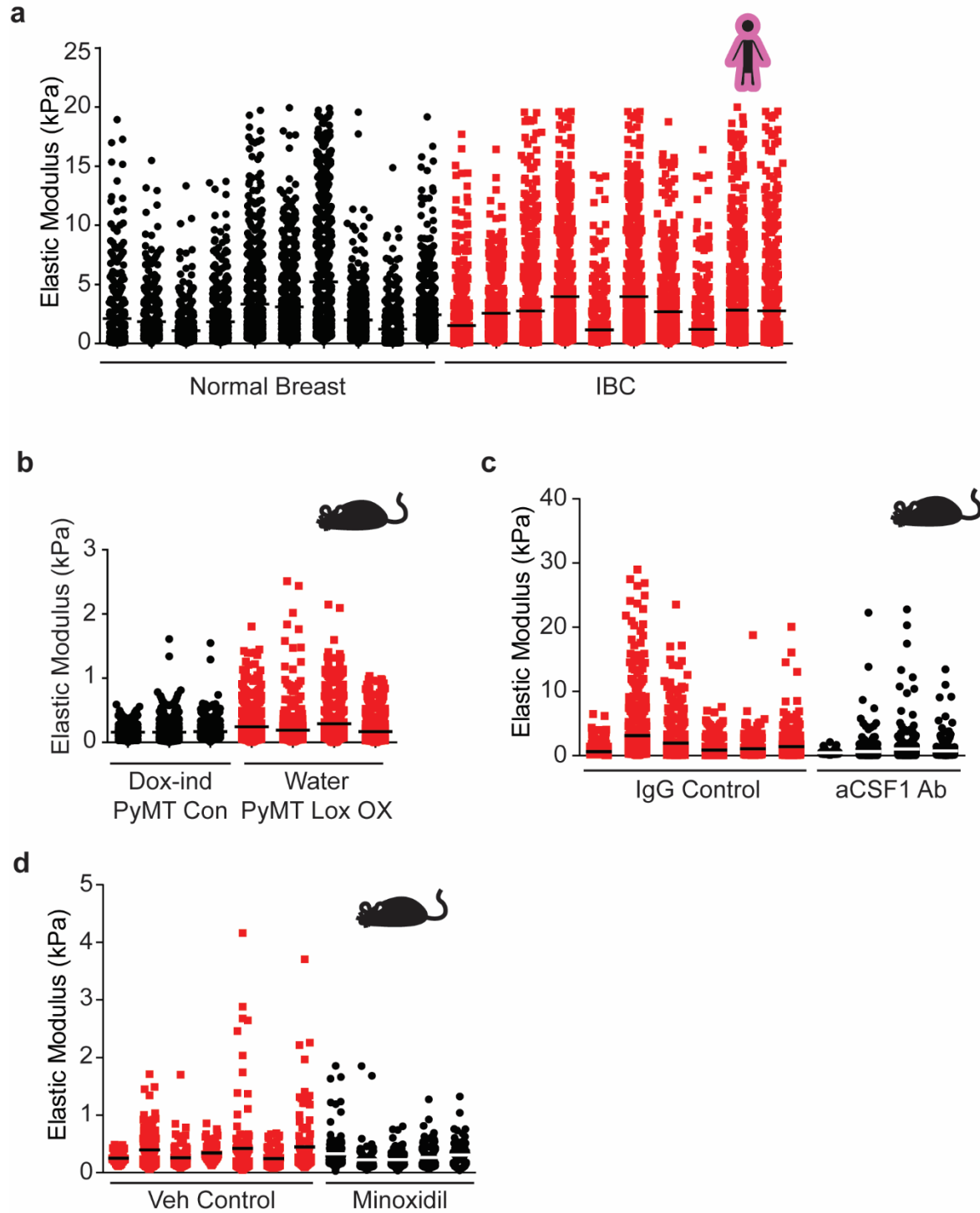
In the absence of Doxycycline:



Supplementary Figure A2.7: (a) PCR results and sequence of PCR primers of N- and C-terminal ends to confirm TetO_mLox transgene incorporation. (b) Diagram of inducible TetOFF system. TetO_mLox transgene is reversibly turned off or on in the presence or absence of doxycycline, respectively.

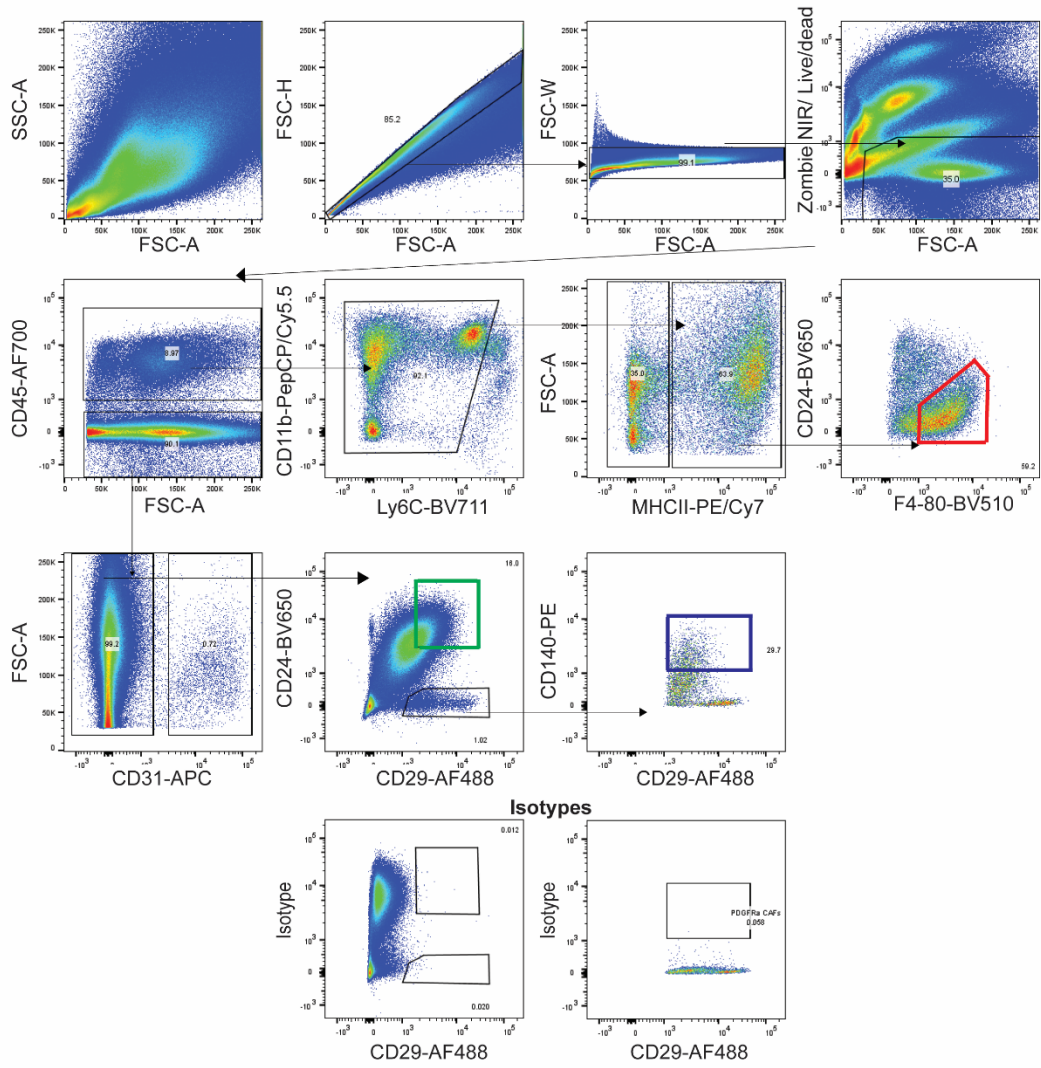


Supplementary Figure A2.8: (a) Scatter plot showing mean \pm SEM of the number of F4/80 positive cells per field of view in IgG1 treated (n = 6) or anti-CSF1 treated (n = 4) PyMT tumors from 8-week-old mice. Statistical analysis was performed using a two-tailed unpaired t-test ($*p < 0.05$). (b) Representative images from 8-week-old IgG1 treated and anti-CSF1 treated PyMT mice stained for cytokeratin 8/18 (green), PDGFR α (magenta), vimentin (yellow), and DAPI (blue). Scale bar is 100 μ m. (c) Scatter plot showing mean \pm SEM of fibroblasts (vimentin $^+$ and PDGFR α^+) per field of view in 8-week-old IgG1 treated (n = 6) and anti-CSF1 (n = 5) treated PyMT mice.

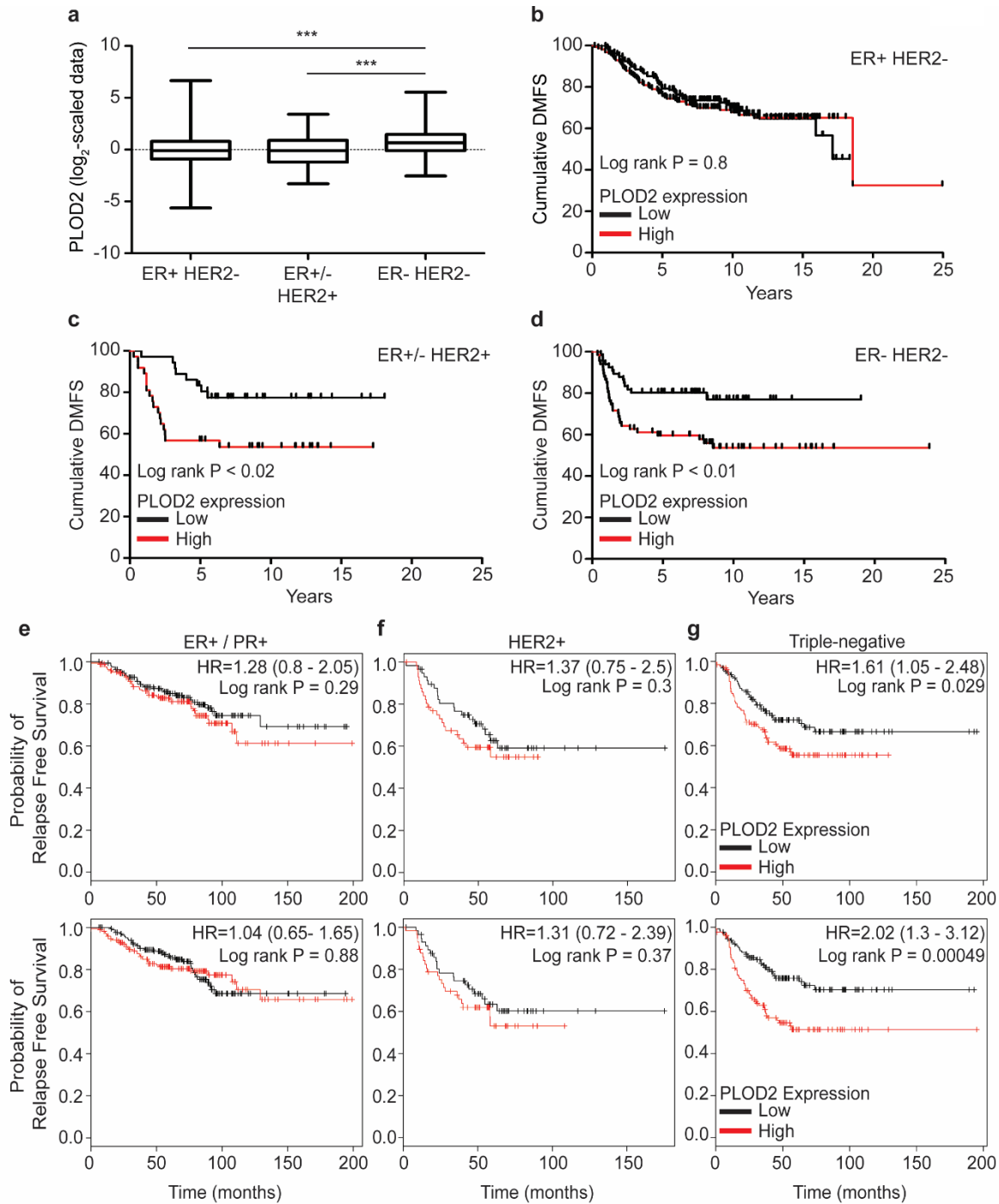


Supplementary Figure A2.9: (a) Scatter plot showing mean and individual values of atomic force microscopy (AFM) microindentation measurements of individual human samples categorized as normal breast tissue (black circles) or invasive ductal carcinoma (IDC; red squares). (b) Scatter plot showing mean and individual values of AFM microindentation measurements of individual mouse mammary tumors from doxycycline treated MMTV-PyMT^{+/-}; Col1a1-tTA^{+/-}; TetO-mLox control mice (DOX-ind PyMT Con; black circles) or water treated mice overexpressing stromal

Lox (Water PyMT Lox OX; red squares). (c) Scatter plot showing mean and individual values of AFM microindentation measurements of individual mouse mammary gland tumors from 8 week old IgG1 treated (IgG Control; red squares) and anti-CSF1 treated (aCSF1 Ab; black circles) PyMT tumors. (d) Scatter plot showing mean and individual values of AFM microindentation measurements of individual mouse mammary gland tumors from PBS vehicle treated (Veh Control; red squares) and minoxidil treated (black circles) PyMT tumors.

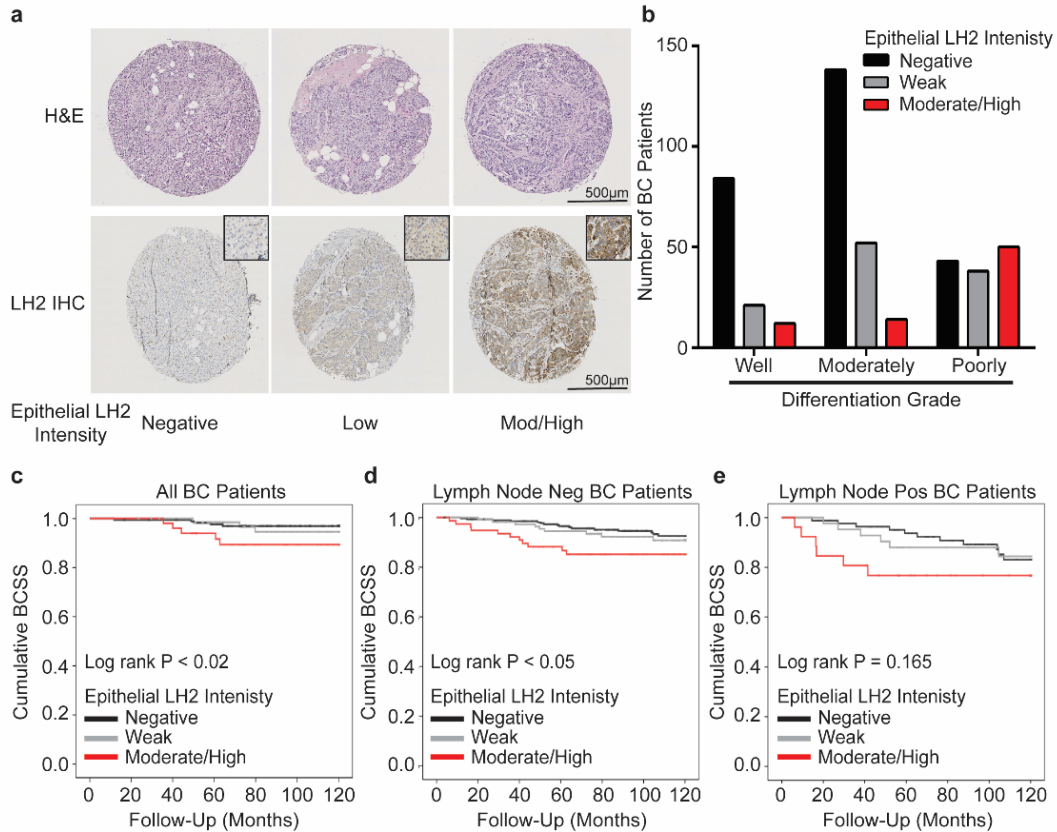


Supplementary Figure A2.10: Gating strategy for sorting tumor cells, cancer-associated fibroblasts, and tumor-associated macrophages from PyMT mice via flow cytometry.



Supplementary Figure A2.11: (a) Log₂ scaled data graphs showing relative PLOD2 gene expression levels in patients stratified by estrogen and epidermal growth factor receptor two (ER/HER2) status (*ER+ HER2-* *n*=314; *ER- or + /HER2+* *n*=73; *ER-/HER2-* *n*=133). Statistical analysis was performed to compare PLOD2 expression levels among subtypes using Kruskal-Wallis test (***p* < 0.001) and Mann-Whitney U test for individual comparisons (***p* < 0.001). (b) Line graphs showing distant metastasis-free survival (DMFS) for patients with estrogen receptor positive and epidermal growth factor receptor two negative breast tumors (*ER+/- HER2-*; *low n*=157 & *high*=157). (c) Line graph of DMFS for patients with estrogen receptor negative or negative and epidermal growth factor receptor two positive breast tumors (*ER- or +/HER2+*; *low*

n=36 & *high*=37). (d) Line graph of DMFS for patients with estrogen receptor negative epidermal growth factor receptor negative breast tumors (ER- HER2-; *low n*=66 & *high*=67). Error bars represent minimum and maximum values for each group. Statistical analyses were performed to compare PLOD2 and DMFS for each subtype or Log-rank (Mantel-Cox) test ($*P<0.02$ and $*P<0.01$ for ER+/-HER2+ and TN, respectively). (e-g) Kaplan-Meier curves indicating the probability of relapse-free survival assessed in ER+/PR+ (e), HER2+ (f), and triple negative (g) breast cancer patients up to 16 years after diagnosis. A correlation between PLOD2 (gene encoding LH2) expression and RFS has been determined using an online tool (<http://kmplot.com/analysis/>) as described in the methods. **Top and bottom panels** represent two distinct Affymetrix PLOD2 probes (202619 and 202620) from the same database. For Kaplan-Meier curves, statistical analyses were performed using LogRank test.

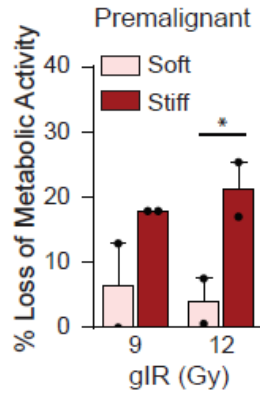


Supplementary Figure A2.12: (a) Tumor samples from incident breast cancer cases were collected, and a tissue microarray (TMA) including two 1-mm cores from each tumor was constructed. Neoplastic epithelial LH2 staining was assessed with semi-quantitative intensity score and stratified as negative, low, or moderate/high. (b) Clinical correlation of neoplastic epithelial LH2 intensity score with tumor grades. (c) Kaplan-Meier curves indicating cumulative breast cancer specific survival (BCSS) based on epithelial LH2 intensity assessed in breast cancer patients up to 10 years after diagnosis (LH2 negative n = 271, weak n = 112, moderate/high n = 77). (d) BCSS curves by epithelial LH2 intensity including only axillary lymph node negative patients (LH2 negative n = 175, weak n = 67, moderate/high n = 50). (e) BCSS curves by epithelial LH2 intensity including only axillary lymph node positive patients (LH2 negative n = 84, weak n = 42, moderate/high n = 26). For tumor grade and LH2 intensity score, statistical analysis was performed using a linear-by-linear association (**p < 0.001). For Kaplan-Meier curves, statistical analyses were using LogRank test.

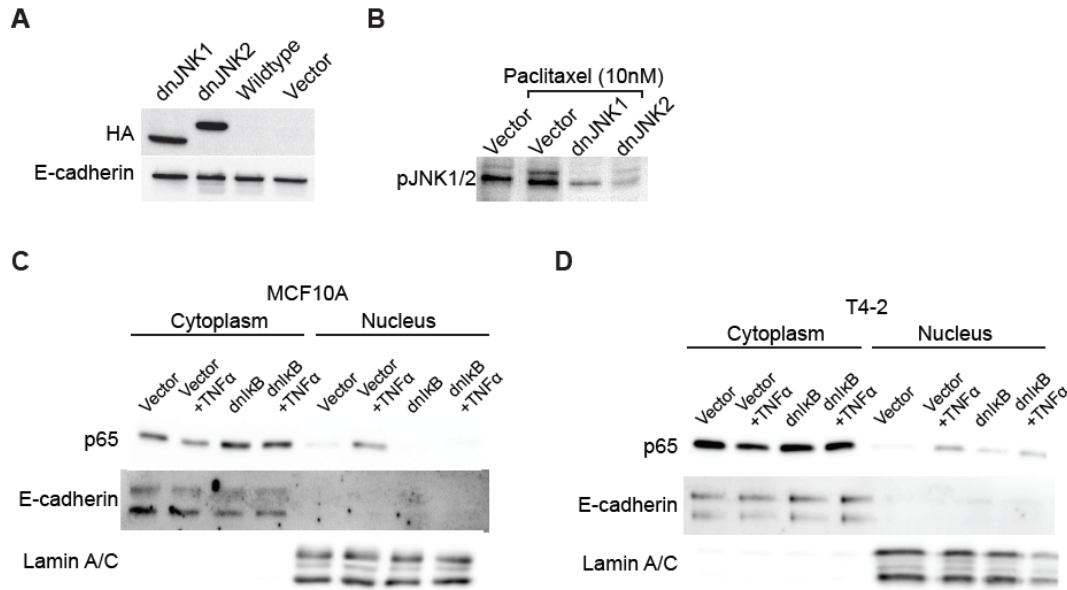
Appendix 3: Supplementary Material for Chapter 4

Supplementary Table A3.1: Human triple negative breast tumor patient data for AFM and picrosirius red analysis

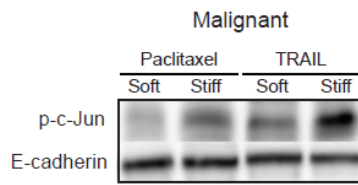
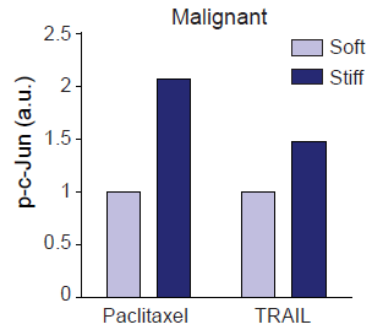
Clinical Data	
Characteristics	Samples (n = 15)
Age (yr)	
Median	61
Molecular Subtype	
Triple negative	15 (100 %)
Neoadjuvant chemotherapy	
Yes	6 (40 %)
No	9 (60 %)



Supplementary Figure A3.1: Bar graph showing mean and SEM of loss of metabolic activity by MTT assay after gamma irradiation treatment in MCF10A cells cultured on soft or stiff substrates (n = 3). Statistical analyses were performed using two-tailed t test (*p < 0.05, **p < 0.01, ***p < 0.001).



Supplementary Figure A3.2: (A) Western blot validating dnJNK construct expression in MCF10A cells. (B) Western blot of phosphorylated JNK 1/2 in vector and dnJNK transduced MCF10A cells treated with 10nM paclitaxel. (C) Western blot for p65 in cytoplasmic and nuclear protein extracts from MCF10A containing the dnIkB construct and treated with recombinant human TNF α . (D) Western blot for p65 in cytoplasmic and nuclear protein extracts from MCF10A containing the dnIkB construct and treated with recombinant human TNF α .

A**B**

Supplementary Figure A3.3: (A) Western blot showing bands for phosphorylated c-Jun (Ser63) in T4-2 cells cultured on soft or stiff substrates after 60 min incubations with 10nM paclitaxel treatment or 200 ng/mL TRAIL. (B) Bar graph showing mean of Western blot quantification of phosphorylated c-Jun (Ser63) in T4-2 cells by pixel density normalized to E-cadherin loading control (n = 1).

Supplementary Table A3.2: Human breast tumor patient data for gene set enrichment analysis.

Clinical Data	
Characteristics	Pretreatment tumor biopsy (n = 138)
Age (yr)	
Median (min-max)	48 (26 - 68)
Molecular Subtype	
Hormone receptor-positive	84 (60.9 %)
HER2-positive	30 (21.7 %)
Triple negative	38 (27.5 %)
pCR	35 (25.4 %)
RCB	
0	35 (25.4 %)
I	9 (6.5 %)
II	55 (39.9 %)
III	32 (23.2 %)
Undetermined	7 (5.1 %)

Publishing Agreement

It is the policy of the University to encourage open access and broad distribution of all theses, dissertations, and manuscripts. The Graduate Division will facilitate the distribution of UCSF theses, dissertations, and manuscripts to the UCSF Library for open access and distribution. UCSF will make such theses, dissertations, and manuscripts accessible to the public and will take reasonable steps to preserve these works in perpetuity.

I hereby grant the non-exclusive, perpetual right to The Regents of the University of California to reproduce, publicly display, distribute, preserve, and publish copies of my thesis, dissertation, or manuscript in any form or media, now existing or later derived, including access online for teaching, research, and public service purposes.

DocuSigned by:

Allison Drain

2416FD62ED384E6...

Author Signature

5/29/2020

Date